Freie Universität Berlin

From Halogen-Bonded Capsules to Polyoxovanadate Cages: Investigating Structure and Reactivity of Molecular Containers by Mass Spectrometry

Inaugural-Dissertation
to obtain the academic degree
Doctor rerum naturalium (Dr. rer. nat.)

submitted to the Department of Biology, Chemistry and Pharmacy
of Freie Universität Berlin

by

Ulrike Warzok

Berlin, February 2018

Die vorliegende Arbeit wurde am Institut für Chemie und Biochemie des Fachbereichs Biologie, Chemie, Pharmazie der Freien Universität Berlin im Zeitraum von September 2014 bis Februar 2018 unter der Betreuung von Prof. Dr. Christoph A. Schalley angefertigt.

1. Gutachter:	Prof. Dr. Christoph A. Schalley
2. Gutachterin:	Prof. Dr. Beate Paulus
Tag der Disputation:	29.03.2018

Für die Menschen, die ich liebe, und in der Hoffnung,
Wichtiges von Unwichtigem unterscheiden zu können.
*Für Heide * 25.07.1988 † 26.12.2017*

Danksagung

Zuallererst gilt mein Dank Christoph A. Schalley, der in mir die Faszination für Massenspektrometrie geweckt und mir die Möglichkeit zur Promotion in seiner Arbeitsgruppe gegeben hat. Bei der Durchführung meiner Doktorarbeit hat er mir jedes Maß an Freiheit gewährt, das ich mir wünschen konnte. Ich habe an den Dingen geforscht, die mich interessieren, und konnte daran wachsen. Gleichzeitig stand er in wichtigen Momenten mit Rat zur Seite und ich konnte viel von ihm lernen. Ich möchte mich für seine Förderung und sein Verständnis, sowie für das mir entgegengebrachte Vertrauen bedanken.

Beate Paulus möchte ich für die Übernahme des Zweitgutachten und für viele interessante Diskussionen im Laufe meiner Arbeit danken.

Hans-Ulrich Reißig bin ich sehr dankbar für seine stete Unterstützung weit über meine Masterarbeit hinaus, sein offenes Ohr und viele wertvolle Ratschläge.

Ich möchte mich sehr herzlich bei all meinen Kooperationspartnern bedanken, ohne die diese Arbeit nicht entstanden wäre. Viele spannende Diskussionen haben mir Einblicke in ganz unterschiedliche Bereiche der Chemie gegeben, die meine Faszination für diese Wissenschaft bereichert haben. Besonders gilt hier mein Dank Lisa Mahnke, Lotta Turunen, Mateusz Marianski und Michael Wendt, mit denen ich sehr intensiv an tollen Projekten arbeiten durfte. Ich hatte viel Freude daran, mit ihnen meine Wissenschaft zu teilen und gleichzeitig von ihnen lernen zu können.

Großer Dank gilt meinen Kollegen aus der Massenspektrometrie, vor allem Fabian und Xuan, mit denen ich viele vergnügliche Stunden verbracht habe, und auf deren Hilfe ich mich immer verlassen konnte. Mein besonderer Dank gilt hier Andreas Springer, der mir das 1x1 der praktischen Massenspektrometrie beigebracht hat, dessen Ruhe mich stets beeindruckt und mir Sicherheit gegeben hat und dessen Mantra „Wer nichts macht, macht nichts falsch“ mir die Angst vor den großen Geräten genommen hat.

Ich möchte mich für die experimentelle Hilfe von Marc Röger, Xuan Pham und Sebastian Müller bedanken.

Allen aktuellen und ehemaligen Mitgliedern meiner Arbeitsgruppe, die mir die ganze Zeit über viel Freude, Kraft und Unterstützung gegeben haben, möchte ich Danke sagen. Wir haben viele schöne und lustige Stunden während und nach der Arbeitszeit verbracht. Mein besonderer Dank gilt hier meinen langjährigen Kollegen und Freunden Henrik Hupatz und Stefan Schoder, die mir nicht nur dabei geholfen haben wissenschaftlich, sondern auch persönlich zu wachsen und auf deren Unterstützung ich mich jederzeit verlassen konnte. Zusammen mit Anneli Kruve-Viil, Georgi Tadeus und Lisa Mahnke haben sie mich bei der Korrektur dieser Doktorarbeit unterstützt.

Ich möchte meinen Freunden danken, mit denen ich unzählige schöne Stunden verbringen durfte und die mich in den letzten Jahren geerdet haben, wenn ich manchmal Gefahr lief mich von dieser Arbeit verschlingen zu lassen. Besonders danke ich meinen Freunden vom Chor und vom Bouldern und natürlich den Menschen in meinem Leben, die mich in meiner Zeit in Berlin teilweise seit fast zehn Jahren begleiten: Georgi, Henrik, Jana, Moritz, Paul und Sara, mit denen ich unzählige glückliche und auch traurige Momente geteilt habe und auf die ich immer blind vertrauen konnte.

Ich danke meiner Familie, insbesondere meiner Mutter, für ihre Liebe, ihr Verständnis und ihre stete Unterstützung natürlich nicht nur während meiner Promotion, sondern während meines gesamten Lebens. Ich bin dankbar für das riesige Vertrauen, das sie mir entgegengebracht haben. Es hat mir ermöglicht meinen Weg zu gehen und meine Träume zu verwirklichen, während ich mir immer ihres Rückhalts sicher sein konnte.

Ich möchte Volker für seine Liebe und Unterstützung während der gesamten Zeit meiner Promotion danken. Wir haben alle unsere Erfolge und auch Misserfolge unserer Doktorarbeiten geteilt und er hat mir auf dem Weg immer wieder die Kraft gegeben weiterzumachen und an mich zu glauben.

Abstract

Synthetic molecular containers are fascinating supramolecular structures which resemble natural complexes. Comparable to enzymes or viruses, they possess the ability to recognize, store and transport guest molecules or ions or act as catalysts for chemical reactions within a confined space. Integral research questions not only focus on their generation, but also on the analysis of their structure and reactivity. Electrospray ionization mass spectrometry (ESI-MS) and ion mobility mass spectrometry (IMS) are well-suited analytical tools which offer insights into these two aspects.

In this dissertation, gas-phase techniques were employed to investigate the structure and reactivity of selected synthetic molecular containers – halogen-bonded supramolecular capsules, antimonato polyoxo-vanadate cages and an amide-ammonium cryptand-host molecule.

A variety of supramolecular capsules assembled from different resorcinarene-based cavitands and supported by neutral or coordinative halogen bonds were analyzed by ESI-MS. The coordinative [N···I^+···N]-type capsules proved to be especially stable and allowed a detailed structural investigation in the gas phase. IMS and theoretical calculations revealed the well-defined gas-phase structures of the dimeric and hexameric capsules: a face-to-face and an octahedral arrangement of the cavitands connected by linear [N···I^+···N] halogen bonds. The capsules form host-guest complexes with tosylate counterions for which the different binding modes were elucidated. Tandem MS experiments revealed aspects of their intrinsic reactivity and the general reactivity of coordinative halogen bonds. Investigation of the complexes` solution reactivity showed that the large halogen-bonded hexameric capsule is in a solvent-dependent equilibrium with a pentameric [N···I^+···N] halogen-bonded capsule. This novel structure was revealed to possess an unusual trigonal bipyramidal geometry with the combination of ESI-MS, IMS and theoretical calculations.

The first water-soluble antimonato polyoxovanadate cages were investigated in solution and gas phase by mass spectrometry. The $\{V_{15}Sb_6\}$ cluster was demonstrated to be present in solution as two distinct species, which both possess an intact, closed cage-like structure: a water-encapsulating and a water-free cluster core. Its chemical behavior is greatly dependent on the encapsulated water molecule, since a transduction of inner-phase reactivity of the guest results in changes in the outer-phase reactivity of the cluster cage. Moreover, the surrounding cationic metal-complexes and the ligand environment, as well as additives influence the reactivity of the $\{V_{15}Sb_6\}$ cluster. In this regard, a $\{Sb_6V_{15}\}\rightarrow\{Sb_8V_{14}\}$ cluster transition was discovered by ESI-MS. This reaction enables in combination with a change in the ligand sphere the formation of an unusual, meta-stable α_1*-$\{V_{14}Sb_8\}$ isomer which forms dimeric superstructures. These were observed in solution and in the gas phase by mass spectrometry.

The guest binding in an amide-ammonium cryptand receptor was investigated in a side project. ESI-MS demonstrated the formation of 1:1 host-guest complexes upon binding of a series of dicarboxylates.

Kurzzusammenfassung

Synthetische molekulare Container sind faszinierende supramolekulare Strukturen. Sie ähneln natürlichen Komplexen wie Enzymen oder Viren in ihrer Fähigkeit Gastmoleküle oder -ionen zu erkennen, zu speichern und zu transportieren oder chemische Reaktionen in begrenzten Räumen zu katalysieren. Ihre Erforschung richtet sich nicht nur auf ihre Bildung, sondern auch auf die Analyse ihrer Struktur und Reaktivität. Elektrosprayionisations-Massenspektrometrie (ESI-MS) und Ionenmobilitäts-Massenspektrometrie (IMS) sind geeignete analytische Werkzeuge, um Einblicke in diese beiden Aspekte zu erhalten.

In dieser Dissertation wurden Gasphasentechniken genutzt, um die Struktur und Reaktivität von ausgewählten synthetischen molekularen Containern zu erforschen. Im Detail wurden Halogen-gebundene supramolekulare Kapseln, Antimonatopolyoxovanadat-Käfige und ein Amid-Ammonium Kryptanden-Wirtsmolekül untersucht. Eine Vielzahl von supramolekularen Kapseln zusammengesetzt aus unterschiedlichen Resorcinaren-basierten Cavitanden und neutralen oder koordinativen Halogenbindungen wurde mittels ESI-MS untersucht. Die koordinativen [N···I^+···N]-Typ Kapseln erwiesen sich als stabiler und konnten in der Gasphase detailliert auf ihrer Struktur hin untersucht werden. IMS und theoretische Rechnungen zeigten die wohldefinierte Struktur der dimeren und hexameren Kapseln: eine Face-to-Face und eine oktaedrische Anordnung der Cavitanden, verbrückt durch lineare [N···I^+···N]-Halogenbindungen. Die Kapseln bilden Wirt-Gast-Komplexe mit Tosylat-Gegenionen und deren unterschiedliche Bindungsmodi wurden aufgedeckt. Tandem MS Experimente offenbarten Aspekte ihrer intrinsischen Reaktivität, als auch die der koordinativen Halogenbindung. Die Untersuchung der Lösungsreaktivität der Komplexe zeigte, dass sich die große hexamere Halogen-gebundene Kapsel in einem Lösungsmittel-abhängigen Gleichgewicht mit einer pentameren [N···I^+···N] Halogen-gebundenen Kapsel befindet. Die Kombination aus ESI-MS, IMS und theoretischen Rechnungen konnte dieser neuen Struktur eine ungewöhnliche trigonal-bipyramidale Geometrie zuweisen.

Die ersten wasserlöslichen Antimonatopolyoxovanadat-Käfige wurden in Lösung und in der Gasphase mittel Massenspektrometrie untersucht. Der {$V_{15}Sb_6$} Cluster liegt in Lösung als zwei unterscheidbare Spezies vor, die beide eine intakte, geschlossene und Käfig-artige Struktur besitzen: ein Wasser-verkapselnder und ein Wasser-freier Clusterkern. Sein chemisches Verhalten ist stark abhängig vom eingeschlossenen Wassermolekül, da eine Übertragung der inneren Reaktivität des Gastes in einer Änderung der äußeren Reaktivität des Clusters resultiert. Zusätzlich haben die umgebenden kationischen Metallkomplexe und die Ligandenumgebung, sowie Additive Einfluss auf die Reaktivität des {$V_{15}Sb_6$} Clusters. In diesem Zusammenhang wurde eine {Sb_6V_{15}}→{Sb_8V_{14}} Clusterumlagerung mittels ESI-MS entdeckt. Diese Reaktion ermöglichte in der Kombination mit einer Änderung der Ligandensphäre die Bildung eines außergewöhnlichen meta-stablilen α_1*-{$V_{14}Sb_8$} Isomers, welches dimere Superstrukturen bildet. Diese wurden sowohl in Lösung, als auch in der Gasphase mittels Massenspektrometrie beobachtet.

Die Gasteinlagerung in einen Amid-Ammonium Kryptanden wurde in einem Nebenprojekt untersucht. ESI-MS zeigte dabei die Bildung von 1:1 Wirt-Gast-Komplexen mit einer Reihe von Dicarboxylaten.

Table of Content

1. Introduction

The analysis of newly synthesized chemical structures is an integral part of chemical research. The understanding of the structure and reactivity of compounds is necessary for the development of new synthetic methods and further applications. The fast advancements of both fields – generation and characterization of novel species – over the last decades have greatly influenced each other and contributed to the overall progress in chemistry. On the one hand, the synthesis of larger and more complicated molecules created the need for improved analytical methods, while, on the other hand, their development then inspired chemists to aim for ever more sophisticated structures. Mass spectrometry in combination with soft-ionization methods, such as electrospray ionization, can be named as one of these great scientific breakthroughs in this field. It enabled scientists to investigate a multitude of analytes under less drastic conditions than before, yielding ions from intact, large complexes and directly from solution. This opened the gate for the investigation of intriguing assemblies of increasing complexity, both natural and synthetic.

In the work presented here, electrospray ionization mass spectrometry was employed to study synthetic molecular containers. The questions, what molecular containers are and why they might be an interesting research topic worth pursuing, can be addressed by regarding natural phenomena as an example.

Compartmentalization presents one of the key features of living systems. GÁNTI described this as one of the requirements for life itself in his theory on the "Principle of Life" with the chemoton model.[1] It states that a system can be considered 'alive' if it possesses a metabolism, is able to self-replicate and is enclosed within a chemical boundary. The requirement for a container – a compartmentalization – originates from the need to separate the system from the surrounding, while still allowing the exchange of matter and energy.[2] Cells, as the smallest living units, are certainly the most prominent example of compartmentalization in nature. A lipid bilayer forms the cell membrane, a natural molecular container which is specific in its function of protection, transport and reactivity-controlled metabolism. But it can, for one type of cell, vary in size and exact composition with a variable number of building blocks embedded in the structure. A second intriguing example for natural molecular containers are viruses. They are not alive by GÁNTI`s definition, but rather infectious agents that are dependent on the metabolism of living cells of other organisms. However, they fulfil the requirement of compartmentalization, as their DNA is encapsulated in an outer shell called capsid. In contrast to cell membranes, the capsid is of a discrete size and contains a specific number of aggregated protein monomers. It most often exhibits a rod-like or spherical morphology with an expansion of up to ca. 100 nm.[3] Spherical capsids are usually composed of multiples of 60 proteins which corresponds to the symmetry of the different icosahedral structures that can be formed (Figure 1a, b). The formation mechanism involves a stepwise self-assembly of protein subunits, first into smaller oligomers called capsomeres, then into a regular polyhedron (Figure 1c).[4] The capsid protects the genetic material of the virus and delivers it to host cells for replication. It forms the interface between the virus and the host, making it crucial for the infection pathway, as it needs to be able to adapt its structure accordingly for successful cell invasion.[5]

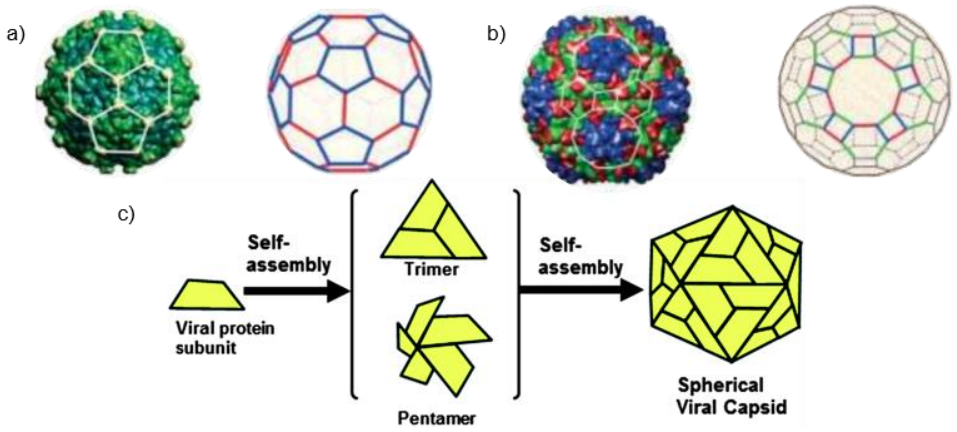

Figure 1: Virus capsids as natural molecular containers. a) Structure of the pariacoto virus with a truncated icosahedron; b) structure of the cow-pea chlorotic virus with a rhombicosidodecahedron. Reprinted with permission from Andersson[6]. (© 2008 WILEY-VCH Verlag GmbH & Co. KGaA, Weinheim). c) Hierarchical self-assembly of a capsid. Reprinted with permission from Matsuurua[4] (© 2013, Royal Society of Chemistry).

With nature as a potent role model, it is no surprise that chemists have set out to create synthetic molecular containers. They should likewise or at least similarly be able to recognize, store and transport guest molecules or ions or to act as catalysts for chemical reactions within a confined space. This challenge is one of the integral questions with which supramolecular chemistry is concerned. This field of research focusses in general on the formation of complex molecular assemblies on the basis of noncovalent interactions, in order to achieve functionality similar to natural processes or beyond them. The aim for functionality implies the need to selectively generate and understand structures that are capable of a certain reactivity. In the field of molecular containers, the last few decades of research have put forth several different approaches to this endeavor, making use of biological or synthetic organic, hybrid organic/inorganic or purely inorganic systems and a variety of different noncovalent interactions. Significant progress has already been made; yet, the results on functionality are still scarce and rather rudimentary compared to nature`s sophistication.

When again considering nature as the role model, it becomes obvious that structural diversity leads to the highly specialized functionality of biological assemblies which, for instance, can sustain a whole living organism. Consequently, the development of novel synthetic molecular containers with the long-term goal of creating functional systems should take advantage of all chemical means available. If a great pool of diverse structures existed by using well-understood interactions and by extending the knowledge of rather unexplored binding motifs, tailor-made solutions might be applicable to chemical problems. Or alternatively, an unsolved challenge or a still unasked question could be found for which novel molecular assemblies might provide a solution.

In addition to diversity, a second requirement is the detailed understanding of the structure of new molecular containers, as it determines their chemical and physical properties, as well as their reactivity. In this context, reactivity can be understood in a very broad meaning, referring to the interaction of a complex with other molecules or ions in a greater system or to its intrinsic behavior in isolation. Thirdly, comprehensive insights into the reactivity of molecular containers might open the way to discover possible functionality.

Additionally, this might even create a feedback loop that offers a greater understanding of the original natural role models.[7]

The three aspects just outlined – chemical diversity, knowledge of structure and reactivity – were taken as a guideline throughout the thesis presented herein to contribute to the field of synthetic molecular containers. This could assist to pave a way to the long-term goal of their application in functional systems. To meet these objectives, research topics have been selected which cover a broad spectrum of different chemical architectures.

Molecular containers have been investigated that are of hybrid organic/inorganic, purely inorganic and purely organic nature, namely halogen-bonded supramolecular capsules, antimonato polyoxovanadates cages and an amide-ammonium cryptand-host molecule in a side project. These complexes exhibit significant structural differences, starting with the prevailing interaction that leads to their formation – halogen bonding, metal coordination in form of metal-oxo complexes or covalent bonds. The specific research questions consequently differ for each project; however, the focus was in all cases set on the investigation of their structure and reactivity.

Mass spectrometry was used as the analytical method of choice for the research presented, posing a second unifying aspect for all three projects. This powerful and versatile tool can serve the purpose of this research to a great extent. State-of-the-art techniques including electrospray ionization mass spectrometry (ESI-MS) and tandem mass spectrometric experiments as well as the fast-emerging ion mobility mass spectrometry (IMS) were utilized to elucidate the structure of new architectures and their reactivity in gas phase and solution.

Specific objectives were defined for the three main topics:

- **Halogen-bonded supramolecular capsules** are a new subclass of supramolecular containers which make use of the only recently 'rediscovered' halogen bond. At the beginning of this thesis in 2014, very little was known about these complexes or their reactivity in solution and they have not been analyzed in the gas phase at all. This lack in mass spectrometric measurements is likely due to the challenge of transferring these noncovalent complexes into the gas phase. Therefore, the research objectives were the following:
  - finding efficient ways to transfer novel halogen-bonded capsules intact into the gas-phase
  - analysis of their structure in the gas-phase using ESI-MS and IMS
  - investigation of their intrinsic gas-phase reactivity with tandem MS
  - exploring the reactivity of large capsules in solution, investigating the resulting reaction products and determining their structure

- Prior to this thesis in 2014, **antimonato polyoxovanadates cages** have only been accessible under drastic solvothermal conditions. Due to the absence of a well-soluble precursor, the discovery process relayed solely on serendipity, rather than rational synthesis. The solution and gas-phase chemistry of antimonato polyoxovanadate cages was virtually unexplored, which left fundamental questions

concerning their formation mechanisms, stability and host-guest chemistry unanswered. This lack of knowledge could to some extent account for the relatively slow progress to generate more complex, functional assemblies from polyoxovanadates, as compared to the other members of the polyoxometalate class. With the emergence of the first water-soluble antimonato polyoxovanadate compounds, the scientific questions posed in this thesis were the following:

- characterization of novel compounds in solution by ESI-MS
- investigation of their solution reactivity with isotope exchange experiments and aging studies
- investigation of their gas-phase reactivity by tandem MS experiments
- elucidation of the reaction mechanism for the observed reactivity

- The guest binding in a novel **amide-ammonium cryptand** receptor was covered in a side project. Complementary to solution and solid-state characterization, the complex structure of the host-guest complexes upon binding of dicarboxylates were investigated in the gas phase.

The work presented in this thesis is primarily analytical; yet, relies greatly on the synthesis of novel molecular containers or at least of their building blocks. Therefore, all three topics have been investigated in teams together with researchers who synthesized the samples of interest and/or who extended the analytical investigations with complementary methods.

The following chapters will cover the theoretical background relevant to this work.

2. Theoretical Background

2.1. Introduction to Supramolecular Chemistry

2.1.1. Noncovalent Interactions

While single molecules are constructed from covalent bonds between different atoms, biomolecules and biological structures are governed by noncovalent interactions between different molecules and ions. They have progressed to an outstanding complexity and are able to provide a magnitude of different functions, sustaining highly evolved living creatures. For proteins and protein complexes as an example, only the primary, still unfolded structure is formed by the covalent bonds between the amino acids. The formation of the secondary, tertiary and quaternary structure, that involve the folding of the peptide chain into local and global structures, as well as the co-assembly of several folded proteins into a protein complex, is driven by the formation of numerous noncovalent or in some cases reversible covalent bonds. Supramolecular chemistry is based on the objective to construct complex and functional synthetic systems and takes natural architectures very often as the role model or at least as an inspiration. This results in a "chemistry beyond the molecule", as expressed by LEHN.[8] During the last 50 years, this field has steadily grown and is nowadays one of the pillars of chemical research.

A series of different noncovalent interactions was identified during the last decades, which are also present in natural complexes. Both, their detailed investigation concerning energetics and structural motifs to answer fundamental questions, as well as their application to form interesting architectures is an integral part of supramolecular chemistry. Numerous applications of noncovalent interactions and the resulting supramolecular architectures are available for sensing and separation, for catalysis and biomedical technologies or for nanotechnology like molecular machines.[9] The different types of interactions cover a wide range of binding energies and can in some cases even compete with covalent bonds (Table 1). The strongest are electrostatic interactions between two charged species (ion-ion interaction) and coordinative bonds between a metal center and a ligand. Electrostatic interactions between a charged species and a dipole or two dipoles are significantly weaker due to the decreased Coulomb attraction. Hydrogen bonds and halogen bonds are both directional interactions of an electron deficient atom (or ion) with a Lewis base. Their strength depends strongly on the binding partners and for both cases, charged hydrogen bonds and halogen bonds are significantly stronger than bonds between two neutral components. The interactions of π-systems are manifold and can range from an attractive bond with cations over neutral molecules, such as other aryl systems, to anions, depending on the electronic properties of the aromatic system involved. Electron-rich aromatics bind electron-poor species, such as cations, and *vice versa*. The weakest noncovalent interactions are van der Waals forces between unpolar molecules like alkanes that result from the dispersion interaction between two induced dipoles.[9–11] The binding energies for each interaction span a wide range and reflect the high dependency of noncovalent interactions on subtle structural or electronic variations of the binding partners or of the medium.

Table 1: Overview of different interactions with typical binding energies.[9–11]

Interaction	Binding energy / kJ·mol^{-1}	Example
covalent bonds (σ-bonds)	up to 450 (570 for HF)	H_3C-CH_3
ion-ion	100 - 350	$Na^+\cdots Cl^-$
ion-dipole	50 - 200	$Na^+\cdots O{=}CMe_2$
dipole-dipole	5 - 50	$O{=}CMe_2\cdots O{=}CMe_2$
coordinative bonds	100 - 350	$[Fe(CN)_6]^{3-}$
hydrogen bonds	2 - 120	NH···O=C
halogen bonds	1 - 40	F_5C_6-I···Cl^-
cation-π	5-80	Na^+ ···benzene
anion-π	1-7	Cl^- ···perfluorobenzene
π-π	2 - 50	benzene···perfluorobenzene
van der Waals	< 5	alkyl···alkyl

For the work presented in this thesis, directional noncovalent interactions were important to construct organic and inorganic molecular containers and to bind different guests within their cavities. Halogen bonding (XB) and metal coordination, and to some extend also hydrogen bonding (HB) have been employed (Figure 2). The directionality of hydrogen bonds stems in general from the polarization of the R-H hydrogen (R = C, N, O and F) that is maximal on the opposite end of the R-H bond. The optimal bond angle for strong HB is 180°, yet smaller angles down to ca. 110° were also observed for weaker HB interactions. Halogen bonding is one of the less common, but fast emerging interactions investigated in different fields of supramolecular chemistry and will be covered in greater detail in chapter 2.2. The geometry and directionality of metal-ligand-coordination complexes depends on the metal center, its oxidation and spin state, as well as the electronic and steric properties of the ligand. In the case of metal-oxo complexes, which have been investigated as part of this thesis, different binding modes can be found for the combination of oxo ligands (O^{2-}) and early transition metals: $L_nM{\equiv}O$, $L_nM{=}O$ and μ^2 to μ^4-bridged, dinuclear, trinuclear or even tetranuclear complexes.

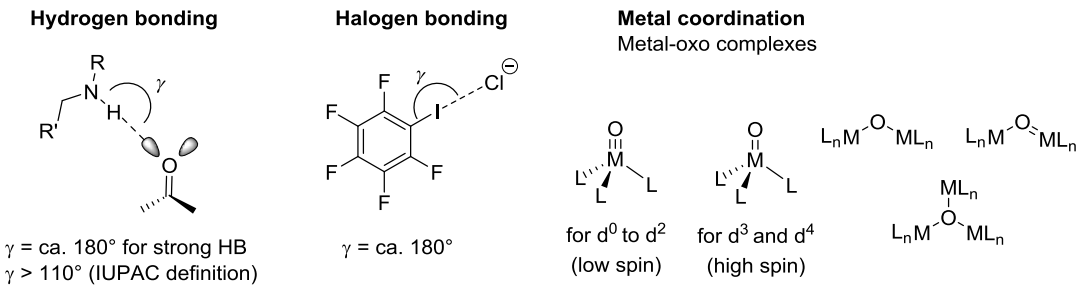

Figure 2: Selected examples for complexes formed by directional noncovalent interactions.

Transition metals usually form aqua complexes in aqueous solution which can be deprotonated due to the increased acidity of the aqua ligand upon binding to the electron-deficient metal center. This results in the formation of hydroxy (OH^-) or oxo (O^{2-}) complexes. Oxo ligands are strong σ- and π-donors; they can contribute up to four electron pairs to one or more metal centers which may lead to a high degree of bridging

within the complex. The M-O bond length is usually between 1.6 and 1.7 Å. Different binding modes for metal-oxo complexes are depicted in Figure 3.[12,13] If the oxo ligand participates in one or more π-bonds, it becomes increasingly electron-deficient which does not promote reprotonation, but rather the attack of nucleophiles. Tetragonal L_3MO complexes with π-bonds are only known for the transition metals from group 1 to 8. This complex type requires a low number of d-electrons on the metal and, hence, would need a very high oxidation state for late transition metals. However, the corresponding complexes of cobalt, rhodium, iridium and so on are unstable and eliminate H_2O_2 or O_2.[13]

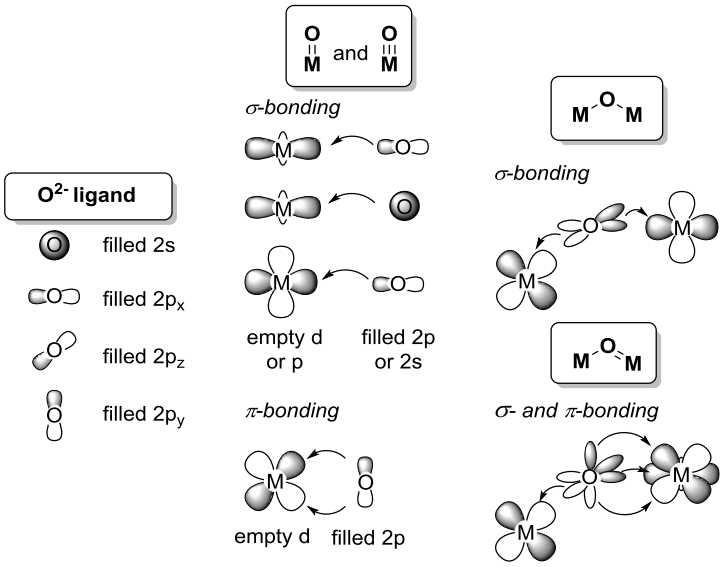

Figure 3: Examples for possible binding modes of metal-oxo complexes.

2.1.2. Self-assembly

As WHITESIDES stated it, "molecular self-assembly is the spontaneous association of molecules under equilibrium conditions into stable, structurally well-defined aggregates joined by noncovalent bonds". It is one of the main formation strategies for complex natural structures and most likely the only way to reach the size and complexity of biological nanoscale systems with synthetic molecular chemistry as opposed to purely covalent chemistry.[14] The formation of noncovalent and also reversible covalent bonds, such as imines or disulfides, are the key tool for self-assembly, but these interactions have mostly inherently smaller binding energies and are more labile than covalent bonds. Hence, the contribution of entropy is more significant to the overall system, as this term is in the majority of the cases unfavorable for complex formation. The assembly of thermodynamically stable complexes is therefore dependent on the interplay between enthalpy and entropy. It is usually supported by the formation of several weak noncovalent interactions which cooperate in their formation.[14] An important aspect is that the single components of a self-assembled complex need to contain all information necessary for a correct assembly. This includes the complementarity of size and shape of the single components to each other, as well as the complementary of their binding sites for the different shape-dependent interactions, e.g. van der Waals interaction or solvophobic effects, or directed interactions, such as hydrogen bonds, coordinative bonds or halogen

bonds.[15] Preorganization of the subcomponents is normally beneficial to the formation of entropically unfavored complexes; however a certain degree of flexibility has also been found to be of advantage.[16] Self-assembly always leads to the energetically favored minimum structure in a closed system, driven only by the Brownian motion of the molecules and without the influence of an external energy source. This requires the pathways to be fully reversible and dynamic to allow for error correction of mismatched components or the disassembly of kinetic products. A well-known example from nature of a self-assembled structure is the DNA double helix. It forms from two strands into a stable and robust complex by the hydrogen-bonding pattern between complementary oligonucleotides (Figure 4a). Nucleation, which is the assembly of the first four base pairs, is still endergonic, while the subsequent propagation of the double strand is exergonic.[15] Numerous examples of synthetic self-assembled complexes will be explained in the following chapters.

Hierarchical self-assembly is an extension to this concept that involves the assembly of several components bearing binding sites for noncovalent interactions of different strength. In equilibrium, the strongest interactions will determine the organization of substructures, while weaker interactions then drive the assembly further to a higher degree of order (Figure 4b).

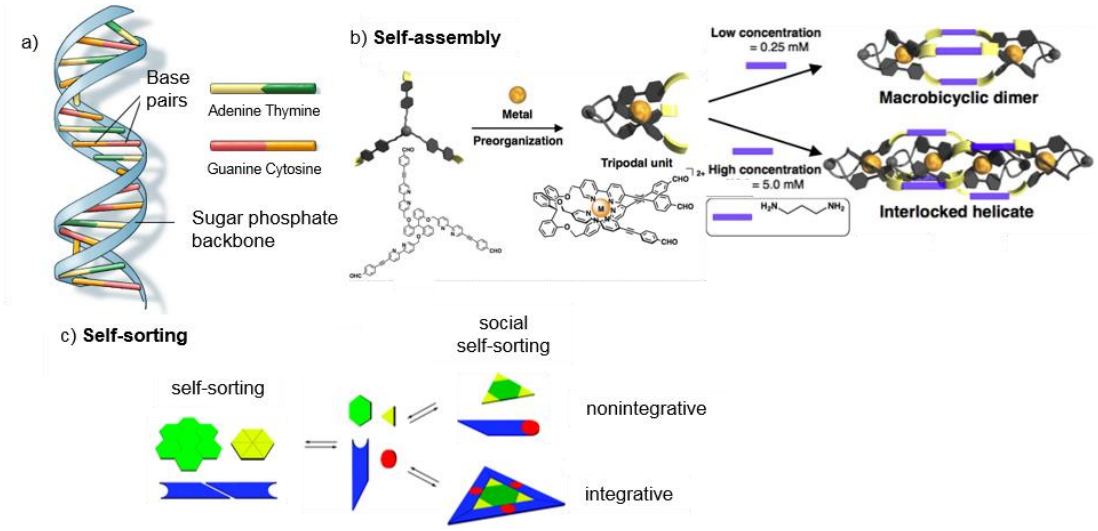

Figure 4: a) Self-assembled DNA double helix (Credit: U.S. National Library of Medicine)[17]. b) Hierarchical self-assembly enables formation of an interlocked helicate from three components; reprinted and adapted with permission from Nakamura *et al.*[18] (© 2016 American Chemical Society). c) Schematic representation of the different types of self-sorting; reprinted and adapted with permission from Safont-Sempere *et al.*[19] (© 2011 American Chemical Society).

A mixture of several self-assembled complexes or their components can either lead to a statistical mixture of their components in newly formed complexes or to a so-called self-sorted system of higher order. SCHALLEY and coworkers give the following definition in their related review: "The term self-sorting describes the ability of mixtures of different molecules to recognize their mutual counterparts selectively so that specific pairs are formed rather than a library of all possible noncovalent complexes of the compounds present in the mixture."[20] These processes of recognition and self-recognition between molecules or ions within complex mixtures can lead to an affinity for the components for themselves or for others (narcissistic vs. social self-sorting) and is most often under thermodynamic control (Figure 4c).[19]

2.2. Halogen Bonding

2.2.1. History and Definition

At first glance, halogen atoms in organic molecules will likely be considered sites of high electron density due to the number of free electron pairs located at the halogen atoms and their considerably high electronegativity. They range from 4.0 to 2.7 when going from fluorine to iodine, as compared to 2.6 for carbon. Consequently, they would be expected to take part in noncovalent interactions primarily as electron-donor sites, e.g. as hydrogen-bonding (HB) acceptors. However, it was found as early as 1814 that their chemistry is more diverse and involves attractive interactions with other electron donors. These first reports showed that iodine forms complexes with ammonia, amylose[21] or iodide[22] and that it forms solutions of different colors from brown over red to violet, greatly depending on the nature of the solvent.[23] At this time, the understanding of these phenomena was poor and only later, it was rationalized with the concept of halogen bonding. The electron density of a halogen atom was found to be anisotropic exhibiting a region of higher and a region of lower electron density. This results in the formation of a σ-hole which can form attractive interactions with electron donors in the direction of the elongated covalent R-X bond.[24,25] ODD HASSEL received the Nobel prize in chemistry in 1969 for the discovery that, among over things, halogens can act as electrophiles to assemble with electron donors to highly structured, crystalline charge-transfer complexes (Figure 5).[26] This seminal work was the basis for a greater understanding of the interactions driving the formation of such complexes.[27]

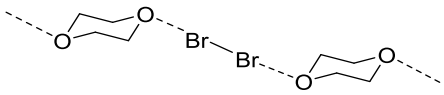

Figure 5: First X-ray crystallography study done by HASSEL in 1954 presented halogen bonding that led to the chain-like *n*:*n* complex of 1,4-dioxane and bromine.[26]

However only in the early 1990s, computational studies could provide a detailed rationale for halogen bonding including its striking stereo-electronic properties. A unifying IUPAC project settled in 2013 on the term "halogen bonding" (XB) and provided an official definition for this noncovalent interaction. It states that "a halogen bond occurs when there is evidence of a net attractive interaction between an electrophilic region associated with a halogen atom in a molecular entity and a nucleophilic region in another, or the same, molecular entity" (Figure 6).[28]

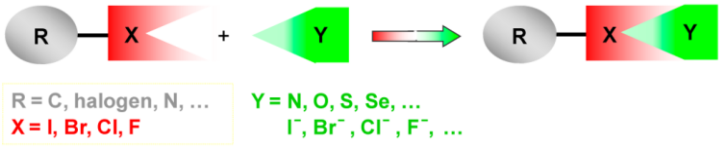

Figure 6: Schematic presentation of the halogen bond; reprinted with permission from Cavallo *et al.*[21] (© 2016 American Chemical Society).

Halogen bonding is the frontrunner for a set of attractive interactions, which are currently drawing increasing scientific interest, involving elements of groups XIV−XVI and nucleophiles to form so-called chalcogen bonds, pnicogen bonds or tetrel bonds. A corresponding IUPAC initiative has also been

announced to account for the anisotropic charge distribution and amphoteric behavior as a common property for many elements.[29]

2.2.2. Classical Halogen Bonds

Classical halogen bonds were used as the connective motifs for the assembly of neutral supramolecular capsules in this thesis. Halogen bonds are often compared to hydrogen bonds and these two noncovalent interactions are indeed similar to some extent. Their binding energies lie in a similar range, with free energies of XB between neutral donors and acceptors spanning from ~0 to ca. 40 kJ mol^{-1} in solution.[11] Among them, inorganic donors such as ICl, IBr and I_2 form the strongest XB. Charged XB complexes like I_3^- exhibt generally stronger binding, this complex was shown to have a binding energy of 126 kJ mol^{-1} in the gas phase.[30] The foremost characteristic of halogen bonds is their strong directionality with a bonding angle R−X···Y of close to 180°, especially for short and strong XBs.[31] This characteristic is much more pronounced than for HB.

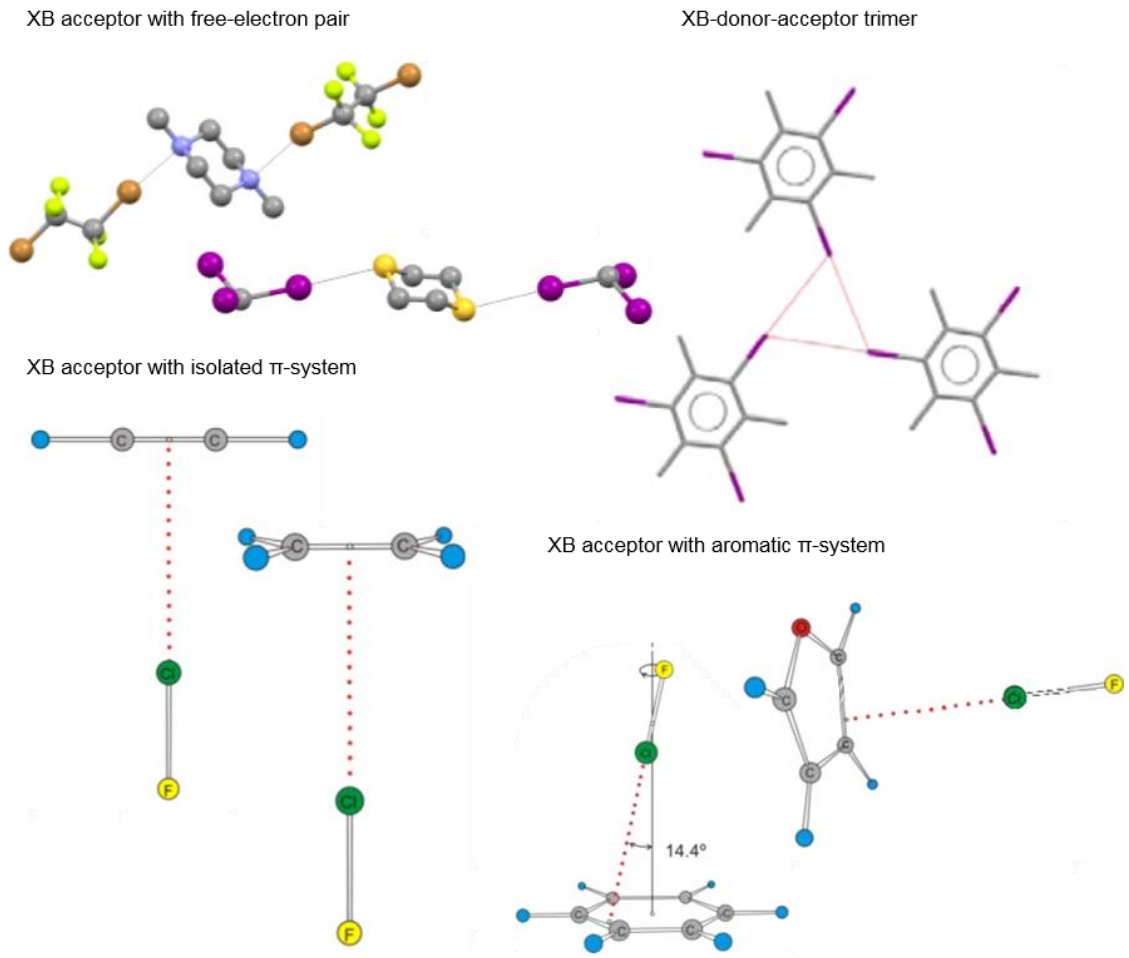

Figure 7: Examples of halogen-bonded complexes showing different geometries depending on the nature of the XB acceptor (C in gray, N in violet, O in red, H in blue, I in purple, Br in light brown, Cl in green, F in light yellow, S in dark yellow). Reprinted and adapted with permission from Cavallo *et al.*[21] (© 2016 American Chemical Society) and from Gilday *et al.*[21,32] (© 2015 American Chemical Society).

Depending on the nature of the XB acceptor, complex geometries can differ. Generally, the bond forms along the direction of the donating free electron pair (n) or along the symmetry axis of the π-bonding orbital. In the presence of an acceptor with both, a free electron pair and aromatic π-bonds, the n-pair is usually preferred (Figure 7).[33,34] An interesting example is the XB-donor-acceptor trimer triiodomesitylene in which the covalently bound halogen atoms act both as the XB acceptor and donor.[35]

Bonding situation

The nature of the bonding situation in XB as an attractive noncovalent interaction has been subject of numerous theoretical studies. Several different bonding components have been identified to contribute to the strength and directionality of XBs, namely electrostatic, charge-transfer and polarization interactions as well as dispersion and a repulsive component which results from the Pauli exclusion principle.

The most frequently described model involves electrostatics; that is, the region of positive electrostatic potential along the C−X covalent bond on the opposing part of the halogen surface, which POLITZER *et al.* described as a "σ-hole".[36] The halogen atom is furthermore surrounded by a belt of negative electrostatic potential. This combination makes covalently bound halogens amphoteric and rationalizes well the observed binding pattern of linear interactions with nucleophiles and lateral interactions with electrophiles (Figure 8).[21] Furthermore, several theoretical and experimental studies showed a good linear correlation between the interaction energy ΔE of the halogen-bonded adduct and the most positive electrostatic potential $V_{S,max}$ of the σ-hole.[25,37]

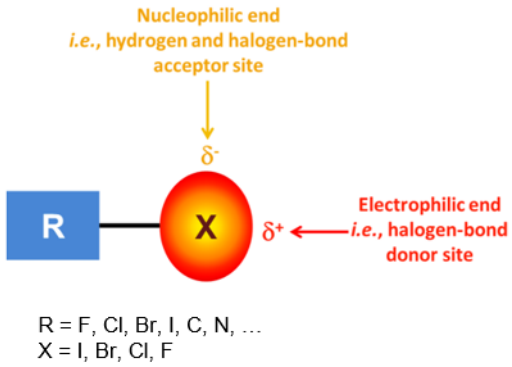

Figure 8: Anisotropic distribution of the electron density around a covalently bound halogen atom and resulting pattern for the interactions with electrophils and nucleophils. Reprinted with permission from Cavallo *et al.*[21] (© 2016 American Chemical Society).

A different approach classifies halogen bonds as charge-transfer complexes where electron density is donated from the XB acceptor into the antibonding σ*-orbital of the R-X bond. This is well in line with a Lewis acid-base interaction.[27,38] The resulting n→σ* or π→σ* interactions account for the high XB directionality. Several experimental and theoretical studies are supporting this model. For UV/Vis studies in solution, ROSOKHA *et al.* used the same XB donor with different XB acceptors and found a linear correlation between the absorption energies and the oxidation potential of XB acceptor.[39]

X-ray analysis of several halogen-bonded structures revealed the elongation of the R-X bond as in 1,4-Diiodotetrafluorobenzene or in different aliphatic bromocarbons that are in agreement with

charge-transfer interactions.[40,41] A substantial HOMO and LUMO overlap that is an indicator for a significant covalent component of the XB due to a charge transfer, as well as a good linear correlation between charge-transfer energies and total interaction energies were shown by theoretical studies.[42]

As an additional minor contribution to the halogen bond, two atoms with high polarizability and in closer contact than the sum of their van der Waals radii will likely be involved in dispersion and polarization. In this context, chloromethane was predicted to be a XB donor in a theoretical complex $CH_3Cl\cdots O{=}CH_2$, even though it exhibits a completely negative electrostatic surface around the chlorine atom. The electron density of both components of the complex are polarized by the electric field of the other, which results in a positive σ-hole on the chlorine and an attractive interaction between chloromethane and formaldehyde.[43]

Factors influencing the XB bond

The strength of halogen bonds can be tuned over a wide energy range by a series of possible adjustments. The XB donor ability increases with higher polarizability and decreased electronegativity of the halogen atom. The positive character of corresponding σ-holes grows from fluorine to iodine, as shown in Figure 9a for CF_3X complexes. Fluorine is generally the poorest XB donor and in CF_4 without a positive electron density. Nevertheless, it can still exhibit a positive σ-hole when in its elemental composition or when substituted with very strongly electron-withdrawing groups, such as $-SO_2OCOF$ (Figure 9b).[36,44] For organohalides, the bonding strength depends greatly on the hybridization of the carbon atom directly connected to the halogen, as a greater s component in an sp^x-hybridized carbon results in a greater electron-withdrawing ability. Hence, the order to arrive at the stronger XB donor is $C(sp){-}X > C(sp^2){-}X > C(sp^3){-}X$.[45] Further possible adjustments involve other compositional or structural modifications that affect the electron-withdrawing ability of the whole donor molecule, e.g. a high fluorination grade of an aryl moiety, the presence of haloheteroarenes or the introduction of a positive charge close to the halogen atom.[46]

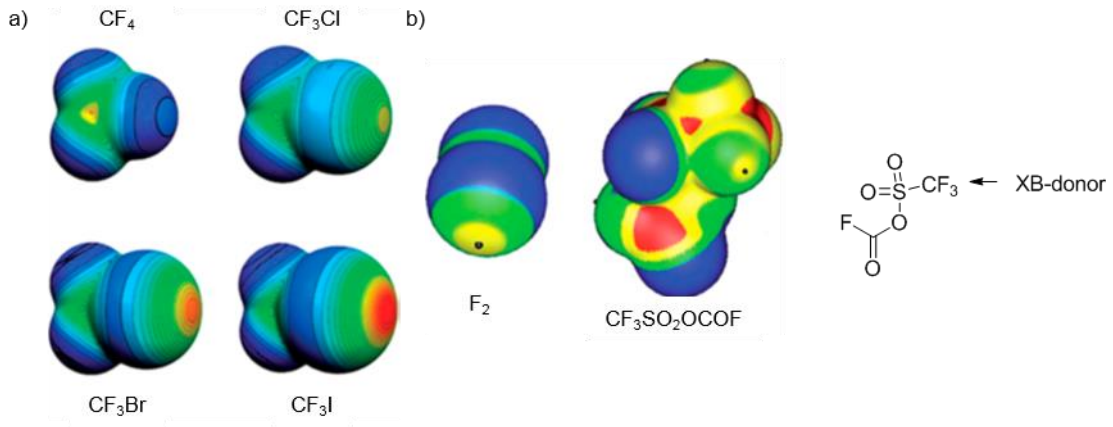

Figure 9: Molecular electrostatic potential at the isodensity surface with 0.001 au for a) CF_3X molecules; red is greater than 27 kcal mol^{-1}, yellow is between 20 and 14 kcal mol^{-1}, green is between 12 and 6 kcal mol^{-1}, blue is negative; reprinted and adapted with permission from Clark *et al.*[36] (© 2006, Springer Nature). b) F_2 as well as CF_3SO_2OCOF; red is greater than 20 kcal mol^{-1}, yellow is between 20 and 9 kcal mol^{-1}, green is between 9 and 0 kcal mol^{-1}, blue is negative; reprinted and adapted with permission from Metrangolo *et al.*[44] (© 2011, Royal Society of Chemistry).

The group of RESNATI recently published an XB donor ability ranking obtained by a combination of IR

spectroscopy and structural characterization data from X-ray crystallographic, as well as computational studies. The strongest XB donors in their study were (Iodoethynyl)-4-iodobenzene and 1,4-diiodotetrafluorobenzene with very similar σ-hole magnitudes $V_{S,max}$ (Figure 10).[47]

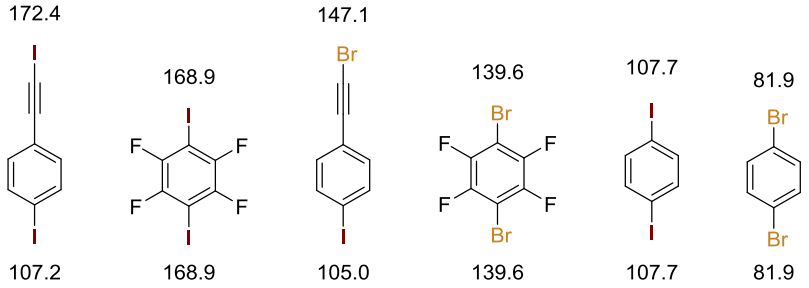

Figure 10: Chemical structures of different XB donors ranked by their XB donor ability in the solid state. $V_{S,max}$ values in kJ·mol^{-1} are written next to the corresponding halogen atom.[47]

In contrast to hydrogen bonds, halogens as well as halogen bonds are hydrophobic residues; a fact which offers some useful and complementary applications. Halogen bonds were found to have an increased lipophilicity and their ability to pass through cell membranes for the purpose of drug delivery was presented by MATILE and coworkers (see chapter 2.2.4).[48,49] A further characteristic is the bulkiness of halogen bonds which makes them more sensitive to steric hindrance than HBs. This become obvious when comparing the van der Waals radii of the different donor atoms with 1.47, 1.75, 1.85, and 1.98 Å for F, Cl, Br and I and 1.20 Å for hydrogen.[50]

A great variety of different XB acceptors has found application in the assembly of halogen-bonded complexes. Thereby, compounds with free electron pairs are most commonly employed due to their high directionality and their high XB acceptor strength. The bicyclic amine quinuclidine has been presented by several studies as the strongest XB acceptor.[51–53]

TAYLOR and coworkers performed studies on the solvent dependence of the XB complex triethylamine-iodoperfluorooctane which showed that the interaction is relatively insensitive towards solvent polarity, however significantly weakened in solvents which can serve as hydrogen bond donors and compete for the available acceptor.[52] It was furthermore demonstrated that the influence of Lewis-basic solvents is destabilizing, however, the effect is less pronounced than would be predicted by a simple electrostatic model, underlining that additional charge-transfer contributions are significant.[53]

XB in the gas phase

Only a limited number of studies on XB in the gas phase has been published so far. LEGON and coworkers employed microwave spectroscopy and gas-phase rotational spectroscopy to investigate XB complexes.[34,54] They studied the interaction of dihalogen molecules, e.g. ClI, and simple halogen-containing molecules such as CF_3I with simple Lewis bases in the gas phase and found that geometries and charge distributions are very similar to the same complexes in condensed phase. Among other characteristics, the great tendency to linearity of the R−X···Y bond angle is retained. Lattice and solvent effects had only minor influence on basic XB features of the complexes under study. Recently, also mass spectrometry studies to investigate XB in the gas phase have been presented.[55] GILLIS *et al.* investigated

the binding trends and energies of anion-receptor complexes of mono-, bi-, and tridentate donors with a variety of anions using blackbody infrared radiative dissociation (BIRD) and theoretical approaches.[56] For the most parts, their results agreed with corresponding solution studies and resulted in the trend of interaction energies following the XB acceptor order $Cl^- > Br^- > H_2PO_4^- > NO_3^-$, $I^- > HSO_4^-$, TsO^-. In many cases, the limiting factor for further investigations of XB complexes in the gas phase is the positive Gibbs energy ΔG often associated with their formation in the gas phase where solvent stabilization is absent.[32] The entropic penalty upon fixation of the complex is usually large due to the reduction of translational and rotational degrees of freedom. Then, only strong σ-hole interactions of charged XB donors or acceptors exhibit enthalpies high enough to compensate for that and can then form stable complexes in the gas phase.[30,56,57]

2.2.3. Coordinative Halogen Bonds

A special case of XB donors are monocationic halonium ions which were also used as a connective motif for the assembly of supramolecular capsules in this thesis. Hence, a more detailed introduction on this topic will be included here.

Halonium ions were first employed in the assembly and systematic investigation of halogen-bonded complexes in combination with two pyridines or divalent pyridine derivatives in 2012 (Figure 11).[58] ERDÉLYI and coworkers have greatly contributed to this research topic. They have shown that the complexes are symmetric in dichloromethane solution by NMR studies, Raman and IR spectroscopy as well as DFT calculations. That is, the two [N···X$^+$] halogen bonds are of equal distance and strength, characterized by a single-well energy potential.[59] Consequently, they are denoted as [N···X$^+$···N] halogen bonds. The synthesis of these complexes is straightforward and proceeds by reaction of the pyridine component with Br_2 or I_2 in the presence of silver triflate. This offers a very convenient way for the installation of halogen bonds for the assembly of more complex assemblies, as classical XB donors often need significantly more synthetic effort.

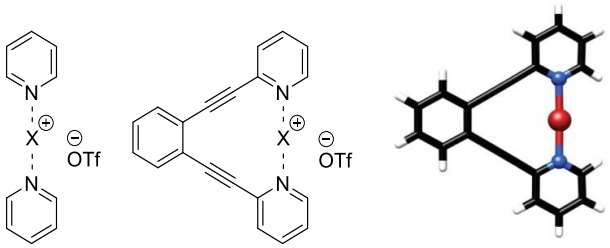

Figure 11: Complexes with coordinative halogen bonds as investigated by ERDÉLYI and coworkers (X = I, Br) and DFT structure optimization showing static, symmetric [N···Br···N]$^+$ XB complex; reprinted with permission from Carlsson *et al.*[58] (© 2012, American Chemical Society).

These halogen bonds are 3-center-4-electron bonds and exceptionally strong in solution. DFT calculations predicted binding energies of up to 123 kJ·mol^{-1} in dichloromethane.[58] This is significantly higher than the binding energy of the corresponding HB complexes. It was shown that acetonitrile, as a potentially competing Lewis-basic solvent, does neither affect the bond length nor the linear, symmetric arrangement

of the 3-center halogen bond, nor its charge distribution. It merely modulates the energy of the interaction slightly due to its higher polarity.[60] A study on the effect of counter ions demonstrated that none of the weakly, moderately or strongly coordinating anions tested showed any influence on the intrinsically preferred linear, centrosymmetric geometry of the [N···X$^+$···N] complexes in solution or in the solid state. The reported bond length $d_{N–I}$ are on average 2.26 Å.[61] The similarity concerning structure and electron density of the XB complexes to the corresponding metal-coordinated [Donor···Ag···Donor]$^+$ complexes are often emphasized. In this context, the XB bond is described as a coordinative bond since the iodonium ion is a very strong XB donor.[62] Nevertheless, a comparison of different halogen-bonded and silver-coordinated complexes illustrates significant differences. ERDÉLYI and coworkers showed that [N···Ag$^+$···N] complexes only formed monomeric and symmetrical structures in combination with weakly coordinating counterions. With moderately or strongly coordinating anions, they formed distorted pseudo-tetracoordinated, dimeric arrangements. In contrast, [N···I···N]$^+$ complexes were found to be monomeric and symmetrical, independent of the counter anion (Figure 12).[61]

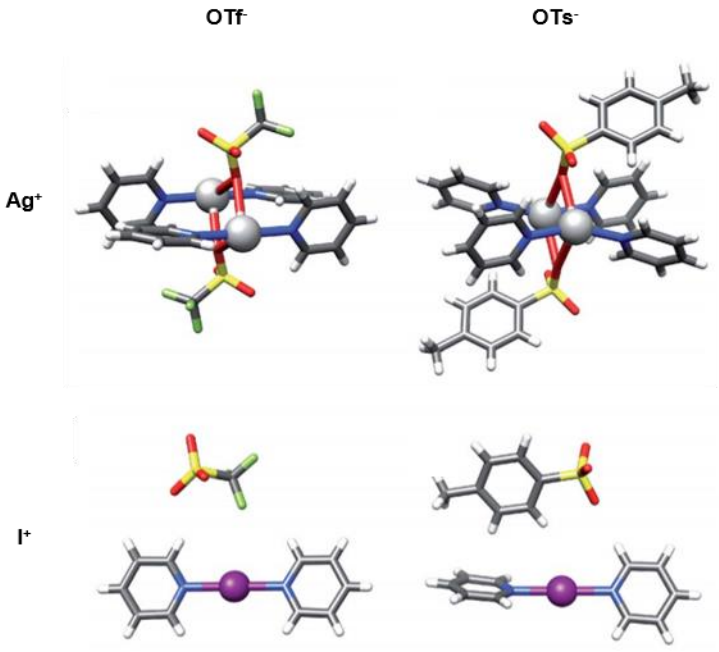

Figure 12: Comparison of X-ray crystal structures of [bis(pyridine)silver] triflate and [bis(pyridine)silver] tosylate (top row) with [bis(pyridine)iodine] triflate and [bis(pyridine)iodine] tosylate (bottom row). In the presence of moderately coordinating counterions, silver(I) complexes form pseudo-tetracoordinated dimers, whereas those of iodine(I) form linear, bis-coordinated [N···I$^+$···N] complexes. Reprinted and adopted with permission from Bedin *et al.*[61] (Royal Society of Chemistry).

Studies by GEORGIOU *et al.* demonstrated the reversible formation of the noncovalent interaction by ligand-exchange experiments when employing stronger Lewis-basic XB acceptors.[63] Furthermore, the substitution effect on the [N···I···N]$^+$ XB was evaluated by introducing electron withdrawing and donating functionalities to the pyridine in the [bis(pyridine)iodine]$^+$ and [1,2-bis((pyridine-2-ylethynyl)benzene) iodine]$^+$ complexes.[64] As can be expected for charge-transfer complexes, the bond is stabilized by an increased electron density and destabilized by electron deficiency. Yet, the bond length and geometry are virtually unaffected by changes of the electron density, neither in solution nor in the solid state.

2.2.4. Halogen Bonding for the Assembly of Supramolecular Systems

XB Assemblies in the solid state

With the rediscovery of halogen bonding within the last two decades, it has gained increasing influence as a tool for the construction of supramolecular systems.[32] As of yet most investigated is their application in crystal engineering in order to harness the unique characteristics of XB in terms of strength, selectivity and interaction geometry for the development of new functional materials. Numerous examples of solid state structures of one-, two- and three-dimensional architectures have been published to date which make use of this binding motif.[45] XB is generally in the same order of strength as HB. Therefore, they can either compete or cooperate in crystal structures. This opens the way for extensive fine tuning of the resulting structures.[32]

One-dimensional chain-like structures are especially interesting for materials with conducting and magnetic properties.[32] METRANGOLO and RESNATI showed the formation of helices by crystallization of *N*-methyl dibromopyridinium iodide.[65] The helical structure is stabilized by [C-Br···I$^-$] XB bonds (Figure 13a, b). SAMAI and BIRADHA presented sheet-like structures comprised of bis((4-halophenyl)-amido)alkanes which feature a combination of XB and HB interactions.[66] MUNIAPPAN *et al.* produced chiral, layered architectures by employing XB bonds of asymmetrically functionalized tetraaryl-porphyrins.[67] The porphyrins feature one single pyridyl function and three diverging iodophenyl groups which can take part in [C-I···N] and [C-I···π] XB bonds (Figure 13a, c). This results in flat supramolecular layers of porphyrin units all aligned in the same direction in the crystal structure, imparting chirality upon the entire assembly. An interesting three-dimensional structure was reported by RISSANEN and coworkers who aimed for the construction of novel porous materials without the use of metals. Cocrystallization of hexamethylenetetramine and *N*-iodosuccinimide gave a flexible network structure stabilized by [N-I···N] XB bonds. It can accommodate different solvent guests in nanosized channels *via* an induced-fit mechanism due to the "breathing" nature of the framework (Figure 13a, d).[68]

Several applications for solid-state halogen-bonded structures have been described, e.g. the chiral resolution of racemic halogen-functionalized perfluorocarbon species by cocrystallization[41] or the solid-phase extraction of perfluorinated iodoalkanes.[69] A valuable method for synthetic organic chemistry could be the use of XB as a means to introduce heavy atoms into the structure of a chiral molecule *via* cocrystallization to allow for determining the absolute configuration of an enantiomer.[70] Furthermore, great progress to establish XB for the design and formation of supramolecular gels, dendrimers, liquid crystals, polymers and other functional materials has been made.[32]

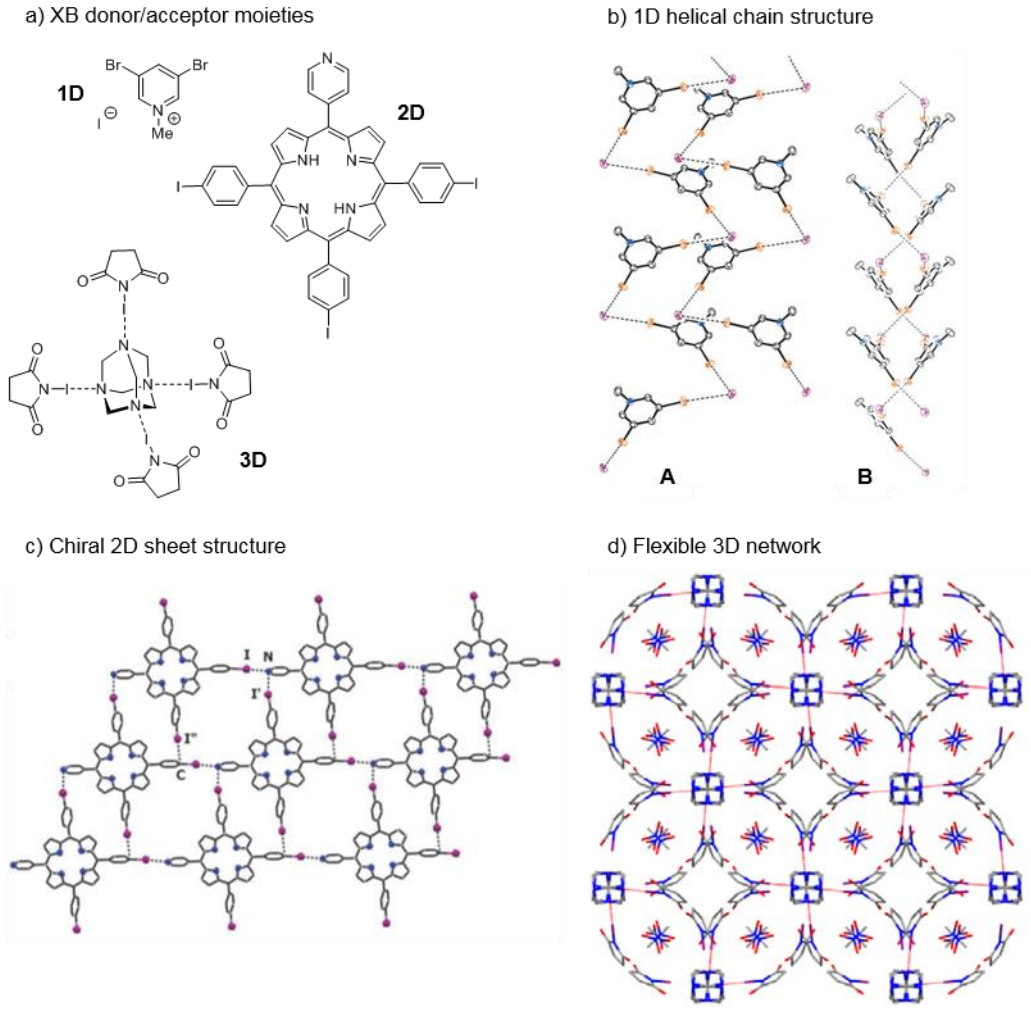

Figure 13: Selected examples for solid state structures stabilized by halogen bonds. a) Molecular structures of XB donor/acceptor moieties which form the presented 1D, 2D or 3D solid state structures; b) 1D helical chain structure stabilized by [C-Br···I$^-$] XB bonds from different persectives; reprinted with permission from Logothetis *et al.*[65] (© 2004, Royal Society of Chemistry). c) Chiral 2D sheet structure stabilized by [C-I···N] and [C-I···π] XB bonds; reprinted with permission from Muniappan *et al.*[67] (© 2008, Royal Society of Chemistry). d) Flexible 3D network structure stabilized by [N-I···N] XB bonds; reprinted with permission from Gilday *et al.*[32] (© 2015 American Chemical Society).

XB Assemblies in solution

In comparison to solid state structures, the use of halogen bonding for the formation of discrete supramolecular assemblies in solution is still less advanced.[11,71] In this context, the design of receptors which employ XB as the key interaction for the noncovalent binding of anions has attracted most attention so far.[72] BEER and coworkers have greatly contributed to this field with their extensive work on mechanically-bonded hosts for enhanced anion recognition and sensing[32,73] and for the development of molecular machines.[74] For the synthesis of rotaxanes and catenanes, an anion-templation methodology using XB is very commonly used. They presented a pseudorotaxane consisting of a 2-bromoimidazolium chloride axle and an isophthalamide-donor macrocycle which forms due to a cooperative XB/HB-mediated chloride binding.[75] Using the same approach, the first XB-interlocked structure could be accessed by the bromide anion-templated formation of an iodotriazolium-functionalized rotaxane. So far, BEER and

coworkers have published a number of catenanes,[76] rotaxanes[77] and simpler, non-interlocked structures[78] that exhibit high affinities for different anion classes by XB or a combination of HB and XB. In general, these systems are superior to the corresponding assemblies which offer only HB binding sites. The group was able to obtain a rotaxane which selectively binds and senses halides over oxoanions by XB in aqueous solvent mixtures of up to 1:1 H_2O/MeCN.[79] The rotaxane consists of a photoactive rhenium(I)-bipyridyl-bis(iodotriazole) macrocycle and a bis(iodotriazolium)-functionalized carbazole axle and offers four XB-donor sites which point into the preorganized binding pocket (Figure 14a). Binding affinities increase from chloride over bromide to iodide (K_a = 5.1 × 10^2, 5.8 × 10^3, 2.4 × 10^4 M^{-1}, 295 K, 1:1 H_2O/MeCN). An inverted trend was obtained with a XB catenane that selectively binds chloride and bromide (K_a = 3.7 × 10^6 and 1.5 × 10^5 M^{-1}, 295 K, MeCN) over oxoanions in acetonitrile.[80] The preorganized cavity created between the two bromoimidazolium XB-donor units of the interlocked macrocycles can host the halide and the resulting emission from the integrated naphthalene motifs can then be measured by fluorescence spectroscopy (Figure 14b).

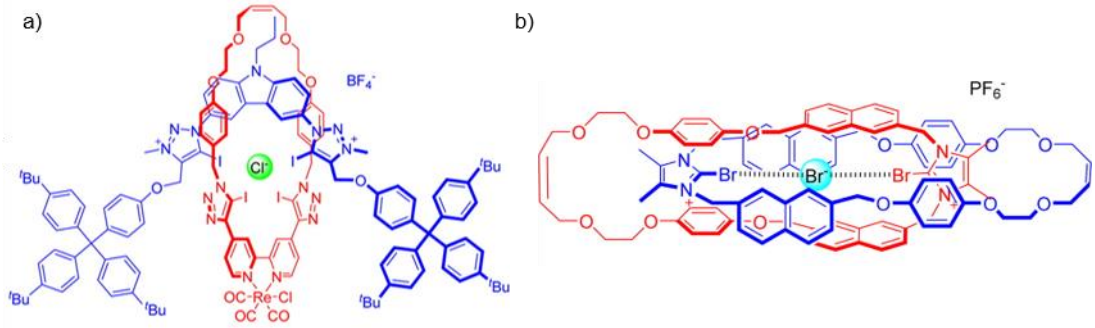

Figure 14: Interlocked systems for anion recognition and sensing using XB by BEER and coworkers: a) Rotaxane for selective sensing of halides in aqueous media; b) catenane for selective sensing of halides in acetonitrile. Reprinted and adapted with permission from Gilday *et al.*[32] (© 2015, American Chemical Society).

A very recent example by BEER and coworkers features the chiral discrimination of enantiomeric guests by chiral XB-donor rotaxanes.[81] The most crucial influence for efficient enantiodiscrimination was found to be the rotaxane`s chiral interlocked cavity installed by the use of a BINOL-derived macrocycle and furthermore the preorganization of four XB-donor iodotriazole motifs around the cavity (Figure 15). These geometric constrains result in enantioselective anion binding of different chiral carboxylates with varying preference for the (*R*)- or (*S*)-enantiomer. The highest selectivities were observed for *N*-Boc-(*R*)-leucine in combination with rotaxane **2** resulting in an *ee* of 55% and for *N*-Boc-(*S*)-proline with rotaxane **1** giving an *ee* of 51%.

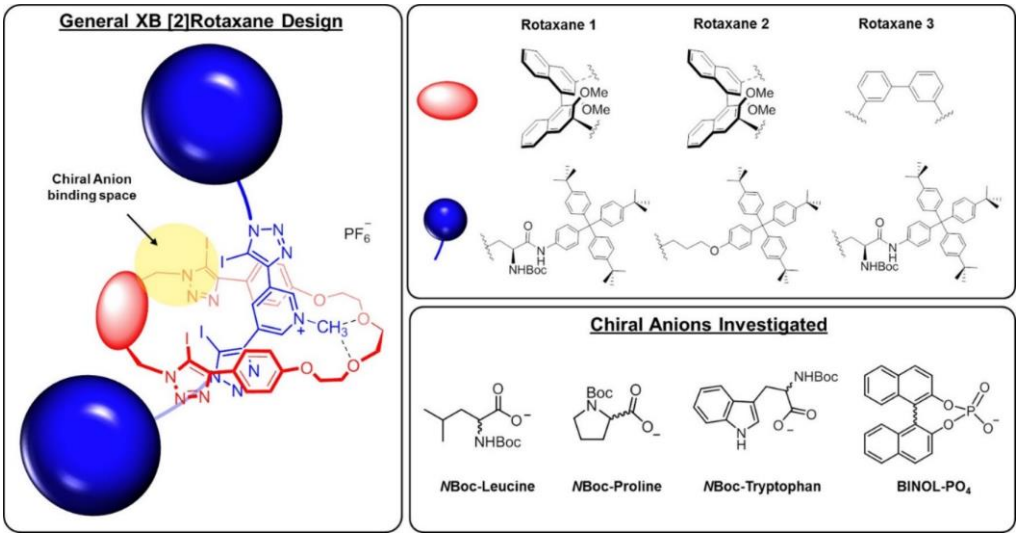

Figure 15: Structures of the chiral XB [2]rotaxanes and anions investigated by BEER and coworkers; reprinted with permission from Lim *et al.*[81] (© 2017, American Chemical Society).

A system with biological relevance for the application of halogen bonding was introduced by MATILE and coworkers who published a series of synthetic anion transporters to cross lipid bilayer membranes.[48,49,82] As a first concept, a calix[4]arene-derived anion transporter was synthesized that can bind cations within the calix[4]arene scaffold and the anion by XB interaction with four iodobenzene substituents (Figure 16a).[82] However, the relatively high anion-binding strength of the cyclic, tetravalent array resulted in a low transporter ability. Their next approach therefore aimed at reducing the anion binding strength and made use of small monovalent, aromatic and aliphatic XB donors which significantly increased the transporter activity (Figure 16b).[49] Furthermore, linear XB donor arrays consisting of *p*-oligophenyl scaffolds proved to be suitable by facilitating transmembrane anion hopping (Figure 16c).[48] With these studies, XB was shown to be ideal for anion transport in a membrane. The advantage lies in its comparably high binding strength. Additionally, it is in comparison to HBs also hydrophobic enough that no large lipophilic domain is needed to compensate for a hydrophilic anion binding site.

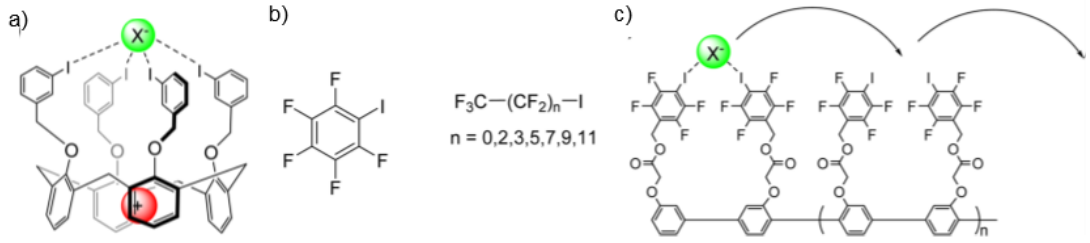

Figure 16: Systems employing XB for anion transport across lipid bilayer membranes by MATILE and coworkers. Reprinted and adapted with permission from Gilday *et al.*[21,32] (© 2015 American Chemical Society).

JIANG and coworkers recently presented a single-stranded supramolecular helix whose formation is driven by intermolecular XB.[83] An alanine-based bilateral *N*-amidothiourea substituted with two iodobenzene rings forms two *β*-turn structures by intramolecular HB. It serves as the monomeric helical fragment (Figure 17a). "Head-to-tail" intermolecular [C–I···π] XB interactions induce helix formation which was

demonstrated to occur in solution beyond a critical aggregation concentration of ca. 6 μM and resulted in the obtained X-ray crystal structure (Figure 17b-d).

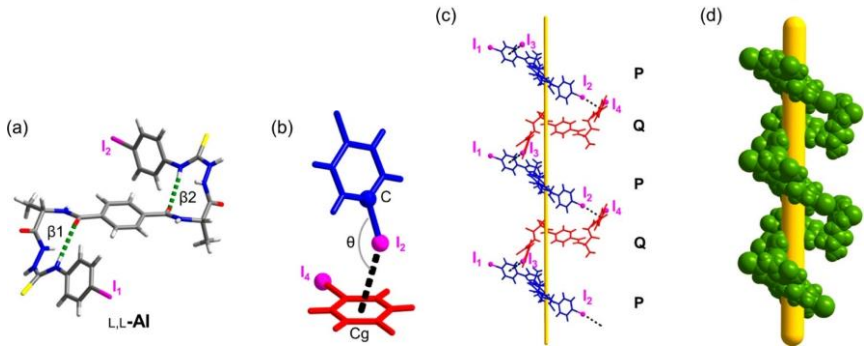

Figure 17: JIANG and coworkers` single-stranded supramolecular helix: a) X-ray crystal structure of monomeric helix fragment with *β*-turn at each side; b) intermolecular [C–I···π] XB interaction between two monomers; c) assembly of monomeric helix fragments to helix structure; d) single-stranded left-handed helix in the crystal packing. Reprinted and adapted with permission from Cao *et al.*[83] (© 2017, American Chemical Society).

The self-assembly of supramolecular capsules is an important field for the application of XB and integral to the presented work. Key contributions over the last couple years have come from the groups of RISSANEN, RESNATI and DIEDERICH. Details and relevant examples will be discussed in chapter 2.3.2.

2.3. Molecular Containers

2.3.1. Host-Guest Chemistry

Initiated by the achievements of DONALD CRAM, JEAN-MARIE LEHN and CHARLES J. PEDERSEN who received the Nobel prize in chemistry in 1987 for their pioneering work on host-guest chemistry, this field of supramolecular chemistry has greatly developed over the last four decades.[8,84] A host-guest complex forms by the spontaneous self-assembly of a ring-, bowl- or cage-shaped host molecule and a guest molecule or ion by a reversible, noncovalent interaction. This takes place due to the molecular recognition of the two parts. That is, they are complementary to each other with respect to their binding site with its intrinsic steric and electronic properties, as well as their size and shape, given that the guest is bound within the cavity of the host. The binding event can be described by a simple chemical equilibrium between the host-guest complex $H{\cdot}G$ and the unbound species H and G. In this context, the equilibrium constant is referred to as the binding constant K which is directly related to the Gibbs energy for complex formation ΔG^0 (equation 1).[85]

$$H + G \leftrightharpoons H \cdot G$$

$$K = \frac{[H \cdot G]}{[H] \cdot [G]} = e^{-\frac{\Delta G^0}{RT}} \qquad (1)$$

The formation of a complex is most often enthalpically favored as new intermolecular interactions are formed, however the desolvation energy of host and guest need to be considered. The entropic contribution is less unambiguous, and several effects need to be taken into account. Complex formation as an isolated event can be assumed to be negative in entropy due to the decrease in particle number from two to one and the decrease in degrees of freedom of the single components as compared to the more rigid arrangement in the new complex. To truly rationalize guest binding in solution, the solvent needs to be considered as an integral part of the system. A number of well-ordered solvent molecules is released from the solvated single components into the bulk, resulting in an increase in degrees of freedom. In particular, solvophobic effects play a crucial role in the guest-binding behavior of some of the macrocyclic hosts.[85]

Host molecules

Figure 18 depicts some of the most commonly used types of host molecules which show an affinity for a great variety of different guests. Crown ethers and oxygen-based cryptands can bind cationic guests like metal ions by ion-dipole interactions or ammonium ions by hydrogen bonding and ion-dipole interactions. When regarding the binding of alkali-metal ions within crown ethers, the size complementarity of guest and host becomes evident: [15]Crown-5 binds selectively sodium ions, while [18]crown-6 forms host-guest complexes preferentially with potassium cations. Tetralactam macrocycles bear amide groups which point into the cavity and can act as HB donor to HB-acceptor guests, such as carbonyl compounds or anions. Cyclodextrines and cucurbit[*n*]urils have the common feature of a hydrophobic cavity interior and a polar, hydrophilic cavity rim which makes them soluble in water. They can bind unpolar molecules within their cavity, even though the contribution of the newly formed noncovalent interaction, mainly van der Waals

interactions, is usually not very high. However, water is released into the bulk solution upon guest binding, which was originally only very weakly bound within the cavity and to the unpolar guest for solvation. The gain in enthalpy and entropy for the respective water molecules causes the strong hydrophobic effect which greatly enhances the binding strength of the host-guest complex in water.[85,86] Additionally, cucurbit[*n*]urils bind cationic guest by ion-dipole interactions in combination with the hydrophobic effect. Resorcinarenes, pillar[*n*]arenes and calix[4]arenes all exhibit an electron-rich cavity with aromatic walls and can bind electron-poor neutral species or cations by cation-π, hydrogen bonding or π-π interactions. They differ in their general shape: While pillar[*n*]arenes are symmetric and tube-shaped, resorcinarenes and calix[*n*]arenes are bowl-shaped. The hydroxyl groups sit on the upper, wider rim in case of the resorcinarenes and on the lower, narrower rim for the calix[4]arenes and stabilize the respective concave conformation to some extent.[85–88]

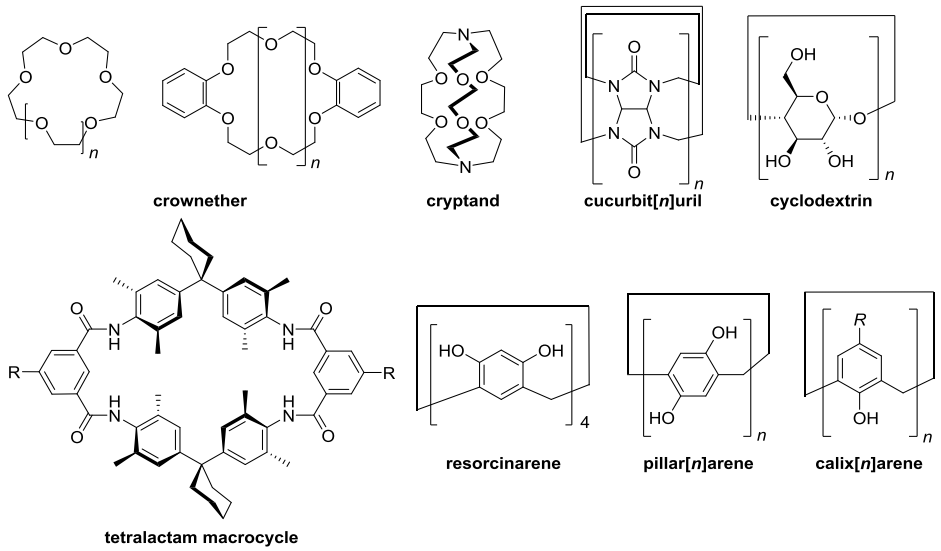

Figure 18: Selection of macrocycles commonly used as hosts in supramolecular chemistry.

The described macrocycles are archetypical and frequently used as such for a variety of different applications, including the formation of interlocked structures like rotaxanes or catenanes, sensing of guests or supramolecular catalysis. Moreover, they can be functionalized to further modulate the host structure regarding its size, steric and electronic features to tailor the desired guest-binding selectivity or reactivity. Resorcinarenes can in general be functionalized in three different positions: at the hydroxyl groups (Y) or the 2-position (X) of the aryl rings at the upper rim or the substituent at the lower rim (R). While mostly the lower-rim substituent R is preserved as an alkyl group from the synthesis, X and Y can vary greatly, as broadly explored by REBEK and coworkers.[89] The connection of the hydroxyl groups by an alkyl or aryl group fixes the concave conformation of the resorcinarene and results in so-called cavitands which have a diameter of approximately 1 nm at the wider rim (Figure 19).[90] Furthermore, the introduction of aromatic groups and additional functional groups at the upper rim creates walls which greatly enhance the size and influence electronic properties of the cavity, making them versatile for a variety of different applications.[91,92,93,94] Resorcinarene-based cavitands were used for several projects presented in this thesis.

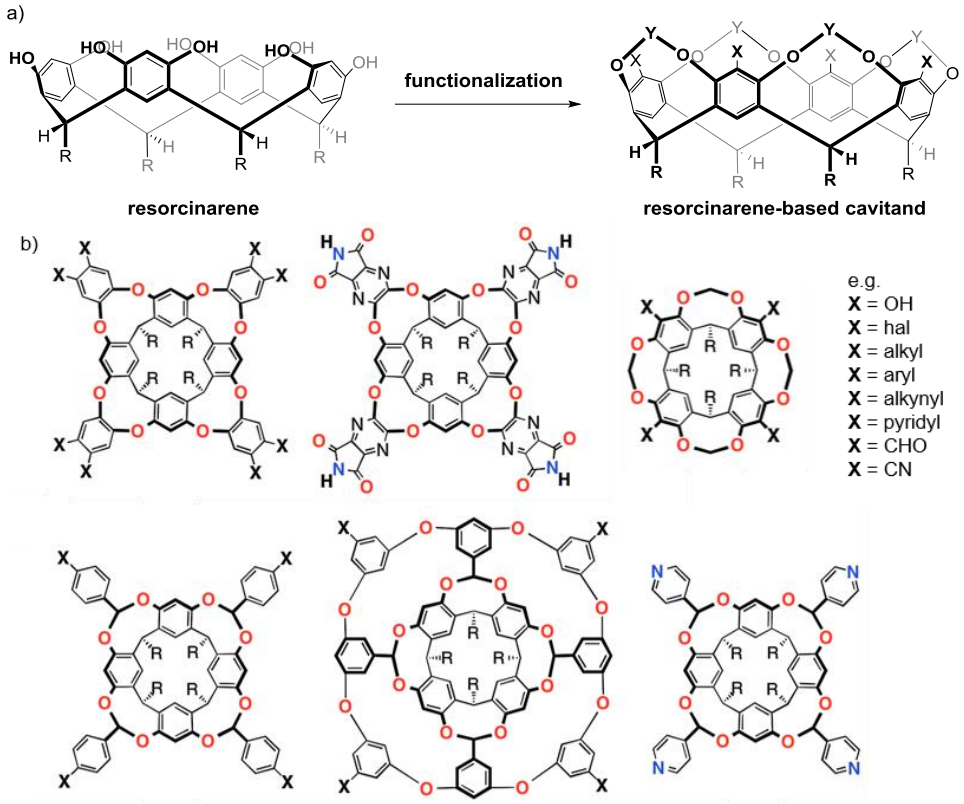

Figure 19: a) Functionalization of resorcinarenes to cavitands; b) selection of resorcinarene-based cavitands; reprinted and adapted with permission from Kobayashi *et al.*[91] (© 2014, Royal Society of Chemistry).

After deprotonation of four hydroxyl groups, simple resorcinarenes bind small metal ions and simple ammonium ions such as tetramethylammonium in water by electrostatic and cation-π interactions.[17,95] Functionalized cavitands can selectively bind a variety of different guests depending on their properties, ranging from cations over neutral molecules to anions and ion pairs.[92,96]

Applications for cavitands

DIEDERICH and coworkers reported a so-called "molecular gripper" when they prepared a resorcinarene-based cavitand which is redox-switchable between a quinone and a hydroquinone form.[97] The latter can form a network of hydrogen bonds around the walls of the cavitand by interaction between the alcohol and the amide substituents. This changes the conformation of the cavitand from the preferentially open kite form in the oxidized state to a fixed and closed vase form in the reduced state (Figure 20, top). The cavitand is furthermore equipped with two triptycene moieties which close off the cavitand at the top when it is in its vase conformation. This thereby causes the sterically enhanced encapsulation of guests such as cycloalkanes and 1,4-cylohexandione with very slow guest-exchange rates in mesitylene, which cannot act as a guest due to steric hindrance. These characteristics resulted in a system which can be switched between a state of weak guest binding with fast release and uptake and a state of enhanced binding with very slow release and update rates (Figure 20, bottom).

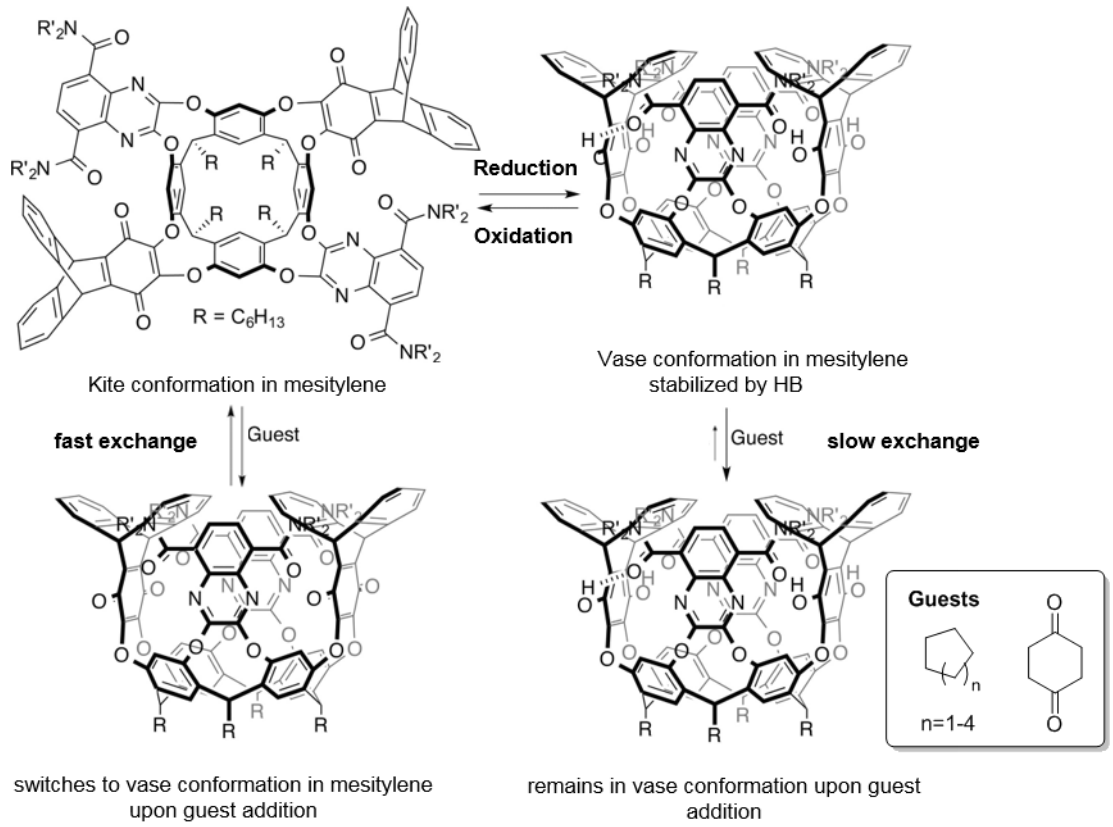

Figure 20: DIEDERICH`s redox-switchable cavitand provides a state for strong guest binding with slow release rates and a state for weak binding with fast exchange rates for cycloalkanes and cyclohexane-1,4-dione as guests in mesitylene. Reprinted and adapted with permission from Pochorovski *et al.*[94] (© 2014 American Chemical Society).

Foremost, REBEK and coworkers initially demonstrated the ability of their cavitands to act as supramolecular catalysts in series of different reactions.[98] They can take the role of an organocatalyst which provides a confined space for the reaction to occur, resembling one of the characteristic of enzyme catalysis. This can be favorable, e.g. for bimolecular reactions when both substrates are bound inside the cavity in the optimal 1:1 stoichiometry at a greatly enhanced local concentration than in bulk solution. This preorganization can also lead to unusual selectivities. The stereoelectronic properties of the cavity can increase the stability of reaction intermediates and transition states, making the reaction more likely to occur.[98] Furthermore, examples have been presented where the cavitands are substituted with phosphine, carbene or nitrogen-containing ligands which can bind catalytically active transition metals. In these examples, the cavitand provides a confinement for the metal which then increases the substrate selectivity or the reaction rate by additional noncovalent interactions.[88] IWASAWA and coworkers recently demonstrated cross-coupling reactions of terminal alkynes using different cavitand catalysts (Figure 21).[99] The best yields with the highest selectivity were obtained with the cavitand bearing two quinoxaline walls. The authors rationalize this result with the more confined reaction space of the quinoxaline cavitand which limits the number of accessible transition states. They further argue that the more expanded π-system as compared to the pyrazine cavitand interacts more strongly with the two alkynes during the reaction, providing additional stabilization.

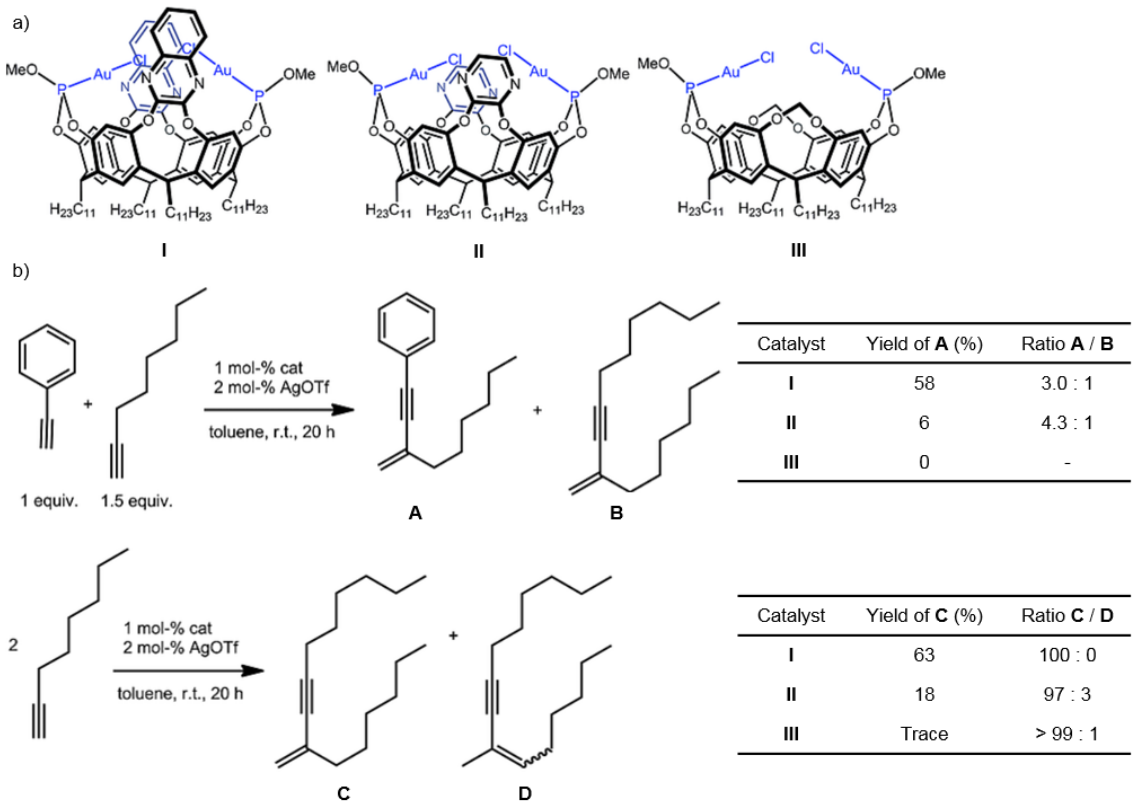

Catalyst	Yield of **A** (%)	Ratio **A** / **B**
I	58	3.0 : 1
II	6	4.3 : 1
III	0	-

Catalyst	Yield of **C** (%)	Ratio **C** / **D**
I	63	100 : 0
II	18	97 : 3
III	Trace	> 99 : 1

Figure 21: a) Resorcinarene-based cavitands bearing catalytically active gold centers; b) catalytic cross-coupling reactions of terminal alkynes using different cavitand catalysts, best results in both cases showed the quinoxaline cavitand **I**. Reprinted and adapted with permission from Natarajan *et al.*[88] (© 2017 WILEY-VCH Verlag GmbH & Co. KGaA, Weinheim).

This concept of supramolecular catalysis with molecular containers was then further explored with supramolecular capsules and cages, as they provide a larger space within their cavities for reactions to occur.

2.3.2. Supramolecular Capsules and Cages

The ability of cavitands and other concave hosts to encapsulate specific guest molecules or ions encourages more sophisticated applications. However, these compounds are intrinsically restricted to a relatively small size and an extension of the cavity volume by means of covalent bond formation becomes a synthetic challenge. The generation of larger assemblies, so-called supramolecular coordination cages or capsules, can be achieved in a modular fashion from relatively simple building blocks. Meanwhile, this approach is widely agreed on as the more promising for the synthesis of large and elaborate complexes with discrete inner cavities. It offers the opportunity to use these molecular containers in similar fashion as nature uses confined spaces – for recognition, storage and transport of guest molecules, as well as catalysis.[100,101,102]

REBEK and coworkers published the first so-called "tennis ball" capsule in 1993 (Figure 22a).[103] This capsule is comprised of two glycoluril-containing building blocks which form a stable dimer in solution by the formation of eight hydrogen bonds. Since then, numerous examples were introduced which make use

of diverse binding motifs. They include hydrogen bonding,[104] metal coordination,[105–107] ion pairing,[108] the hydrophobic effect,[109] and recently also halogen bonding (Figure 22b, c, d). The self-assembled containers are usually comprised of either rigid or semi-rigid, planar molecules or concave cavitands as building blocks. They need to be equipped with functional groups compatible with the intended noncovalent interaction. The early examples of capsules and cages shown in Figure 22 demonstrate the principles used to obtain these in a rational, predetermined fashion. The combination of preorganized, complementary building blocks and directional, noncovalent bonding yields discrete molecular containers. These principles have been employed in numerous examples and especially hydrogen bonding and metal coordination could already prove to be very versatile in this regard.[110]

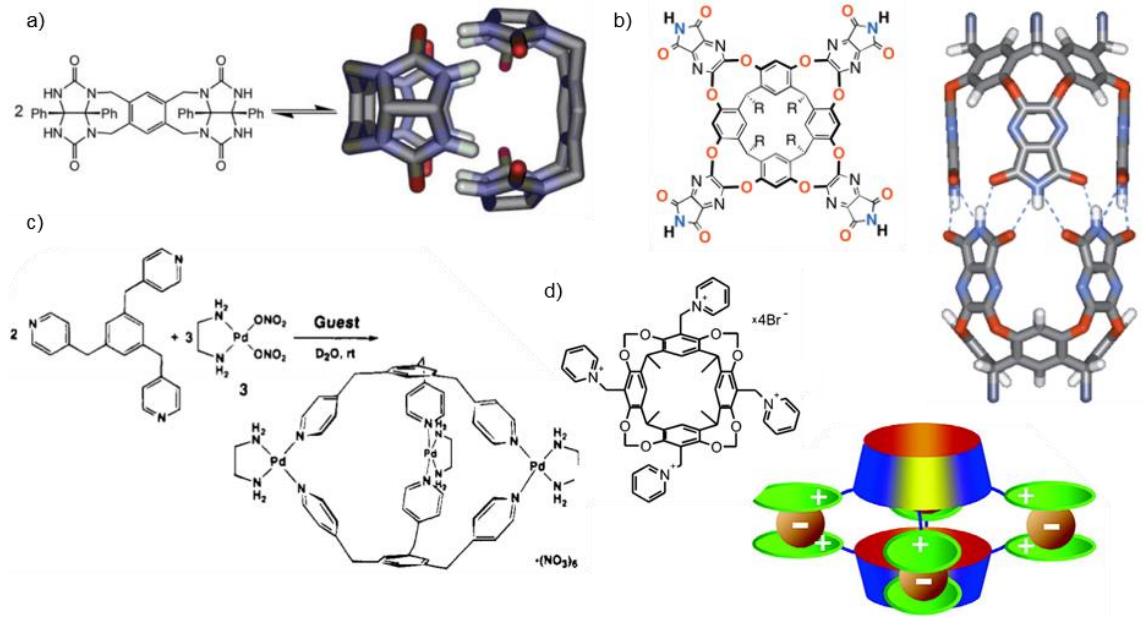

Figure 22: Early examples of dimeric capsules and cages. a) REBEK`s HB "softball"; reprinted with permission from Palmer *et al.*[102] (© 2004, Royal Society of Chemistry). b) REBEK`s HB cylindrical resorcinarene-based capsule; reprinted and adapted with permission from Kobayashi *et al.*[91] (© 2014, Royal Society of Chemistry). c) FUJITA`s first metal-coordinated cage; reprinted with permission from Fujita *et al.*[106] (© 1995, American Chemical Society). d) VERBOOM`s ion-interaction capsule; reprinted and adapted with permission from Oshovsky *et al.*[108] (© 2006, American Chemical Society).

Halogen-bonded capsules

Only a few examples of discrete molecular capsules supported by halogen bonds have been presented until 2015, when the presented research work was started. The first halogen-bonded capsule was introduced by RESNATI and coworkers in 2012, who could show the solid state structure of the discrete 1:1 assembly of a calix[4]arene-based XB-donor and a resorcinarene-based XB-acceptor cavitand (Figure 23a).[111] In 2015, RISSANEN and coworkers published the solid-state structure of a functionalized resorcinarene which forms a dimeric capsule stabilized by a combination of halogen bonds between chloride ions and molecular iodine as well as hydrogen bonds between the ammonium and the chloride ions (Figure 23b).[112]

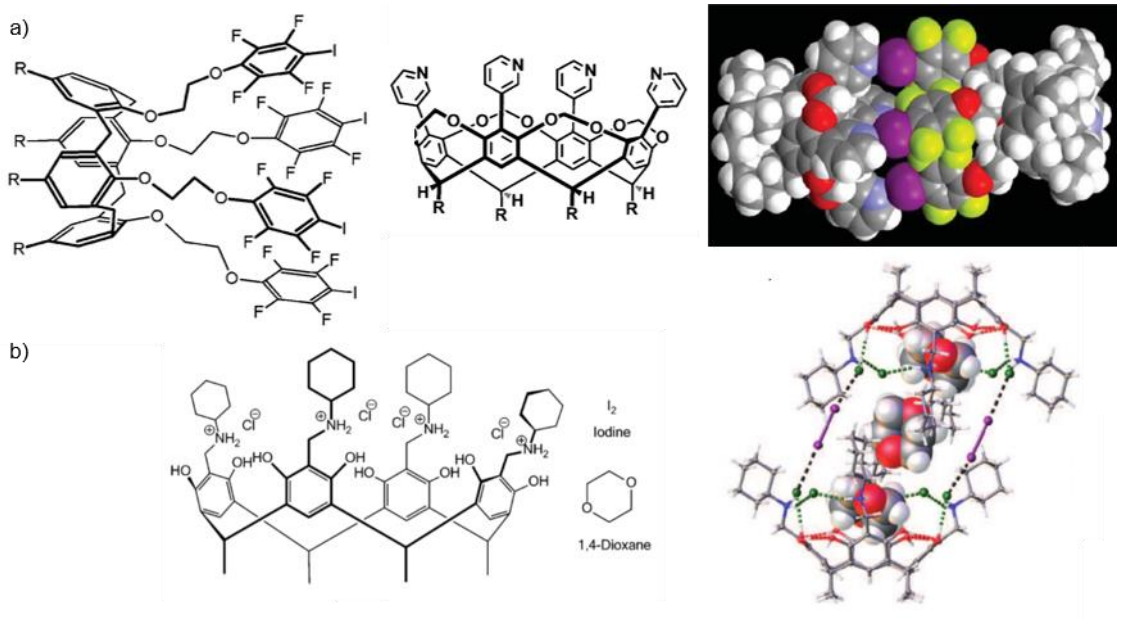

Figure 23: Halogen-bonded dimeric capsules observed solely in the solid state with molecular structures and corresponding X-ray crystal structures. a) RESNATI`s heterodimeric capsule held together by [C-I···N] halogen bonds; reprinted and adapted with permission from Aakeröy *et al.*[111] (© 2012, Royal Society of Chemistry). b) RISSANEN`s homodimeric capsule held together by [I-I···Cl^-] halogen bonds and [N-H^+···Cl^-] hydrogen bonds; reprinted and adapted with permission from Beyeh *et al.*[112] (© 2015 WILEY-VCH Verlag GmbH & Co. KGaA, Weinheim).

Shortly afterwards, the same group presented a similar system that resulted in a capsular assembly stable in both, solid state and solution (Figure 24a).[113] As compared to the first example, the XB donor was changed from iodine to 1,3-diiodo-perfluoropropan and the acceptor moiety for the halogen and the hydrogen bond was a bromide ion in this system. Also in 2015, DIEDERICH and coworkers succeeded in the design and synthesis of a heterodimeric capsule stabilized by four neutral halogen bonds between two differently substituted cavitands.[114] This assembly was the first example of a solely halogen-bonded capsule stable in solution as shown by extended NMR studies and a DFT-calculated molecular model (Figure 24b). The group demonstrated the guest binding of small heterocycles inside the capsule. Furthermore, they performed thermodynamic studies in solution which revealed that the formation of overall four halogen bonds between the two multidentate, preorganized cavitands compensates for the unfavorable entropic term associated with the formation of a single XB. The enthalpic contribution thereby enables the formation of the stable capsule. The group of GRIMME subsequently presented more refined theoretical calculations on DIEDERICH`s heterodimeric capsule which were performed with dispersion-corrected density functional theory and with their lower-cost composite method PBEh-3c developed for supramolecular complexes.[115] Their calculations could further affirm the proposed structure of this only-halogen-bonded, face-to-face assembly. Additionally, they gave more insight into the thermodynamics of its formation and provided suggestions for synthetic alteration of the cavitands to obtain thermodynamically more stable structures (Figure 24c, see also chapter 3.1.1).

Mass spectrometry could not be applied successfully for the analysis of any of the aforementioned halogen-bonded capsules. This method would not only provide the means to confirm complex stoichiometries, but could also give detailed insight into their structure and reactivity. This lack in mass spectrometric

measurements is likely due to the challenge of transferring these noncovalent complexes into the gas phase (see also chapter 2.4.2).

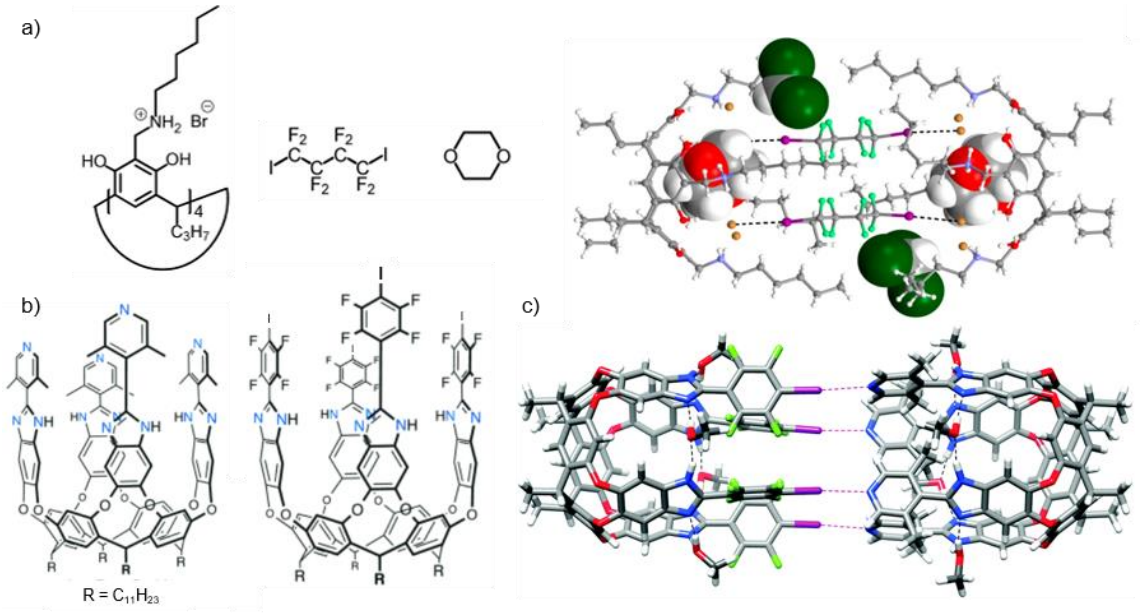

Figure 24: Halogen-bonded dimeric capsules observed in solution. a) RISSANEN`s homodimeric capsule held together by [C-I···Cl$^-$] halogen bonds and [N-H$^+$···Cl$^-$] hydrogen bonds, molecular structures of components and X-ray crystal structure; reprinted and adapted with permission from Pan *et al.*[113] (© 2015, American Chemical Society). b) DIEDERICH`s heterodimeric capsule held together by [C-I···N] halogen bonds, molecular structure of cavitands; reprinted and adapted with permission from Dumele *et al.*[114] (© 2015 WILEY-VCH Verlag GmbH & Co. KGaA, Weinheim) and c) corresponding DFT-calculated structure by GRIMME; reprinted with permission from Sure *et al.*[115] (© 2016, Royal Society of Chemistry).

Large supramolecular capsules

The major focus in the field of supramolecular capsules and cages nowadays lies on the design and selective synthesis of very big molecular containers. Some examples are capable of encapsulating complex molecules, such as proteins or DNA fragments, or performing elaborate "tasks" like supramolecular catalysis.[116,117] Alike the synthesis of smaller molecular containers, different general approaches to this problem have been followed. Among others, the group of FUJITA excels in the generation of very large coordination cages by the self-assembly of transition metals with finely tuned bridging ligands (see also chapter 2.4.2).[107,118,119] Some examples could also demonstrate the value of concave, preorganized building blocks. The first such exemplar was the hydrogen-bonded resorcinarene hexamer, published now two decades ago by ATWOOD and MACGILLIVRAY who were able to obtain a crystal structure of the assembly (Figure 25a).[120] The complex is robust and readily forms in apolar solvent from the monomer, once traces of water are present which are necessary to close the network of 60 hydrogen bonds. It can encapsulate a variety of different cationic guests by cation-π and ion-dipole interactions.[121] Similarly, tetrahydroxyresorcinarene (pyrogallarene) forms a hexameric capsule as evidenced by MATTAY and coworkers who presented its crystal structure (Figure 25b).[122] The self-assembly proceeds without the need for additional water, however, the complex was reported to be less stable than the resorcinarene hexamer and an initial attempt to analyze it by mass spectrometry failed. SCHALLEY and coworkers then published

an ESI mass spectrometry study on the two aforementioned hexameric capsules, demonstrating that both complexes can be transferred into the gas phase without fragmentation.[123] In their work, charge-tagging of the complexes by different cationic guests ensured an undisturbed HB framework (see also chapter 2.4.2). It became evident that the right size, shape and symmetry of the guest was integral to the assembly of the capsules in solution, as different guests could template the formation of the capsule which matched their size (dimer or hexamer).

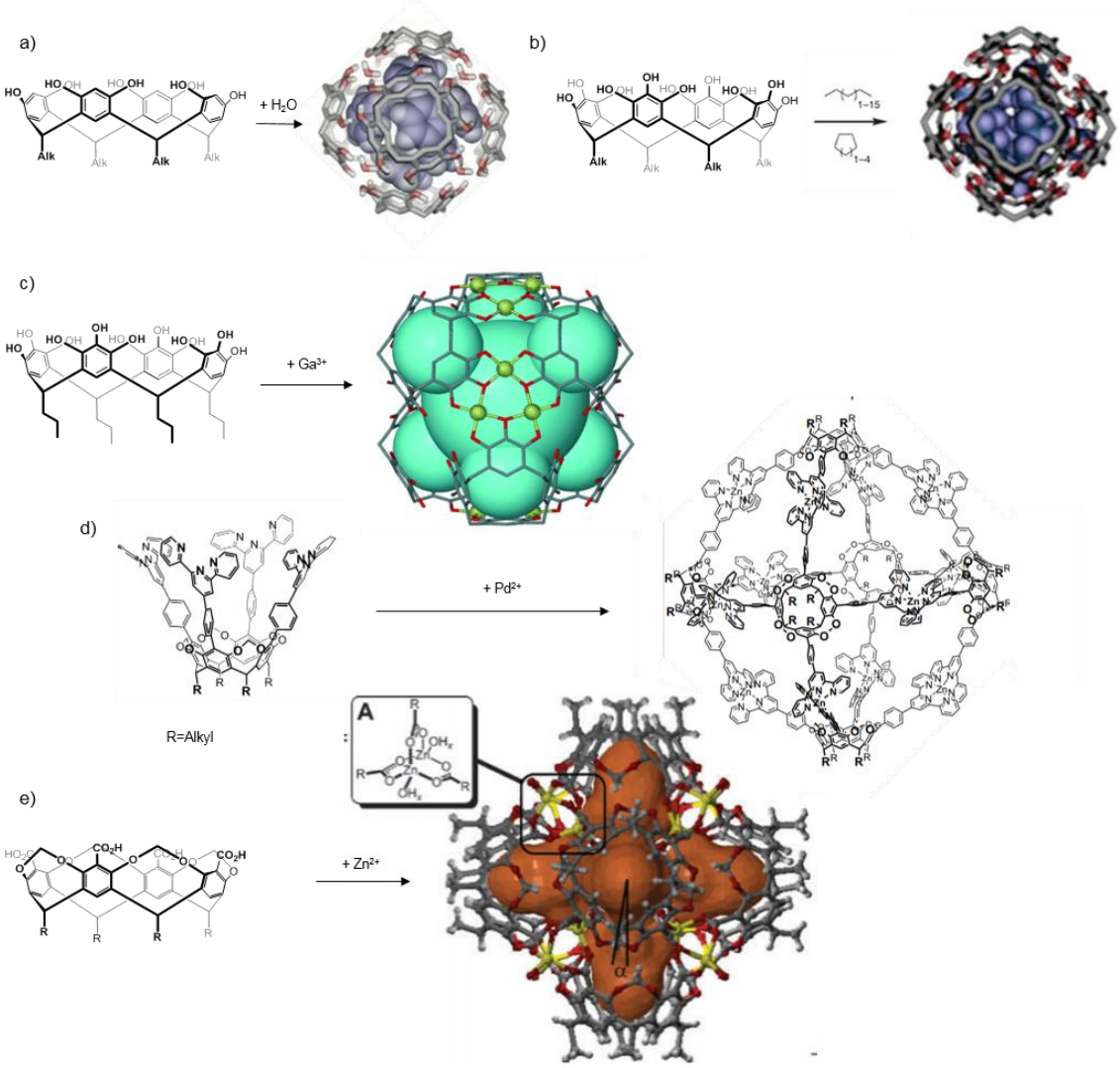

Figure 25: Hexameric macrocycle- or cavitand-based capsules. a) ATWOOD`s resorcinarene capsule held together by hydrogen bonds upon addition of water; b) MATTEY`s pyrogallarene capsule stabilized by hydrogen bonds; reprinted and adapted with permission from Avram *et al.*[125] (© 2011, Royal Society of Chemistry). c) ATWOOD`s pyrogallarene capsule (2nd generation) held together by coordinative bonds upon addition of gallium; reprinted and adapted with permission from McKinlay *et al.* (© 2005 Wiley-VCH Verlag GmbH & Co. KGaA, Weinheim). d) MATTAY`s resorcinarene-based capsule held together by coordinative bonds upon addition of palladium ions; reprinted and adapted with permission from Schröder *et al.*[126] (© 2008 Elsevier Ltd. All rights reserved.) e) HOLMAN`s resorcinarene-based capsule held together by coordinative bonds upon addition of zinc ions; reprinted and adapted with permission from Ugono *et al.*[127] (© 2008, Royal Society of Chemistry).

In this regard, REBEK established in the late 1990s the so-called 55%-rule, stating that the packing coefficient of a complex is ideally in the range of 55%, provided that the overall shape of a guest is

complementary to the host.[124] Here, the packing coefficient means the ratio between the volume of a guest species and the cavity volume of a molecular container based on their van der Waals radii. This value reflects the space filling in typical organic solvents and can be higher or smaller in polar solvents or if particular favorable noncovalent interactions are involved.[124]

A different synthetic strategy was employed by ATWOOD and coworkers to assemble their hexameric metal-coordinated pyrogallarene capsule for which they could obtain an X-ray crystal structure.[128] The preassembled hydrogen-bonded pyrogallarene capsule served as the template and after a subsequent insertion of copper ions, the resulting octahedral complex was stabilized by an array of three coordinative bonds on each face of the octahedron. The generality of this method was demonstrated by the synthesis of several other metal-coordinated hexameric capsules bearing different metals (Figure 25c).[129] The groups of MATTAY and HOLMAN presented the assemblies of two hexameric metal-coordinated capsules based on resorcinarene cavitands which are functionalized with suitable ligands at the 2-position of the aromatic rings.[126,127] The first capsule was characterized by NMR and small-angle X-ray scattering (SAXS) and is stabilized by the formation of twelve $[Pd(tripy)_2]^{2+}$ complexes which sit on the edges of the octahedron (Figure 25d).[126] The latter capsule could be characterized by X-ray crystal-structure analysis upon complexation of the cavitand with zinc ions and exhibits eight dinuclear μ-OH-linked $[Zn_2(ArCOO)_3]^+$ complexes which are located on the faces of the octahedron (Figure 25e).[127]

Reactivity of supramolecular capsules and cages

Supramolecular containers have been shown to undergo a variety of structural transformations due to the dynamic nature of noncovalent bonds. Changes can be induced by different external stimuli, such as solvents, concentration, counter ions, guests, change in component fractions or chemical compositions, light or post-modification reactions. These transformations result in new structures with often significantly different properties and thereby increase the diversity of supramolecular architectures. This allows the probing of structure-dependent properties and can give valuable insight into making functional, stimuli-responsive materials.[101,130] SEVERIN and coworkers published the solvent-induced structural rearrangement from a dimeric Ru_8L_2 cage to a slightly distorted monomeric Ru_4L complex upon change of the solvent from chloroform to dichloromethane which were observed by NMR and X-ray crystal analysis (Figure 26).[131] They rationalize this observation with the different thermodynamic stabilities of the two complexes in chloroform and dichloromethane. These seem to originate from the combination of the metallacrown units and a flexible ligand structure, which allow the generation of solvent-specific binding pockets, as observed in the solid state. The analysis of large supramolecular containers in general and their dynamic structural changes, in particular, can be very challenging as self-assembly and self-sorting processes can be very fast and often lead to complex product mixtures, short-lived intermediates or products of low concentration. This problem will be discussed in greater detail in chapter 2.4.

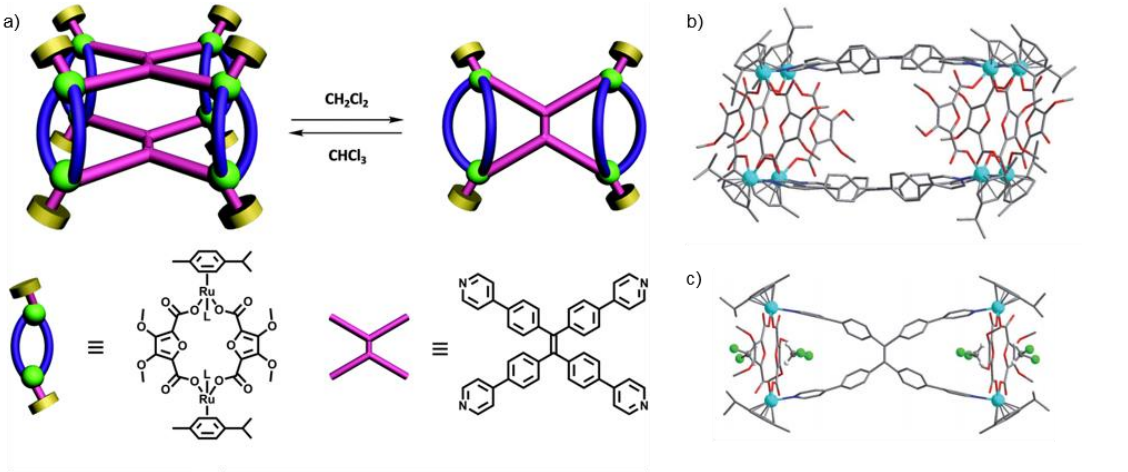

Figure 26: SEVERIN`s solvent-responsive coordination cage. a) Solvent-induced rearrangement of the Ru_8L_2 cage to a Ru_4L complex; reprinted with permission from Wang *et al.*[130] (© 2016, Royal Society of Chemistry). b, c) X-ray crystal structures of the Ru_8L_2 and Ru_4L complexes; reprinted with permission from Kilbas *et al.*[131] (© 2011, Royal Society of Chemistry).

Supramolecular catalysis is a fast-growing field within supramolecular chemistry and employs the ability of molecular containers to specifically encapsulate guest molecules or ions inside their cavities to promote reactions. Thereby, intermolecular interactions are exploited as an alternative basis for the control over chemical reactivity.[132] The role models from nature are certainly enzymes which can activate substrates in their highly specialized, hydrophobic cavities by the combined influence of noncovalent interactions. Hence, supramolecular catalysis strives to emulate enzymatic active sites to achieve reactivity different from or superior to synthesis in bulk solution.[117,132] Within the last decade, numerous examples have been presented of self-assembled supramolecular containers which are able to act as catalysts on their own or in combination with transition metal complexes, organocatalysts or enzymes in a variety of different reactions.[133] Capsules and cages were shown to influence the outcome of chemical reactions e.g. by the shifting of chemical equilibria to the thermodynamically less favorable product,[134] by stabilizing reactive species[135] or by promoting unfavorable conformations of guest species or transition state geometries within their cavity. Bimolecular reactions might profit from rate enhancements due to an increase in local concentration within the confined space and cascade reactions were shown to proceed smoothly which were normally not feasible in bulk solution. Furthermore, introducing stereochemical information in the host results in a lower symmetry of an achiral guest by which the outcome of an asymmetric reactions can be influenced.[136]

RAYMOND and coworkers presented the enantioselective aza-Cope rearrangement of an enammonium substrate by an enantiopure $Ga_4L_6^{12-}$ coordination cage (Figure 27a).[137] Here, the cage stabilizes the cyclic transition state by its constrained environment and the change of the charge state from the strongly binding substrate to the product ensures catalytic turnover without product inhibition.

TIEFERBACHER and coworkers recently published an example of supramolecular catalysis using the resorcinarene hexamer in combination with iminium catalysis.[138] An 1,4-reduction of the investigated

α,*β*-unsaturated aldehydes yielded the products with an increased or even inverted enantioselectivity, as compared to the reaction in bulk solution employing only iminium catalysis (Figure 27b).

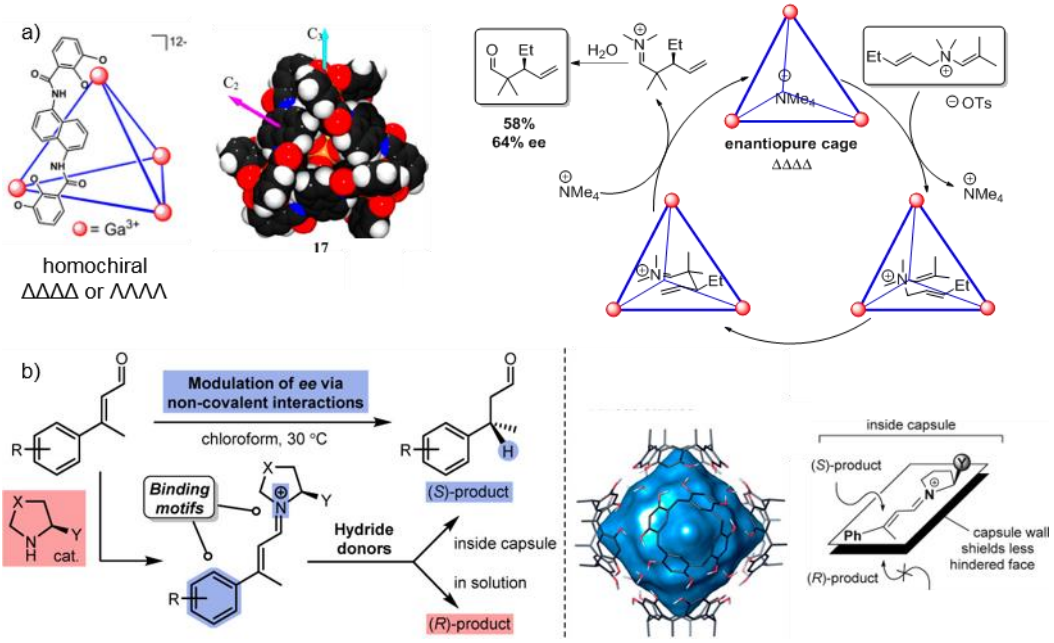

Figure 27: Supramolecular catalysis. a) RAYMOND`s $Ga_4L_6$ cage with molecular structure and X-ray crystal structure and enantioselective aza-Cope rearrangement of an enammonium substrate catalyzed by the cage; reprinted with permission of Brown *et al.*[133] (© 2015, American Chemical Society). b) TIEFENBACHER`s enantioselective 1,4-reduction of *α*,*β*-unsaturated aldehydes inside the resorcinarene hexamer in combination with iminium catalysis; iminium intermediate binds to the inner walls of the capsule from the less hindered side favoring the attack of the nucleophile from the top (*Si*)-face; reprinted and adapted with permission of Bräuer *et al.*[138] (© 2017, American Chemical Society).

2.3.3. Polyoxometalate Cages†

The earlier described concepts of self-assembly, host-guest chemistry and the formation of molecular containers are not exclusive for organic or metal-organic systems, but can be applied to inorganic systems, as well. In particular, polyoxometalates (POMs) have been intensively studied in this regard over the last couple decades. This class of compounds consists of the polyoxoanions of the early transition metal elements, especially vanadium, molybdenum, tungsten as well as niob and includes a waste number of structurally interesting complexes.[7,139] In contrast to other metals, these elements can form M=O double bonds. This structural motif yields discrete, often concave or even cage-like structures, since the double bonds are outwards directed and virtually seal off the complex from further aggregation.[7] Consequently, POMs can be distinguished from other metal oxides by the formation of molecular species, rather than infinite bulk materials. The early transition metals in groups 5 and 6 can exist in high oxidation states of +4

† Parts of this chapter have been published in the minireview "Soluble Hetero-Polyoxovanadates and Their Solution Chemistry Analyzed by Electrospray Ionization Mass Spectrometry" and are reproduced and adapted here with the kind permission of U. Warzok, L. Mahnke, W. Bensch, *Chem. Eur. J.* **2018**, Accepted Author Manuscript, https://doi.org/10.1002/chem.201803291 (Copyright © 2018, John Wiley and Sons).

to +6. Furthermore, they exhibit the appropriate charge density and charge-to-ionic-radius ratio to form the structurally determining M=O double bonds with strongly π-donating oxo ligands.[139–141] The resulting coordination polyhedra range from tetrahedral (coordination number 4) to pentagonal bipyramidal (coordination number 7) which enables a great structural variety.

POMs cover a broad spectrum of interesting properties related to their size and shape, their redox behavior, magnetic and photochemical characteristics. Applications range from catalysis, molecular electronics, material science and medicine to the use as molecular magnets, nanosensors and nanoreactors, for the molecular uptake and storage, as well as for battery research and artificial cell models.[7,141,142]

POM structures

The formation of POMs proceeds most often in acidic aqueous solution with the self-assembly of small and reactive oxometalate precursors in a combination of hydrolysis and condensation reactions.[140] The earliest POMs resulting from molybdenum were reported by BERZELIUS in the 19th century;[143] yet, only the development of X-ray diffraction methods in the early 20th century allowed the unambiguous analysis of these compounds. The first such example came from KEGGIN in 1933 who presented the classical $\{PM_{12}O_{40}\}$ cluster.[144] Its formation starts with the expansion of tetrahedral hydroxide metal complexes to octahedral hydroxide/oxo complexes which then condense to an edge-linked trigonal $\{M_3O_{13}\}$ unit. Four of these so-called triads self-assemble around a templating phosphate ion by corner connection and form the $\{PM_{12}O_{40}\}$ Keggin anion (Figure 28).[139,140]

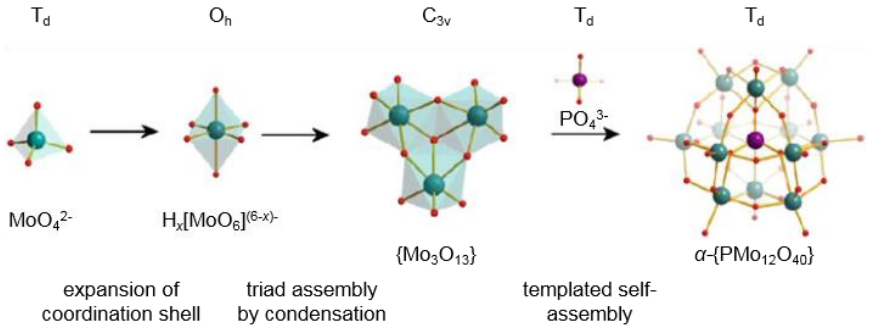

Figure 28: Self-assembly of a *α*-$[PMo_{12}O_{40}]^{3-}$ Keggin anion; reprinted and adapted with permission from Streb[140] (© 2017, Springer Nature).

POMs in general include a vast number of possible structures and can incorporate different heteroatom templates, additional heterometallic centers, organic cations or ligands. This makes their classification for many parts only possible in broad categories.[139] Heteropolyanions include heteroanions such as sulfate or phosphate which are crucial to their formation as they are likely to act as templates. This group forms often very stable compounds and is the most widely explored subset of POM clusters. It includes the important archetypal Lindqvist $[M_6O_{19}]^{n-}/\{M_6\}$, Anderson-Evans $[XM_6O_{24}]^{n-}/\{XM_6\}$, the already-mentioned Keggin $[XM_{12}O_{40}]^{n-}/\{XM_{12}\}$ and Wells-Dawson $[X_2M_{18}O_{62}]^{n-}/\{X_2M_{18}\}$ clusters (Figure 29).

In terms of denotation for POMs, the formula given in curly brackets does not match the complete stoichiometry or charge state of the compound which is usually written in square brackets. It rather emphasizes the important structural features including nuclearity, types of metal centers, as well as

encapsulated heteroions. This notation in curly brackets is somewhat flexible depending on the purpose of the description.

A second subclass of POMs form isopolyanions which do not contain an internal heteroanion or molecule and are usually more reactive than the corresponding heteropolyanions. Even more extended structures can self-assemble by simple one-pot procedures to form huge molybdenum blue or molybdenum brown-type clusters. These large wheel or sphere-shaped architectures are formed under highly reducing conditions from simple metal precursors and a variety of additional ligands.[139,145]

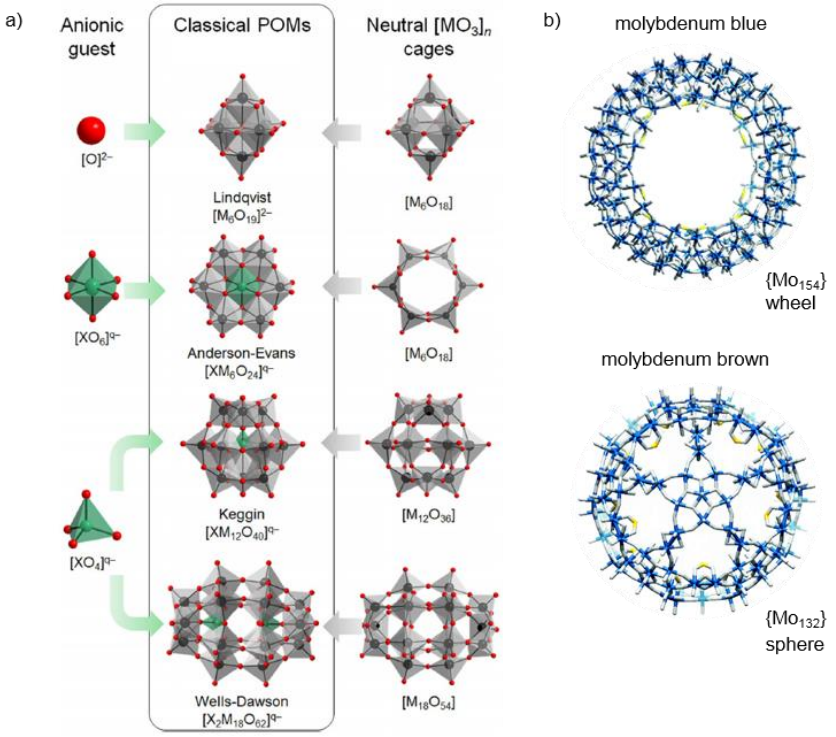

Figure 29: Structures of the classical polyoxometelates. a) M= Mo, W or V in black, O in red, X= B, P, Si, Ge and other heteroatoms in green, $\{MO_6\}$ as gray polyhedra, $\{XO_6\}$ and $\{XO_4\}$ as green polyhedra; reprinted with permission from Kondinski *et al.*[146] (© 2017 Wiley-VCH Verlag GmbH & Co. KGaA, Weinheim) b) Mo in blue, O in grey, heteroatoms in yellow; reprinted and adapted with permission of Miras *et al.*[141] (© 2014, Royal Society of Chemistry).

Synthesis of POM architectures

The synthesis of POM is generally performed by the pH-dependent speciation of small metal precursors, often hydroxide complexes, in acidic aqueous or non-aqueous media. However, the design principles are still rather empirical, as different interconnected self-assembly steps can be involved. The variation of reaction parameters, such as the concentration and the type of metal-oxide anion, the pH of the solution as well as reaction temperature and pressure is usually performed to tune the structure and properties of new compounds.[139,141] Moreover, the nature and amount of reducing agent, the type and concentration of heteroatoms and the presence of templating anions or ligands can have major effects. Several general types of POM syntheses have been developed, such as rational hydrolytic assembly, hydrothermal or solvothermal methods, post-functionalization or partial decomposition of a parent cluster. Rational hydrolytic assembly works by dosing small amounts of water to the precursor in non-aqueous media for a

controlled stepwise hydrolysis. Hydrothermal or solvothermal methods allow the assembly of POMs from soluble precursors other than oxides under increased temperature and pressure. Another valuable synthetic method involves the surface reactivity of preassembled cluster compounds which leads to new compounds by post-functionalization.[147] This way, larger building blocks can be connected to more extended assemblies. Furthermore, the partial decomposition of a parent clusters, e.g. by careful hydrolysis under basic conditions, leads to so-called lacunary structures which exhibit some vacant positions in their cluster shell. These can be filled by additional cations and are suitable connecting points to crosslink POM clusters to more extended architectures.[139,141] This is particularly useful for the generation of large supramolecular POM assemblies. Here, the building blocks should possess a certain degree of preorganization to obtain architectures with well-defined geometries and the desired chemical properties.[7,148]

A very recent example for an impressive supramolecular architecture containing several POMs was presented by WANG and coworkers in 2017. They demonstrate the formation of the host-guest complex $\{As_4Cu_{16}\}@\{Nb_7\}_4$ (Figure 30).[149] A one-pot reaction starting from the Lindqvist-type $\{Nb_6\}$ cluster, as well as homonuclear copper and arsenic precursors in basic aqueous media led to the stepwise self-assembly of the complex as evidenced by X-ray crystal structure analysis. The initial extension of the $\{Nb_6\}$ to a $\{Nb_7\}$ cluster core is crucial for the formation of the tetrahedral, concave $\{Nb_7\}_4$ host framework and for the encapsulation of the guest as it enables the formation of oxo bridges between host and guest. The formed tetrameric $\{As_4Cu_{16}\}$ guest cluster features an interesting high-nuclearity magnetic core which is stabilized within the $\{Nb_7\}_4$ framework. ESI-MS experiments showed that the compound is stable in basic aqueous solution over a wide pH range.

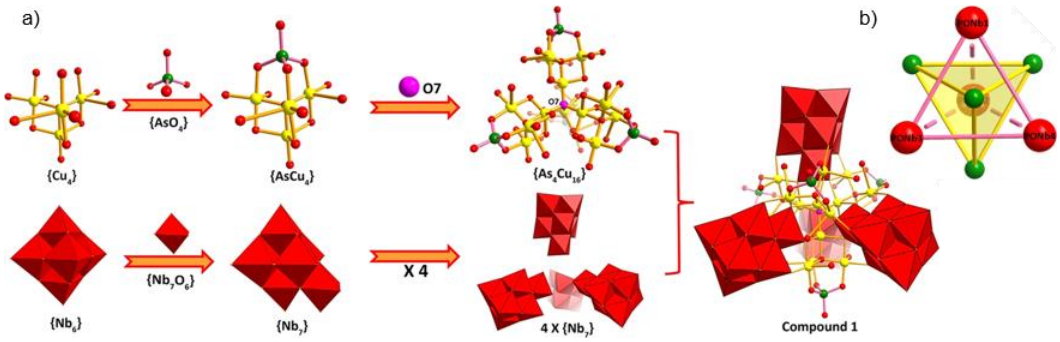

Figure 30: a) Self-assembly of a host-guest complex of an $\{As_4Cu_{16}\}$ cluster within a tetrameric $\{Nb_7\}$ host; NbO_6 as red octahedra, Cu in yellow, As in green, O in red; b) ball-and-stick depiction of the complex; $\{Nb_7\}$ in red, $\{As_4Cu_{16}\}$ in green. Reprinted and adapted with permission from Li *et al.*[149] (© 2017 Wiley-VCH Verlag GmbH & Co. KGaA, Weinheim).

An even larger and highly ordered architecture from a total of 13 substructures was presented by LUBAN and coworkers. They applied the combination of a supramolecular templating effect and a kinetic competition approach to selectively generate the complex $\{Mn_{40}W_{224}\}$ polyanionic architecture which was characterized by X-ray crystallography (Figure 31a).[150] From the complex structure and the knowledge of the synthetic procedure, they proposed an assembly mechanism: The initial $\{P_2W_{18}\}$ Dawson-type precursor transforms in solution to both, a $\{P_8W_{48}\}$ macrocycle and, in combination with a manganese building block, to Mn-containing $\{P_2W_{14}Mn_4\}$ and $\{P_2W_{15}Mn_3\}$ Dawson-type clusters. These reactions

proceed *via* a common $\{P_2W_{12}\}$ intermediate. The $\{P_8W_{48}\}$ macrocycle then templates the formation of the superstructure by the formation of Mn-O=W bridges between the subunits (Figure 31b). The final assembly contains four identical trimeric Dawson-type clusters which encapsulate the central $\{P_8W_{48}\}$ ring.

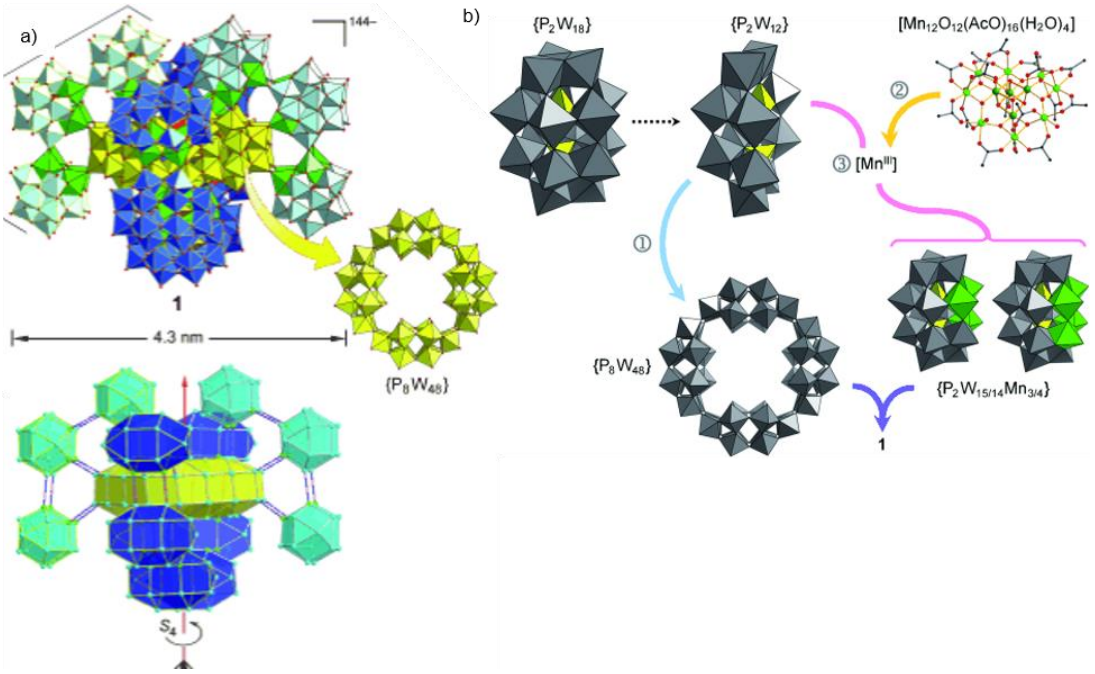

Figure 31: a) Structure of the $\{Mn_{40}W_{224}\}$ complex consisting of an encapsulated $\{P_8W_{48}\}$ macrocycle (yellow) and 12 corner-sharing Dawson-type clusters (green and blue) with stabilizing Mn-O=W bonds (violet, lower picture); b) proposed self-assembly mechanism shows formation of the D_{4h}-symmetric $\{P_8W_{48}\}$ macrocycle from the $\{P_2W_{12}\}$ precursor, the incorporation of Mn^{3+} ions into new $\{P_2W_{14}Mn_4\}$ and $\{P_2W_{15}Mn_3\}$ Dawson-type intermediates and their condensation onto the templating $\{P_8W_{48}\}$ ring by the formation of Mn-O=W bonds. Reprinted and adapted with permission from Fang *et al.*[150] (Copyright © 2011 WILEY-VCH Verlag GmbH & Co. KGaA, Weinheim).

Polyoxovanadates

Polyoxovanadates (POVs) are a subclass of POMs and research object of this thesis. POVs have found application in the fields of catalysis, sol-gel chemistry, gas sensing, geochemistry, sorption and intercalated layered material, surface and nano sciences, as well as secondary electrode materials for advanced lithium ion batteries and vanadium redox-flow batteries.[151,152] They are also in the focus of scientific research as possible single-molecular magnets since they can be magnetically functionalized.[151]

The compound class differs from Mo- and W-containing POM compounds especially in their structural diversity. $\{MoO_x\}$ and $\{WO_x\}$ form predominantly octahedral coordination polyhedra, whereas POVs feature homo- or heterovalent V atoms in square-pyramidal, octahedral or tetrahedral coordination geometries in oxidation states +IV, +V, mixed +IV/+V or even +III.[151] As the charge state is usually lower than those of Mo and W in POMs, POVs often have a slightly higher metal-to-oxygen ratio than the archetypal cluster types (Figure 29). This way, the overall charge of the cluster core is somewhat reduced and can still be compensated by the surrounding counter cations.[140,151] This results in cluster cores such as the fully-oxidized $[PV^{V}_{14}O_{42}]^{9-}$ that contains a Keggin $[PV^{V}_{12}O_{40}]^{15-}$ polyoxoanion capped by two VO^{3+} moieties. Syntheses under acidic conditions, as common for the other POM elements, yield almost

exclusively the thermodynamically very stable $[V^{V}_{10}O_{28}]^{6-}$ cluster. Hence, structural variation for POVs need to be achieved by different methods. They are most often synthesized from basic media under reducing conditions, in marked contrast to Mo- or W-containing POMs.[140] A resulting classical compound is the fully reduced, archetypical $[V^{IV}_{18}O_{42}]^{12-}$ cluster cage which exhibits edge-sharing {O=VO_4} square pyramids, as compared to the octahedral {VO_6} units in {V_{10}}.[140,151] It was first introduced by JOHNSON and SCHLEMPER in 1978.[153] This cluster core is at least *formally* derived from the fully-oxidized *α*-Keggin anion $[V^{V}_{12}O_{36}]^{12-}$ by the introduction of two {VO} units giving the experimentally observed Keggin-like $[V^{V}_{14}O_{38}]^{6-}$ and by four additional {VO} units to the hypothetical $[V^{V}_{18}O_{42}]^{6+}$ structure, which gives the fully-reduced species after a complete reduction of all V^{V} to V^{IV} (Figure 32).

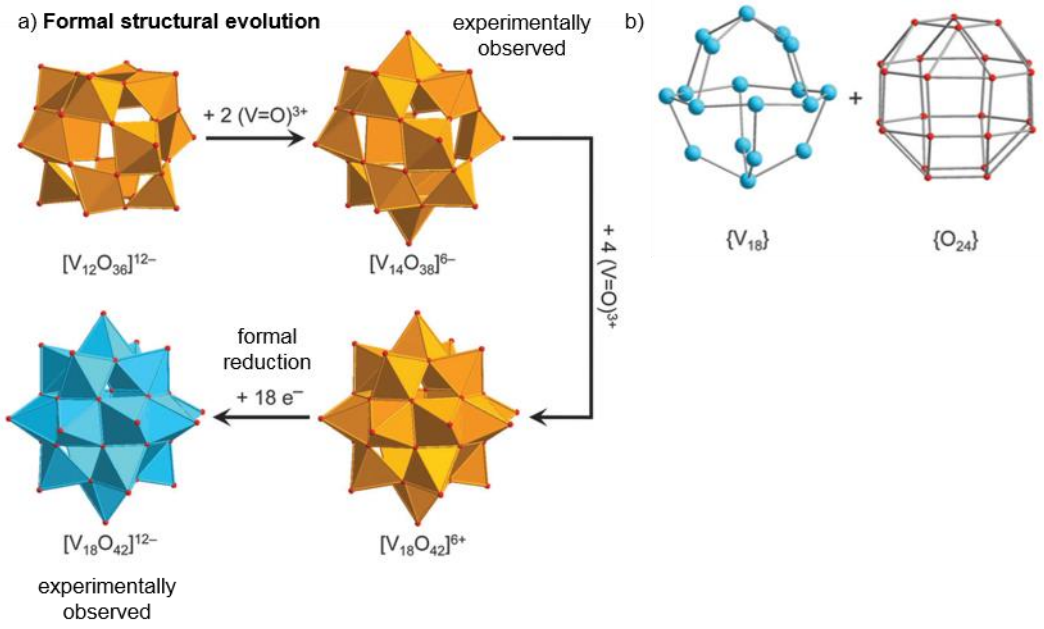

Figure 32: Archetypical {$V_{18}O_{42}$} cluster. a) Fully-reduced $[V^{IV}_{18}O_{42}]^{12-}$ POV structure is *formally* derived from the fully-oxidized *α*-Keggin-anion $[V_{12}O_{36}]^{12-}$; O in red, $V^{IV}O_5$ as blue polyhedral, $V^{V}O_5$ as orange polyhedral; b) schematic decomposition of {$V_{18}O_{42}$} into {V_{18}} and {O_{24}} (for bridging oxygen sites) skeleton. Reprinted and adapted from Monakhov *et al*.[151] (Published by The Royal Society of Chemistry).

Host-guest chemistry of POVs

The formation of concave POV structures with central voids is often templated by different small molecules, anions or cations which results in a great variety of host-guest complexes.[151] The shape and symmetry of the templating anion can thereby determine the overall cluster architecture.[140] In the examples presented in Figure 33, the spherical chloride induces an overall spherical shape and the azide ion an ellipsoidal shape, whereas nitrate and chlorate anion templates result in a flat and a tetrahedral shape, respectively.[140,154] This approach offers a valuable means to predetermine to resulting cluster shape. A significantly more advanced example introduced by SCHMITT and coworkers in 2011 features the self-assembly of a large {$V_{24}As_8$} cluster cage around a total of six chlorides anions.[155] They are arranged in an octahedral geometry with a distance $d_{Cl\cdots Cl}$ of ca. 4 Å (Figure 33b). Each chloride interacts with four V centers and templates the formation of a square {V_4} "cap" on the cluster surface. These {V_4} building blocks possess an electrophilic inner-surface and nucleophilic outer one, as the group has shown by theoretical calculations. This assists

the formation of the $Cl^-@\{V_4\}$ host-guest complexes and the hierarchical self-assembly of the whole complex against the Coulomb repulsion of six anions within the cavity.

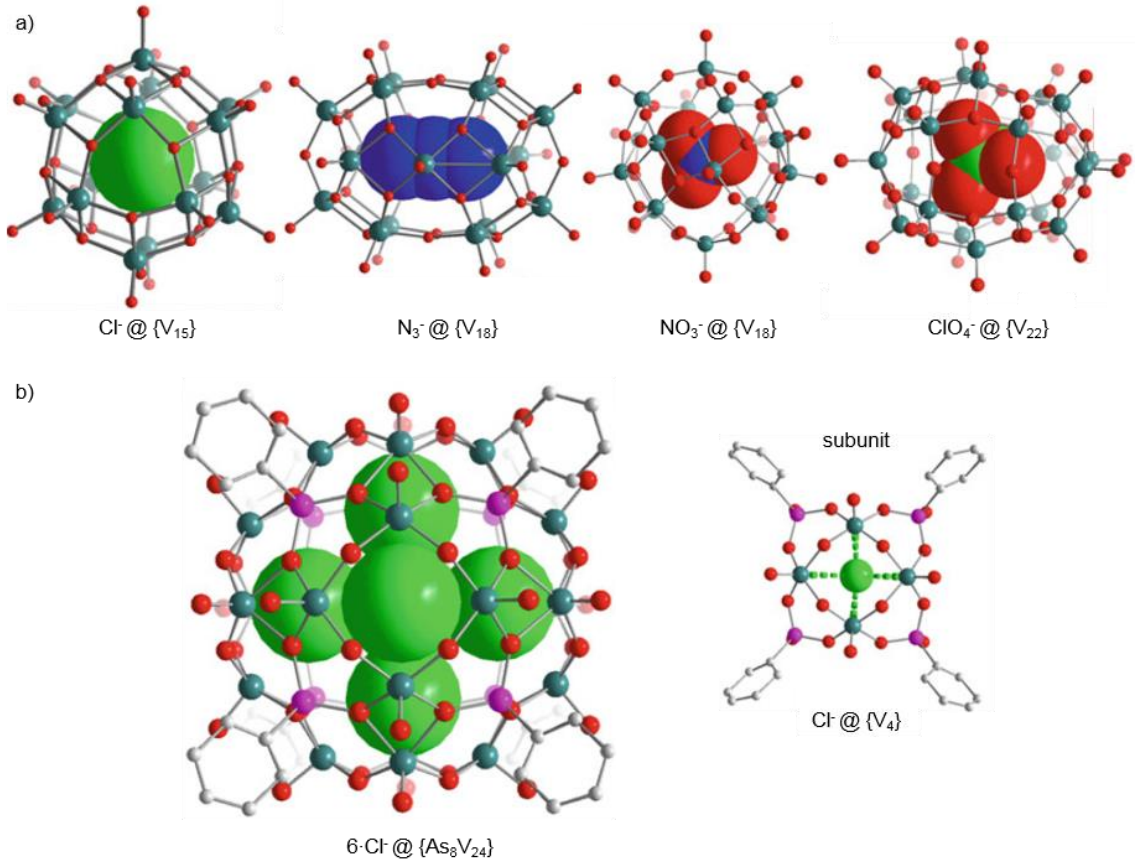

Figure 33: Selected examples for anion-templated POV cages. a) The symmetry of the template anions determines the cluster structures; b) $6Cl^-@\{As_8V_{24}\}$ cluster, its formation is templated by six chloride ions arranged in an octahedral fashion, each chloride templates a tetranuclear $\{V_4\}$ ring. V in teal, O in red, As in magenta, C in gray, Cl in green, N in blue; reprinted and adapted with permission from Streb[140] (© 2017, Springer Nature).

In general, the nature of the guest can have significant impact on the chemical, magnetic and electrochemical properties of the host cage.[140] This was evidenced, *inter alia*, by STREB and coworkers for the photooxidation of an organic dye by two isostructural POV complexes.[156] The two $\{X@Bi_2V^V_{12}O_{33}\}$ cages only differed in their encapsulated halide template ($X = Cl^-, Br^-$), but they gave significantly different oxidation rates. This implies a strong influence of the anionic guest inside the cavity on the overall cluster reactivity.

SCHMITT and coworkers achieved the assembly of molecular capsules by connecting two open $\{V_5\}$ bowls by ditopic phosphate ligands (Figure 34).[157] By varying the linker length, the capsule size could be tuned in the nanometer region which make these capsules interesting for selective guest binding.[140]

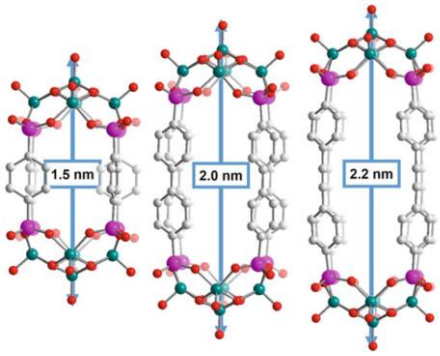

Figure 34: Hybrid organic-inorganic capsules self-assemble from open {V_5} caps with aromatic diphosphonate linkers; reprinted with permission from Streb[140] (© 2017, Springer Nature).

Antimonato polyoxovanadates

POVs can be functionalized by the introduction of different heteroelements (heteroPOVs) into the cluster structure, such as Si, Ge, As or Sb. The kind and number of heteroatoms modulate the electronic and magnetic properties of the clusters by influencing their redox potentials as well as by altering the steric and electronic environment around the terminal V=O groups. Especially the heteroPOV chemistry of As and Sb is well developed and mainly characterized by the lone electron pairs at As and Sb. They present a steric hindrance around the heteroatom and the terminal oxygen atoms and can, furthermore, act as bonding mediators which generally makes the formation of larger assemblies possible.[151] The solution and gas-phase chemistry of antimonato polyoxovanadates (Sb-POV) has been investigated during the course of this work, therefore some structural features will be described in more detail in the following.

Several Sb-POV compounds have been presented which feature the fully-reduced {V_{14}}, {V_{15}}, {V_{16}} or {V_{20}} cluster cores and which are formally derived from the {$V_{18}O_{42}$} archetype (Figure 35, see also Figure 32).[151,158] {VO_5} groups are stepwise replaced by handle-like {Sb_2O_5} groups with the Sb ions in trigonal pyramidal {SbO_3} coordination geometry and a formal oxidation state of +3. The Sb–O bonds are about as long as V–O bonds, but longer than V=O bonds ($d_{Sb–O}$ = 1.90–2.04 Å). Depending on the arrangement of the vanadium skeleton, different structural isomers have been shown to exist and numerous more are imaginable.[151]

At the begin of the work presented here, Sb-POVs were only accessible under hydrothermal or solvothermal conditions starting frequently from V_2O_5 or NH_4VO_3, less often from $NaVO_3$, $VOSO_4$ or vanadium halides. As no soluble precursor of higher nuclearity was available for post-functionalization, the synthesis of new compounds has so far been highly serendipitous.[151] Moreover, the solution chemistry and gas-phase chemistry of Sb-POVs in particular and heteroPOVs in general was virtually unexplored, which left fundamental questions concerning their formation mechanisms, stability and host-guest chemistry unanswered. This lack of knowledge can to some extend be held accountable for the slow progress to generate more complex, functional assemblies from POVs, as compared to the other classes of POMs.[151]

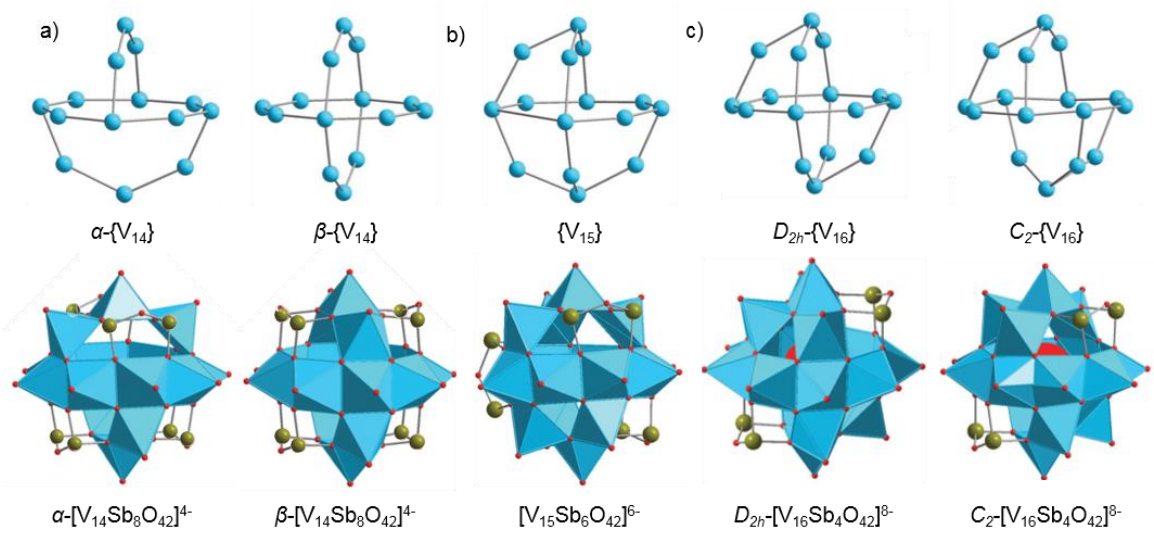

Figure 35: Experimentally observed fully-reduced Sb-POVs with V skeletons on top and polyhedral representation on the bottom. a) Different isomers of $\{V_{14}Sb_8\}$ clusters; b) $\{V_{15}Sb_6\}$ cluster; c) different isomers of $\{V_{16}Sb_4\}$ clusters with encapsulated water molecule. V in light blue, O in red, Sb in green, $V^{IV}O_x$ as blue polyhedral. Reprinted and adapted from Monakhov *et al.*[151] (Published by The Royal Society of Chemistry).

2.4. Mass Spectrometry for the Analysis of Molecular Containers[†]

2.4.1. General Aspects

Electrospray ionization mass spectrometry (ESI-MS) was extensively used in the course of this work to elucidate the structure and reactivity of supramolecular containers, namely supramolecular capsules and polyoxometalate cages. Hence, relevant aspects and techniques involving this analytical method will be discussed in the following chapter.

Mass spectrometry is an analytical technique employed to obtain the mass and charge of an ion. The basic principle involves the generation of gas-phase ions from inorganic or organic compounds by a suitable method, followed by their separation according to their mass-to-charge ratio (*m*/*z*) and the subsequent detection of the ion signal. A multitude of different techniques has been developed, the most important technical aspect relevant for this thesis will be explained in the following chapters. Besides the simple analytical characterization of a complex by determining the exact mass and charge state of an ion to obtain the stoichiometry, mass spectrometry offers a variety of experiments to elucidate more complex structural aspects, reactivity and thermochemistry. When ions are transferred into a region of high vacuum, they lose their solvation shell and do not interact with each other due to charge repulsion. This enables the study of isolated ions and their intrinsic properties without the influence of the surrounding system. Mass spectrometry thereby functions complementary to methods such as NMR spectroscopy or X-ray crystal structure analysis.[159] The advantages of the method lie furthermore in the three "S" - specificity, sensitivity and speed - as expressed by McLafferty.[160,161] Modern mass spectrometers often provide high resolution as the standard setting, instruments with ultra-high resolution even enable the distinction of the isotope-fine structure. The monitoring of reactions, for example, is possible on the time scale of milliseconds to seconds and can result in the detection of reactive species in the low micromolar to nanomolar concentration regime.[10] Due to the development of ion mobility instruments, a fourth "S", which relates to "separation", could likely be added to this list. Details will be discussed in chapters 2.4.5 and 2.4.6.

Organic and inorganic molecular containers grow steadily in size and complexity, making their analysis ever more challenging. A variety of suitable methods to study these assemblies has come forth over the last couple of decades.[162] In the field of mass spectrometry, the development of soft ionization techniques which enable the transfer of large, intact assemblies into the gas phase has been an essential methodological progress. The development of matrix-assisted laser-absorption ionization (MALDI) and electrospray ionization (ESI) was in the beginning mostly powered by the aspiration in the life sciences for a better understanding of large biomolecules, e.g. protein complexes and enzymes.[163] Additionally, this offers the valuable opportunity to investigate large synthetic assemblies in the gas phase to elucidate their structure and conformation, to solve stereochemical questions or to compare properties in solution to those of isolated

[†] Parts of this chapter have been published in the minireview "Soluble Hetero-Polyoxovanadates and Their Solution Chemistry Analyzed by Electrospray Ionization Mass Spectrometry" and are reproduced and adapted here with the kind permission of U. Warzok, L. Mahnke, W. Bensch, *Chem. Eur. J.* **2018**, Accepted Author Manuscript, https://doi.org/10.1002/chem.201803291 (Copyright © 2018, John Wiley and Sons).

gas-phase species. When fast building block or guest exchanges are most commonly observed in solution, the reactivity in the gas phase will rather reveal intramolecular rearrangements.[10,159] The effect of the environment onto supramolecular assemblies in solution is significant since the strengths of individual noncovalent interactions lies commonly in the same range as interaction with the solvent molecules. Therefore, the ionization and transition of supramolecular complexes from solution to environment-free conditions in the gas phase denotes a crucial change. Attributes like binding energy, directionality and geometry of noncovalent complexes may be altered upon ionization, resulting in changes in binding selectivity or stability of a large assembly. Interactions are in general strengthened upon solvent evaporation if they compete with the solvent in solution, like HB or electrostatic interactions in polar solvents. On the contrary, interactions like salt bridges and the hydrophobic effect will be diminished in the gas phase, as the stabilization or the excluding effect of the polar solvent is absent.[10,159,164]

2.4.2. Electrospray Ionization

Technical details

Electrospray ionization (ESI) as a soft ionization technique has been employed for all projects discussed in this thesis. JOHN B. FENN was awarded the Nobel prize in 2002 for its development which enables at atmospheric pressure the transfer of ions generated from sample molecules or complexes in solution into the gas phase.[165] ESI can be coupled to liquid chromatography, mixed-flow devices and microfluidic systems or samples can be injected directly *via* a syringe pump.[161] In any case, the solution is pumped through a steel capillary which is attached to a strong electric field of up to ca. 5 kV inducing charge separation. The so-called Taylor cone forms at the end of the capillary and Coulomb repulsion then causes the formation of charged droplets (Figure 36). Ongoing desolvation from the charged droplets and their further shrinkage result in Coulomb explosions leading ultimately to ever smaller droplets in a fine spray. The evaporation of the volatile solvent is facilitated by the usage of a stream of nebulizer gas surrounding the Taylor cone. Fully desolvated ions can be formed following either the charge-residue model or the ion-evaporation model and are then transferred into the high vacuum region of the mass spectrometer.[10,166,167]

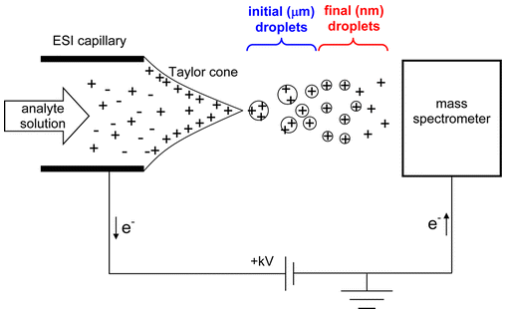

Figure 36: Schematic depiction of an ESI source operated in positive ion mode; reprinted with permission from Konermann *et al.*[166] (© 2013, American Chemical Society).

Depending on the ionization mode, ESI induces the protonation or deprotonations of sufficiently basic or acidic molecules to give often multiply charged $[M+nH]^{n+}$ or $[M-nH]^{n-}$ ions. With Lewis basic or acidic

molecules, it can result in the formation of cation or anion adducts, e.g. $[M+nNa]^{n+}$ or $[M+nCl]^{n-}$, whereas intrinsically charged complexes usually lose counter ions. This often leads to a broad charge distribution of multiply-charged ions for larger analytes. Ionization of noncovalent complexes can be very challenging if, for instance, protonation or deprotonation is either impossible or hampers the binding motif of the complex and subsequently leads to its fragmentation. A number of so-called charge-tagging approaches, in which charges are either introduced by covalent connections, by oxidation or reduction of the complex prior or during the ionization or by complex formation with e.g. charged guests, has been introduced to overcome this problem.[10,168,169] The choice of the spray solvent or a suitable solvent mixture is crucial to obtain a stable ESI spray. While polar solvents like methanol might often compete with interactions like HB or XB, unpolar solvents are for the most parts less suitable since their ability to stabilize charges is not as good. Moreover, the electric field at the ESI capillary can more easily penetrate the solution in case of solvents with high dielectric constants and permittivity. Additionally, the concentration used for mass spectrometric measurements is a critical key parameter, since low concentrations result automatically in the dissociation of noncovalent complexes in solution. However, high concentrations above a certain limit usually lead to unspecific binding or clustering, greatly diminishing the meaningfulness of the obtained results, in addition to the negative impact of highly concentrated solutions on the mass spectrometer device.

Nano-ESI (nESI) and coldspray ionization (CSI) are closely related to ESI and can in some cases ensure more reliable ionization without fragmentation of unstable compounds. Also, heating of ions that may lead to structural rearrangement during or after the ionization process can be suppressed to some extent. Nano-ESI is often used as a so-called offline source with the sample being injected into a metal coated glass capillary and directly ionized from it. The opening of the needle is narrower, the initial droplets smaller and both, the flow rates and the applied high voltage lower than for ESI.[167] A CSI source is cooled and uses cool drying gas to stabilize weakly bound ions. However, this often results in incomplete desolvatization.[170]

Applications

During the last two decades, ESI-MS has become one of the standard methods for the analysis of supramolecular complexes and numerous impressive assemblies could be detected and investigated.[171] Most relevant results are summarized in a number of instructive reviews by SCHALLEY and coworkers, which not only cover the ionization of supramolecular complexes by ESI, but also their investigation in the gas phase and in solution (see also chapters 2.4.3 to 2.4.6).[10,159,161,164,172] In the following, more recent examples on the topic of mass spectrometric investigations on molecular container will be discussed.

FUJITA and coworkers presented the formation of a $M_{30}L_{60}$ cage in 2016.[118] CSI-MS results enabled them to discover that the self-assembly of their first-generation thiophene-based ligand with palladium ions yielded a smaller $M_{24}L_{48}$ cage as the kinetic product and only over time resulted in the thermodynamic mixture of the $M_{24}L_{48}$ and the $M_{30}L_{60}$ assemblies (Figure 37a, b). Based on these results, small adjustments to the ligand structure were made. The second-generation ligand gave selectively the $M_{30}L_{60}$ assembly which is the largest supramolecular cage reported to date. It was analyzed by a combination of X-ray crystallography, NMR techniques and CSI-MS (Figure 37c).

In the field of large inorganic assemblies, the group of CRONIN has shown a variety of impressive architectures which were routinely analyzed with ESI-MS.[173–175] Recently, they presented the assembly of several POM cluster-of-clusters architectures based on an inorganic $\{Mo_{24}Fe_{12}\}$ macrocycle that forms around a templating anion (Figure 38a, b).[176] In the case of $\{Mo_{12}O_{36}(HPO_3)_2\}$ as the template cluster anion, the intact host-guest complex of macrocycle and template could be detected by ESI-MS (Figure 38c).

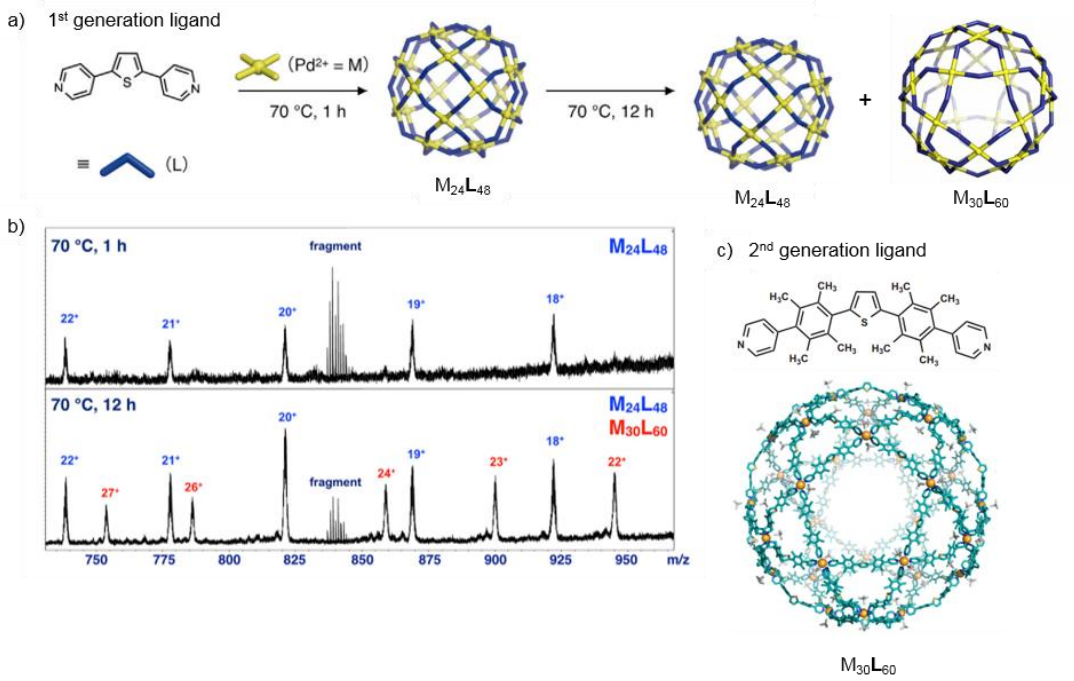

Figure 37: FUJITA`s $M_{30}L_{60}$ cage. a) Initial ligand resulted in a mixture of $M_{24}L_{48}$ and $M_{30}L_{60}$ cage. b) Reaction products in solution where observed by CSI-MS. c) Second-generation ligand resulted in formation of first stable $M_{30}L_{60}$ cage (X-ray crystal structure). Reprinted and adapted with permission from Fujita *et al.*[118] (© 2016 Elsevier Inc.).

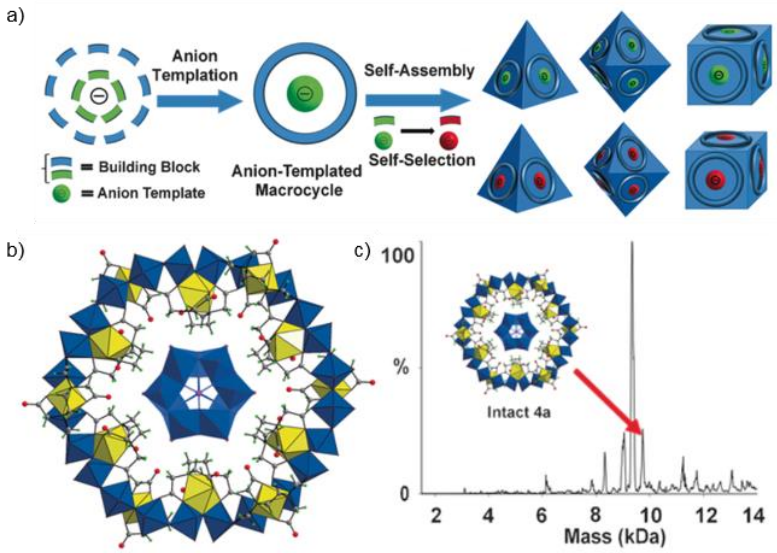

Figure 38: CRONIN`s cluster-of-clusters architectures. a) Schematic representation of the dynamic assembly of the anion-templated macrocycle, followed by cluster-of-clusters assembly; b) X-ray crystal structure of the host-guest complex of macrocycle and template cluster $\{Mo_{12}O_{36}(HPO_3)_2\}$; c) deconvoluted neutral ESI mass spectrum showing host-guest complex in water. Reprinted and adapted from Xuan *et al.*[176] (© 2016 The Authors. Published by Wiley-VCH Verlag GmbH & Co. KGaA.).

2.4.3. Mass Analyzers

Many different mass analyzers have been developed over time which make use of various physical principles to achieve the separation of ions according to their *m*/*z*. Mass spectrometers used for the experiments in the present thesis exhibit a time-of-flight analyzer and quadrupole which are therefore presented herein.

Time-of-flight (TOF) analyzers are frequently used in combination with ESI sources and use the acceleration of ions along an electric field to separate them by their *m*/*z*. In detail, ions with different masses *m* and charges *ze* are divided into ion packages and accelerated by a voltage *U* in an electric field. All ions then have the same kinetic energy E_{Kin}, but travel with different velocity *v* depending on their *m*/*z*. When measuring the time *t* that an ion needs to cover a constant distance *s*, its *m*/*z* can be calculated by applying equation 2, which can be rearranged to give equation 3.[177]

$$E_{Kin} = zeU = \frac{mv^2}{2} = \frac{ms^2}{2t^2} \quad (2)$$

$$\frac{m}{z} = \frac{2eUt^2}{s^2} \quad (3)$$

Different techniques are available to increase resolution. They ensure that the exact starting time for all ions in one package is known and that the time frame of ions entering the flight tube is as short as possible. Moreover, reflectron TOF analyzers are available which feature higher mass accuracy and resolution by using electrostatic potentials to reflect ions back into the flight tube. This not only virtually doubles the flight path, but also refocuses the ions according to their kinetic energy. TOF analyzers can cover a very high *m*/*z* range at high resolution and sensitivity.[177]

Quadrupole-mass analyzers can separate ions based on the stability of their trajectories in oscillating electric fields. The quadrupole is composed of four parallel, round-shaped metal rods. To each of these rods, an oscillating voltage is attached that consists of a constant and an alternating potential. At a given electric field, the ions travel in between the metal rods in a wave-like trajectory depending on their *m*/*z*. Stable trajectories lead the ions further on to the detector; ions on unstable trajectories either fly out of the quadrupole or are neutralized when getting in contact with metal rods and do not proceed further (Figure 39). By varying the voltage applied to the rods, a wide range of *m*/*z* can be scanned and hence detected. Quadrupoles are often used for mass selection of ions prior to tandem MS experiments. For this, the voltage is set to allow only the ions with the desired *m*/*z* to pass through the quadrupole.[10,177]

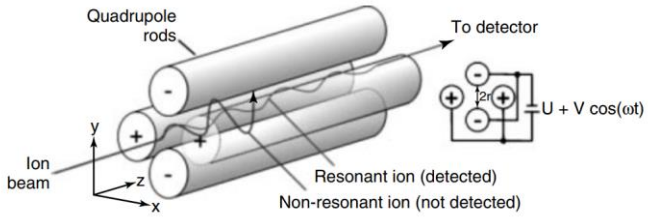

Figure 39: Schematic representation of a quadrupole with stable and unstable ion trajectories; Reprinted with permission from Weimann *et al.*[10] (© 2012 Wiley-VCH Verlag GmbH & Co. KGaA)

2.4.4. Solution Reactivity

An integral aspect in the field of research concerned with the assembly of molecular containers, both supramolecular organic and inorganic type, is the investigation of their reactivity in solution. This comprises the tasks to unravel the formation mechanism of a complex structure or to investigate its kinetic and thermodynamic stability in solution, as well as the elucidation of possible stimuli-induced reactions. Some studies on large complexes employing solution methods like NMR or fluorescence resonance energy transfer (FRET) spectroscopy have been presented for the investigation of supramolecular assemblies, but they often suffer from the incapacity to explore complex mixtures.[178] However, NMR spectroscopy is not possible for most inorganic POM cages. The commonly incorporated metals are usually not well-suited for NMR experiments, due to their paramagnetism, low receptivity or qua

drupolar nuclei. Moreover, the cost of ^{17}O- enriched water usually limits the synthesis of isotopically labelled POMs. Hence, ESI-MS is certainly the most suitable and straightforward technique for the solution investigations for these types of molecular containers.[161,174,179] Especially when the formation of different isomers, short-lived reaction intermediates or products of low abundance complicate the analysis.

Once it is established that ionization of the desired intact complexes can be achieved by electrospray ionization, it furthermore needs to be secured that the observed signal intensities are directly corresponding to the concentration of the investigated species in solution. This is not necessarily the case, as the so-called

ESI response factor can be very different. That is, the factor of how efficiently different complexes or molecules in the same solution are ionized and desolvated is usually not the same.[10] Nonetheless, for structurally similar complexes of the same charge state, similar ESI response factors can usually be assumed or established by suitable titration experiments.[180,181] This enables the quantitative to semi-quantitative interpretation of the results obtained from ESI-MS experiments.

In addition to the straightforward monitoring of a reaction mixture over time or to applying different reaction conditions to study the formation mechanism and the dynamics of capsules and cages in solution,[118,182] the exchange of building blocks is often investigated. This process can be detected by ESI-MS, if building blocks are isotopically labeled[181] or if they exhibit minor structural differences that do not affect the properties of the system. FUJITA and coworkers presented an CSI-MS study on the kinetics of a multicomponent self-assembly of a $M_{12}L_{24}$ cage.[180] Monitoring the exchange of two rigid, divalent pyridine ligands over time, that only differ in a pendant alkyl chain, demonstrated an assembly mechanism in three stages on different time scales. Regarding the investigation of inorganic POM clusters, exchange experiments are commonly performed in the form of isotopic labeling studies.[183] Dosing of small amounts of a suitable labeling reagent, often $H_2{}^{18}O$, or dissolution of the cluster in the reagent makes it possible to observe the exchange of oxygen atoms in an oxo cluster by the shift and broadening of its isotopic pattern. Information on the structural features and the kinetic stability of different positions can be deduced from this.[184,185]

Numerous stimuli-responsive supramolecular systems investigated by ESI-MS that exhibit a complex solution reactivity have been reported.[10,161,164,186] NITSCHKE and coworkers studied the self-sorting

behavior of two homoleptic Zn_4L_6 cages containing naphthalene diimide (N_6) or porphyrin (P_6) ligands that form a dynamic-covalent library (DCL) upon mixing (Figure 40).[187] Applying ESI-MS, the adaptation of the DCL to two different chemical stimuli was monitored which induced either the formation of host-guest complexes or of catenated structures. It was shown that the addition of C_{70} leads to the self-sorting of ligands into their homoleptic cages to form the host-guest complex $C_{70}@P_6$. Addition of the crown ether C leads to the preferred formation of heteroleptic cages, with a maximum number of interactions between the naphthalene diimide ligands and the crown ether, given that the incorporation of more than two macrocycles is not possible for steric reasons.

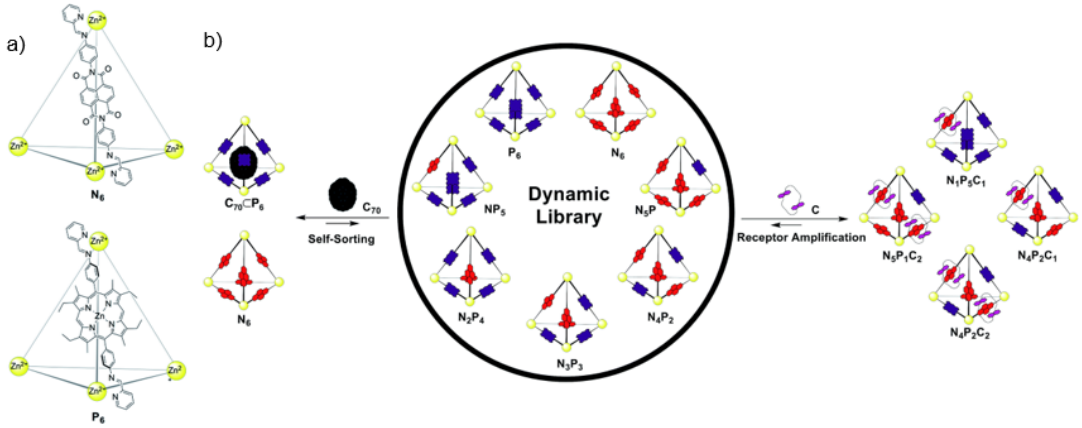

Figure 40: NITSCHKE`s stimuli-responsive Zn_4L_6 cages. a) Homoleptic Zn_4L_6 cages; b) different templating effects observed in the DCL formed upon mixing of N_6 and P_6. Reprinted and adapted from Black *et al.*[187] (Published by The Royal Society of Chemistry).

The synthesis of new POMs often occurs by template-induced post-functionalization or rearrangement processes of a substrate cluster into another one. To rationalize and explore these processes, ESI-MS is commonly applied.[149,174,175,179,188,189] CRONIN and coworkers presented the oscillatory guest-exchange process driven by competing redox processes in a POM capsule system (Figure 41).[190]

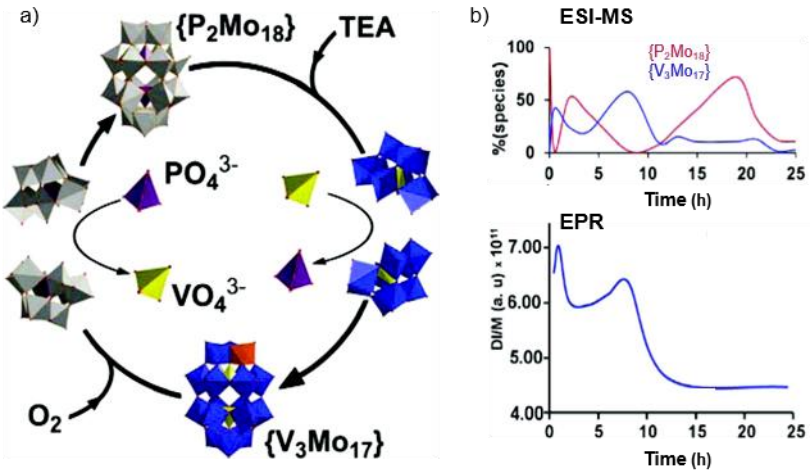

Figure 41: a) Redox-driven guest-exchange reaction interconverting $\{P_2Mo_{18}\}$ into $\{V_3Mo_{17}\}$ by dissociation of $\{P_2M_{18}\}$ capsules into two $\{PM_9\}$ halves. b) Amounts of the $\{P_2Mo_{18}\}$ and $\{V_3Mo_{17}\}$ capsules in the reaction mixture over time as observed by ESI-MS and EPR indicate oscillation of the reactive system. Reprinted and adapted with permission from Miras *et al.*[190] (© 2012, American Chemical Society).

Using ESI-MS, EPR und UV/Vis spectroscopy, they could demonstrate that the addition of ammonium vanadate and triethanolamine (TEA) to their system resulted in six complete oscillations. The Dawson-type $\{P_2Mo_{18}\}$ capsule bearing two encapsulated phosphate guests converts into the $\{V_3Mo_{17}\}$ capsule with two vanadate guests and one vanadium incorporated into the cluster shell. They postulated a reaction mechanism that involves the opening and closing of the cluster capsules and that is driven by a competition between reductive and oxidative processes.

2.4.5. Gas-Phase Reactivity

Technical details

Tandem mass spectrometry, also called MS/MS, is a technique to probe the structure and intrinsic reactivity of a complex without the influence of a solvent in the gas phase. Such an experiment involves in general the mass selection of the ion of interest, its activation and the resulting gas-phase reaction, followed by mass analysis and detection of the resulting product ions. A variety of tandem mass spectrometers is available to conduct these experiments, e.g. triple quadrupoles, hybrid quadrupole/TOF instruments, ion-trap instruments, Fourier-transform ion cyclotron resonance (FT-ICR) mass spectrometers or TOF/TOF instruments. The mass-selection step in a quadrupole (Figure 42, top), as it was used for all studies presented in this thesis, is described in chapter 2.4.3. Depending on the instrument used and the ion abundance observed after the first gas-phase reaction step, a reselection of product ions followed by multiple gas-phase reactions (MS^n) is possible.[10]

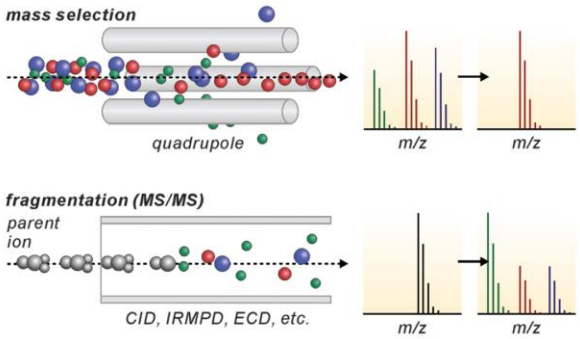

Figure 42: General setup for a tandem MS experiment resulting in the fragmentation of the ions under investigation; reprinted and adapted from Qi *et al.*[161] (Published by The Royal Society of Chemistry).

The activation of the ion inducing the following gas-phase reaction can generally lead to a decrease or an increase in ion mass, depending on the type of experiment. Fragmentation reactions that result in a mass loss can either be triggered by an increase of the ion`s internal energy, by introduction of radicals or a combination of both that lead to homolytic and heterolytic bond cleavages.[167] The available fragmentation methods, such as collision-induced dissociation (CID), infrared-multiphoton dissociation (IRMPD), electron-capture dissociation (ECD) or blackbody-infrared dissociation (BIRD), vary in the physical principle applied (Figure 42, bottom).[167] This results in different modes of activation with an inherent

amount of energy transferred. Furthermore, the various activation modes proceed on different timescales. This is a crucial parameter to the question, whether the imparted energy is distributed over all vibrational degrees of freedom of the ion, prior to the first bond cleavage, or if it is not. This ergodic or, respectively, nonergodic behavior greatly influences the fragmentation mechanism. Hence, the application of different fragmentation methods can provide complementary information.[167]

CID is the most commonly used method for ion activation and involves the collision of ions with inert gas molecules like helium, nitrogen and argon or even heavier gases, e.g. xenon. In a CID experiment, ions are accelerated in an electric field and upon their collision with the stationary gas, their kinetic energy is converted into internal energy. If the collision energy applied is high enough, this rovibrational excitation, meaning transitions that involve changes in both vibrational and rotational states, induces bonds to break or rearrangements with possible subsequent fragmentations. CID experiments can be classified by their energy regime. For high-energy collisions over ca. 100 eV, rearrangement reactions are often suppressed in favor of direct bond cleavages.[167] This predominantly provides information on the connectivity of the analyte. Low-energy collisions of less than 100 eV can induce rearrangement reactions which yield information on the spatial arrangement. Reactions that involve noncovalent bonds usually proceed in this lower energy window and can provide information about the arrangement of the subunits in the complex relative to each other.[161,168,172,191] The reactivity of ionized supramolecular complexes is commonly closely related to its structural and energetic features.[192]

The collision activation generally results in a broad energy distribution over different vibrational modes within an ion population. This enables competing fragmentation pathways with different activation barriers. The obtained fragmentation patterns can be related to the relative energy demand of competing reactions which in turn elucidates structural details of the investigated complexes.[164] In some cases, noncovalent bonds were found to be more stable upon collision activation than covalent bonds, allowing for valuable insights into the energetics of the noncovalent interaction.[164] Furthermore, the stability of a series of similar complex ions and the ranking of their binding energies in the gas phase can be accomplished by determining the so-called CID threshold energy.[193] These CID threshold energies need to be corrected for the charge state and the mass difference between the investigated ions to allow a comparison of the complexes.

Applications

KAPPES and coworkers recently published a study on a series of supramolecular “nanoprism” cages as originally introduced by FUJITA and coworkers.[194,195] The host-guest complexes are comprised of a prismatic coordination complex which encapsulates different azaporphyrins (Figure 43a). The aim of this research was to study the influence of the different azaporphyrins guests on the energetics of these host-guest complexes by a combination of ESI-MS, CID tandem MS and analytical ultracentrifugation. The tandem MS experiments demonstrated different fragmentation patterns for the host-guest complexes and the empty nanoprism which indicates the stabilization of the cage by the azaporphyrins guest (Figure 43b). This was further confirmed by the comparison of their gas-phase stabilities which showed a significantly lower CID threshold energy for the fragmentation of the empty cage (Figure 43c, d).

CID tandem MS is also frequently used in the analysis of POMs, often in combination with isotopic labeling of the analyte prior to the experiment.[174,179,189] The fragmentation of the parent cluster can in some cases lead to fragments with the same or similar stoichiometries as observed for solution-phase species and can thereby give information about formation mechanisms in solution.[196] However, this approach cannot be applied to all systems as the sequence of bond cleavages starting typically with the weakest bonds does not necessarily resemble the order of assembly. Rather, reactions in the gas phase can provide valuable information on the intrinsic properties of the analyte, if reactions are observed which do not occur in solution.[185]

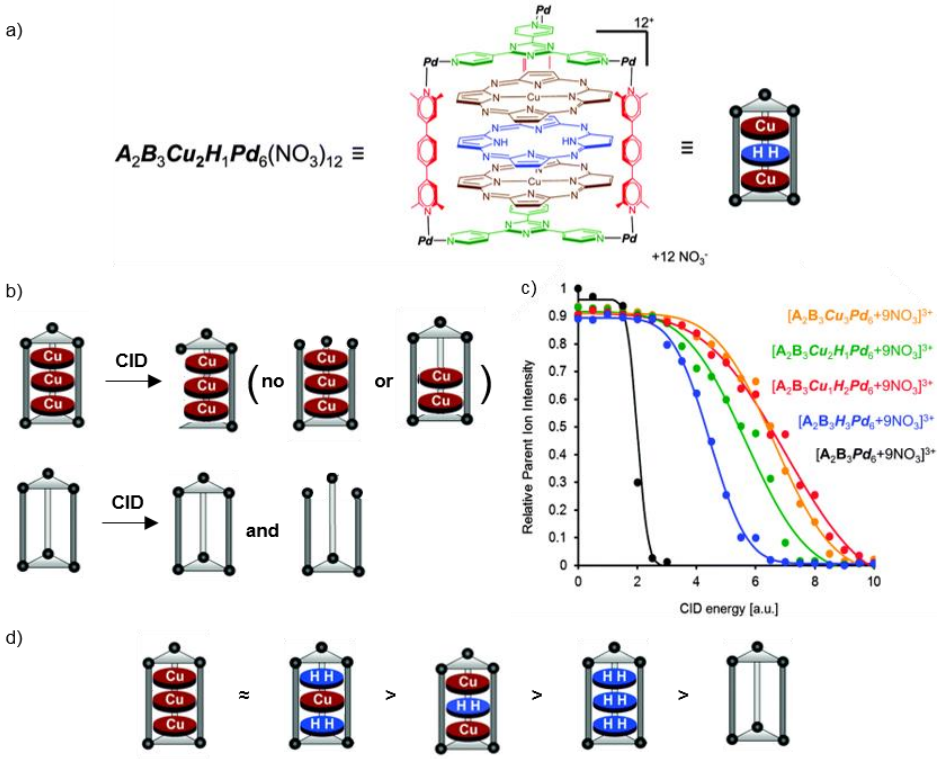

Figure 43: a) Structure of "nanoprism" cage (example); b) CID fragmentation pattern observed for all host-guest complexes and for the empty cage; c) CID threshold energies of different complexes; d) order of relative gas-phase stability as obtained from CID experiment. Reprinted and adapted from Weis *et al.*[194] (Published by The Royal Society of Chemistry).

A second major type of tandem MS experiments are bimolecular gas-phase reactions between an ion and a neutral molecule, e.g. in gas-phase isotope-exchange reactions. Volatile reagents like methanol-d_4, D_2O or $H_2{}^{18}O$ can be introduced into an ion trap, such as a hexapole, an FT-ICR cell or an orbitrap and react with ions which are kept in it over the course of the experiment (Figure 44).[161,164]

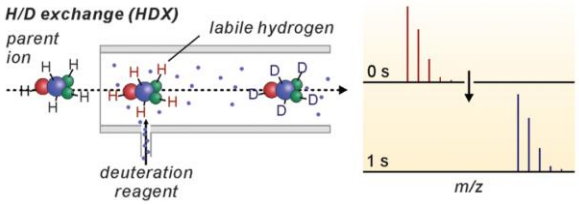

Figure 44: General setup for a H/D exchange in the gas phase; reprinted and adapted from Qi *et al.*[161] (Published by The Royal Society of Chemistry).

In the context of molecular containers, H/D exchange experiments have been applied by SCHALLEY and coworkers to hydrogen-bonded supramolecular capsules. They were able to elucidate structural questions, e.g. if a closed or an open hydrogen-bonded capsule is present in the gas-phase, and mechanistic aspects concerning the intramolecular dynamics in the complexes.[197] $^{16}O/^{18}O$ exchange experiments in the gas phase are less common,[198] but could provide mechanistic details on the activation of water by a $\{Mn_4O_4\}$ cluster in the gas phase as shown by LANDMAN and coworkers.[199] In another study, ROESCH *et al.* demonstrated with a set of $^{16}O/^{18}O$ isotope-exchange experiments the stark contrast between the solution and the gas-phase reactivity of a siloxanediol.[185]

2.4.6. Ion Mobility

Ion mobility mass spectrometry (IMS) is a gas-phase technique which separates ions based on their *m*/*z* as well as their size and shape. It can be regarded as an analog to electrophoresis in the condensed phase. The physical property related to size and shape relevant for these experiments is the collision-cross section (CCS). That is, the effective area quantifying the likelihood that an ion collides with a gas atom or molecule. In time-based IMS methods, this results in a faster travel of compact structures through the gas than of more extended ions due to fewer interactions with the so-called drift gas (Figure 45).[161,200]

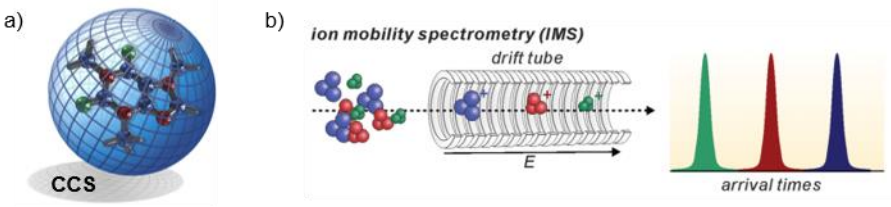

Figure 45: a) Collision-cross section (CCS) of an ion relates to the average area when tumbling through a gas; provided by Waters Corporation.[201] b) General setup for an ion mobility experiment; reprinted and adapted from Qi *et al.*[161] (Published by The Royal Society of Chemistry).

The characteristic CCS of an ion offers structural information and can be compared to values based on theoretical calculation, NMR experiments or X-ray crystallography. However, compared to the other methods, significantly smaller quantities of the substance of a much lower purity are needed. It can be used for the differential separation of ions in a complex mixture prior to their mass-analysis and is very valuable as it does not only provide ensemble-averaged information, but rather for each single species.[200] The differences in ion mobility relate to the CCS of the analyte and can give information about their connectivity, configuration, conformational dynamics and their topology. IMS has so far primarily been used for the analysis of large biomolecules,[202] but presents a valuable extension to mass spectrometric methods also relevant for the analysis of molecular containers. Two instruments with different general IMS techniques were used over the course of this thesis and will be presented in the following section.

Drift tube ion mobility mass spectrometry

In a drift tube ion mobility spectrometry (DT-IMS) experiment, ions are subjected into a drift tube which is filled with an inert gas, most often helium, and to which a static uniform electric field (usually 5-100 V) is applied (Figure 46a).[200] Under the influence of the electric field, the ions pass through the drift tube and undergo low-energy collisions with the drift-gas molecules. As stated above, small and compact ions will undergo fewer collisions than larger ions and arrive, therefore, faster at the detector. As the electric field is constant, the measured drift time of one specific ion can be directly related to its CCS value Ω. The velocity v of an ion is equal to the product of its mobility K and the strength of the electric field E; it can be determined by measuring the time t_D the ion needs to traverse a drift tube of a known length d (equation 4). The reduced mobility K_0 of the ion, which is independent of temperature T and pressure p inside the drift tube, can be calculated from this relationship (equation 5). The Mason-Schamp equation (6) connects the reduced mobility K_0 with the CCS value Ω of the ion by taking into account known experimental parameters (charge state of the ion z, number density of the drift gas N, reduced mass of ion-neutral pair μ, gas temperature T) and natural constants (elemental charge e, Boltzmann constant k_B).[203] The equation is valid if the 'low-field limit' is small (below $2 \cdot 10^{-17}$ V·cm^2). That is, the ratio between the electric field strength E and the buffer gas density N, as it ensures that the mobility of an ion is still independent of the drift field.[203,204]

$$v = \frac{d}{t_D} = KE \tag{4}$$

$$K_0 = K\frac{273}{T}\frac{p}{760} = \frac{d}{Et_D}\frac{273}{T}\frac{p}{760} \tag{5}$$

$$\Omega = \frac{3ze}{16N}\left(\frac{2\pi}{\mu k_B T}\right)^{\frac{1}{2}}\frac{1}{K_0} \tag{6}$$

For determining experimental CCS values of the halogen-bonded capsules investigated in this thesis, an inhouse-constructed DT-IMS instrument called iMob at the Fritz-Haber Institute Berlin was used.[205] At this instrument, ions are generated by nano-ESI and then travel through a drift tube filled with helium to a quadrupole for mass selection and analysis (Figure 46b). To calculate reliable CCS values from measured drift times, several measurements are performed applying different electric fields to the drift tube and the resulting data is fitted to the Mason-Schamp equation (6).

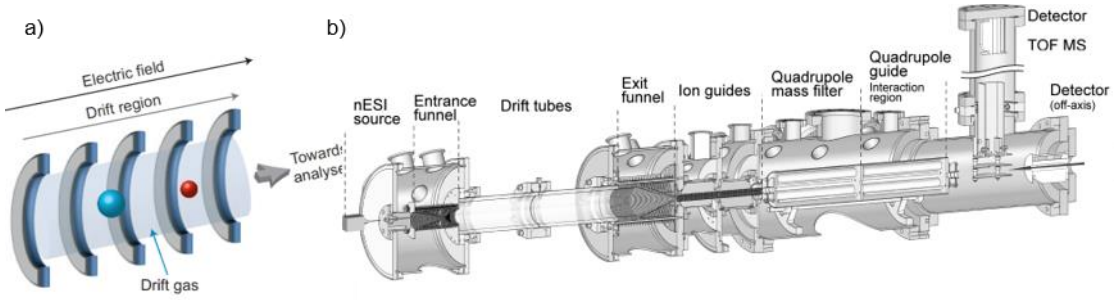

Figure 46: a) Schematic depiction of a DT-IMS cell; reprinted and adapted with permission from Lanucara *et al.*[200] (© 2014, Springer Nature). b) In-house constructed DT-IMS instrument used in this thesis for measurements for CCS

values; reprinted with permission from Warnke *et al.*[206] (© 2015, American Chemical Society).

Traveling-wave ion mobility mass spectrometry

A second method commonly used for IMS is travelling-wave ion mobility mass spectrometry (TW-IMS). The IMS cell consists of several ring electrodes stacked to a ring-ion guide (Figure 47a). These are charged with alternating phases of a radio-frequency voltage and a superimposing traveling voltage wave. Ions are then pushed by the potential and 'surf' on these waves to the end of the IMS cell. The drift gas flows in the opposite direction and causes an opposing force by which the separation of ions is possible. More extended ions with lower mobility roll over the crest of the waves and thereby traverse the IMS cell more slowly, while more compact ions tend to 'surf' fast on the potential waves.[200] Velocity and height of the traveling voltage wave influence the drift time of the ions and are hence adjusted to achieve an optimal separation. Due to the constantly changing electric field in a TW-IMS cell, measured drift time and CCS value cannot directly be correlated to each other. Therefore, CCS values need to be calculated based on the drift times of a suitable calibrant with known CCS measured under identical conditions. To obtain meaningful values, this calibrant needs to possess similar physical and chemical features as the investigated analyte.[207] For container molecules like capsules, this would need to be a calibrant with a concave structure also including voids, which is, however, not available. Instead, measured arrival-time distributions (ATD) of different ions can be evaluated and compared to each other, to obtain qualitative results on their gas-phase structure.

The great majority of ESI-MS and IMS experiments performed for the work presented in this thesis was conducted using the commercial TW-IMS instrument SYNAPT G2-Si (Waters, Manchester). Ions are generated by ESI, then transferred into the high vacuum regime of the instrument and focused by a stepwave-ion guide and mass-selected in the adjacent quadrupole (Figure 47b). In the following three cells (trapping/collision cell, ion mobility cell, transfer/collision cell), a variety of different gas-phase experiments can be performed. This arrangement enables to conduct combined tandem MS-IMS experiments and even MS^3 measurements. Finally, the ions are then subjected to the TOF analyzer.

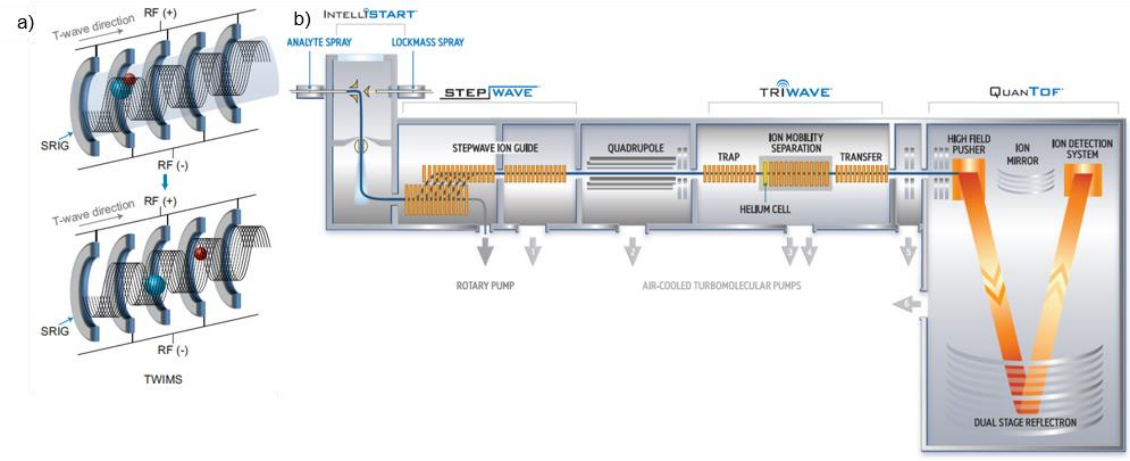

Figure 47: a) Schematic depiction of a TW-IMS cell (RF for radio-frequency voltage); reprinted and adapted with permission from Lanucara *et al.*[200] (© 2014, Springer Nature). b) Commercial TW-IMS instrument from Waters. SYNAPT G2-Si was used for the majority of ESI-MS and IMS experiments presented in this thesis. Provided by Waters Corporation.

Obtaining CCS values

Even though helium is most commonly used as the drift gas for IMS, other inert gases also find application. It was shown that higher resolution can be achieved by switching between drift gases of different polarity or by adding volatile dopants to the gas, as this can favor the interaction between analyte and drift gas.[208] CCS values are usually compared to data derived from other experimental methods or to data generated by theoretical calculations, including structure optimization and molecular dynamic simulations. Different computational algorithms are available to obtain theoretical CCS from structures derived from calculation or X-ray crystal-structure analysis. The projection approximation method is computationally inexpensive as it assumes the CCS as the average of all geometric projection areas that result from all possible ion orientations. It does not include long-range interactions or the scattering between the ions and the drift gas. Therefore, this method is predominantly applied to small molecules. The exact hard-sphere scattering method accounts for the scattering and the collisions of the ions with the drift gas, but does not include long-range interactions. It is often used for large systems as it presents a compromise between computation cost and accuracy. The trajectory method is seen as the most accurate of these common approaches, since it includes long-range interactions and the effect of collisions between drift gas and analyte. It is often applied to complex systems, even though the computing time is relatively high.[200]

Applications

The scientific interest in harnessing IMS for the investigation of complex supramolecular organic and inorganic systems is steadily growing, as it provides the opportunity to observe and monitor e.g. self-assembly and self-sorting processes, the formation of host-guest complexes or gas-phase reactions.[161,164,209,210,211,212] IMS is frequently used to separate and analyze complex product mixtures after covalent synthesis or self-assembly processes.[176,212,213] A growing number of examples has been introduced were IMS was utilized as a supporting analytical method next to X-ray crystal structure analysis and NMR spectroscopy to confirm the formation of molecular containers.[214] Some groups have employed IMS even for the major part of the analysis of their supramolecular complexes.[186,209,211,215] CRONIN and coworkers have published studies on the structural elucidation by IMS of inorganic cages in solution, for which no X-ray crystal structures could be obtained.[216] For example, they presented a combined ESI-MS and IMS study in which the hierarchical self-assembly of an icosahedral nanoscale Keplerate cluster is shown.[217] Twelve pentagonal $\{Mo^{V}Mo^{IV}_{5}\}$ building blocks are connected by thirty Fe^{III} centers and form an overall $\{Mo_{72}Fe_{30}O_{252}\}$ shell around an encapsulated Keggin-type $\{SiMo_{12}O_{40}\}$ cluster (Figure 48a).[218] In addition to the intact Keplerate nanocluster, higher order supramolecular structures were observed in the gas phase for the first time. The different oligomers could be resolved by IMS. The group proposed similar structures as were observed earlier for these so-called Keplerate ‘blackberries’ in solution and in the solid state (Figure 48b).

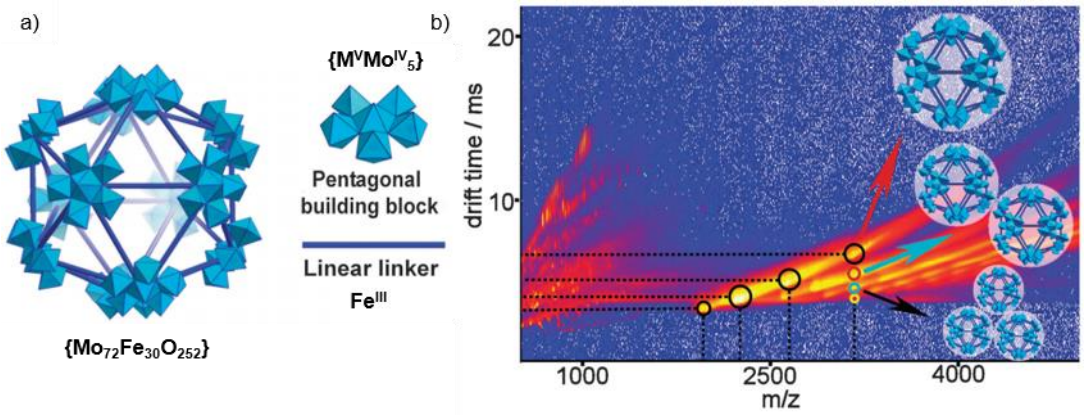

Figure 48: CRONIN`s supramolecular assembly of Keplerate clusters. a) Schematic representation of Keplerate cluster structure and of building blocks; b) 2D-IMS plot resolves intact cluster ions (black circles) and oligomeric assemblies (red, blue and yellow circles). Reprinted with permission from Robbins *et al.*[217] (© 2013, Royal Society of Chemistry).

KALENIUS and coworkers presented in 2017 the formation of a pyridine[4]arene capsule and its guest binding behavior using a combination of ESI-MS, IMS, DFT calculations, X-ray crystallography and NMR spectroscopy.[191] They found the simultaneous *endo* complexation of solvent molecules like acetone and dichloromethane within the capsule and *exo* complexation of PF_6^- anions between the alkyl chains in all three physical states (Figure 49a, b). Such ternary complexes are rarely observed in the gas phase, but could be evidenced by their gas-phase study. A CID tandem MS experiment indicated the weak *exo* complexation of PF_6^-, as the anion was eliminated first from the complex (Figure 49c). Furthermore, DT-IMS showed two different complex types with the PF_6^- complexes exhibiting larger CCS values than the deprotonated dimers. These results agree with their proposed complex structure.

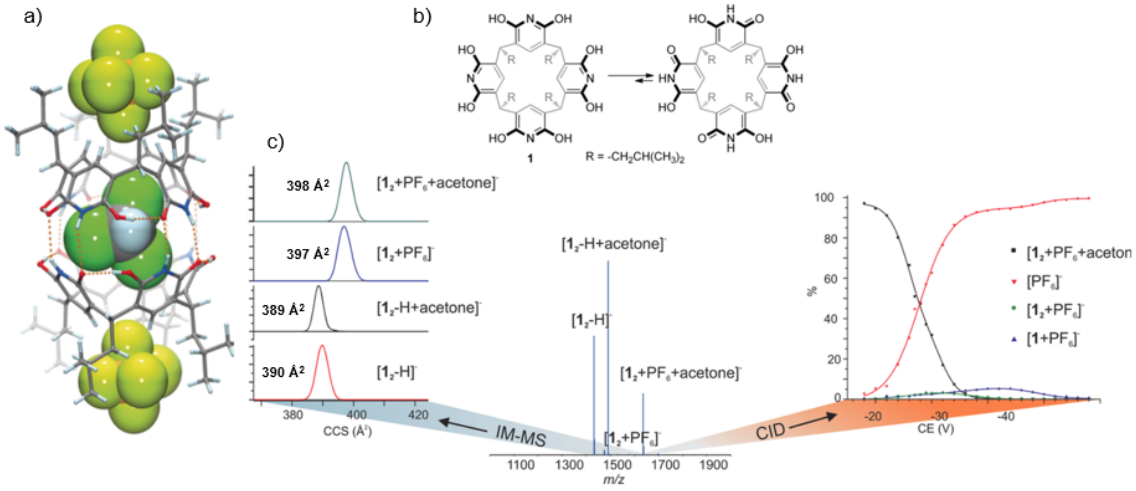

Figure 49: KALENIUS`S pyridine[4]arene dimer. a) X-ray crystal structure of dimeric capsule with *endo*-complexed $CHCl_3$ and *exo*-complexed PF_6^-; b) chemical structure of pyridine[4]arene; c) DT-IMS and CID tandem MS experiments show ternary capsule complex in the gas phase. Reprinted with permission from Kiesilä *et al.*[191] (© 2017, Wiley-VCH Verlag GmbH & Co. KGaA, Weinheim).

Very recently, DE PAUW and coworkers published an impressive study on the folding and unfolding mechanism of an oligorotaxane in the gas phase using ESI-MS, IMS, tandem MS and molecular dynamics calculations.[219] The rotaxane features two different noncovalent interactions which are decisive for its

conformation; namely, the intramolecular π–π interactions between naphthalene and viologen moieties, as well as Coulombic interactions between the viologens and the PF_6^- counterions (Figure 50a, b). They could demonstrate that the ionized complex at low charge states exhibits a folded, compact structure which is dominated by π–π stacking. At higher charge states, the complex is fully stretched due to Coulomb repulsions between the viologens (Figure 50c). These gas-phase conformations were then modulated *via* tandem MS experiments. First, low charge-state ions were unfolded to the elongated structure by low-energy CID activation. Furthermore, higher charge-state ions were reduced in the gas phase using an electron-transfer by a radical anion, which was reacted with the rotaxane complex before it entered the IMS cell. This led to the folding of the elongated structure into the compact conformation. Here, mass spectrometry techniques in combination with theoretical methods could elucidate the interplay between the existing π–π interactions and Coulomb interactions which determine the foldamer conformation.

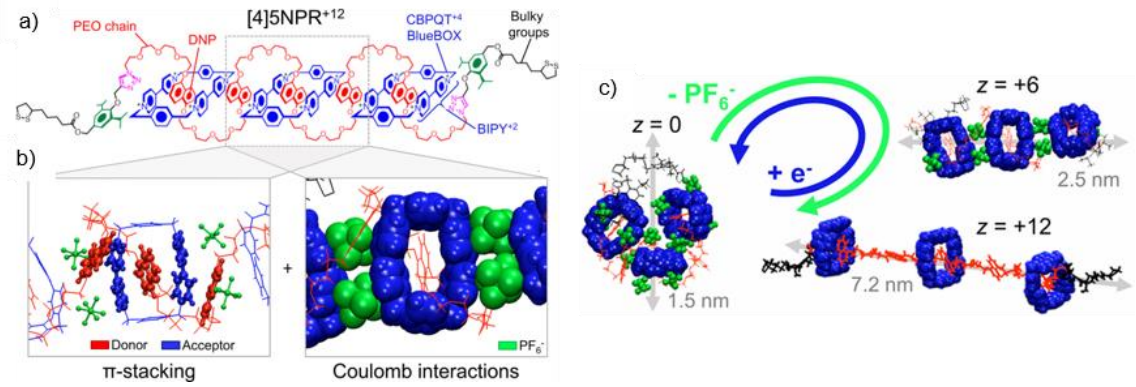

Figure 50: DE PAUW`S folding cascade of an oligorotaxane. a) Chemical structure of the investigated donor–acceptor oligorotaxane; b) noncovalent interactions decisive for gas-phase conformation; c) stimuli-induced folding and unfolding of the oligorotaxane as observed by IMS. Reprinted with permission from Hanozin *et al.*[219] (© 2017, American Chemical Society).

3. Results

3.1. Halogen-Bonded Supramolecular Capsules

3.1.1. Halogen-Bonded Supramolecular Capsules in the Solid State, in Solution, and in the Gas Phase

Oliver Dumele, Benedikt Schreib, Ulrike Warzok, Nils Trapp, Christoph A. Schalley, and François Diederich

Angew. Chem. Int. Ed. **2017**, *56*, 1152–1157; *Angew. Chem.* **2017**, *128*, 1172–1177.

Submitted on November 7, 2016, first published on January 13, 2017 in Angewandte Chemie International Edition and Angewandte Chemie in German language. For copyright reasons, the article (Appendix 6.3.1) is not included in the online version of this thesis.

An electronic version of the article is available (https://doi.org/10.1002/anie.201610884, https://doi.org/10.1002/ange.201610884).

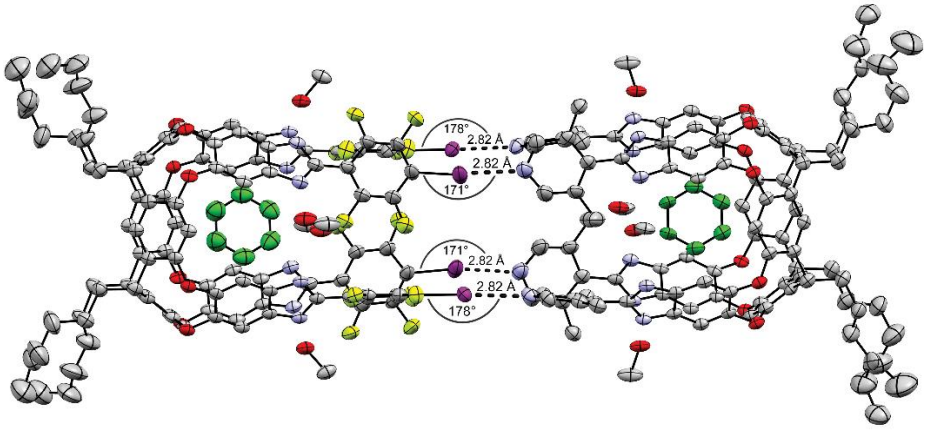

Figure 51: X-ray crystal structure of XB capsule $\mathbf{1}_{C6}\cdots\mathbf{2}_{C6}$ (ORTEP ellipsoids shown at 40% probability at 100 K) confirming fourfold XB geometry between donor and acceptor hemisphere. Each cavitands encapsulates one benzene molecule (green) and is rigidified by four MeOH molecules. Color code: C_{host} in grey, N in blue, O in red, I in purple, F in yellow, C_{guest} in green. Reprinted with permission from Dumele *et al.*[220] (© 2017, Wiley-VCH Verlag GmbH & Co. KGaA, Weinheim).

Project summary

The basis for this first project on supramolecular halogen-bonded capsules is the previous work of DUMELE *et al.* which covers the formation of the first dimeric XB capsule **1**···**2** based on functionalized resorcinarenes, as well as its association and guest binding properties in solution (see also chapter 2.3.2).[114] In the present work, different structural variations of the established XB donor and acceptor motifs were introduced and their effects on the capsule formation were studied in the solid state, in solution and in the gas phase. The first X-ray crystal structure of a neutral halogen-bonded capsule was obtained from $\mathbf{1}_6\cdots\mathbf{2}_6$, an analogue of **1**···**2** with shorter side chains. It shows a highly ordered 12-components assembly which confirms the fourfold XB geometry between the two capsule hemispheres (Figure 51).

The structural variation on the donor and acceptor moieties revealed large solvent effects on the capsule formation. Strengthening of the XB acceptor from a lutidyl to a quinuclidyl cavitand (**2** → **3**) resulted only in a modest increase of the capsule association constant for **1**···**3** as determined by NMR experiments in a benzene/acetone/methanol solvent system (70:30:1), and a slow exchange rate on the ^{19}F NMR time scale (Figure 52a). Van`t Hoff analysis demonstrated that its formation is enthalpy-driven; however, only with an unexpectedly low binding enthalpy and virtually no entropy contribution. This behavior was rationalized with the strong solvation of the quinuclidyl residues in the free cavitand **3** by methanol, as was observed in the solid state. A certain methanol content is necessary for all cavitands to maintain a stable vase conformation in solution by forming a ring of hydrogen bonds between the benzimidazole walls and the methanol. Nevertheless, the desolvation of the acceptor cavitand prior to the halogen-bond formation hampers the capsule association.

Employing the stronger XB donor motif tetra(iodoethynyl) of cavitand **4**, as compared to the tetrafluoro-4-iodophenyl moiety in donor **1**, made a significant impact on the association strength. The capsule **2**···**4** exhibits the highest association constant with $K_a = 2.11 \cdot 10^5\ M^{-1}$ at fast exchange rates. It was hereby shown that the tuning of the XB donor cavitand has a significantly stronger influence on the capsule association in XB-competitive solvents than structural variations on the XB acceptor. Furthermore, an additional third guest-binding site for 1,4-dithianes was found within the elongated iodoethynyl capsule **2**···**4** as compared to the original **1**···**2** capsule (Figure 52b).

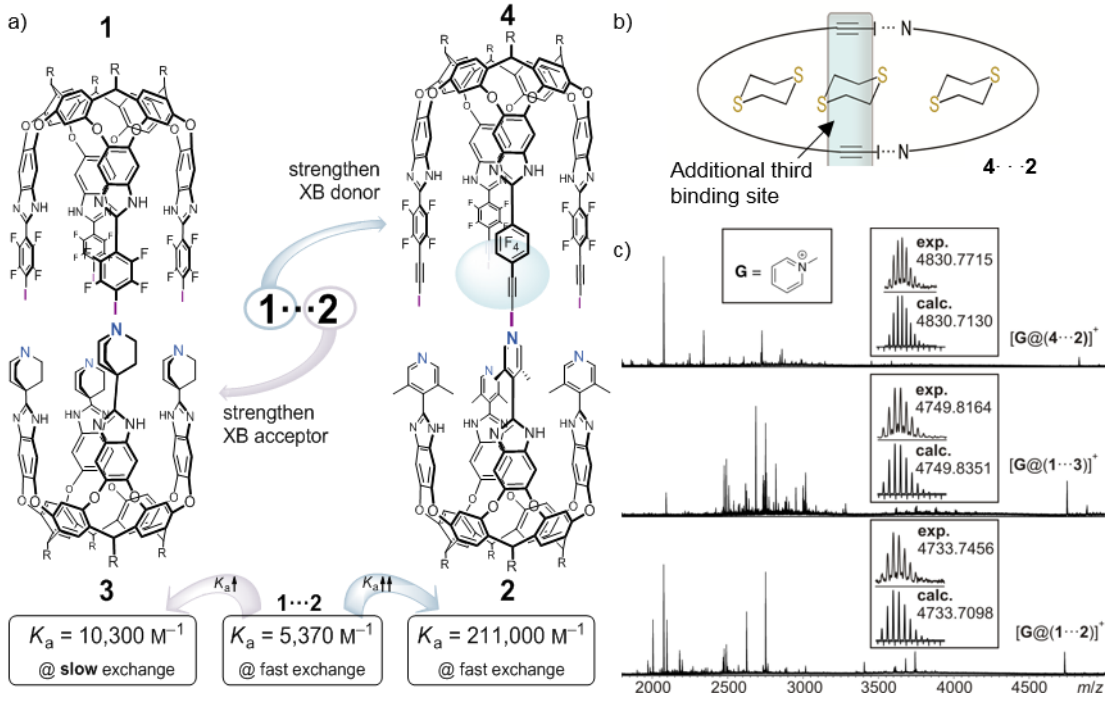

Figure 52: a) Structural tuning of XB hemispheres of capsule **1**···**2** to tetraquinuclidyl cavitand **3** and to tetra(iodoethynyl) cavitand **4** results in capsules **1**···**3** and **4**···**2** with corresponding binding constants K_a; b) elongated capsule **2**···**4** hosts one additional 1,4-dithiane guest compared to **1**···**2** or **1**···**3**; c) ESI-MS spectra of host-guest complexes of XB capsules **2**···**4**, **1**···**3** and **1**···**2** with *N*-methylpyridinium **G**. Reprinted and adapted with permission from Dumele *et al.*[220] (© 2017, Wiley-VCH Verlag GmbH & Co. KGaA, Weinheim).

Using ESI-MS to obtain mass spectra from the inherently neutral XB capsules remained unsuccessful in both ionization modes. Likely, protonation blocks the XB acceptor for XB formation and deprotonation causes a destabilization of the cavitand conformation. The halogen-bonded capsules were therefore charge-tagged by encapsulating an *N*-methylpyridinium guest. This approach enabled the ionization of these noncovalent complexes and the resulting ESI-MS spectra confirm the presence and stability of all three capsules in the gas phase (Figure 52c). Even though the mass spectra display a number of other ions, the absence of homodimeric complexes indicates that the heterodimeric XB capsules are indeed formed due to specific XB interactions of the different cavitand hemispheres in the gas phase.

This work demonstrates the versatility of neutral halogen bonds to serve as the sole noncovalent interaction to assemble supramolecular capsules. The presented complexes are the first of their kind to be stable in all three physical states – solid state, solution and gas phase. A more detailed investigation on their gas-phase structure and reactivity using tandem MS or IMS would have been very interesting. Comparing the impact of the different adjustments on the XB acceptor and donor structures in solution and gas phase might have provided valuable insight into the nature of halogen bonding. However, the rather challenging ionization of these inherently neutral capsules and the resulting low ion intensities made these studies unfortunately unfeasible.

Author contributions

Precursor compounds and the cavitands were synthesized by Oliver Dumele and Benedrikt Schreib. Oliver Dumele conducted and evaluated NMR studies on the formation of dimeric capsules and their guest-binding behavior. He furthermore obtained a crystal of the halogen-bonded capsule suitable for X-ray crystal-structure analysis, which was performed and analyzed by Nils Trapp. I synthesized the charged guest employed to sufficiently ionize the capsule complexes by ESI, performed all ESI-MS measurements and performed the data analysis and interpretation. Oliver Dumele wrote the manuscript with contributions from my side for the part on mass spectrometry. All authors contributed to the final version of the manuscript.

3.1.2. [N···I⁺···N] Halogen-Bonded Dimeric Capsules from Tetrakis(3-pyridyl)ethylene-cavitands

Lotta Turunen, Ulrike Warzok, Rakesh Puttreddy, Ngong Kodiah Beyeh, Christoph A.Schalley, Kari Rissanen

Angew. Chem. Int. Ed. **2016**, *55*, 14033–14036; *Angew. Chem.* **2016**, *128*, 14239–14242.

Submitted on August 10, 2016, first published on October 28, 2016 in Angewandte Chemie International Edition and Angewandte Chemie.

An electronic version of the article is available (https://doi.org/10.1002/anie.201607789, https://doi.org/10.1002/ange.201607789).

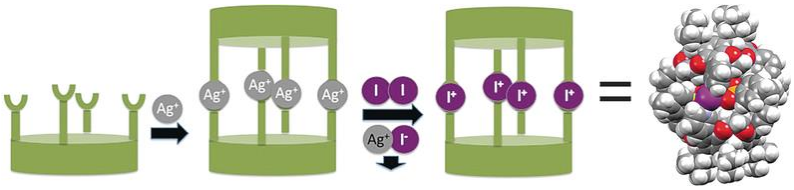

Figure 53: Graphical abstract showing assembly of the silver-coordinated and halogen-bonded dimeric capsules with modelled structure of the iodonium capsule. Reprinted with permission from Turunen *et al.*[221] (© 2016 Wiley-VCH Verlag GmbH & Co. KGaA, Weinheim).

Project summary

This project focused on the assembly and analysis of novel dimeric halogen-bonded capsules in solution and in the gas phase (Figure 53). In contrast to the preceding project 3.1, coordinative [N···I⁺···N] halogen bonds were employed to achieve capsule formation with the tetrakis(3-pyridyl)ethylene cavitand $\mathbf{C_D}$.[1] The synthesis followed a two-step procedure of reacting the cavitand first with silver(I) *p*-toluenesulfonate and subsequently with molecular iodine to induce an [N···Ag⁺···N] → [N···I⁺···N] exchange reaction (**Scheme 1**).

The structure of the silver-coordinated precursor capsule **Ag-Dim** was confirmed by X-ray crystal structure analysis which evidenced two structurally different assemblies $(CH_2Cl_2)_2$@[2$\mathbf{C_D}$+4Ag+2·H_2O+4·OTs] and $(CH_2Cl_2)_2$@[2$\mathbf{C_D}$+4Ag+4·H_2O+4·OTs] (Figure 54d). In both cases, the capsule contains two encapsulated dichloromethane molecules, while the tosylate anions are located on the exterior. The anions interact directly with the silver cations which exhibit distorted trigonal or tetragonal coordination geometries. As demonstrated by ^{1}H NMR, the complex **I-Dim** forms symmetrical assemblies with [N···I⁺···N] halogen bonds in solution. Diffusion-ordered NMR experiments yielded a hydrodynamic diameter of 2.22 nm, which is in good agreement with the molecular model of **I-Dim**, optimized on a molecular-mechanics level (Figure 54d).

[1] The cavitand was available with two different side chains (*i*-butyl, *n*-hexyl). As formation of the capsules did not depend on this substituent, only the results for the *i*-butyl cavitand will be discussed in this chapter.

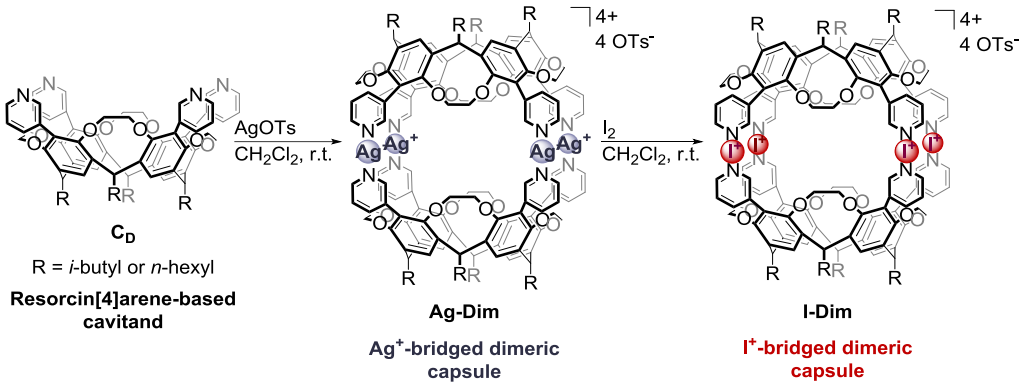

Scheme 1: Syntheses of the Ag^+- and I^+-bridged capsules. Reprinted and adapted with permission from Turunen *et al.*[221] (© 2016, Wiley-VCH Verlag GmbH & Co. KGaA, Weinheim).

ESI-MS experiments evidenced the selective formation of the silver-coordinated precursor capsule **Ag-Dim**, as well as of the halogen-bonded capsule **I-Dim**. For the latter, the maximum and furthermore optimal number of four bound I^+ ions strongly suggests a closed capsular structure with four well-defined [N···I^+···N] binding motifs (Figure 54a). CID tandem MS experiments demonstrated significant differences in the gas-phase reactivity of the two complex types. Ions derived from the Ag^+-bridged capsule **Ag-Dim** showed a charge-separating, symmetric fragmentation into monomers. In contrast, ions derived from the I^+-bridged capsule **I-Dim** underwent a stepwise elimination of two neutral I·OTs ion pairs. This indicates a higher gas-phase stability of the halogen-bonded capsule than of the corresponding metal-coordinated capsules, as two [N···I^+···N] interactions are apparently sufficient to maintain an intact capsule in the gas phase.

TW-IMS studies indicated well-defined and very similar gas-phase structures for both, the halogen-bonded complexes and their silver-coordinated precursors. This is apparent from the symmetric and narrow arrival-time distributions of the single ions and furthermore from the linear trends of the dimer signals in the *m*/z *versus* drift-time plots (Figure 54c). Identical absolute drift times of the most abundant complex ions derived from **I-Dim** and **Ag-Dim** capsules give evidence that they possess the same desired capsular structures, as was also supported by the X-ray structure of **Ag-Dim_A/B** and molecular modelling of **I-Dim** (Figure 54b, d).

This proof-of-principle study nicely illustrates the potential of coordinative halogen bonds for the selective assembly of stable and well-defined supramolecular capsules. The advantage lies in the robustness of the [N···I^+···N] binding motif. As the resulting capsular complexes are ionic, ESI mass spectrometry and especially ion mobility have proven to be highly versatile tools for the analysis of the structure and conformation of these complexes, especially when information from X-ray crystal structure analysis are absent. Moreover, the approach yields symmetric assemblies by employing relatively simple building blocks equipped with an XB acceptor in combination with the very easily accessible iodonium ion as the XB donor. This greatly encourages the application of this method for the assembly of more complex architectures.

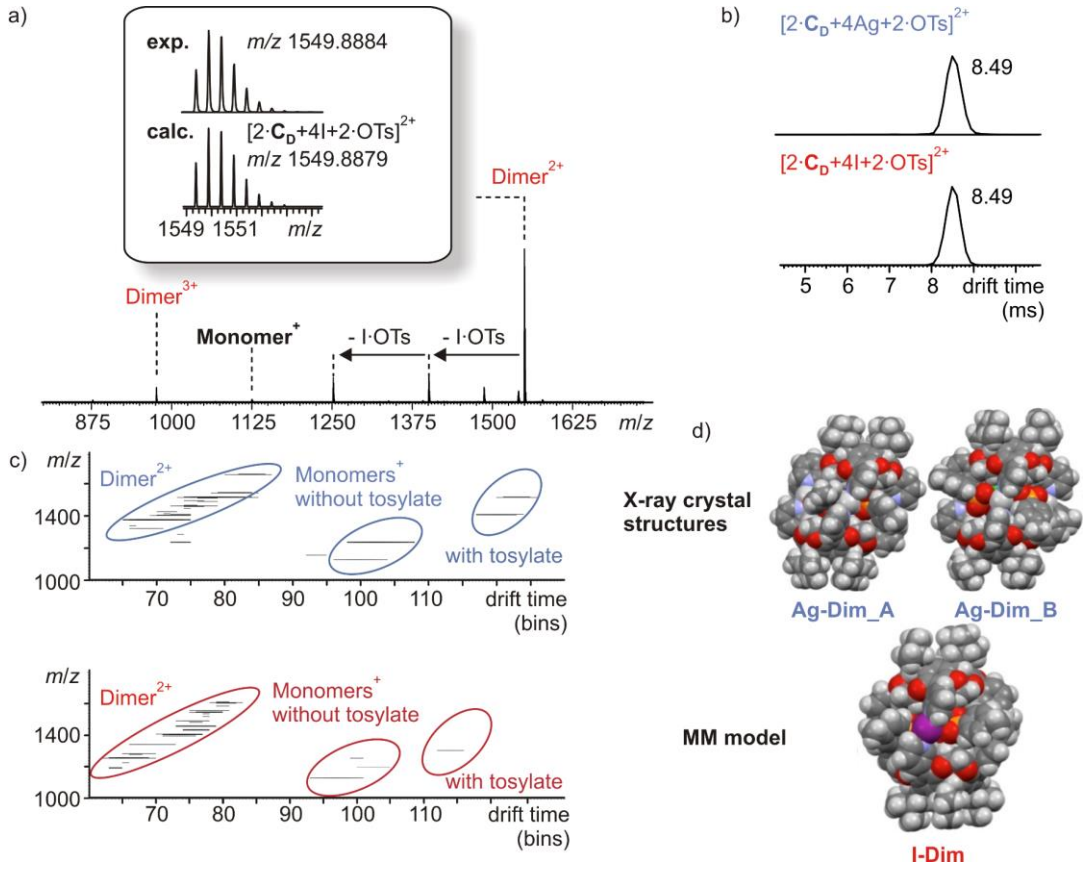

Figure 54: a) ESI-MS spectrum of halogen-bonded capsule **I-Dim**; b) arrival-time distributions of most abundant ions derived from silver-coordinated capsule **Ag-Dim** (blue) and halogen-bonded capsule **I-Dim** (red); c) TW-IMS *m/z versus* drift time plot of capsules capsule **Ag-Dim** (blue) and **I-Dim** (red); d) crystal structures of the capsules **Ag-Dim_A** and **Ag-Dim_B** and the modeled structure of the halogen-bonded capsule **I-Dim**. Reprinted and adapted with permission from Turunen *et al.*[221] (© 2016, Wiley-VCH Verlag GmbH & Co. KGaA, Weinheim).

Author contributions

Kari Rissanen developed the approach for the assembly of the halogen-bonded capsules by a [N···Ag^+···N] → [N···I^+···N] exchange reaction. Precursor compounds and the cavitands were synthesized by Lotta Turunen. Lotta Turunen conducted and evaluated NMR, as well as DOSY NMR experiments on the dimeric capsules. She obtained a crystal of the silver-coordinated precursor capsule suitable for X-ray crystal structure analysis which was performed and analyzed by Rakesh Puttreddy. Kari Rissanen worked on the molecular modelling of the dimeric XB capsule. I performed all ESI-MS, tandem MS experiments and IMS measurements on the dimeric capsules. Data analysis and interpretation were performed by myself. Lotta Turunen and I discussed all results and worked on the general concept of the manuscript together. Lotta Turunen and I wrote the manuscript with equal contributions. All authors contributed to the final version of the manuscript.

3.1.3. Nano-sized $I_{12}L_6$ Molecular Capsules based on the [N···I⁺···N] Halogen Bond

Lotta Turunen, Ulrike Warzok, Christoph A.Schalley, Kari Rissanen

Chem **2017**, *3*, 861–869.

Submitted on May 29, 2017, first published on November 9, 2017 in Chem. For copyright reasons, the article (Appendix 6.3.3) is not included in the online version of this thesis.

An electronic version of the article is available (https://doi.org/10.1016/j.chempr.2017.08.010).

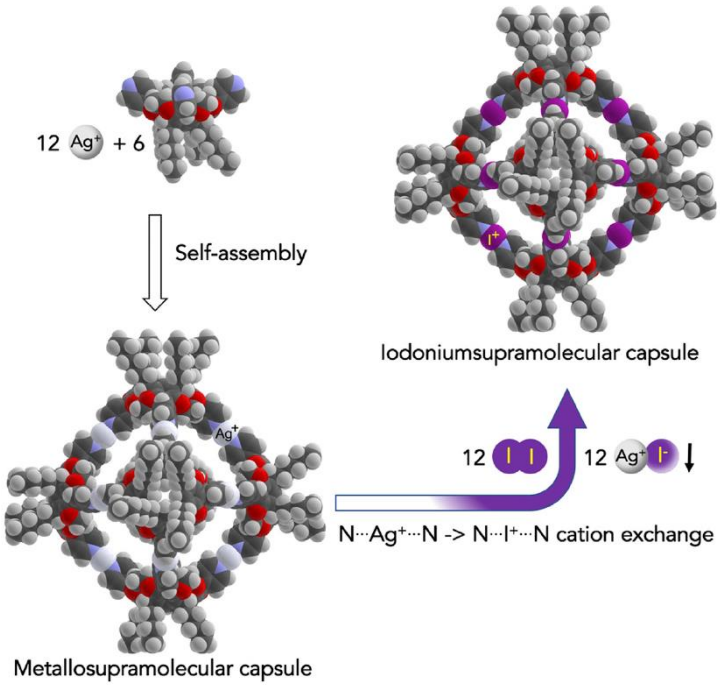

Figure 55: Graphical abstract showing assembly of the silver-coordinated and halogen-bonded hexameric capsule, both depicted as modeled structures. Reprinted with permission from Turunen *et al.*[222] (© 2017, Elsevier Inc.).

Project summary

Based on the successful establishment of the coordinative halogen bond as a suitable binding motif for the assembly of supramolecular capsules (chapter 3.1.2), this project aimed to show the generality of the [N···Ag⁺···N] → [N···I⁺···N] exchange reaction to generate large supramolecular complexes (Figure 55). It presents the formation and analysis of a hexameric halogen-bonded capsule in solution and in the gas phase.

In comparison to the tetrakis(3-pyridyl)ethylene cavitand $\mathbf{C_D}$, which yielded selectively dimeric halogen-bonded capsules, the geometry of the cavitand needed to be adjusted in order to achieve the formation of the desired octahedral hexameric complex. Molecular modeling showed that the corresponding tetrakis(4-pyridyl)ethylene cavitand $\mathbf{C_H}$ possesses the necessary spatial requirements. The positioning of the *para*-pyridine-N atoms and the flexibility of the ethylene bridges results in an angle between the opposing rings of close to 90° (Figure 56, molecular model, planes 1 and 2). Hence, complexation of cavitand $\mathbf{C_H}$ with

silver(I) *p*-toluenesulfonate and subsequent [N···Ag^+···N] → [N···I^+···N] exchange reaction gave the hexameric halogen-bonded capsule **I-Hex** (Figure 56, top).

^{1}H NMR experiments confirmed the formation of highly symmetric and discrete complexes by the appearance of only one set of signals and with the indicative chemical shifts corresponding to Ag^+-N and I^+-N coordination bonds for the complexes **Ag-Hex** and **I-Hex**, respectively. A ^{1}H,^{15}N-HMBC experiment shows one single, significantly upfield shifted ^{15}N NMR signal which belongs to the [N···I^+···N] motif as compared to the free cavitand. ^{1}H DOSY NMR measurements gave hydrodynamic diameters of ca. d = 4.0 nm for the silver-coordinated precursor capsule **Ag-Hex** and the halogen-bonded capsule **I-Hex**, which are in good agreement with diameters predicted from the molecular models of the two complexes.

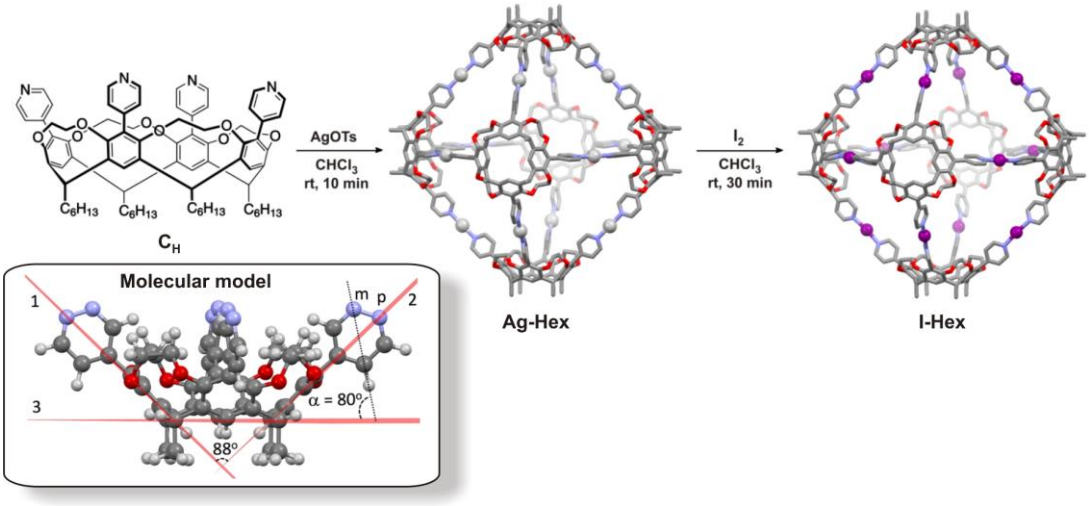

Figure 56: Synthesis of silver-coordinated and halogen-bonded hexameric capsules (hexyl-side chains reduced to methyl groups and counter ions omitted for clatrity) and molecular structure modeled at MM-level of ethylene-bridged cavitand. Reprinted and adapted with permission from Turunen *et al.*[222] (© 2017, Elsevier Inc.).

Analysis of the capsules **Ag-Hex** and **I-Hex** by ESI mass spectrometry revealed that both complex types are stable in the gas phase and confirmed the selective formation of the desired [N···I^+···N] bonded hexameric capsule (Figure 57). The high abundancy of peaks that belong to ions with a formal [6$\mathbf{C_H}$+12I]$^{12+}$ core and a varying number of stabilizing anions gives a strong indication for a closed octahedral arrangement for capsule **I-Hex** with twelve well-defined [N···I^+···N] bonds along the edges.

These results demonstrate that a carefully chosen, however synthetically simple variation of the cavitand structure and geometry results in the selective formation of a large hexameric supramolecular capsule. Furthermore, this finding emphasizes the general applicability of the [N···I^+···N] bond-forming procedure and especially of the [N···Ag^+···N] → [N···I^+···N] exchange reaction which proceeds smoothly and efficiently for this large assembly.

The presented $I_{12}L_6$ capsule has a cavity volume of 6,850 Å^3 and a diameter of ca. 4 nm, as calculated from a molecular model, and is the only example of a halogen-bonded hexameric capsule reported to date. The combination of synthetic ease to obtain the structure and its robustness might pave the way for the development of halonium-ion-based nanotechnology.

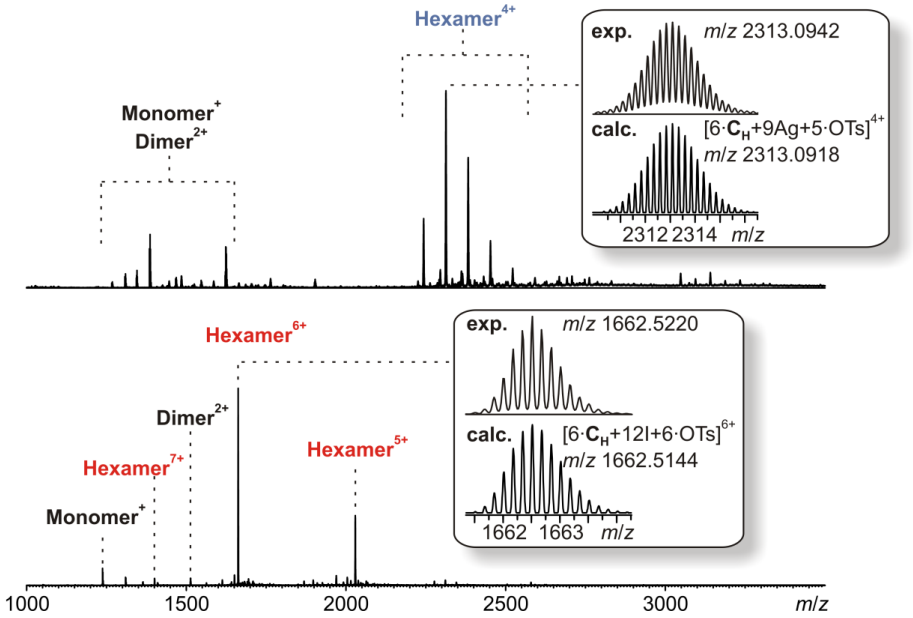

Figure 57: ESI-MS spectra of silver-coordinated capsule **Ag-Hex** (top) and halogen-bonded capsule **I-Hex** (bottom). Reprinted and adapted with permission from Turunen *et al.*[222] (© 2017 Elsevier Inc.).

For this purpose, it would be highly advantageous to gain a more detailed understanding of the structure and reactivity of this newly developed, outstanding class of supramolecular containers.

Author contributions

Kari Rissanen conceived and designed the project, performed the ligand design, as well as molecular modeling. Synthesis of the cavitand was done by Lotta Turunen. Furthermore, she conducted and evaluated NMR, as well as DOSY NMR experiments on the hexameric capsules. I performed ESI-MS measurements of the hexameric capsules as well as the following data analysis and interpretation. Lotta Turunen and I discussed the results and worked on the general concept for the manuscript together. Lotta Turunen wrote the manuscript in collaboration with me. All authors contributed to the final version of the manuscript.

3.1.4. Surprising Solvent-Induced Structural Rearrangements in Large [N···I⁺···N] Halogen-Bonded Supramolecular Capsules: An Ion Mobility-Mass Spectrometry Study

Ulrike Warzok, Mateusz Marianski, Waldemar Hoffmann, Lotta Turunen, Kari Risannen, Kevin Pagel, and Christoph A. Schalley.

Chem. Sci. **2018**, Accepted Manuscript, DOI: 10.1039/C8SC03040E.

Submitted on July 09, 2018, first published on September 05, 2018 in Chemical Science. The article (Appendix 6.3.4) is included in the online version of this thesis.

An electronic version of the article is available (https://doi.org/10.1039/C8SC03040E).

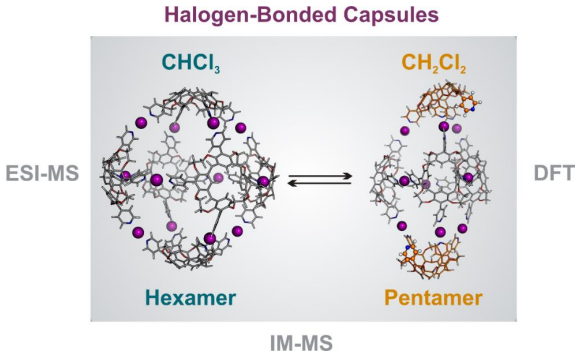

Figure 58: Graphical abstract showing ion-mobility mass spectrometry and DFT calculations to reveal the surprisingly solvent-dependent formation of large pentameric halogen-bonded capsules. Reproduced from Warzok *et al.*[223] (Published by The Royal Society of Chemistry).

Project summary

This project focused on the detailed structural analysis of the dimeric and hexameric halogen-bonded capsules presented in chapters 3.1.2 and 3.1.3 by IMS, as well as the solution and gas-phase reactivity of the hexameric complex. The formation and structure of a novel pentameric capsule was elucidated (Figure 58).

The CCS values of the dimeric [N···I⁺···N] halogen-bonded capsule were determined by DT-IMS and found to be virtually identical with around 558 Å^2 for dimeric complexes of different charge states, independent of the number of bound tosylate anions (Figure 59a). This indicated that both anions present are bound inside the capsule cavity. Theoretical structure optimization was performed with a hybrid approach for all XB capsules: DFT level calculations for the [pyridine···I⁺···pyridine] motif and the tosylate ions to properly assess the noncovalent interactions and a semi-empirical method for the cavitand scaffold. These calculations supported the proposed structure of the dimeric complex with a face-to-face arrangement of the two cavitands and linear [N···I⁺···N] halogen bonds (Figure 59b). They also proposed the binding of up to two tosylates within the capsule in an antiparallel arrangement and stabilized by van der Waals and [C_{aryl}-H···O$^-$] interactions, instead of a direct interaction with the cationic halonium ion. The CCS values predicted from this structure agreed well with the experimental data.

DT-IMS experiments on the hexameric capsule **I-Hex** indicated a well-defined structure for the complexes in the gas phase with CCS values of around 1,500 Å^2. Again, ions in different charge states had very similar

CCS values, suggesting that the counter ions occupy the space inside the capsule's cavity (Figure 59c). This assumption was confirmed by theoretical calculations which predicted that tosylates bind above the upper rim and inside a pocket of the cavitands by [C_{aryl}-H···O^-] interactions. Six spatially distributed binding pockets at such positions can provide binding sites for six tosylates (Figure 59d). The calculated CCS values agreed well with experimental results. This shows that the hexameric capsule remains intact in the gas phase, possesses the proposed octahedral geometry with linear [N···I^+···N] halogen bonds along the edges and binds up to six anions in its cavity by [C_{aryl}-H···O^-] hydrogen bonds.

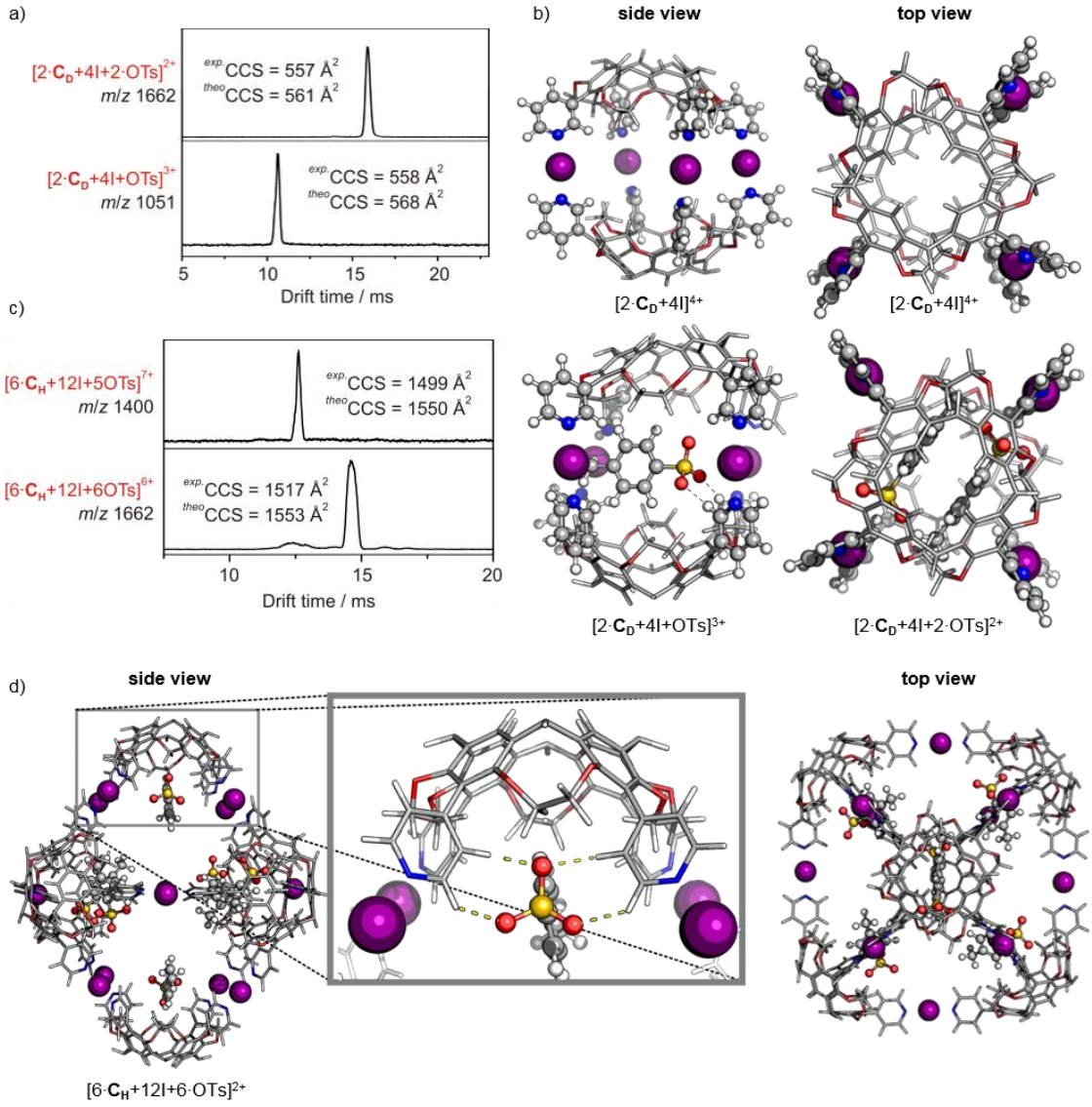

Figure 59: a) DT-IMS ATDs of ions derived from dimeric halogen-bonded capsule **I-Dim** with experimental and theoretical CCS values. b) Calculated structures of dimeric halogen-bonded capsules **I-Dim** without, with one and two tosylate counterions inside the cavity. c) DT-IMS ATDs of ions derived from hexameric halogen-bonded capsule **I-Hex** with experimental and theoretical CCS values. d) Calculated structure of hexameric halogen-bonded capsule **I-Hex** with six tosylate anions with zoom into binding situation of a tosylate in the hexameric complex. For the theoretical calculations, PBE0/def2-SVP was used for I^+, pyridines, tosylates and AM1 for cavitand scaffold; [C_{aryl}-H···O^-] interactions are marked with dotted lines. For clarity, the *n*-hexyl side chains have been reduced to hydrogens in the images, but were included in the calculations. Reproduced and adapted from Warzok *et al.*[223] (Published by The Royal Society of Chemistry).

The first investigation of the solution reactivity of the hexameric capsule by ESI-MS demonstrated a solvent-dependent transition into a novel pentameric halogen-bonded capsule **I-Pent**, when chloroform as the solvent was exchanged to dichloromethane. The selective formation of this trigonal bipyramidal pentameric capsule was also achieved, when the [N···Ag$^+$···N] → [N···I$^+$···N] exchange reaction starting from the silver-coordinated hexameric precursor capsule **Ag-Hex** was performed in dichloromethane (Figure 60a, b).

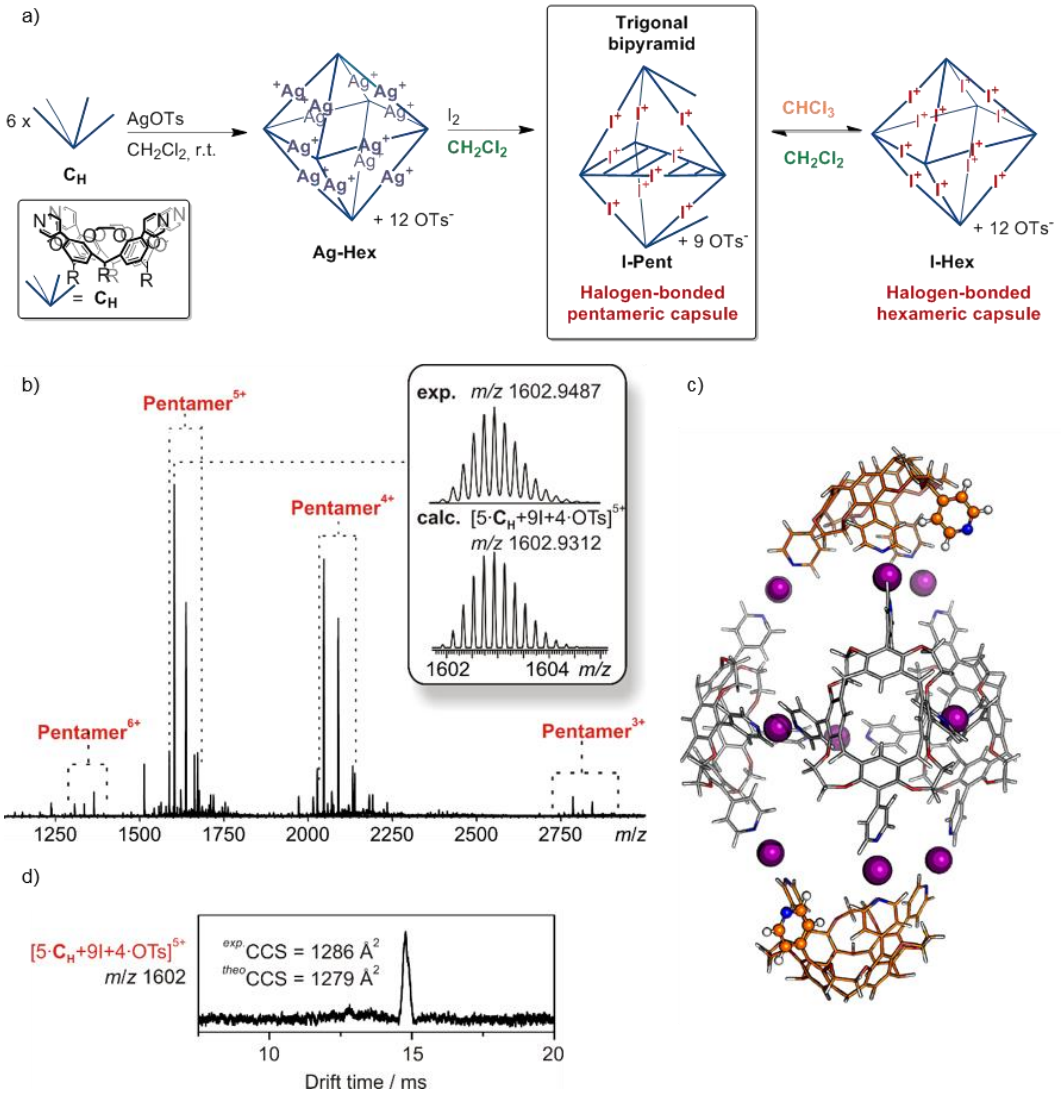

Figure 60: a) Selective formation of the novel pentameric halogen-bonded capsule **I-Pent** from the halogen-bonded or silver-coordinated hexameric capsules upon usage of CH_2Cl_2 as the reaction solvent. b) ESI-MS spectrum of pentameric halogen-bonded capsule **I-Pent.** c) Calculated structure of pentameric halogen-bonded capsule [5·**C$_H$**+9I]$^{9+}$; PBE0/def2-SVP was used for the I+ ions and the pyridines, AM1 for the cavitand. Cavitands in apical positions, unbound pyridines and tosylates are highlighted. For clarity, the *n*-hexyl side chains have been reduced to hydrogens in the images, but were included in the calculations. d) DT-IMS ATD of ion derived from pentameric halogen-bonded capsule **I-Pent** with experimental and theoretical CCS values. Reproduced and adapted from Warzok *et al.*[223] (Published by The Royal Society of Chemistry).

Theoretical calculations confirmed a stable structure for this highly unusual complex: Three cavitands in equatorial positions participate with all four pyridine groups in linear [N···I$^+$···N] bonds and two cavitands in the apical positions adopt a distorted conformation and form three [N···I$^+$···N] bonds each. The fourth

pyridine moiety on each of these two cavitands remains unbound and is positioned between two [N···I⁺···N] bonds (Figure 60c). DT-IMS experiments confirmed the presence of one well-defined species for **I-Pent** in the gas phase with a measured CCS of 1286 Å^2, which is ca. 20% smaller than value of the hexameric capsule. The optimized structure of the trigonal bipyramidal capsule with four tosylates within the cavity yielded a calculated CCS value which is in excellent agreement with the experimental value (Figure 60d). The combination of these three methods thus elucidated the structure of this novel complex type.

The gas-phase reactivity of the hexameric capsule **I-Hex** was examined with a CID tandem MS experiment. The results showed that the hexameric, octahedral capsule does not yield pentameric product ions, but rather smaller oligomeric fragments at higher collision energies. It shows that the observed hexamer-pentamer transition does not occur in the gas phase. Consequently, the solution equilibrium relies on the reaction of several complexes, most likely involving the monomer $\mathbf{C_H}$, and is governed by solvent effects. Instead of a hypothetical hexamer-pentamer transition in the gas phase, a complex fragmentation behavior involving rearrangements was observed for both complex types. This will be further explored in the future.

Overall, this study highlights the value of mass spectrometry and ion mobility in combination with theoretical calculations for the analysis of structure and reactivity of halogen-bonded capsules. The evidence for the anion binding inside the investigated capsules and the involved binding mode gave a first impression of their host-guest chemistry. The anions do not interact or interfere with the linear [N···I⁺···N] XB bonds, which is in agreement with the earlier work of ERDÉLYI and coworkers on similar, yet smaller systems (see chapter 2.2.3). Furthermore, the structural differences between the silver-coordinated precursor capsules and the halogen-bonded complexes could be explored, as the former where found to bind counterions on the exterior of the cavity and in direct interaction with the silver cations. Additionally, a new type of large, well-behaved supramolecular complex solely based on [N···I⁺···N] halogen bonds was found. It represents the first example of a pentameric supramolecular capsule not based on metal coordination. This selective formation of a pentameric capsule illustrates the possible interplay of preorganized, but inherently flexible cavitands and directional halogen-bonds being modulated by a third factor – solvent effects. The more detailed investigation of the responsiveness of the halogen-bonded capsules towards chemical stimuli could lead to the discovery of more complex chemical reactivity.

Author contributions

Lotta Turunen synthesized the cavitands, following a known procedure. I investigated the solvent-dependent solution reactivity of the hexameric capsule by ESI-MS and optimized reaction conditions for the selective formation of the pentameric capsule. I analyzed and interpreted the resulting data. DT-IMS measurements on the dimeric, hexameric and pentameric capsules and the corresponding data analysis were performed by Waldemar Hoffmann with my assistance. The interpretation of the results was done by myself. Theoretical calculations on the halogen-bonded capsules were made by Mateusz Marianski with whom I interpreted the results. CID tandem MS experiments on the hexameric and pentameric capsules were measured by myself. I analyzed the data and interpreted the results. I developed the general concept of the manuscript and wrote the manuscript with help from Mateusz Marianski on the parts concerning the theoretical calculations. All authors contributed to the final version of the manuscript.

3.2. Antimonato-Polyoxovanadate Cages

3.2.1. Catalysis of "outer-phase" oxygen atom exchange reactions by encapsulated "inner-phase" water in {$V_{15}Sb_6$}-type polyoxovanadates

Michael Wendt*, Ulrike Warzok*, Christian Näther, Jan van Leusen, Paul Kögerler, Christoph A. Schalley, and Wolfgang Bensch

* Authors contributed equally to this work.

Chem. Sci. **2016**, *7*, 2684–2694.

Submitted on November 27, 2015, first published on January 8, 2016 in Chemical Science. The article (Appendix 6.3.5) is included in the online version of this thesis.

An electronic version of the article is available (https://doi.org/10.1039/C5SC04571A).

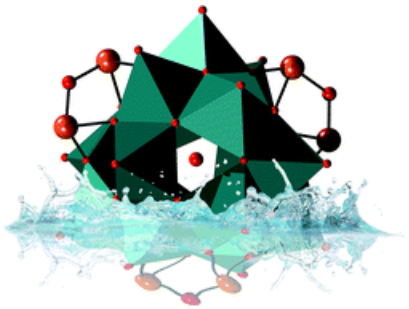

Figure 61: The graphical abstract shows the water-soluble {$V_{15}Sb_6$} antimonato-polyoxovanadate cage with an encapsulated water molecule that accelerates the oxygen-exchange reaction in the cluster periphery. Reproduced from Wendt *et al.*[224] (Published by The Royal Society of Chemistry).

Project summery

This first comprehensive study on the topic of antimonato polyoxovanadates (Sb-POVs) presents the first water-soluble compounds of this compound class and focusses on the investigation of the {$V_{15}Sb_6$} cluster core in solution and gas phase by mass spectrometry (Figure 61).

Four novel complexes with the composition $\{M(en)_3\}_3[V_{15}Sb_6O_{42}(H_2O)_x]\cdot nH_2O$ ($n \approx 15$ or 28; x = 0, 1; M = Ni^{II} , Co^{II}, Fe^{II}; en = ethylenediamine) were obtained by solvothermal synthesis. The cobalt and iron complexes crystallize in the non-centrosymmetric monoclinic space group C*2*. For the nickel complex, two pseudopolymorphs exist in the monoclinic space group C*2* and the trigonal space group P*321*, depending on the reaction conditions. All four compounds consist of the known $[V_{15}Sb_6O_{42}(H_2O)_x]^{6-}$ (x = 0, 1) cluster (see chapter 2.3.3) and isolated, charge-compensating $\{M(en)_3\}^{2+}$ complexes (Figure 62). For all four compounds under study, their magnetic properties can be described qualitatively by the additive combination of the contributing, strongly antiferromagnetically coupled {$V_{15}Sb_6$} cluster units and the three high-spin $\{M(en)_3\}^{2+}$ complexes. Between these two magnetically active groups, there is virtually no exchange due to the relatively large metal–metal distances and the absence of bridging ligands.

All four complexes exhibit a relatively high water solubility which is the first reported case for Sb-POVs

and also highly unusual for POVs, in general. This offered the opportunity to study their reactivity in greater detail on the nickel compound $\{Ni(en)_3\}_3[V_{15}Sb_6O_{42}(H_2O)_x]\cdot 15H_2O$ (x = 0,1) (**I**) as a selected example. Generally, their solution chemistry is as yet only poorly understood due to the lack of soluble species and their preparation consequently restricted to the highly serendipitous method of solvothermal synthesis with low-nuclearity precursors.

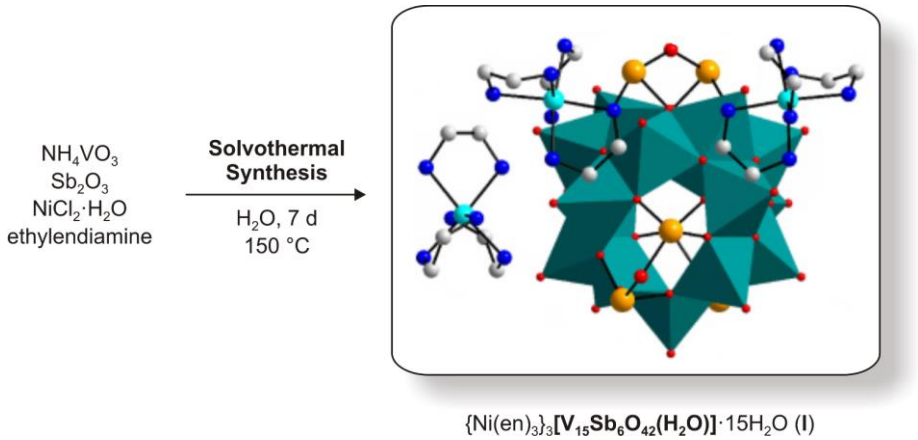

Figure 62: Solvothermal synthesis and X-ray crystal structure of compound **I**. Reprinted and adapted from Wendt *et al.*[224] (Published by The Royal Society of Chemistry).

ESI-MS studies on compound **I** demonstrated that the $\{V_{15}Sb_6\}$ cluster stays indeed intact upon dissolution. However, an Sb-richer $\{V_{14}Sb_8\}$ cluster is formed in solution over the course of days by a formal exchange of a VO against an Sb–O–Sb unit. This rearrangement reveals an astonishing reactivity as all compounds with a $\{V_{14}Sb_8O_{42}\}$ clusters known so far were prepared under solvothermal conditions. These results demonstrate that compound **I** can be used to gain access to other cluster compounds by post-functionalization. Mass spectrometry furthermore revealed the presence of an encapsulated water molecule inside part of the cluster cages which could subsequently also be confirmed by the X-ray crystal structure analysis. This inner-phase water molecule is protected inside the cavity of the cage against a fast H/D exchange in aqueous solution. It could be deduced from this that the closed cage-like structure of the cluster is maintained upon dissolution (Figure 63a, b, d).

Interestingly, CID tandem MS experiments exhibited the loss of the neutral water molecule from the cluster cavity in the gas phase as the major fragmentation pathway. The fragmentation yielded a fully intact, but empty cluster core (Figure 63c). It was rationalized that the guest can participate in the cluster's reactivity by opening an oxo-bridge upon attack of a vanadium ion from the inside of the cavity. After proton transfer steps, the oxo-bridge is reformed with the water molecule as the leaving group on the outside of the cage. This process is entropically favored in the gas phase due to the increase in particle number (Figure 63d, left side).

The influence of the cluster`s inner-phase reactivity on the outer-phase reactivity became even more evident when the $^{16}O/^{18}O$ isotope exchange in solution was regarded. Cluster cages with an encapsulated water molecule exhibited a significantly faster oxygen-atom exchange in the cluster periphery than those with an empty cavity (Figure 63e). First of all, this showed that the ions with and without encapsulated water are

derived from two distinct solution species which are not in fast equilibrium with each other. The proposed mechanism accounting for this effect of different exchange rates proceeds through similar initial steps as the gas-phase fragmentation mechanism (Figure 63d, right side). The acceleration of the exchange is achieved by the initial opening of an oxo-bridge by the inner-phase water which is not facilitated in case of the empty clusters. The following exchange step and the closing of the oxo-bridge to reform the closed cluster cage likely proceed at similar rates for both species. The loss of the encapsulated inner-water is in solution neither favored by enthalpy nor by entropy as the cluster is surrounded by bulk water. Hence, the retention of the guest inside the container sustains the catalysis of the oxygen exchange in the cluster`s periphery.

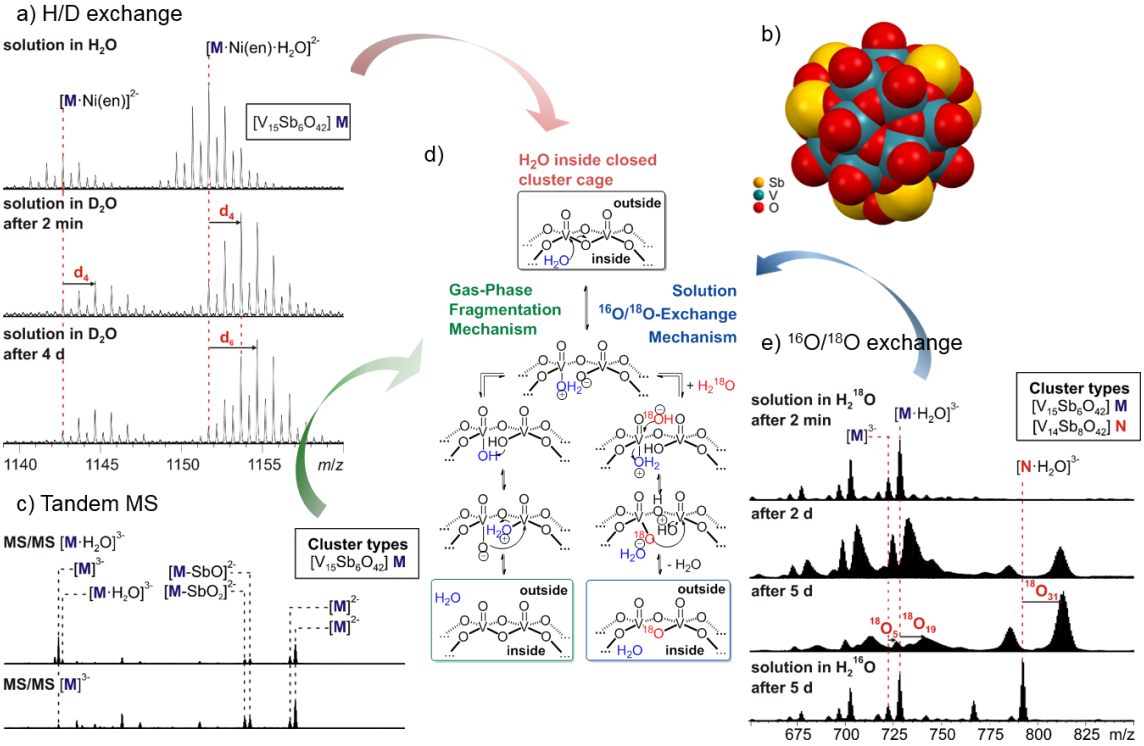

Figure 63: Solution and gas-phase reactivity of the {$V_{15}Sb_6$} cage. a) Solution H/D exchange experiment shows fast exchange for labile protons of en and slow exchange for encapsulated water. b) The space-filling representation shows that the cluster is tightly closed thereby trapping the encapsulated water within the cage cavity. c) CID tandem MS experiment exhibits water loss and electron loss as competing fragmentations. d) Mechanisms for solution and gas-phase reactivity of the {$V_{15}Sb_6$} cluster. e) Solution $^{16}O/^{18}O$ exchange experiment. Reprinted and adapted from Wendt *et al.*[224] (Published by The Royal Society of Chemistry).

This reactivity study is the first reported example in polyoxovanadate chemistry for the transduction of inner-phase reactivity of an encapsulated guest molecule into changes in the outer-phase reactivity of the cluster cage. The insight gained hereby is highly valuable for the further development of Sb-POV chemistry. It can serve as the rational basis for the preparation of new POVs, given that the presented compound **I** has been shown to serve as a suitable starting material for post-functionalization in solution.

Author contributions

Cluster syntheses and standard characterization were performed by Michael Wendt. X-ray crystallography was performed by Christian Näther and Michael Wendt. Magnetic characterization of the clusters was

carried out by Paul Kögerler and Jan van Leusen. I performed all ESI-MS experiments and data analysis including aging studies, H/D and $^{16}O/^{18}O$ exchange experiments, as well as tandem MS experiments. I interpreted the data and detailed the reaction mechanisms. Michael Wendt and I discussed the results and worked on the general concept of the manuscript together. We furthermore wrote the manuscript with equal contributions. All authors contributed to the final version of the manuscript.

3.2.2. Configurational Isomerism in Polyoxovanadates

Lisa K. Mahnke, Aleksandar Kondinski, Ulrike Warzok, Christian Näther, Jan van Leusen, Christoph A. Schalley, Kirill Y. Monakhov, Paul Kögerler, Wolfgang Bensch

Angew. Chem. Int. Ed. **2018**, *57*, 2972–2975; *Angew. Chem.* **2018**, *130*, 3024–3028.

Submitted on June 19, 2017, resubmitted on December 4, 2017, first published online as an accepted manuscript on January 12, 2018 in Angewandte Chemie International Edition and Angewandte Chemie. For copyright reasons, the article (Appendix 6.3.6) is not included in the online version of this thesis.

An electronic version of the article is available (https://doi.org/10.1002/anie.201712417, https://doi.org/10.1002/ange.201712417).

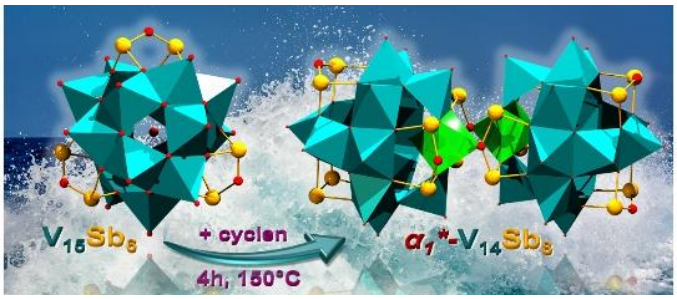

Figure 64: Graphical abstract shows the reaction of the water-soluble {$V_{15}Sb_6$} Sb-POV cage to the novel configurational α_1*-isomer of {$V_{14}Sb_8$} which forms dimeric assemblies in water by supramolecular interactions. Reprinted from Mahnke *et al.*[225] (© 2018 WILEY-VCH Verlag GmbH & Co. KGaA, Weinheim).

Project summary

In this project, the transformation of the water-soluble {$V_{15}Sb_6$} cluster cage **I** introduced in chapter 3.2.1 into dimers of the metastable α_1* conformational isomer of the contracted {$V_{14}Sb_8$} cluster was studied in the solid state, in solution, in the gas phase and by theoretical calculations (Figure 64).

Reaction of precursor **I** with cyclen in aqueous solution yielded the novel Sb-POV {Ni(cyclen)(en)}$_2$[$V_{14}Sb_8O_{42}(H_2O)$]·*ca* 10H_2O (**II**) after short reaction time as a result of ligand metathesis and the {$V_{15}Sb_6$}→{$V_{14}Sb_8$} cluster transformation which was first observed by ESI-MS (see chapter 3.2.1, Figure 65a). The compound is the first example of an α_1*-{$V_{14}Sb_8$} structure and furthermore the first example of configurational isomerism in POV chemistry. The crystal structure of **II** shows the {$V_{14}Sb_8$} core with an inverted orientation of one of the edge-sharing VO_5 pyramids toward the center of the cage. The cluster cavity is sufficiently large to accommodate both, the inward-oriented oxygen atom and an additional H_2O guest that interact by strong hydrogen bonds (Figure 65b, c). Interestingly, the α_1*-{$V_{14}Sb_8$} cages form unprecedented dimeric structures in the solid state by supramolecular Sb-O···V and Sb-O···Sb contacts (Figure 66a).

ESI-MS studies revealed the presence of intact cluster ions of the {$V_{14}Sb_8$} cage and of its dimers in solution (Figure 66b), thereby demonstrating the specific noncovalent interaction between two cluster cores of the α_1*-{$V_{14}Sb_8$} isomer even in water. The different ions with partially overlapping isotope patterns could be unambiguously assigned by employing TW-IMS for their separation in the gas phase prior to detection.

Furthermore, the formation of compound **II** and its dimerization over time were studied by mass spectrometry. It was found that both processes, the $\{V_{15}Sb_6\} \rightarrow \{V_{14}Sb_8\}$ transformation and the formal α_1*-$\{V_{14}Sb_8\} \rightarrow [\alpha_1$*-$\{V_{14}Sb_8\}]_2$ dimerization have been completed after the initial heating period of the reaction mixture. Product **II** subsequently crystalizes from the mixture with its well-soluble precursor.

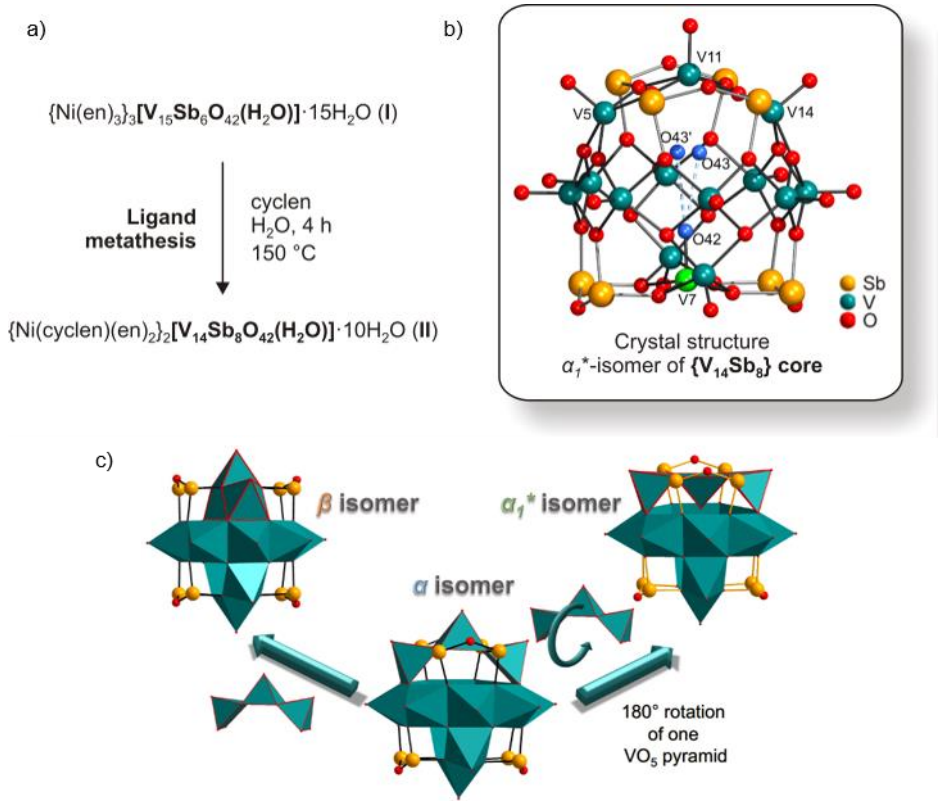

Figure 65: a) Synthesis of compound **II**; b) crystal structure of α_1*-$\{V_{14}Sb_8\}$ isomer, V7 and O42 of the inverted VO_5 pyramid highlighted light green and blue, 50:50 disordered O43/O43' of the H_2O guest in blue; c) reported isomers of $\{V_{14}Sb_8\}$-type clusters. Reprinted and adapted from Mahnke *et al.*[225] (© 2018 WILEY-VCH Verlag GmbH & Co. KGaA, Weinheim).

Complementing the analysis of the novel dimeric cluster complex in the gas phase, a CID tandem MS experiment could demonstrate the remarkable binding energy connecting the two α_1* monomers in the gas phase (Figure 66c). Two competing fragmentation pathways were observed: The very prominent dimer cleavage into monomeric ions, which is clearly favored by the reduction of charge repulsion, and the loss of neutral water and hydroxyl radicals from the dimer ions. The later process yielded still-intact dimeric product ions.

Relativistic density functional theory (DFT) was employed to rationalize the formation, describe the electronic structure of the α_1*-$\{V_{14}Sb_8\}$ cage and its stability relative to other (possible) $\{V_{14}Sb_8\}$ isomers. It is less stable than the "conventional" $\alpha/\gamma/\beta$-isomers by a difference of 50, 33 and 12 $kJ \cdot mol^{-1}$ in their relative bonding energies, respectively (see also chapter 2.3.3). Moreover, DFT calculations predicted possible other α* and γ* isomers which are similar in energy. The structural comparison between the metastable α_1*-$\{V_{14}Sb_8\}$ and its $\{V_{15}Sb_6\}$ precursor disclosed a common $\{V_7Sb_4O_{21}\}$ fragment at which the necessary inwards-inversion of one of the VO_5 pyramids could take place.

Concerning the magnetic properties of complex **II**, it exhibits strong antiferromagnetic couplings which are due to a combination of two high-spin Ni^{2+} centers and considerable contributions from α_1*- $[V_{14}Sb_8O_{42}]^{4-}$, suggesting a multiplet ground state. The latter was not observed so far for other $\{V_{14}Sb_8\}$ isomers and is rationalized with the inward-orientation of the VO_5 pyramids and new exchange pathways generated thereby.

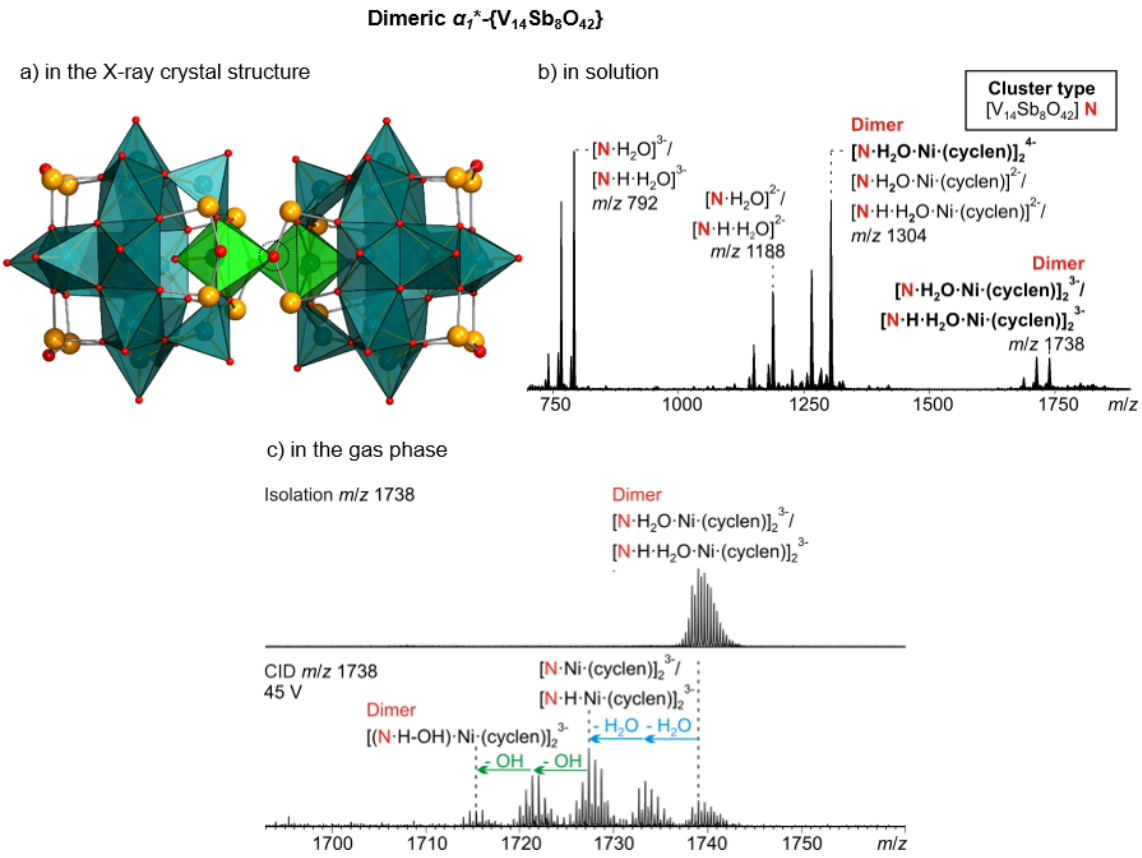

Figure 66: a) Two VO_6 octahedra (O=VO_4···O-Sb-O in light green) join neighboring cluster anions into $\{V_{14}Sb_8\}_2$ dimers in the solid state. b) ESI-MS spectrum shows specific formation of $\{V_{14}Sb_8\}_2$ dimers in solution, **N** = $V_{14}Sb_8O_{42}$. c) CID tandem MS experiment shows elimination of neutral species from dimeric ion, indicating remarkable stability of the α_1*-dimer in the gas phase. Reprinted and adapted from Mahnke *et al.*[225] (© 2018 WILEY-VCH Verlag GmbH & Co. KGaA, Weinheim).

This work emphasizes the value of the soluble precursor **I** and the knowledge about its solution reactivity for the synthesis of complex new Sb-POV compounds. It also demonstrates that an array of small, yet cooperative effects including the changes to the counter-cation-ligand environment and the intramolecular noncovalent interaction between cluster-cage dimers can drive the formation of the high-energy conformational α_1*-$\{V_{14}Sb_8\}$ isomer.

Author contributions

Cluster syntheses and standard characterization were done by Lisa K. Mahnke. She also obtained crystals of cluster **II** suitable for X-ray crystal structure analysis which was performed and analyzed by Christian Näther. I performed ESI-MS, TW-IMS and tandem MS experiments and the corresponding data analysis and interpretation. DFT calculations on the formation, electronic structure and stability of the

α_1*-{$V_{14}Sb_8O_{42}$} cage were conducted by Aleksandar Kondinski and Kirill Y. Monakhov. Magnetic characterization of the cluster was carried out by Jan van Leusen and Paul Kögerler. Lisa K. Mahnke, Aleksandar Kondinski, Kirill Y. Monakhov, Jan van Leusen and myself wrote the parts of the manuscript concerning their field of expertise. All authors contributed to the final version of the manuscript.

3.2.3. The New Water-Soluble Cluster Compound $\{Zn(en)_3\}_3[V_{15}Sb_6O_{42}(H_2O)]$-(ethylenediamine)$_3$·10$H_2O$ as a Synthon for the Generation of two New Antimonato Polyoxovanadates

Lisa K. Mahnke, Ulrike Warzok, Mengxi Lin, Christian Näther, Christoph A. Schalley, Wolfgang Bensch

Chem. Eur. J. **2018**, *24*, 5522–5528.

Submitted on December 4, 2017, first published online on February 21, 2018 in Chemistry- A European Journal. For copyright reasons, the article (Appendix 6.3.7) is not included in the online version of this thesis.

An electronic version of the article is available (https://doi.org/10.1002/chem.201705732).

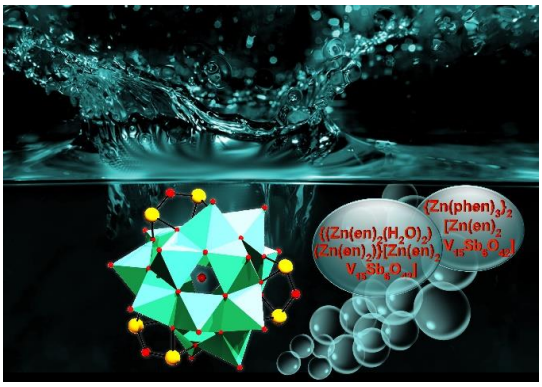

Figure 67: The graphical abstract shows the water-soluble precursor $\{Zn(en)_3\}_3[V_{15}Sb_6O_{42}(H_2O)]\cdot 3en\cdot 10H_2O$ which exhibits an increased stability in solution, resulting in post-functionalization products with intact $\{V_{15}Sb_6\}$ cores. Reprinted from Mahnke *et al.*[226] (© 2018 WILEY-VCH Verlag GmbH & Co. KGaA, Weinheim).

Project summary

This publication presents a second new, water-soluble Sb-POV precursor $\{Zn(en)_3\}_3[V_{15}Sb_6O_{42}(H_2O)]\cdot 3en\cdot 10H_2O$ (**III**) and mass spectrometric studies on its solution reactivity which provide a rationale for the formation of two new Sb-POV compounds, which could be obtained by post-functionalization of **III** (Figure 67).

Compound **III** was obtained by solvothermal synthesis and exhibits a significantly increased solubility in water as compared to the first water-soluble Sb-POV compound **I** (see chapter 3.2.1). Two new Sb-POV compounds $\{Zn(phen)_3\}_2[Zn(en)_2V_{15}Sb_6O_{42}(H_2O)]\cdot 23H_2O$ (**IV**) and $\{(Zn(en)_2(H_2O)_2)(Zn(en)_2)\}$-$[Zn(en)_2V_{15}Sb_6O_{42}(H_2O)]\cdot 8.5H_2O$ (**V**) could be obtained by very convenient post-functionalization procedures in short reaction times starting from **III** (Figure 68).

ESI-MS experiments showed that the $\{V_{15}Sb_6\}$ cluster remains intact upon dissolution of **III** in water, yet transforms into $\{V_{14}Sb_8\}$ after several days. This is a common feature of the observed reactivity of the $\{V_{15}Sb_6\}$-containing compounds **I** and **III**. Interestingly, the new compounds **VI** and **V** contain an unchanged $\{V_{15}Sb_6\}$ cluster cage, while post-functionalization of **I** in aqueous solution yielded products with mostly $\{V_{14}Sb_8\}$-type clusters (see chapters 3.2.1, 3.2.2 and other recent literature[227–229]). Time-dependent ESI-MS measurements gave a rationale for this distinct behavior. Monitoring the $\{V_{15}Sb_6\}$ →

$\{V_{14}Sb_8\}$ transformation for compounds **I** and **III** attested an increased stability to the $\{V_{15}Sb_6\}$ cluster core in **III** as compared to that of **I** (Figure 69). Furthermore, the rate of the $\{V_{15}Sb_6\} \rightarrow \{V_{14}Sb_8\}$ cluster transformation significantly increases in both cases, when ammonium acetate is added. These results indicate that the reactivity of the cluster cage is not only determined by the encapsulated water molecule as shown in chapter 3.2.1, but also by the surrounding cationic metal-complex and ligand environment, as well as additives.

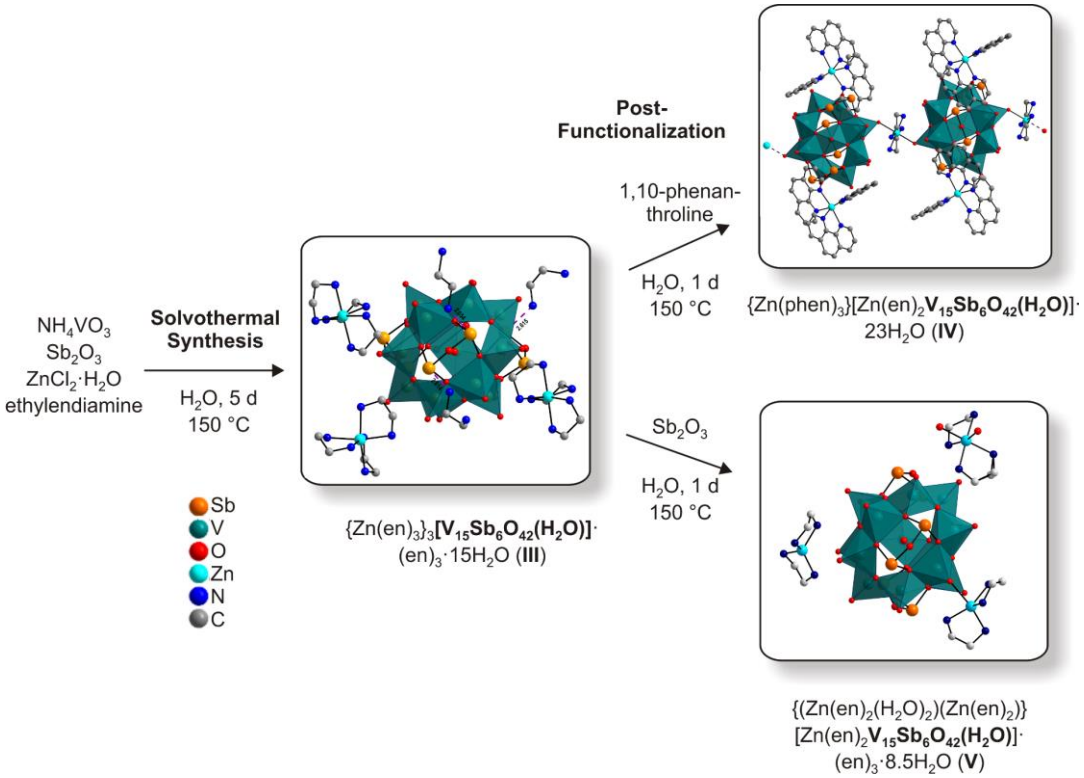

Figure 68: Solvothermal synthesis of compound **III** and formation of Sb-POV compounds **VI** and **V** by post-functionalization with respective crystal structures showing intact $\{V_{15}Sb_6\}$ cluster core.

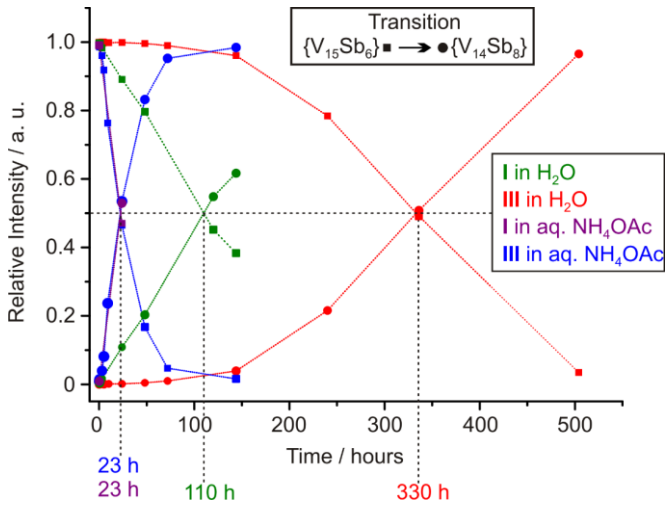

Figure 69: Time-dependent formation of the $\{V_{14}Sb_8\}$ cluster from $\{V_{15}Sb_6\}$ cluster cage for compounds **I** and **III** in aqueous solution and in aqueous ammonium acetate solution (1%) as obtained from ESI-MS experiments, with corresponding times after which 50% conversion is reached. Reprinted and adapted from Mahnke *et al.*[226] (© 2018 WILEY-VCH Verlag GmbH & Co. KGaA, Weinheim).

All new compounds **III-V** presented in this study have the $\{V_{15}Sb_6\}$ cluster cage with an encapsulated water molecule inside the cavity as the common motif, identical to compound **I** (see chapter 3.2.1, 3.2.2 and 2.3.3). In all of them, strong interactions between the cluster and the ethylendiamine ligand or one of the $Zn(en)_2$ complexes are present which underline the potential of Sb-POVs to form complex structures by supramolecular interactions (Figure 68). Compound **III** features a close interaction between one nitrogen atom of all three ethylendiamine molecules and three of the Sb atoms with Sb-N distances significantly shorter than the sum of their van der Waals radii. In the structure of **IV**, $\{V_{15}Sb_6\}$ clusters are connected to their next neighbors by $[Zn(en)_2]^{2+}$ complexes forming a chain along which $[Zn(phen)_3]^{2+}$ complexes are located in a sandwich-type arrangement. $(Zn(en)_2(H_2O)_2)(Zn(en)_2)\}[Zn(en)_2V_{15}Sb_6O_{42}(H_2O)]\cdot 8.5H_2O$ (**V**) contains three different Zn^{2+} complexes in different coordination geometries. One of the zinc cations is connected to the cluster by a Zn···O interaction and exhibits a distorted trigonal bipyramidal environment.

In conclusion, this work demonstrates the value of reactivity studies on Sb-POV compounds by mass spectrometry for the rational and selective preparation of new Sb-POV compounds. It also encourages the use of additives like ammonium acetate for future studies which aim for the systematic synthesis of $\{V_{14}Sb_8\}$ cluster compounds from the known $\{V_{15}Sb_6\}$ precursors.

Author contributions

Cluster syntheses and standard characterization was done by Lisa K. Mahnke. She also obtained crystals of compounds **III-V** suitable for X-ray crystal structure analysis which was performed and analyzed by Christian Näther. I performed time-dependent ESI-MS experiments on compounds **I** and **III** in water and with different additives, as well as the corresponding data analysis and interpretation. Lisa Mahnke and I discussed the results and worked on the general concept of the manuscript together. Lisa Mahnke wrote the manuscript in collaboration with me. All authors contributed to the final version of the manuscript.

3.3. Polyamide–Polyamine Cryptand as Dicarboxylate Receptor: Dianion Binding Studies in the Solid State, in Solution, and in the Gas Phase

Sourav Chakraborty, Subrata Saha, Luís M. P. Lima, Ulrike Warzok, Sayan Sarkar, Bidyut Akhuli, Mandira Nandi, Somnath Bej, Nayarassery N. Adarsh, Christoph A. Schalley, Rita Delgado, and Pradyut Ghosh

J. Org. Chem. **2017**, *82*, 10007–10014.

Submitted on 09 June 2017, first published on 28 August 2017 in Journal of Organic Chemistry. For copyright reasons, the article (Appendix 6.3.8) is not included in the online version of this thesis.

An electronic version of the article is available (https://doi.org/10.1021/acs.joc.7b01431).

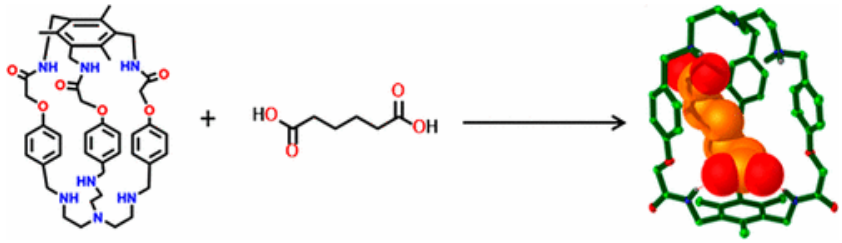

Figure 70: The graphical abstract shows the binding of adipic acid to the polyamide-polyamine hybrid macrobicycle and the resulting X-ray crystal structure. Reprinted with permission from Chakraborty *et al.*[230] (© 2017, American Chemical Society).

Project summary

This side project aimed at the investigation of the hybrid amide-ammonium macrobicyclic receptor **L**, with respect to its ability to bind dicarboxylates in aqueous solution, solid state and in the gas phase (Figure 70).

Potentiometric studies in a H_2O/DMSO solvent mixture revealed that the protonated cavitand **L** forms 1:1 complexes with a series of dicarboxylates with the highest association constant generally between a pH of 6 and 7. The highest absolute value for the effective binding constant K_{eff} was observed for adipate as the guest (Figure 71a, b, figure caption for definition of K_{eff}). In general, the binding constants increase from gluterate to adipate and then continuously decrease with the length of the alkyl chain between the carboxylates. For succinate and for α-keto gluterate, the binding behavior differs likely due to the shorter chain and the additional carbonyl group, respectively.

The X-ray crystal structures of the host-guest complexes with α-keto gluterate, gluterate and adipate show the guests clearly within the cavity of the protonated host. The best size-shape complementarity was observed for adipate, evidenced by the relatively short hydrogen bonds between the carboxylates and the amide and ammonium groups of **L** (Figure 71c). The next larger guests are only partially encapsulated inside the host or bind on its exterior as side-on complexes due to the elongated chain length.

Negative-mode ESI-MS measurements from aqueous solutions of the cryptand-dicarboxylate ($\mathbf{A}^{2-}$) complexes confirmed the selective formation of 1:1 complexes $[\mathbf{L}+\mathrm{H}\mathbf{A}]^-$ for all combinations. However, it was not possible to perform measurements in the positive ionization mode. This would have been more meaningful, allowing for a direct comparison of mass spectrometric resulting from potential complexes in

the +1 charge state to the potentiometric studies in solution. Furthermore, results from TW-IMS measurements in the negative ionization mode are inconclusive regarding the gas-phase conformation of the assemblies.

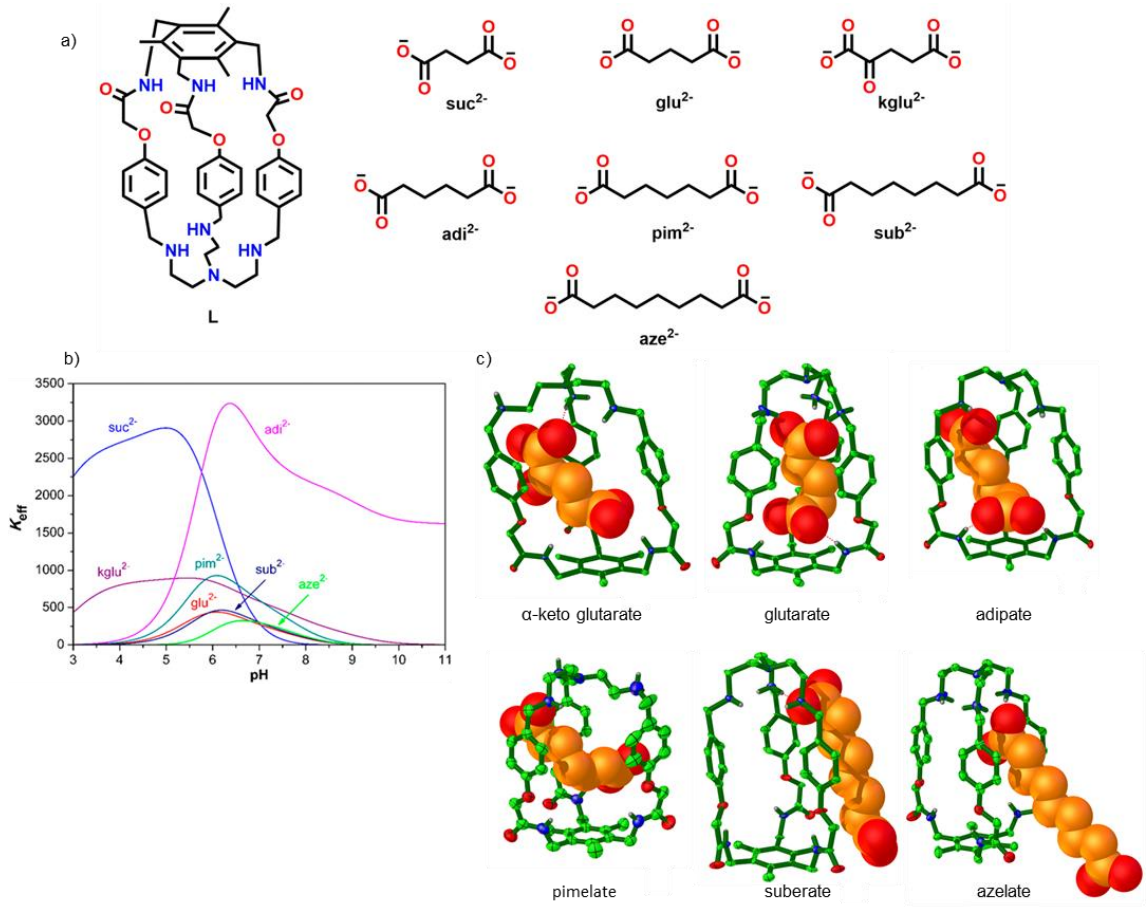

Figure 71: a) Chemical structures of the studied macrobicycle **L** and dicarboxylate anions $\mathbf{A}^{2-}$; b) association of host-guest complex formed between receptor and studied anions in dependence of pH; at a given pH: $\boldsymbol{K_{eff} = \frac{\sum[\mathbf{H}_h\mathbf{LA}]}{\sum[\mathbf{H}_a\mathbf{A}]\cdot\sum[\mathbf{H}_i\mathbf{L}]}}$ **with** $\boldsymbol{h = 0-5(a+i), a = 0-2}$ **and** $\boldsymbol{i = 0-3}$; c) X-ray crystal structures of host-guest complexes. Reprinted with permission from Chakraborty *et al.*[230] (© 2017, American Chemical Society).

This study presents the heteroditopic macrobicycle **L** as a well-suited receptor for the recognition of aliphatic dicarboxylate anions in aqueous medium. Results from the solid state and solution indicated the chain-length-selective recognition of the dianions based on size complementarity of host and guests. For the most strongly bound complexes, a maximum number of electrostatic interactions and strong hydrogen bonds between the carboxylate guest and the amide and ammonium groups of the host were observed. ESI-MS or IMS experiments could not confirm any trend in binding affinity, other than the selective formation of 1:1 complexes between host and all dicarboxylates. These results underline the limitations of electrospray ionization when applied to noncovalent, pH-sensitive supramolecular systems. As ionization can hamper or interfere with the binding process when complexes are transferred into the gas phase, results might not be as informative as was hoped for (see also chapters 2.4.1 and 2.4.2). A critical eye needs to be kept on the question if ESI-MS is always the suitable method for the system under study.

Author contributions

Sourav Chakraborty, Subrata Saha and Bidyut Akhuli obtained crystals of the different host-guest complexes suitable for X-ray crystal structure analysis, which was performed and analyzed by Sourav Chakraborty, Subrata Saha, Bidyut Akhuli and Nayarassery N. Adarsh. Sourav Chakraborty and Sayan Sarkar recorded and analyzed NMR spectra of the different host-guest complexes. Potentiometric studies and the corresponding data analysis were conducted by Luís M. P. Lima and Rita Delgado. I performed all ESI-MS and TW-IMS experiments and performed the data analysis and interpretation. Sourav Chakraborty wrote the manuscript with contributions from my side for the part on mass spectrometry. All authors contributed to the final version of the manuscript.

4. Conclusion

The aim of this thesis was the detailed investigation of structure and reactivity of novel molecular containers by mass spectrometry. This work should help to pave the way for the long-term goal of their application in functional systems. Numerous intriguing and unexpected results highlight the pronounced value of electrospray ionization mass spectrometry and ion mobility for this objective. Halogen-bonded capsules, polyoxovanadate cages and an amide-ammonium cryptand were selected as the research topics, covering a broad spectrum of different chemical architectures.

The investigation of halogen-bonded supramolecular capsules by ESI-MS and IMS is covered in a series of four publications. Two conceptionally different complex types were investigated: Neutral XB donor/acceptor capsules in cooperation with the DIEDRICH group from the ETH Zürich (Switzerland) and charged [N···I^+···N]-type capsules in cooperation with the RISSANEN group from the University of Jyvaskyla (Finland) and the PAGEL group from the Fritz Haber Institute, Berlin (Germany).

Furthermore, antimonato polyoxovanadate (Sb-POV) cages with {$V_{15}Sb_6$} and {$V_{14}Sb_8$} cluster cores were investigated in three publications in close collaboration with the BENSCH group from the Christian Albrechts University, Kiel (Germany).

Detection of novel molecular containers in the gas phase

The transfer of noncovalent complexes from the condensed phase into the gas phase is a necessary requirement to use mass spectrometric methods for the investigation of these new molecular containers. Prior to this work, this posed a major challenge in the analysis of the respective complexes and was the first objective for the performed research presented herein.

The detection of intact halogen-bonded capsules could be achieved by ESI-MS. While the neutral XB donor/acceptor capsules were charge-tagged by the encapsulation of a cationic guest, the use of weakly coordinating tosylate counter ions for the charged [N···I^+···N]-type capsules enabled their efficient ionization. For both systems, the choice of an appropriate solvent system as well as the fine-tuning of the sample concentration and ionization conditions proved to be crucial to the success of the work. These mass spectrometric experiments provided evidence for the selective formation of dimeric XB donor/acceptor capsules, as well as dimeric and hexameric [N···I^+···N]-type capsules and were consequently an integral contribution to the characterization of these novel supramolecular architectures. Moreover, they represent the first successful studies on halogen-bonded capsules in the gas phase.

The discovery of water-soluble Sb-POV cluster complexes enabled the first solution investigation of this compound class by mass spectrometry. Electrospray ionization allowed for a facile transfer of {$Ni(en)_3$}$_3$[$V_{15}Sb_6O_{42}(H_2O)_x$], {$Zn(en)_3$}$_3$[$V_{15}Sb_6O_{42}(H_2O)$]·3en and {Ni(cyclen)(en)}$_2$[$V_{14}Sb_8O_{42}(H_2O)$] into the gas phase, thereby confirming the dissolution of these compounds in aqueous media without degradation.

Additionally, the binding of dicarboxylates in an amide-ammonium cryptand in aqueous medium was

investigated by ESI-MS. These experiments provided evidence for the selective formation of 1:1 host-guest complexes. Yet, these noncovalent systems formed in a narrow pH range by the combination of electrostatic interactions and hydrogen bonding and were too sensitive for the positive ionization mode. Instead, only negative ions could be detected. This prevented the comparison of these results with complementary solution studies and a more detailed investigation.

The successful ionization of these molecular container, especially of the halogen-bonded capsules and the Sb-POV cages, enabled a more detailed analysis of their structure and reactivity by mass spectrometry.

Structure elucidation

Depending on the nature of the molecular container under study, different MS techniques were suited to probe their structure in solution and in the gas phase.

[N···I^+···N]-type capsules were analyzed in detail by IMS and DFT-level calculations. This combination of experimental and theoretical methods demonstrated a closed face-to-face arrangement and a regular octahedral structure for the dimeric and hexameric capsule, respectively. Both complexes feature linear [N···I^+···N] halogen bonds. Moreover, the first evidence for their guest-binding behavior was provided: Up to two tosylate anions in case of the dimeric and up to six anions for the hexameric capsule can be encapsulated within their cavities. They exhibit two different binding modes involving [C_{aryl}-H···O^-] hydrogen bonds depending on the size of the complex and leave the XB motif undisturbed.

In case of the Sb-POVs, IMS was not sensitive enough to allow the differentiation of small structural differences, such as the configurational isomers of an {$V_{14}Sb_8$} cluster core. Instead, an indirect approach using isotope-exchange experiments proved successful. This allowed to draw conclusions on the {$V_{15}Sb_6$} cluster structure by regarding its dynamics in solution and emphasizes the close relationship between these two properties of a chemical species. The cluster core is present in solution as a fully closed, cage-like structure. Interestingly, two distinct species were discovered: a water-encapsulating and a water-free cluster core, which are not in a fast equilibrium with each other. These ESI-MS results provided the basis for a reevaluation of the crystal structure obtained during the working process, which then confirmed the presence of an encapsulated water molecule in part of the cluster hosts.

Reactivity

A fascinating solution reactivity has been discovered for the [N···I^+···N]-type capsules and the Sb-POV cages. ESI-MS was in both cases the analytical method which could capture these changes in solution and provide information detailed enough for the elucidation of the reaction products. Additionally, tandem MS fragmentation experiments pointed for both compound types at pronounced differences between intrinsic reactivity of the complexes in the gas phase and in solution.

The first investigation on the reactivity of the hexameric [N···I^+···N]-type capsule revealed a solvent-dependent equilibrium with a previously unobserved pentameric complex. With the combination of ESI-MS, IMS and DFT calculations, this novel structure could be identified to possess an unusual trigonal bipyramidal geometry. Nine [N···I^+···N] halogen bonds form along the edges and two of the five

incorporated cavitands are partially uncomplexed. The pentameric capsule can encapsulate up to five tosylate counter ions in a binding mode similar to the larger hexameric complex. In the gas phase, this hexamer-pentamer transition does not occur. The fragmentation experiment rather leads to the formation of smaller oligomers for both large capsules. This implies that the observed solution equilibrium relies on the reaction of several complexes, most likely involving the monomeric cavitand, and is governed by solvent effects.

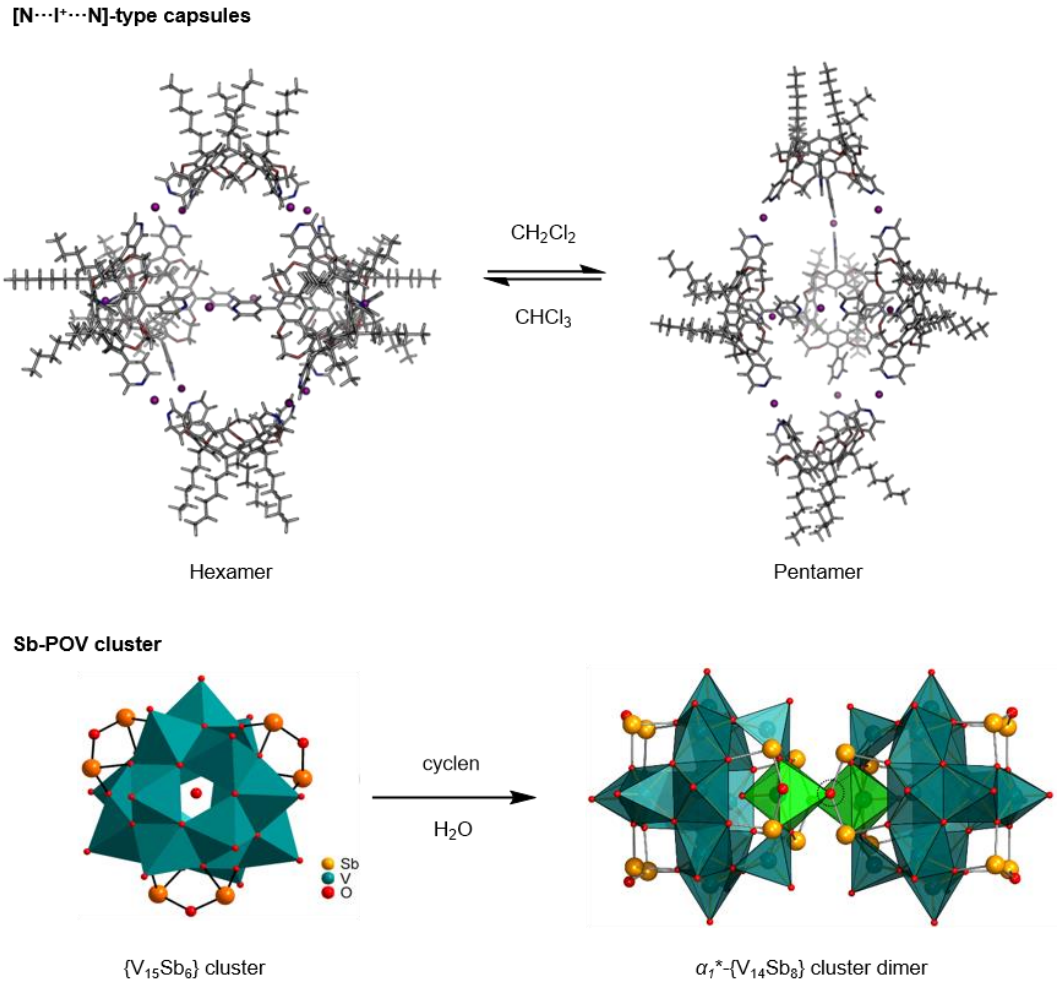

Figure 72: Solution reactivity of molecular containers observed by mass spectrometry. Reprinted and adapted from Wendt *et al.*[224] (Published by The Royal Society of Chemistry) and Mahnke *et al.*[225] (© 2018, WILEY-VCH Verlag GmbH & Co. KGaA, Weinheim).

In comparison, the $\{V_{15}Sb_6\}$ cluster revealed an intriguing gas-phase reactivity. The encapsulated water molecule participates in the fragmentation and influences the reactivity of the cluster from within. Several important discoveries on the solution reactivity of the $\{V_{15}Sb_6\}$ cluster were made by ESI-MS, which also point to the importance of the guest molecule for the behavior of the $\{V_{15}Sb_6\}$ host. Firstly, the oxygen-atom exchange in the cluster periphery is catalysed by the encapsulated water. Secondly, the $\{V_{15}Sb_6\}$ cluster transforms in solution into a $\{V_{14}Sb_8\}$ cage by a formal exchange of a VO_5 against an Sb_2O_5 unit. The reaction product carries predominantly water in its cavity, indicating that the encapsulated water might act as a template for this transition. Furthermore, the two investigated $\{V_{15}Sb_6\}$ compounds with nickel and

zinc complexes as counter ions differ from each other in a prolonged reaction time for the $\{V_{15}Sb_6\}\rightarrow\{V_{14}Sb_8\}$ transformation in case of the zinc complex. The reactivity of the cluster cage is hence not only determined by the encapsulated water molecule, but also by the surrounding cationic metal-complex and ligand environment. Consequently, these two new Sb-POVs could already be employed as high-nuclearity precursors for first post-functionalizations. The knowledge about their solution reactivity solely provided by mass spectrometry enabled the rational synthesis of a number of new compounds prepared by BENSCH and coworkers.[227,229]

Among them, a compound derived from of the Ni-$\{V_{15}Sb_6\}$ complex was discovered which forms self-assembled superstructures in the solid state. ESI-MS and IMS experiments demonstrated that the cluster cage had not only undergone the $\{V_{15}Sb_6\}\rightarrow\{V_{14}Sb_8\}$ transformation, but additionally formed selectively stable dimers from a meta-stable α_1*-$\{V_{14}Sb_8\}$ isomer in solution and in the gas phase. The analysis of this fascinating new compound highlights the ability of mass spectrometry to provide detailed structural insights into hierarchical self-assembly phenomena of Sb-POVs.

Outlook

In the field of halogen-bonded capsules, future studies should focus on expanding the understanding of the reactivity and chemical behavior of the different [N···I$^+$···N]-type capsules depending on external stimuli. Especially experiments on the guest binding ability towards different anionic or neutral substrates are believed to be promising. Subsequently, exploring the self-sorting behavior of the complexes would be an interesting research subject, as the addition of differently sized or shaped guests to preformed capsules might template the formation of different capsule types. Based on the knowledge gained from the advanced studies on the reactivity of halogen-bonded capsules, functional systems could be accessible, e.g. for their application in supramolecular catalysis. As details on the guest-binding behavior are still scarce, a detailed prediction on possible reaction types proceeding within the cavity is difficult. However, it might be possible as a long-term goal to employ both in concert – the assembled enzyme-like cavity and the reactivity of the integrated iodonium ions – to obtain novel or enhanced reactivity. The latter aspect could involve reactivity similar to the Barluenga's reagent, an iodonium bispyridine complex, which was recently applied as the catalyst for an alkyne-carbonyl metathesis of unactivated alkynes (Figure 73).[231]

Future work on the topic of Sb-POVs could focus on an even more detailed investigation of their solution chemistry. It should take advantage of the three soluble complexes studied during this thesis to expend the structural diversity of this compound class to higher-order species. A more detailed mechanistic investigation of the $\{V_{15}Sb_6\}\rightarrow\{V_{14}Sb_8\}$ cluster rearrangement in solution, for which the understanding is still rudimentary, would be highly interesting. This might open pathways to unexplored, more complex structures by e.g. intercepting reaction intermediates when introducing interlinking ligands or additional cluster types. Initial results indicate a strong influence of additives like ammonium acetate on the solution reactivity of the $\{V_{15}Sb_6\}$ cage independent of the counter ion. This approach could be extended to other additives and might result in the formation of still unobserved, but theoretically predicted cluster cages. In this regard, it might be possible to exchange the encapsulated water within the cluster cavity to

another guest molecule or ion. The possible template effect on structure and reactivity of the resulting species would certainly be a fascinating research topic.

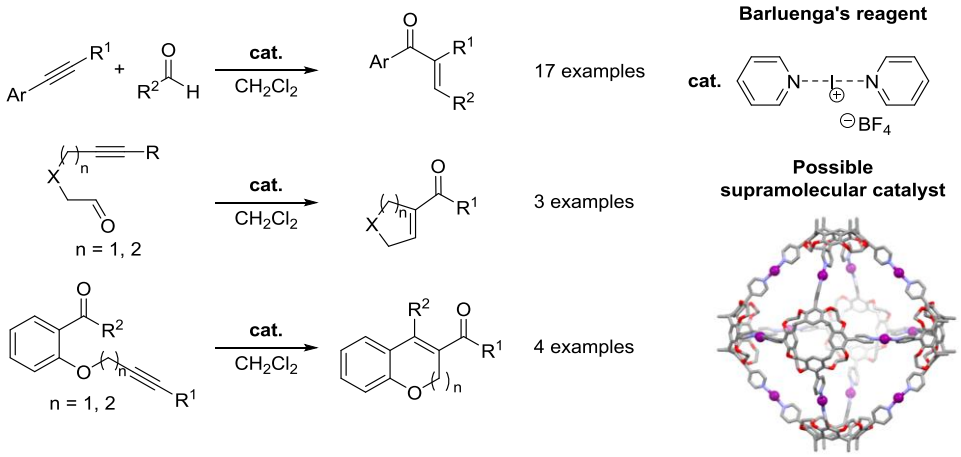

Figure 73: Use of Barluenga's reagent as the catalyst for different alkyne-carbonyl metathesis reactions of unactivated alkynes as a possible guideline to use of [N···I⁺···N] halogen-bonded capsules as supramolecular catalysts. Reprinted and adapted with permission from Turunen *et al*.[222] (© 2017 Elsevier Inc.).

In the context of future studies on these molecular containers, mass spectrometry and ion mobility could serve as a probe for the elucidation of solution reactivity, as well as the identification and structural analysis of new products. These methods can provide the rational guideline for the synthesis of new compounds and for the assembly of complex supramolecular architectures, as was already successfully done in the presented work.

5. Literature

[1] T. Ganti, E. Szathmary, J. Griesemer, *The Principles of Life*, Oxford University Press, Oxford, **2003**.

[2] B. C. Buddingh, J. C. M. van Hest, *Acc. Chem. Res.* **2017**, *50*, 769–777.

[3] M. G. Mateu, *Arch. Biochem. Biophys.* **2013**, *531*, 65–79.

[4] K. Matsuurua, *RSC Adv.* **2014**, *4*, 2942–2953.

[5] a) J. G. Heddle, S. Chakraborti, K. Iwasaki, *Curr. Opin. Struct. Biol.* **2017**, *43*, 148–155; b) J. R. Perilla, A. M. Gronenborn, *Trends Biochem. Sci.* **2016**, *41*, 410–420.

[6] S. Andersson, *Z. Anorg. Allg. Chem.* **2008**, *634*, 2161–2170.

[7] M. T. Pope, A. Müller (Eds.) *Polyoxometalate Chemistry From Topology via Self-Assembly to Applications*, Kluwer Academic Publishers, Dordrecht, **2002**.

[8] J.-M. Lehn, *Angew. Chem. Int. Ed. Engl.* **1988**, *27*, 89–112.

[9] F. Biedermann, H.-J. Schneider, *Chem. Rev.* **2016**, *116*, 5216–5300.

[10] C. A. Schalley (Ed.) *Analytical methods in supramolecular chemistry*, Wiley-VCH, Weinheim, **2012**.

[11] T. M. Beale, M. G. Chudzinski, M. G. Sarwar, M. S. Taylor, *Chem. Soc. Rev.* **2013**, *42*, 1667–1680.

[12] a) C. Elschenbroich, *Organometallchemie*, Vieweg+Teubner, Wiesbaden, **2008**; b) K.-B. Cho, H. Hirao, S. Shaik, W. Nam, *Chem. Soc. Rev.* **2016**, *45*, 1197–1210.

[13] J. R. Winkler, H. B. Gray in *Structure and Bonding* (Eds. D. M. P. Mingos, P. Day, J. P. Dahl), Springer, Berlin, Heidelberg, **2012**.

[14] G. Whitesides, J. Mathias, C. Seto, *Science* **1991**, *254*, 1312–1319.

[15] D. Philp, J. F. Stoddart, *Angew. Chem. Int. Ed. Engl.* **1996**, *35*, 1154–1196.

[16] L. K. S. von Krbek, A. J. Achazi, S. Schoder, M. Gaedke, T. Biberger, B. Paulus, C. A. Schalley, *Chem. Eur. J.* **2017**, *23*, 2877–2883.

[17] https://ghr.nlm.nih.gov/primer/basics/dna. [17.12.2017].

[18] T. Nakamura, H. Kimura, T. Okuhara, M. Yamamura, T. Nabeshima, *J. Am. Chem. Soc.* **2016**, *138*, 794–797.

[19] M. M. Safont-Sempere, G. Fernández, F. Würthner, *Chem. Rev.* **2011**, *111*, 5784–5814.

[20] Z. He, W. Jiang, C. A. Schalley, *Chem. Soc. Rev.* **2015**, *44*, 779–789.

[21] G. Cavallo, P. Metrangolo, R. Milani, T. Pilati, A. Priimagi, G. Resnati, G. Terraneo, *Chem. Rev.* **2016**, *116*, 2478–2601.

[22] P. H. Svensson, L. Kloo, *Chem. Rev.* **2003**, *103*, 1649–1684.

[23] J. Kleinberg, A. W. Davidson, *Chem. Rev.* **1948**, *42*, 601–609.

[24] J. S. Murray, P. Lane, P. Politzer, *J. Mol. Model.* **2009**, *15*, 723–729.

[25] P. Politzer, J. S. Murray, T. Clark, *Phys. Chem. Chem. Phys.* **2013**, *15*, 11178–11189.

[26] O. Hassel, *Science* **1970**, *170*, 497–502.

[27] R. S. Mulliken, *J. Am. Chem. Soc.* **1950**, *72*, 600–608.

[28] G. R. Desiraju, P. S. Ho, L. Kloo, A. C. Legon, R. Marquardt, P. Metrangolo, P. Politzer, G. Resnati, K. Rissanen, *Pure Appl. Chem.* **2013**, *85*, 1711–1713.

[29] *Chemistry International* **2016**, *38*, 22–24.

[30] K. Do, T. P. Klein, C. A. Pommerening, L. S. Sunderlin, *J. Am. Soc. Mass Spectrom.* **1997**, *8*, 688–696.

[31] a) P. Politzer, J. S. Murray, T. Clark, *Phys. Chem. Chem. Phys.* **2010**, *12*, 7748–7757; b) J. P. M. Lommerse, A. J. Stone, R. Taylor, F. H. Allen, *J. Am. Chem. Soc.* **1996**, *118*, 3108–3116.

[32] L. C. Gilday, S. W. Robinson, T. A. Barendt, M. J. Langton, B. R. Mullaney, P. D. Beer, *Chem. Rev.* **2015**, *115*, 7118–7195.

[33] Q. Chu, Z. Wang, Q. Huang, C. Yan, S. Zhu, *New J. Chem.* **2003**, *27*, 1522–1527.

[34] A. C. Legon, *Angew. Chem. Int. Ed.* **1999**, *38*, 2686–2714.

[35] E. Bosch, C. L. Barnes, *Cryst. Growth Des.* **2002**, *2*, 299–302.

[36] T. Clark, M. Hennemann, J. S. Murray, P. Politzer, *J. Mol. Model.* **2007**, *13*, 291–296.

[37] a) K. E. Riley, J. S. Murray, J. Fanfrlík, J. Rezáč, R. J. Solá, M. C. Concha, F. M. Ramos, P. Politzer, *J. Mol. Model.* **2011**, *17*, 3309–3318; b) K. E. Riley, J. S. Murray, P. Politzer, M. C. Concha, P. Hobza, *J. Chem. Theory Comput.* **2009**, *5*, 155–163.

[38] R. S. Mulliken, *J. Am. Chem. Soc.* **1952**, *74*, 811–824.

[39] S. V. Rosokha, I. S. Neretin, T. Y. Rosokha, J. Hecht, J. K. Kochi, *Heteroatom Chem.* **2006**, *17*, 449–459.

[40] a) R. B. Walsh, C. W. Padgett, P. Metrangolo, G. Resnati, T. W. Hanks, W. T. Pennington, *Cryst. Growth Des.* **2001**, *1*, 165–175; b) S. V. Rosokha, M. K. Vinakos, *Cryst. Growth Des.* **2012**, *12*, 4149–4156.

[41] A. Farina, S. V. Meille, M. T. Messina, P. Metrangolo, G. Resnati, G. Vecchio, *Angew. Chem. Int. Ed.* **1999**, *38*, 2433–2436.

[42] a) M. Palusiak, *J. Mol. Struct.: THEOCHEM* **2010**, *945*, 89–92; b) C. Wang, D. Danovich, Y. Mo, S. Shaik, *J. Chem. Theory Comput.* **2014**, *10*, 3726–3737.

[43] a) T. Clark, P. Politzer, J. S. Murray, *Wiley Interdiscip. Rev. Comput. Mol. Sci.* **2015**, *5*, 169–177; b) P. Politzer, P. Lane, M. C. Concha, Y. Ma, J. S. Murray, *J. Mol. Model.* **2007**, *13*, 305–311.

[44] P. Metrangolo, J. S. Murray, T. Pilati, P. Politzer, G. Resnati, G. Terraneo, *CrystEngComm* **2011**, *13*, 6593–6596.

[45] P. Metrangolo, F. Meyer, T. Pilati, G. Resnati, G. Terraneo, *Angew. Chem. Int. Ed.* **2008**, *47*, 6114–6127.

[46] a) C. Präsang, A. C. Whitwood, D. W. Bruce, *Cryst. Growth Des.* **2009**, *9*, 5319–5326; b) K. Raatikainen, M. Cametti, K. Rissanen, *Beilstein J. Org. Chem.* **2010**, *6*, No. 4; c) R. Liantonio, P. Metrangolo, T. Pilati, G. Resnati, A. Stevenazzi, *Cryst. Growth Des.* **2003**, *3*, 799–803.

[47] C. B. Aakeröy, M. Baldrighi, J. Desper, P. Metrangolo, G. Resnati, *Chem. Eur. J.* **2013**, *19*, 16240–16247.

[48] A. Vargas Jentzsch, S. Matile, *J. Am. Chem. Soc.* **2013**, *135*, 5302–5303.

[49] A. V. Jentzsch, D. Emery, J. Mareda, S. K. Nayak, P. Metrangolo, G. Resnati, N. Sakai, S. Matile, *Nat. Commun.* **2012**, *3*, 905.

[50] A. Bondi, *J. Phys. Chem.* **1964**, *68*, 441–451.

[51] O. Dumele, D. Wu, N. Trapp, N. Goroff, F. Diederich, *Org. Lett.* **2014**, *16*, 4722–4725.

[52] M. G. Sarwar, B. Dragisic, L. J. Salsberg, C. Gouliaras, M. S. Taylor, *J. Am. Chem. Soc.* **2010**, *132*, 1646–1653.

[53] R. Cabot, C. A. Hunter, *Chem. Commun.* **2009**, 2005–2007.

[54] a) J. G. Hill, A. C. Legon, D. P. Tew, N. R. Walker, *Top. Curr. Chem.* **2015**, *358*, 43–77; b) A. C. Legon, *Chem. Eur. J.* **1998**, *4*, 1890–1897; c) A. C. Legon in *Structure and Bonding* (Eds.: P. Metrangolo, G. Resnati), Springer, Berlin and Heidelberg, **2008**.

[55] a) C. Wegeberg, W. A. Donald, C. J. McKenzie, *J. Am. Soc. Mass Spectrom. Chem.* **2017**, *28*, 2209–2216; b) D. Cappelletti, P. Candori, F. Pirani, L. Belpassi, F. Tarantelli, *Cryst. Growth Des.* **2011**, *11*, 4279–4283.

[56] E. A. L. Gillis, M. Demireva, M. G. Sarwar, M. G. Chudzinski, M. S. Taylor, E. R. Williams, T. D. Fridgen, *Phys. Chem. Chem. Phys.* **2013**, *15*, 7638–7647.

[57] K. A. Mason, A. C. Pearcy, I. K. Attah, S. P. Platt, S. G. Aziz, M. S. El-Shall, *Phys. Chem. Chem. Phys.* **2017**, *19*, 18603–18611.

[58] A.-C. C. Carlsson, J. Gräfenstein, A. Budnjo, J. L. Laurila, J. Bergquist, A. Karim, R. Kleinmaier, U. Brath, M. Erdélyi, *J. Am. Chem. Soc.* **2012**, *134*, 5706–5715.

[59] S. B. Hakkert, M. Erdélyi, *J. Phys. Org. Chem.* **2015**, *28*, 226–233.

[60] A.-C. C. Carlsson, M. Uhrbom, A. Karim, U. Brath, J. Gräfenstein, M. Erdélyi, *CrystEngComm* **2013**, *15*, 3087–3092.

[61] M. Bedin, A. Karim, M. Reitti, A.-C. C. Carlsson, F. Topić, M. Cetina, F. Pan, V. Havel, F. Al-Ameri, V. Sindelar, K. Rissanen, J. Gräfenstein, M. Erdélyi, *Chem. Sci.* **2015**, *6*, 3746–3756.

[62] L. Koskinen, P. Hirva, E. Kalenius, S. Jääskeläinen, K. Rissanen, M. Haukka, *CrystEngComm* **2015**, *17*, 1231–1236.

[63] D. C. Georgiou, P. Butler, E. C. Browne, D. J. D. Wilson, J. L. Dutton, *Aust. J. Chem.* **2013**.

[64] A.-C. C. Carlsson, K. Mehmeti, M. Uhrbom, A. Karim, M. Bedin, R. Puttreddy, R. Kleinmaier, A. A. Neverov, B. Nekoueishahraki, J. Gräfenstein, K. Rissanen, M. Erdélyi, *J. Am. Chem. Soc.* **2016**, *138*, 9853–9863.

[65] T. A. Logothetis, F. Meyer, P. Metrangolo, T. Pilati, G. Resnati, *New J. Chem.* **2004**, *28*, 760–763.

[66] S. Samai, K. Biradha, *CrystEngComm* **2009**, *11*, 482–492.

[67] S. Muniappan, S. Lipstman, I. Goldberg, *Chem. Commun.* **2008**, 1777–1779.

[68] K. Raatikainen, K. Rissanen, *Chem. Sci.* **2012**, *3*, 1235–1239.

[69] X. Q. Yan, Q. J. Shen, X. R. Zhao, H. Y. Gao, X. Pang, W. J. Jin, *Anal. Chim. Acta* **2012**, *753*, 48–56.

[70] J.-R. Wang, X. Fan, Q. Ding, X. Mei, *J. Mol. Struct.* **2016**, *1119*, 269–275.

[71] a) S. H. Jungbauer, D. Bulfield, F. Kniep, C. W. Lehmann, E. Herdtweck, S. M. Huber, *J. Am. Chem. Soc.* **2014**, *136*, 16740–16743; b) S. Castro-Fernández, I. R. Lahoz, A. L. Llamas-Saiz, J. L. Alonso-Gómez, M.-M. Cid, A. Navarro-Vázquez, *Org. Lett.* **2014**, *16*, 1136–1139.

[72] a) S. M. Walter, F. Kniep, L. Rout, F. P. Schmidtchen, E. Herdtweck, S. M. Huber, *J. Am. Chem. Soc.* **2012**, *134*, 8507–8512; b) A. Mele, P. Metrangolo, H. Neukirch, T. Pilati, G. Resnati, *J. Am.*

Chem. Soc. **2005**, *127*, 14972–14973; c) M. G. Sarwar, B. Dragisic, S. Sagoo, M. S. Taylor, *Angew. Chem. Int. Ed.* **2010**, *49*, 1674–1677; d) M. G. Chudzinski, C. A. McClary, M. S. Taylor, *J. Am. Chem. Soc.* **2011**, *133*, 10559–10567; e) M. Cametti, K. Raatikainen, P. Metrangolo, T. Pilati, G. Terraneo, G. Resnati, *Org. Biomol. Chem.* **2012**, *10*, 1329–1333; f) L.-Y. You, S.-G. Chen, X. Zhao, Y. Liu, W.-X. Lan, Y. Zhang, H.-J. Lu, C.-Y. Cao, Z.-T. Li, *Angew. Chem. Int. Ed.* **2012**, *51*, 1657–1661.

[73] L. C. Gilday, T. Lang, A. Caballero, P. J. Costa, V. Félix, P. D. Beer, *Angew. Chem. Int. Ed.* **2013**, *52*, 4356–4360.

[74] a) T. A. Barendt, S. W. Robinson, P. D. Beer, *Chem. Sci.* **2016**, *7*, 5171–5180; b) T. A. Barendt, A. Docker, I. Marques, V. Félix, P. D. Beer, *Angew. Chem. Int. Ed.* **2016**, *55*, 11069–11076.

[75] C. J. Serpell, N. L. Kilah, P. J. Costa, V. Félix, P. D. Beer, *Angew. Chem. Int. Ed.* **2010**, *49*, 5322–5326.

[76] a) S. W. Robinson, C. L. Mustoe, N. G. White, A. Brown, A. L. Thompson, P. Kennepohl, P. D. Beer, *J. Am. Chem. Soc.* **2015**, *137*, 499–507; b) J. M. Mercurio, A. Caballero, J. Cookson, P. D. Beer, *RSC Adv.* **2015**, *5*, 9298–9306.

[77] a) J. Y. C. Lim, T. Bunchuay, P. D. Beer, *Chem. Eur. J.* **2017**, *23*, 4700–4707; b) M. J. Langton, I. Marques, S. W. Robinson, V. Félix, P. D. Beer, *Chem. Eur. J.* **2016**, *22*, 185–192; c) N. L. Kilah, M. D. Wise, C. J. Serpell, A. L. Thompson, N. G. White, K. E. Christensen, P. D. Beer, *J. Am. Chem. Soc.* **2010**, *132*, 11893–11895.

[78] a) A. Borissov, J. Y. C. Lim, A. Brown, K. E. Christensen, A. L. Thompson, M. D. Smith, P. D. Beer, *Chem. Commun.* **2017**, *53*, 2483–2486; b) A. Brown, P. D. Beer, *Chem. Commun.* **2016**, *52*, 8645–8658.

[79] B. R. Mullaney, A. L. Thompson, P. D. Beer, *Angew. Chem. Int. Ed.* **2014**, *53*, 11458–11462.

[80] A. Caballero, F. Zapata, N. G. White, P. J. Costa, V. Félix, P. D. Beer, *Angew. Chem. Int. Ed.* **2012**, *51*, 1876–1880.

[81] J. Y. C. Lim, I. Marques, V. Félix, P. D. Beer, *J. Am. Chem. Soc.* **2017**, *139*, 12228–12239.

[82] A. Vargas Jentzsch, D. Emery, J. Mareda, P. Metrangolo, G. Resnati, S. Matile, *Angew. Chem. Int. Ed.* **2011**, *50*, 11675–11678.

[83] J. Cao, X. Yan, W. He, X. Li, Z. Li, Y. Mo, M. Liu, Y.-B. Jiang, *J. Am. Chem. Soc.* **2017**, *139*, 6605–6610.

[84] a) D. J. Cram, *Angew. Chem. Int. Ed. Engl.* **1988**, *27*, 1009–1020; b) C. J. Pedersen, *Angew. Chem. Int. Ed. Engl.* **1988**, *27*, 1021–1027.

[85] H. Dodziuk, *Introduction to Supramolecular Chemistry*, Kluwer Academic Publishers, Dordrecht, **2002**.

[86] Z. Liu, S. K. M. Nalluri, J. F. Stoddart, *Chem. Soc. Rev.* **2017**, *46*, 2459–2478.

[87] V. K. Jain, P. H. Kanaiya, *Russ. Chem. Rev.* **2011**, *80*, 75–102.

[88] N. Natarajan, E. Brenner, D. Sémeril, D. Matt, J. Harrowfield, *Eur. J. Org. Chem.* **2017**, *2017*, 6100–6113.

[89] a) D. M. Rudkevich, G. Hilmersson, J. Rebek Jr., *J. Am. Chem. Soc.* **1997**, *119*, 9911–9912; b) S.

Ma, D. M. Rudkevich, J. Rebek Jr., *J. Am. Chem. Soc.* **1998**, *120*, 4977–4981.

[90] M. Yamanaka, K. Kobayashi, *Asian J. Org. Chem.* **2013**, *2*, 276–289.

[91] K. Kobayashi, M. Yamanaka, *Chem. Soc. Rev.* **2015**, *44*, 449–466.

[92] D. M. Rudkevich, J. Rebek Jr., *Eur. J. Org. Chem.* **1999**, *1999*, 1991–2005.

[93] a) R. Pinalli, E. Dalcanale, F. Ugozzoli, C. Massera, *CrystEngComm* **2016**, *18*, 5788–5802; b) I. Pochorovski, F. Diederich, *Isr. J. Chem.* **2012**, *52*, 20–29.

[94] I. Pochorovski, F. Diederich, *Acc. Chem. Res.* **2014**, *47*, 2096–2105.

[95] S. M. Biros, J. Rebek Jr., *Chem. Soc. Rev.* **2007**, *36*, 93–104.

[96] a) F. Tancini, T. Gottschalk, W. B. Schweizer, F. Diederich, E. Dalcanale, *Chem. Eur. J.* **2010**, *16*, 7813–7819; b) S. S. Zhu, H. Staats, K. Brandhorst, J. Grunenberg, F. Gruppi, E. Dalcanale, A. Lützen, K. Rissanen, C. A. Schalley, *Angew. Chem. Int. Ed.* **2008**, *47*, 788–792.

[97] I. Pochorovski, J. Milić, D. Kolarski, C. Gropp, W. B. Schweizer, F. Diederich, *J. Am. Chem. Soc.* **2014**, *136*, 3852–3858.

[98] R. J. Hooley, J. Rebek Jr., *Chem. Biol.* **2009**, *16*, 255–264.

[99] M. Kanaura, N. Endo, M. P. Schramm, T. Iwasawa, *Eur. J. Org. Chem.* **2016**, *2016*, 4970–4975.

[100] a) L. Adriaenssens, P. Ballester, *Chem. Soc. Rev.* **2013**, *42*, 3261–3277; b) N. Ahmad, H. A. Younus, A. H. Chughtai, F. Verpoort, *Chem. Soc. Rev.* **2015**, *44*, 9–25; c) P. Ballester, *Chem. Soc. Rev.* **2010**, *39*, 3810–3830.

[101] R. Custelcean, *Chem. Soc. Rev.* **2014**, *43*, 1813–1824.

[102] L. C. Palmer, J. Rebek Jr., *Org. Biomol. Chem.* **2004**, *2*, 3051–3059.

[103] R. Wyler, J. de Mendoza, J. Rebek Jr., *Angew. Chem. Int. Ed. Engl.* **1993**, *32*, 1699–1701.

[104] J. Rebek Jr., T. Heinz, D. M. Rudkevich, *Nature* **1998**, *394*, 764–766.

[105] M. Fujita, D. Oguro, M. Miyazawa, H. Oka, K. Yamaguchi, K. Ogura, *Nature* **1995**, *378*, 469–471.

[106] M. Fujita, S. Nagao, K. Ogura, *J. Am. Chem. Soc.* **1995**, *117*, 1649–1650.

[107] M. Fujita, *Chem. Soc. Rev.* **1998**, *27*, 417–425.

[108] G. V. Oshovsky, D. N. Reinhoudt, W. Verboom, *J. Am. Chem. Soc.* **2006**, *128*, 5270–5278.

[109] J. H. Jordan, B. C. Gibb, *Chem. Soc. Rev.* **2015**, *44*, 547–585.

[110] T. Schröder, S. N. Sahu, D. Anselmetti, J. Mattay, *Isr. J. Chem.* **2011**, *51*, 725–742.

[111] C. B. Aakeröy, A. Rajbanshi, P. Metrangolo, G. Resnati, M. F. Parisi, J. Desper, T. Pilati, *CrystEngComm* **2012**, *14*, 6366–6368.

[112] N. K. Beyeh, F. Pan, K. Rissanen, *Angew. Chem. Int. Ed.* **2015**, *54*, 7303–7307.

[113] F. Pan, N. K. Beyeh, K. Rissanen, *J. Am. Chem. Soc.* **2015**, *137*, 10406–10413.

[114] O. Dumele, N. Trapp, F. Diederich, *Angew. Chem. Int. Ed.* **2015**, *54*, 12339–12344.

[115] R. Sure, S. Grimme, *Chem. Commun.* **2016**, *52*, 9893–9896.

[116] a) D. Fujita, K. Suzuki, S. Sato, M. Yagi-Utsumi, Y. Yamaguchi, N. Mizuno, T. Kumasaka, M. Takata, M. Noda, S. Uchiyama, K. Kato, M. Fujita, *Nat. Commun.* **2012**, *3*, 1093; b) S. Zarra, D. M. Wood, D. A. Roberts, J. R. Nitschke, *Chem. Soc. Rev.* **2015**, *44*, 419–432; c) D. Beaudoin, F. Rominger, M. Mastalerz, *Angew. Chem. Int. Ed.* **2016**, *55*, 15599–15603.

[117] C. M. A. Gangemi, A. Pappalardo, G. T. Sfrazzetto, *RSC Adv.* **2015**, *5*, 51919–51933.

[118] D. Fujita, Y. Ueda, S. Sato, H. Yokoyama, N. Mizuno, T. Kumasaka, M. Fujita, *Chem* **2016**, *1*, 91–101.

[119] a) D. Fujita, Y. Ueda, S. Sato, N. Mizuno, T. Kumasaka, M. Fujita, *Nature* **2016**, *540*, 563–566; b) T. R. Cook, Y.-R. Zheng, P. J. Stang, *Chem. Rev.* **2013**, *113*, 734–777; c) M. Han, D. M. Engelhard, G. H. Clever, *Chem. Soc. Rev.* **2014**, *43*, 1848–1860; d) M. M. J. Smulders, I. A. Riddell, C. Browne, J. R. Nitschke, *Chem. Soc. Rev.* **2013**, *42*, 1728–1754.

[120] L. R. MacGillivray, J. L. Atwood, *Nature* **1997**, *389*, 469–472.

[121] A. Shivanyuk, J. Rebek Jr., *Proc. Natl. Acad. Sci. USA* **2001**, *98*, 7662–7665.

[122] T. Gerkensmeier, W. Iwanek, C. Agena, R. Fröhlich, S. Kotila, C. Näther, J. Mattay, *Eur. J. Org. Chem.* **1999**, *1999*, 2257–2262.

[123] N. K. Beyeh, M. Kogej, A. Ahman, K. Rissanen, C. A. Schalley, *Angew. Chem. Int. Ed.* **2006**, *45*, 5214–5218.

[124] S. Mecozzi, J. Rebek Jr., *Chem. Eur. J.* **1998**, *4*, 1016–1022.

[125] L. Avram, Y. Cohen, J. Rebek Jr., *Chem. Commun.* **2011**, *47*, 5368–5375.

[126] T. Schröder, R. Brodbeck, M. C. Letzel, A. Mix, B. Schnatwinkel, M. Tonigold, D. Volkmer, J. Mattay, *Tetrahedron Lett.* **2008**, *49*, 5939–5942.

[127] O. Ugono, J. P. Moran, K. T. Holman, *Chem. Commun.* **2008**, 1404–1406.

[128] R. M. McKinlay, G. W. V. Cave, J. L. Atwood, *Proc. Natl. Acad. Sci. USA* **2005**, *102*, 5944–5948.

[129] a) R. M. McKinlay, P. K. Thallapally, G. W. V. Cave, J. L. Atwood, *Angew. Chem. Int. Ed.* **2005**, *44*, 5733–5736; b) R. M. McKinlay, P. K. Thallapally, J. L. Atwood, *Chem. Commun.* **2006**, 2956–2958; c) A. S. Rathnayake, K. A. Feaster, J. White, C. L. Barnes, S. J. Teat, J. L. Atwood, *Cryst. Growth Des.* **2016**, *16*, 3562–3564.

[130] W. Wang, Y.-X. Wang, H.-B. Yang, *Chem. Soc. Rev.* **2016**, *45*, 2656–2693.

[131] B. Kilbas, S. Mirtschin, R. Scopelliti, K. Severin, *Chem. Sci.* **2012**, *3*, 701–704.

[132] M. Raynal, P. Ballester, A. Vidal-Ferran, P. W. N. M. van Leeuwen, *Chem. Soc. Rev.* **2014**, *43*, 1734–1787.

[133] C. J. Brown, F. D. Toste, R. G. Bergman, K. N. Raymond, *Chem. Rev.* **2015**, *115*, 3012–3035.

[134] a) V. M. Dong, D. Fiedler, B. Carl, R. G. Bergman, K. N. Raymond, *J. Am. Chem. Soc.* **2006**, *128*, 14464–14465; b) M. D. Pluth, R. G. Bergman, K. N. Raymond, *J. Am. Chem. Soc.* **2007**, *129*, 11459–11467.

[135] a) P. Mal, B. Breiner, K. Rissanen, J. R. Nitschke, *Science* **2009**, *324*, 1697–1699; b) W. Cullen, M. C. Misuraca, C. A. Hunter, N. H. Williams, M. D. Ward, *Nat. Chem.* **2016**, *8*, 231–236.

[136] a) J. L. Bolliger, A. M. Belenguer, J. R. Nitschke, *Angew. Chem. Int. Ed.* **2013**, *52*, 7958–7962; b) C. García-Simón, R. Gramage-Doria, S. Raoufmoghaddam, T. Parella, M. Costas, X. Ribas, J. N. H. Reek, *J. Am. Chem. Soc.* **2015**, *137*, 2680–2687; c) C. Zhao, Q.-F. Sun, W. M. Hart-Cooper, A. G. DiPasquale, F. D. Toste, R. G. Bergman, K. N. Raymond, *J. Am. Chem. Soc.* **2013**, *135*, 18802–18805.

[137] D. Fiedler, R. G. Bergman, K. N. Raymond, *Angew. Chem. Int. Ed.* **2004**, *43*, 6748–6751.

[138] T. M. Bräuer, Q. Zhang, K. Tiefenbacher, *J. Am. Chem. Soc.* **2017**, *139*, 17500–17507.

[139] M. Hutin, M. H. Rosnes, D.-L. Long, L. Cronin in *Comprehensive Inorganic Chemistry II* (Eds. J. Reedijk, K. Poeppelmeier), Elsevier, Amsterdam, **2013**.

[140] C. Streb in *Structure and Bonding* (Ed. D. M. P. Mingos), Springer, Berlin and Heidelberg, **2017**.

[141] H. N. Miras, L. Vilà-Nadal, L. Cronin, *Chem. Soc. Rev.* **2014**, *43*, 5679–5699.

[142] C. Boskovic, *Acc. Chem. Res.* **2017**, *50*, 2205–2214.

[143] J. J. Berzelius, *Ann. Phys.* **1826**, *82*, 369–392.

[144] J. F. Keggin, *Nature* **1933**, *131*, 908–909.

[145] W. Xuan, R. Pow, D.-L. Long, L. Cronin, *Angew. Chem. Int. Ed.* **2017**, *129*, 9859–9863.

[146] A. Kondinski, K. Y. Monakhov, *Chem. Eur. J.* **2017**, *23*, 7841–7852.

[147] a) R. J. Errington in *Polyoxometalate Chemistry From Topology via Self-Assembly to Applications* (Eds.: M. T. Pope, A. Müller), Springer, Dordrecht, **2001**; b) A. Müller, S. K. Das, P. Kögerler, H. Bögge, M. Schmidtmann, A. X. Trautwein, V. Schünemann, E. Krickemeyer, W. Preetz, *Angew. Chem. Int. Ed.* **2000**, *39*, 3413–3417.

[148] a) B. Li, W. Li, H. Li, L. Wu, *Acc. Chem. Res.* **2017**, *50*, 1391–1399; b) D.-L. Long, E. Burkholder, L. Cronin, *Chem. Soc. Rev.* **2007**, *36*, 105–121; c) D.-L. Long, R. Tsunashima, L. Cronin, *Angew. Chem. Int. Ed.* **2010**, *49*, 1736–1758; d) C.-H. Zhan, R. S. Winter, Q. Zheng, J. Yan, J. M. Cameron, D.-L. Long, L. Cronin, *Angew. Chem. Int. Ed.* **2015**, *54*, 14308–14312.

[149] L. Li, K. Dong, P. Ma, C. Zhang, J. Niu, J. Wang, *Chem. Eur. J.* **2017**, *23*, 16957–16960.

[150] X. Fang, P. Kögerler, Y. Furukawa, M. Speldrich, M. Luban, *Angew. Chem. Int. Ed.* **2011**, *50*, 5212–5216.

[151] K. Y. Monakhov, W. Bensch, P. Kögerler, *Chem. Soc. Rev.* **2015**, *44*, 8443–8483.

[152] J. L. Ferreira da Silva, M. Fátima Minas da Piedade, M. Teresa Duarte, *Inorg. Chim. Acta* **2003**, *356*, 222–242.

[153] G. K. Johnson, E. O. Schlemper, *J. Am. Chem. Soc.* **1978**, *100*, 3645–3646.

[154] A. Müller, E. Krickemeyer, M. Penk, H.-J. Walberg, H. Bögge, *Angew. Chem. Int. Ed. Engl.* **1987**, *26*, 1045–1046.

[155] L. Zhang, W. Schmitt, *J. Am. Chem. Soc.* **2011**, *133*, 11240–11248.

[156] J. Tucher, K. Peuntinger, J. T. Margraf, T. Clark, D. M. Guldi, C. Streb, *Chem. Eur. J.* **2015**, *21*, 8716–8719.

[157] J. M. Breen, W. Schmitt, *Angew. Chem. Int. Ed.* **2008**, *47*, 6904–6908.

[158] H.-Y. Guo, X. Zhang, L.-N. Xiao, X.-B. Cui, *Dalton Trans.* **2017**, *46*, 8022–8026.

[159] B. Baytekin, H. T. Baytekin, C. A. Schalley, *Org. Biomol. Chem.* **2006**, *4*, 2825–2841.

[160] F. W. McLafferty, *Science* **1981**, *214*, 280–287.

[161] Z. Qi, T. Heinrich, S. Moorthy, C. A. Schalley, *Chem. Soc. Rev.* **2015**, *44*, 515–531.

[162] a) L. Avram, Y. Cohen, *Chem. Soc. Rev.* **2015**, *44*, 586–602; b) K. Rissanen, *Chem. Soc. Rev.* **2017**.

[163] P. Schuck (Ed.) *Protein reviews, v. 5*, Springer Science + Business Media LLC, Boston, **2007**.

[164] L. Cera, C. A. Schalley, *Chem. Soc. Rev.* **2014**, *43*, 1800–1812.

[165] J. B. Fenn, *Angew. Chem. Int. Ed.* **2003**, *42*, 3871–3894.

[166] L. Konermann, E. Ahadi, A. D. Rodriguez, S. Vahidi, *Anal. Chem.* **2013**, *85*, 2–9.

[167] C. Afonso, R. B. Cole, J.-C. Tabet in *Electrospray and MALDI Mass Spectrometry* (Ed. R. B. Cole), John Wiley & Sons, Hoboken, **2010**.

[168] C. A. Schalley, R. K. Castellano, M. S. Brody, D. M. Rudkevich, G. Siuzdak, J. Rebek Jr., *J. Am. Chem. Soc.* **1999**, *121*, 4568–4579.

[169] C. A. Schalley, J. M. Rivera, T. Martín, J. Santamaría, G. Siuzdak, J. Rebek Jr., *Eur. J. Org. Chem.* **1999**, *1999*, 1325–1331.

[170] K. Yamaguchi, *J. Mass Spectrom.* **2003**, *38*, 473–490.

[171] a) H. Yokoyama, Y. Ueda, D. Fujita, S. Sato, M. Fujita, *Chem. Asian J.* **2015**, *10*, 2292–2295; b) F. J. Rizzuto, J. R. Nitschke, *Nat. Chem.* **2017**; c) Y. Ueda, H. Ito, D. Fujita, M. Fujita, *J. Am. Chem. Soc.* **2017**, *139*, 6090–6093.

[172] D. P. Weimann, C. A. Schalley, *Supramol. Chem.* **2008**, *20*, 117–128.

[173] H. N. Miras, E. F. Wilson, L. Cronin, *Chem. Commun.* **2009**, 1297–1311.

[174] H. N. Miras, L. Cronin in *New Strategies in Chemical Synthesis and Catalysis* (Ed. B. Pignataro), Wiley-VCH, Weinheim, **2012**.

[175] J. M. Cameron, L. Vilà-Nadal, R. S. Winter, F. Iijima, J. C. Murillo, A. Rodríguez-Fortea, H. Oshio, J. M. Poblet, L. Cronin, *J. Am. Chem. Soc.* **2016**, *138*, 8765–8773.

[176] W. Xuan, A. J. Surman, Q. Zheng, D.-L. Long, L. Cronin, *Angew. Chem. Int. Ed.* **2016**, *128*, 12895–12899.

[177] E. d. Hoffmann, V. Stroobant, *Mass spectrometry*. *Principles and applications*, John Wiley & Sons, Chichester, **2006**.

[178] C.-B. Huang, L. Xu, J.-L. Zhu, Y.-X. Wang, B. Sun, X. Li, H.-B. Yang, *J. Am. Chem. Soc.* **2017**, *139*, 9459–9462.

[179] C. A. Ohlin, *Chem. Asian J.* **2012**, *7*, 262–270.

[180] S. Sato, Y. Ishido, M. Fujita, *J. Am. Chem. Soc.* **2009**, *131*, 6064–6065.

[181] Y.-R. Zheng, P. J. Stang, *J. Am. Chem. Soc.* **2009**, *131*, 3487–3489.

[182] D. Fujita, H. Yokoyama, Y. Ueda, S. Sato, M. Fujita, *Angew. Chem. Int. Ed.* **2015**, *54*, 155–158.

[183] M. N. Jackson, M. K. Kamunde-Devonish, B. A. Hammann, L. A. Wills, L. B. Fullmer, S. E. Hayes, P. H.-Y. Cheong, W. H. Casey, M. Nyman, D. W. Johnson, *Dalton Trans.* **2015**, *44*, 16982–17006.

[184] a) C. A. Ohlin, R. Brimblecombe, L. Spiccia, W. H. Casey, *Dalton Trans.* **2009**, 5278–5280; b) S. A. Pelster, B. Weimann, B. B. Schaack, W. Schrader, F. Schüth, *Angew. Chem. Int. Ed.* **2007**, *46*, 6674–6677; c) R. Tagore, H. Chen, R. H. Crabtree, G. W. Brudvig, *J. Am. Chem. Soc.* **2006**, *128*, 9457–9465; d) A. F. Panasci, J. G. McAlpin, C. A. Ohlin, S. Christensen, J. C. Fettinger, R. D. Britt, J. R. Rustad, W. H. Casey, *Geochim. Cosmochim. Acta* **2012**, *78*, 18–27; e) P. P. Pescarmona, M. E. Raimondi, J. Tetteh, B. McKay, T. Maschmeyer, *J. Phys. Chem. A* **2003**, *107*, 8885–8892.

[185] P. Roesch, U. Warzok, M. Enke, R. Müller, C. Schattenberg, C. A. Schalley, M. Kaupp, T. Braun, P. Wittwer, *Chem. Eur. J.* **2017**, *23*, 13964–13972.

[186] M. Wang, C. Wang, X.-Q. Hao, X. Li, T. J. Vaughn, Y.-Y. Zhang, Y. Yu, Z.-Y. Li, M.-P. Song, H.-B. Yang, X. Li, *J. Am. Chem. Soc.* **2014**, *136*, 10499–10507.

[187] S. P. Black, D. M. Wood, F. B. Schwarz, T. K. Ronson, J. J. Holstein, A. R. Stefankiewicz, C. A.

Schalley, J. K. M. Sanders, J. R. Nitschke, *Chem. Sci.* **2016**, *7*, 2614–2620.

[188] a) P. Bussian, F. Sobott, B. Brutschy, W. Schrader, F. Schüth, *Angew. Chem. Int. Ed.* **2000**, *39*, 3901–3905; b) K. Eggers, T. Eichner, J. Woenckhaus, *Int. J. Mass Spectrom.* **2005**, *244*, 72–75; c) M. Martin-Sabi, R. S. Winter, C. Lydon, J. M. Cameron, D.-L. Long, L. Cronin, *Chem. Commun.* **2016**, *52*, 919–921; d) J.-H. Son, W. H. Casey, *Chem. Commun.* **2015**, *51*, 1436–1438; e) Q. Zheng, L. Vilà-Nadal, C. Busche, J. S. Mathieson, D.-L. Long, L. Cronin, *Angew. Chem. Int. Ed.* **2015**, *54*, 7895–7899.

[189] Q. Jia, J. Cao, Y. Duan, C. Hu, *Dalton Trans.* **2015**, *44*, 553–559.

[190] H. N. Miras, M. Sorus, J. Hawkett, D. O. Sells, E. J. L. McInnes, L. Cronin, *J. Am. Chem. Soc.* **2012**, *134*, 6980–6983.

[191] A. Kiesilä, L. Kivijärvi, N. K. Beyeh, J. O. Moilanen, M. Groessl, T. Rothe, S. Götz, F. Topić, K. Rissanen, A. Lützen, E. Kalenius, *Angew. Chem. Int. Ed.* **2017**, *56*, 10942–10946.

[192] a) J. Cernochová, P. Branná, M. Rouchal, P. Kulhánek, I. Kuřitka, R. Vícha, *Chem. Eur. J.* **2012**, *18*, 13633–13637; b) C. A. Schalley, *Mass Spectrom. Rev.* **2001**, *20*, 253–309.

[193] a) M. Ceborska, M. Zimnicka, A. A. Kowalska, K. Dąbrowa, B. Repeć, *Beilstein J. Org. Chem* **2017**, *13*, 2252–2263; b) R. Zadmard, A. Kraft, T. Schrader, U. Linne, *Chem. Eur. J.* **2004**, *10*, 4233–4239.

[194] P. Weis, U. Schwarz, F. Hennrich, D. Wagner, S. Bräse, M. Kappes, *Phys. Chem. Chem. Phys.* **2014**, *16*, 6225–6232.

[195] K. Ono, M. Yoshizawa, T. Kato, M. Fujita, *Chem. Commun.* **2008**, 2328–2330.

[196] a) H. N. Miras, D. Stone, D.-L. Long, E. J. L. McInnes, P. Kögerler, L. Cronin, *Inorg. Chem.* **2011**, *50*, 8384–8391; b) L. Vilà-Nadal, S. G. Mitchell, A. Rodríguez-Fortea, H. N. Miras, L. Cronin, J. M. Poblet, *Phys. Chem. Chem. Phys.* **2011**, *13*, 20136–20145; c) L. Vilà-Nadal, E. F. Wilson, H. N. Miras, A. Rodríguez-Fortea, L. Cronin, J. M. Poblet, *Inorg. Chem.* **2011**, *50*, 7811–7819.

[197] H. D. F. Winkler, E. V. Dzyuba, J. A. W. Sklorz, N. K. Beyeh, K. Rissanen, C. A. Schalley, *Chem. Sci.* **2011**, *2*, 615–624.

[198] S. Feyel, D. Schröder, H. Schwarz, *Eur. J. Inorg. Chem.* **2008**, *2008*, 4961–4967.

[199] S. M. Lang, I. Fleischer, T. M. Bernhardt, R. N. Barnett, U. Landman, *J. Phys. Chem. C* **2015**, *119*, 10881–10887.

[200] F. Lanucara, S. W. Holman, C. J. Gray, C. E. Eyers, *Nat. Chem.* **2014**, *6*, 281–294.

[201] http://blog.waters.com/whats-the-big-deal-about-ion-mobility-mass-spectrometry. [14.12.2017].

[202] a) M. Zhou, V. H. Wysocki, *Acc. Chem. Res.* **2014**, *47*, 1010–1018; b) M. Göth, K. Pagel, *Anal. Bioanal. Chem.* **2017**, *409*, 4305–4310; c) Z. Hall, A. Politis, M. F. Bush, L. J. Smith, C. V. Robinson, *J. Am. Chem. Soc.* **2012**, *134*, 3429–3438.

[203] C. Uetrecht, R. J. Rose, E. van Duijn, K. Lorenzen, A. J. R. Heck, *Chem. Soc. Rev.* **2010**, *39*, 1633–1655.

[204] E. S. Baker, B. H. Clowers, F. Li, K. Tang, A. V. Tolmachev, D. C. Prior, M. E. Belov, R. D. Smith, *J. Am. Soc. Mass Spectrom.* **2007**, *18*, 1176–1187.

[205] a) P. R. Kemper, N. F. Dupuis, M. T. Bowers, *Int. J. Mass Spectrom.* **2009**, *287*, 46–57;

b) S. Warnke, C. Baldauf, M. T. Bowers, K. Pagel, G. von Helden, *J. Am. Chem. Soc.* **2014**, *136*, 10308–10314.

[206] S. Warnke, J. Seo, J. Boschmans, F. Sobott, J. H. Scrivens, C. Bleiholder, M. T. Bowers, S. Gewinner, W. Schöllkopf, K. Pagel, G. v. Helden, *J. Am. Chem. Soc.* **2015**, *137*, 4236–4242.

[207] J. Hofmann, W. B. Struwe, C. A. Scarff, J. H. Scrivens, D. J. Harvey, K. Pagel, *Anal. Chem.* **2014**, *86*, 10789–10795.

[208] a) E. Jurneczko, J. Kalapothakis, I. D. G. Campuzano, M. Morris, P. E. Barran, *Anal. Chem.* **2012**, *84*, 8524–8531; b) E. Waraksa, U. Perycz, J. Namieśnik, M. Sillanpää, T. Dymerski, M. Wójtowicz, J. Puton, *Trends Anal. Chem.* **2016**, *82*, 237–249; c) P. M. Lalli, Y. E. Corilo, M. Fasciotti, M. F. Riccio, G. F. de Sa, R. J. Daroda, G. H. M. F. Souza, M. McCullagh, M. D. Bartberger, M. N. Eberlin, I. D. G. Campuzano, *J. Mass Spectrom.* **2013**, *48*, 989–997.

[209] E. R. Brocker, S. E. Anderson, B. H. Northrop, P. J. Stang, M. T. Bowers, *J. Am. Chem. Soc.* **2010**, *132*, 13486–13494.

[210] a) E. S. Baker, J. E. Bushnell, S. R. Wecksler, M. D. Lim, M. J. Manard, N. F. Dupuis, P. C. Ford, M. T. Bowers, *J. Am. Chem. Soc.* **2005**, *127*, 18222–18228; b) G. Carroy, V. Lemaur, C. Henoumont, S. Laurent, J. de Winter, E. de Pauw, J. Cornil, P. Gerbaux, *J. Am. Soc. Mass Spectrom.* **2018**, *29*, 121–132; c) G. Carroy, C. Daxhelet, V. Lemaur, J. de Winter, E. de Pauw, J. Cornil, P. Gerbaux, *Chem. Eur. J.* **2016**, *22*, 4528–4534; d) J.-F. Greisch, K. Y. Amsharov, J. Weippert, P. Weis, A. Böttcher, M. M. Kappes, *J. Am. Chem. Soc.* **2016**, *138*, 11254–11263; e) I. Czerwinska, A. Kulesza, C. Choi, F. Chirot, A.-L. Simon, J. Far, C. Kune, E. de Pauw, P. Dugourd, *Phys. Chem. Chem. Phys.* **2016**, *18*, 32331–32336; f) H. H. L. Lee, H. I. Kim, *Isr. J. Chem.* **2017**, doi:10.1002/ijch.201700073; g) T.-C. Lee, E. Kalenius, A. I. Lazar, K. I. Assaf, N. Kuhnert, C. H. Grün, J. Jänis, O. A. Scherman, W. M. Nau, *Nat. Chem.* **2013**, *5*, 376–382; h) K. Nowosinski, S. Warnke, K. Pagel, D. Komáromy, W. Jiang, C. A. Schalley, *J. Mass Spectrom.* **2016**, *51*, 269–281; i) A. Troć, J. Gajewy, W. Danikiewicz, M. Kwit, *Chem. Eur. J.* **2016**, *22*, 13258–13264; j) L. H. Urner, B. N. S. Thota, O. Nachtigall, S. Warnke, G. von Helden, R. Haag, K. Pagel, *Chem. Commun.* **2015**, *51*, 8801–8804; k) M. Petryk, A. Troć, B. Gierczyk, W. Danikiewicz, M. Kwit, *Chem. Eur. J.* **2015**, *21*, 10318–10321.

[211] Z. Zhang, H. Wang, X. Wang, Y. Li, B. Song, O. Bolarinwa, R. A. Reese, T. Zhang, X.-Q. Wang, J. Cai, B. Xu, M. Wang, C. Liu, H.-B. Yang, X. Li, *J. Am. Chem. Soc.* **2017**, *139*, 8174–8185.

[212] X. Li, Y.-T. Chan, G. R. Newkome, C. Wesdemiotis, *Anal. Chem.* **2011**, *83*, 1284–1290.

[213] a) W. Zhang, A. Abdulkarim, F. E. Golling, H. J. Räder, K. Müllen, *Angew. Chem. Int. Ed.* **2017**, *129*, 2689–2692; b) Y.-T. Chan, X. Li, M. Soler, J.-L. Wang, C. Wesdemiotis, G. R. Newkome, *J. Am. Chem. Soc.* **2009**, *131*, 16395–16397.

[214] a) S. Chakraborty, W. Hong, K. J. Endres, T.-Z. Xie, L. Wojtas, C. N. Moorefield, C. Wesdemiotis, G. R. Newkome, *J. Am. Chem. Soc.* **2017**, *139*, 3012–3020; b) J. W. Purcell, H. N. Miras, D.-L. Long, P. Markopoulou, L. Cronin, *Chem. Eur. J.* **2017**, *23*, 9683–9689; c) O. Jurček, P. Bonakdarzadeh, E. Kalenius, J. M. Linnanto, M. Groessl, R. Knochenmuss, J. A. Ihalainen, K. Rissanen, *Angew. Chem. Int. Ed.* **2015**, *54*, 15462–15467.

[215] a) Y. Li, Z. Jiang, M. Wang, J. Yuan, D. Liu, X. Yang, M. Chen, J. Yan, X. Li, P. Wang, *J. Am. Chem. Soc.* **2016**, *138*, 10041–10046; b) C. Wang, X.-Q. Hao, M. Wang, C. Guo, B. Xu, E. N. Tan, Y.-Y. Zhang, Y. Yu, Z.-Y. Li, H.-B. Yang, M.-P. Song, X. Li, *Chem. Sci.* **2014**, *5*, 1221–1226; c) J. Ujma, M. de Cecco, O. Chepelin, H. Levene, C. Moffat, S. J. Pike, P. J. Lusby, P. E. Barran, *Chem. Commun.* **2012**, *48*, 4423–4425.

[216] L. G. Christie, A. J. Surman, R. A. Scullion, F. Xu, D.-L. Long, L. Cronin, *Angew. Chem. Int. Ed.* **2016**, *55*, 12741–12745.

[217] P. J. Robbins, A. J. Surman, J. Thiel, D.-L. Long, L. Cronin, *Chem. Commun.* **2013**, *49*, 1909–1911.

[218] A. M. Todea, J. Szakács, S. Konar, H. Bögge, D. C. Crans, T. Glaser, H. Rousselière, R. Thouvenot, P. Gouzerh, A. Müller, *Chem. Eur. J.* **2011**, *17*, 6635–6642.

[219] E. Hanozin, B. Mignolet, D. Morsa, D. Sluysmans, A.-S. Duwez, J. F. Stoddart, F. Remacle, E. de Pauw, *ACS nano* **2017**, *11*, 10253–10263.

[220] O. Dumele, B. Schreib, U. Warzok, N. Trapp, C. A. Schalley, F. Diederich, *Angew. Chem. Int. Ed.* **2017**, *56*, 1152–1157.

[221] L. Turunen, U. Warzok, R. Puttreddy, N. K. Beyeh, C. A. Schalley, K. Rissanen, *Angew. Chem. Int. Ed.* **2016**, *55*, 14033–14036.

[222] L. Turunen, U. Warzok, C. A. Schalley, K. Rissanen, *Chem* **2017**, *3*, 861–869.

[223] U. Warzok, M. Marianski, W. Hoffmann, L. Turunen, K. Rissanen, K. Pagel, C. A. Schalley, *Chem. Sci.* **2018**, Accepted Manuscript; DOI: 10.1039/C8SC03040E.

[224] M. Wendt, U. Warzok, C. Näther, J. van Leusen, P. Kögerler, C. A. Schalley, W. Bensch, *Chem. Sci.* **2016**, *7*, 2684–2694.

[225] L. K. Mahnke, A. Kondinski, U. Warzok, C. Näther, J. van Leusen, C. Schalley, K. Y. Monakhov, P. Kögerler, W. Bensch, *Angew. Chem. Int. Ed.* **2018**, *57*, 2972–2975.

[226] L. K. Mahnke, U. Warzok, M. Lin, C. Näther, C. A. Schalley, W. Bensch, *Chem. Eur. J.* **2018**, *24*, 5522–5528.

[227] M. Wendt, P. Polzin, J. van Leusen, C. Näther, P. Kögerler, W. Bensch, *Dalton Trans.* **2017**, *46*, 1618–1623.

[228] M. Wendt, L. K. Mahnke, N. Heidenreich, W. Bensch, *Eur. J. Inorg. Chem.* **2016**, *2016*, 5393–5398.

[229] M. Wendt, C. Näther, W. Bensch, *Chem. Eur. J.* **2016**, *22*, 7747–7751.

[230] S. Chakraborty, S. Saha, L. M. P. Lima, U. Warzok, S. Sarkar, B. Akhuli, M. Nandi, S. Bej, N. N. Adarsh, C. A. Schalley, R. Delgado, P. Ghosh, *J. Org. Chem.* **2017**, *82*, 10007–10014.

[231] a) J. Barluenga, J. M. Alvarez-Gutiérrez, A. Ballesteros, J. M. González, *Angew. Chem. Int. Ed.* **2007**, *46*, 1281–1283; b) D. Fischer, H. Tomeba, N. K. Pahadi, N. T. Patil, Y. Yamamoto, *Angew. Chem. Int. Ed.* **2007**, *46*, 4764–4766; c) J. Barluenga, M. Trincado, E. Rubio, J. M. González, *Angew. Chem. Int. Ed.* **2003**, *42*, 2406–2409; d) K. Murai, K. Tateishi, A. Saito, *Org. Biomol. Chem.* **2016**, *14*, 10352–10356.

6. Appendix

6.1. Curriculum Vitae

The curriculum vitae is not available online due to privacy policies.

6.2. Publications

6.2.1. Peer-Review Journal Articles

1) "Surprising solvent-induced structural rearrangements in large [N···I^+···N] halogen-bonded supramolecular capsules: an ion mobility-mass spectrometry study"
U. Warzok, M. Marianski, W. Hoffmann, L. Turunen, K. Rissanen, K. Pagel, C. A. Schalley,
Chem. Sci. **2018**, Accepted Manuscript; DOI: 10.1039/C8SC03040E.

2) "Soluble Hetero-Polyoxovanadates and Their Solution Chemistry Analyzed by Electrospray Ionization Mass Spectrometry"
U. Warzok, L. K. Mahnke, W. Bensch
Chem. Eur. J. **2018**, Accepted Article; DOI: 10.1002/chem.201803291.

3) "The New Water-Soluble Cluster Compound $\{Zn(en)_3\}_3[V_{15}Sb_6O_{42}(H_2O)]$-(ethylenediamine)$_3$-$10H_2O$ as a Synthon for the Generation of two New Antimonato Polyoxovanadates"
L. K. Mahnke, U. Warzok, M. Lin, C. Näther, C.A. Schalley, W. Bensch
Chem. Eur. J. **2018**, *24*, 5522–5528.

4) "Constitutional Isomerism in Polyoxovanadates"
L.K. Mahnke, A. Kondinski, U. Warzok, C. Näther, J. van Leusen, C.A. Schalley, K.Y. Monakhov, P. Kögerler, W. Bensch
Angew. Chem. Int. Ed. **2018**, *57*, 2972–2975;
Angew. Chem. **2018**, *130*, 3024–3028.

5) "Nano-sized $I_{12}L_6$ Molecular Capsules based on the [N···I^+···N] Halogen Bond"
L. Turunen, U. Warzok, C. A.Schalley, K. Rissanen
Chem **2017**, *3*, 861-869.

6) "A Polyamide-Polyamine Cryptand as a New Generation Dicarboxylate Receptor: Di-anion Binding Studies in the Solid State, in Solution, and in the Gas Phase"
S. Chakraborty, S. Saha, L. M. P. Lima, U. Warzok, S. Sarkar, B. Akhuli, M. Nandi, S. Bej, N. N. Adarsh, C. A. Schalley, R. Delgado, P. Ghosh
J. Org. Chem, **2017**, *82*, 10007–10014.

7) "Reactivity of the Sterically Demanding Siloxanediol $Mes_2Si(OH)(\mu\text{-}O)Si(OH)Mes_2$ Towards Water and Ether Molecules"
P. Roesch, U. Warzok, M. Enke, R. Müller, C. Schattenberg, C. A. Schalley, M. Kaupp, T. Braun, P. Wittwer
Chem. Eur. J. **2017**, *23*, 13964–13972.

8) "Efficient Syntheses of 2,5-Dihydropyrroles, Pyrrolidin-3-ones and Electron-Rich Pyrroles from *N*-Tosylimines and Lithiated Alkoxyallenes"

G. M. Okala Amombo, O. Flögel, S. Kord Daoroun Kalai, S. Schoder, U. Warzok, H.-U. Reissig *Eur. J. Org. Chem.* **2017**, 1965–1972.

9) „Halogen-Bonded Supramolecular Capsules in the Solid State, in Solution, and in the Gas Phase“ O. Dumele, B. Schreib, U. Warzok, N. Trapp, C. A. Schalley, F. Diederich *Angew. Chem. Int. Ed.* **2017**, *56*, 1152-1157; *Angew. Chem.* **2017**, *128*, 1172–1177.

10) „[N···I⁺···N] Halogen-Bonded Dimeric Capsules from Tetrakis(3-pyridyl)ethylenecavitands“ L. Turunen, U. Warzok, R. Puttreddy, N. K. Beyeh, C. A.Schalley, K. Rissanen *Angew. Chem. Int. Ed.* **2016**, *55*, 14033 –14036; *Angew. Chem.* **2016**, *128*, 14239–14242.

11) “Small beautiful and magnetically exotic: $\{V_4W_2\}$- and $\{V_4W_4\}$-type polyoxometallates“ M. Rasmussen, C. Näther, J. van Leusen, U. Warzok, C. A. Schalley, P. Kögerler, W. Bensch *Dalton Trans.* **2016**, *45*, 10519–10522.

12) „Catalysis of “outer-phase” oxygen atom exchange reactions by encapsulated “inner-phase” water in $\{V_{15}Sb_6\}$-type polyoxovanadates“ M. Wendt*, U. Warzok*, C. Näther, J. van Leusen, P. Kögerler, C. A. Schalley, W. Bensch *authors contributed equally to this work *Chem. Sci.* **2016**, *7*, 2684–2694.

6.2.2. Talks

1) “Structure and Reactivity of Antimonato Polyoxovanadates in Solution and in the Gas Phase” XXIInd International Mass Spectrometry Conference, Florence, August 28, 2018.

2) “Halogen-Bonded Capsules – The I^+ Approach” Symposium on Supramolecular Chemistry, Berlin, August 17, 2017.

3) “Investigation of Halogen-Bonded Supramolecular Capsules by MS and IM-MS” 6. Berliner Chemie Symposium, Berlin, April 6, 2017.

4) “Investigation of Dimeric and Hexameric Halogen-Bonded Supramolecular Capsules by MS and IM-MS” 50. Jahrestagung der DGMS, Kiel, February 7, 2017.

5) “Investigation of Halogen-Bonded Supramolecular Capsules by Mass Spectrometry and Ion Mobility-Mass Spectrometry” G4 – Joint Meeting on Supramolecular Chemistry, Berlin, September 14, 2016.

6) “Studying solution and gas phase chemistry of oxido clusters by mass spectrometry” CRC 1109 meeting – Understanding Metal Oxo-Water Systems, Berlin, October 9, 2014.

6.2.3. Poster Presentations

1) "Anion-Binding in Halogen-Bonded Capsules and Dynamic Capsule Rearrangement Elucidated by Mass Spectrometry and Ion Mobility"
U. Warzok, M. Marianski, W. Hoffmann, K. Pagel, C. A. Schalley
13th International Symposium on Macrocyclic and Supramolecular Chemistry, July 2018, Quebec City

2) "Large Halogen-Bonded Capsules: Structure and Reactivity Elucidated by Mass Spectrometry and Ion Mobility"
U. Warzok, M. Marianski, W. Hoffmann, K. Pagel, C. A. Schalley
European Mass Spectrometry Conference, Saarbrücken, March 2018.

3) "Microreactor ESI-MS for the investigation of cluster nucleation and growth and their gas phase chemistry"
U. Warzok, C. A. Schalley
CRC 1109 Evaluation, Berlin, September 2017

4) "Investigation of Dimeric and Hexameric Halogen-Bonded Supramolecular Capsules by ESI-MS and IMS"
U. Warzok, M. Marianski, L. Turunen, W. Hoffmann, K. Pagel, K. Rissanen, C. A. Schalley
GDCh Wissenschaftsforum, Berlin, September 2017.

5) "Probing Solution and Gas-phase Reactivity of Silicon-Oxo and Metal-Oxo Complexes by Means of Mass Spectrometry"
U. Warzok, C. A. Schalley
International Symposium of the CRC 1109: Metal Oxide – Water Systems, Berlin, February 2017

6) "Investigation of halogen-bonded supramolecular capsules by ESI-MS and TW-IMS"
U. Warzok, L. Turunen, R. Puttreddy, K. Rissanen, C. A. Schalley
21st International Mass Spectrometry Conference, Toronto, August 2016.

7) "Water makes the difference – Studies on gas phase and solution reactivity of antimonato polyoxovanadate clusters by ESI-MS"
Ulrike Warzok, Christoph A. Schalley
CRC 1109 Summer School: Strategies for the Synthesis and the Characterization of Metal Oxides, Berlin, September 2015

6.3. Prints of the Published Works

6.3.1. Halogen-Bonded Supramolecular Capsules in the Solid State, in Solution, and in the Gas Phase

Oliver Dumele, Benedikt Schreib, Ulrike Warzok, Nils Trapp, Christoph A. Schalley, and François Diederich

Angew. Chem. Int. Ed. **2017**, *56*, 1152–1157; *Angew. Chem.* **2017**, *128*, 1172–1177.

Submitted on November 7, 2016, first published on January, 13 2017 in Angewandte Chemie International Edition and Angewandte Chemie in German language.

Electronic versions of the article are available (https://doi.org/10.1002/anie.201610884, https://doi.org/10.1002/ange.201610884).

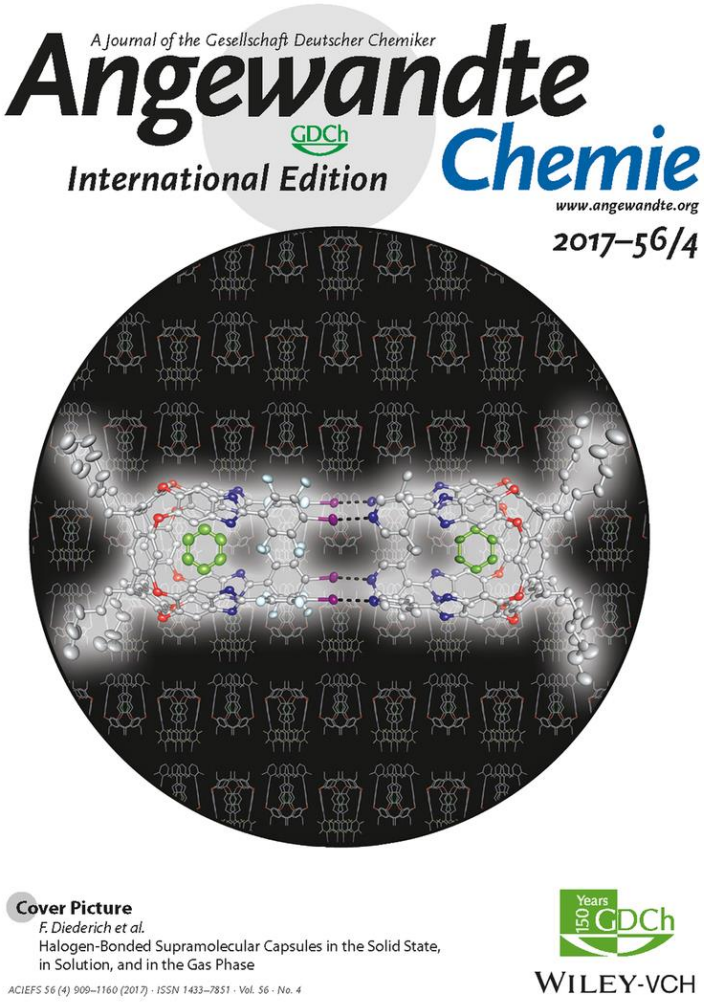

Figure A.1: Cover picture. Reprinted with permission from Dumele *et al.*[220] (© 2017 Wiley-VCH Verlag GmbH & Co. KGaA, Weinheim).

A copy of the original work is not included in the online version due to restrictions by the publisher.

6.3.2. [N···I⁺···N] Halogen-Bonded Dimeric Capsules from Tetrakis(3-pyridyl)ethylene-cavitands

Lotta Turunen, Ulrike Warzok, Rakesh Puttreddy, Ngong Kodiah Beyeh, Christoph A.Schalley, Kari Rissanen

Angew. Chem. Int. Ed. **2016**, *55*, 14033–14036; *Angew. Chem.* **2016**, *128*, 14239–14242.

Submitted on August 10, 2016, first published on October 28, 2016 in Angewandte Chemie International Edition and Angewandte Chemie.

Electronic versions of the article are available (https://doi.org/10.1002/anie.201607789, https://doi.org/10.1002/ange.201607789).

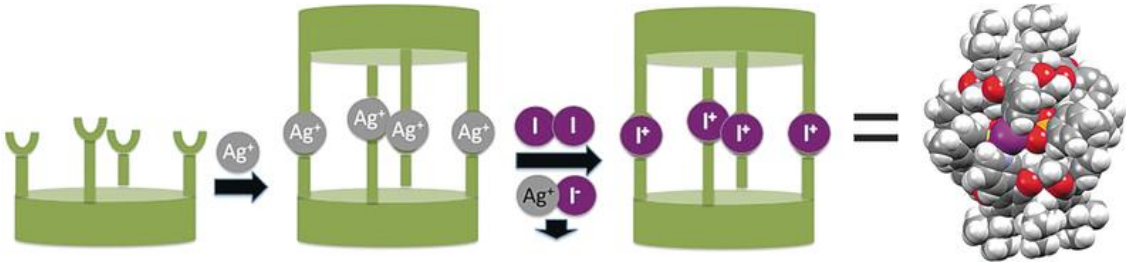

Figure A.2: Graphical abstract. Reprinted with permission from Turunen *et al.*[221] (© 2016 Wiley-VCH Verlag GmbH & Co. KGaA, Weinheim).

A copy of the original work is not included in the online version due to restrictions by the publisher.

6.3.3. Nano-sized $I_{12}L_6$ Molecular Capsules based on the [N···I^+···N] Halogen Bond

Lotta Turunen, Ulrike Warzok, Christoph A.Schalley, Kari Rissanen

Chem **2017**, *3*, 861–869.

Submitted on May 29, 2017, first published on November 9, 2017 in Chem.

An electronic version of the article is available (https://doi.org/10.1016/j.chempr.2017.08.010).

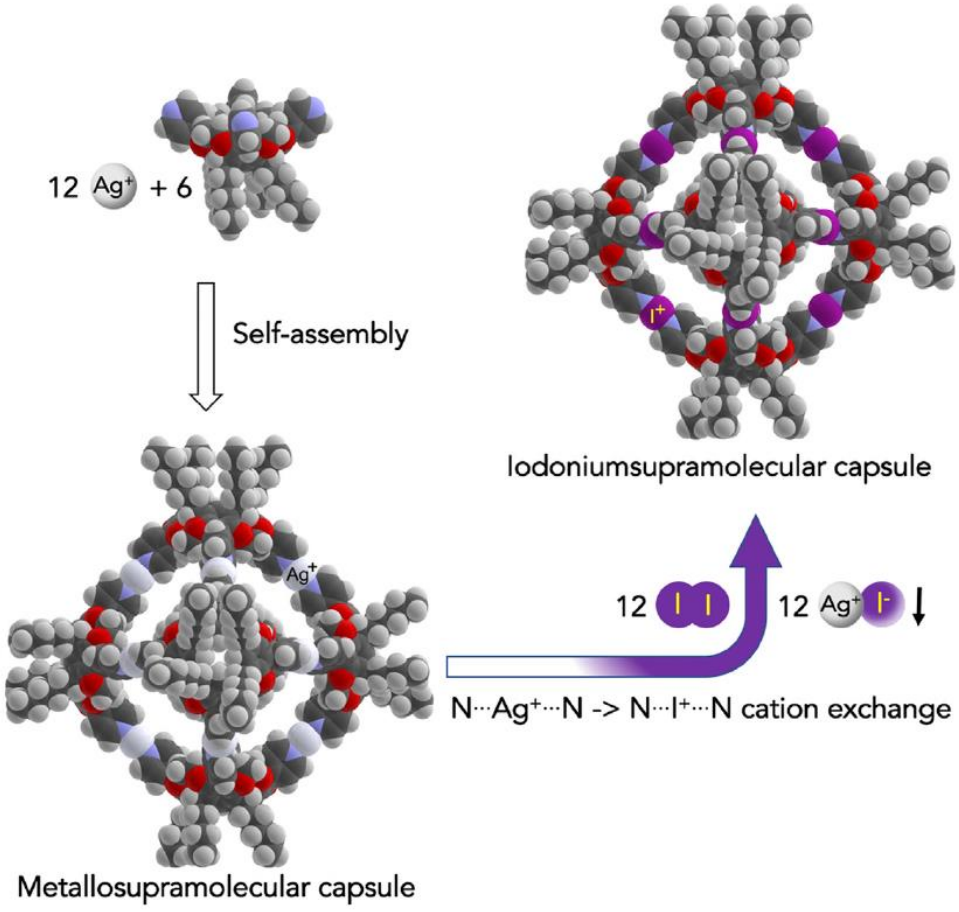

Figure A.3: Graphical abstract. Reprinted with permission from Turunen *et al*.[222] (© 2017, Elsevier Inc.).

A copy of the original work is not included in the online version due to restrictions by the publisher.

6.3.4. Surprising Solvent-Induced Structural Rearrangements in Large [N···I⁺···N] Halogen-Bonded Supramolecular Capsules: An Ion Mobility-Mass Spectrometry Study

Ulrike Warzok, Mateusz Marianski, Waldemar Hoffmann, Lotta Turunen, Kari Risannen, Kevin Pagel, and Christoph A. Schalley.

Chem. Sci. **2018**, Accepted Manuscript, DOI: 10.1039/C8SC03040E.

Submitted on July 09, 2018, first published on September 05, 2018 in Chemical Science. Reprinted with permission from Warzok *et al.*[223] (Published by The Royal Society of Chemistry).

An electronic version of the article is available (http://doi.org/10.1039/C8SC03040E).

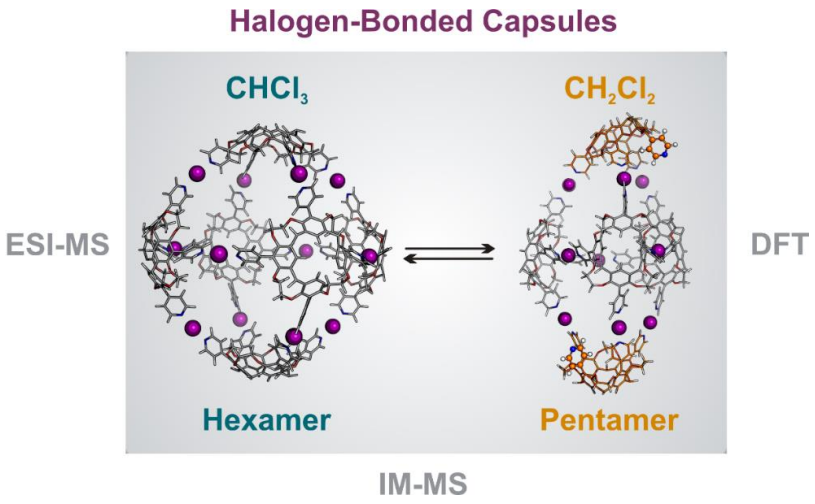

Figure A.4: Graphical abstract. Reproduced from Warzok *et al.*[223] (Published by The Royal Society of Chemistry).

Chemical Science

Accepted Manuscript

This article can be cited before page numbers have been issued, to do this please use: U. Warzok, M. Marianski, W. Hoffmann, L. Turunen, K. Rissanen, K. Pagel and C. A. Schalley, *Chem. Sci.*, 2018, DOI: 10.1039/C8SC03040E.

ROYAL SOCIETY OF CHEMISTRY

rsc.li/chemical-science

View Article Online
DOI: 10.1039/C8SC03040E

Chemical Science

EDGE ARTICLE

Surprising solvent-induced structural rearrangements in large [N···I⁺···N] halogen-bonded supramolecular capsules: an ion mobility-mass spectrometry study

Received 00th January 20xx,
Accepted 00th January 20xx

DOI: 10.1039/x0xx00000x

www.rsc.org/

Ulrike Warzok,[a] Mateusz Marianski,[b,†] Waldemar Hoffmann,[a,b] Lotta Turunen,[c] Kari Rissanen,[c] Kevin Pagel,[a,b] and Christoph A. Schalley[a,d,*]

Coordinative halogen bonds have recently gained interest for the assembly of supramolecular capsules. Ion mobility-mass spectrometry and theoretical calculations now reveal the well-defined gas-phase structures of dimeric and hexameric [N···I⁺···N] halogen-bonded capsules with counterions located inside their cavities as guests. The solution reactivity of the large hexameric capsule shows the intriguing solvent-dependent equilibrium between the hexamer and an unprecedented pentameric [N···I⁺···N] halogen-bonded capsule, when the solvent is changed from chloroform to dichloromethane. The intrinsic flexibility of the cavitands enables this novel structure to adopt a pseudo-trigonal bipyramidal geometry with nine [N···I⁺···N] bonds along the edges and two pyridine binding sites uncomplexed.

Introduction

Supramolecular capsules have attracted continuous attention since Rebek introduced his famous hydrogen-bonded "tennis ball" in 1993.[1] A plethora of examples have been described in the literature, which feature a broad range of different binding motifs such as hydrogen bonding,[2] metal coordination,[3] ion-pair interactions[4], or more recently, halogen bonding.[5,6–8] Among these interactions, the strength and directionality of the halogen bond (XB) renders it exceptionally promising for the development of novel, structurally well-defined supramolecular complexes.[9]

The halogen bond is a noncovalent interaction between a polarized halogen atom and a Lewis base.[10] Positively charged iodonium ions are a special case of XB donor, as they can bind two Lewis bases in a three-center-four-electron bond.[11,12] Since these two Lewis bases can be identical, building block synthesis for larger supramolecular assemblies is more easily achieved, as no attention needs to be paid to complementary couples of matching XB donors and acceptors. This renders iodonium ions excellent synthons for the self-assembly of novel supramolecular capsules.[6,7,13]

The structural analysis of large supramolecular capsules,[14] as well as the investigation of their dynamic rearrangements in condensed phase are challenging.[15,16] Self-assembly and self-sorting processes can be very fast, produce transient intermediates, or numerous products of low abundance. Standard condensed phase techniques, such as NMR, often struggle to provide information on the composition of these mixtures due to substantial signal superposition or fast dynamic processes averaging the signal positions. Moreover, the ability to target individual complexes in the mixture to conduct a detailed structural analysis is limited. However, these analytical shortcomings can be readily overcome by complementary gas-phase techniques.[17]

Electrospray ionization (ESI) is a soft ionization method capable of transferring even large noncovalent complexes from solution into the gas phase with minimal to no fragmentation.[18] The transfer of ions into the gas phase interrupts the operation of underlying solution equilibria, thereby enabling their separation and subsequent analysis. Mass spectrometry (MS) offers a range of gas-phase experiments to investigate the structure and reactivity of a mass-selected ion of interest.[19] Moreover, traditional MS experiments can be augmented with orthogonal separation techniques such as ion mobility spectrometry (IMS), which adds another dimension by separating analytes beyond their mass-to-charge (m/z) ratio. In a drift tube IMS (DT-IMS) experiment, ions are guided by a weak electric field through a drift tube filled with an inert buffer gas typically at pressures of a few millibars. During their migration, more extended ions are decelerated by a larger number of collisions with the buffer gas than compact ions of the same m/z and, as a result, leave the IMS cell after longer drift times. Consequently, the combination of IMS and MS to ion mobility-mass spectrometry

[a] Institut für Chemie und Biochemie, Freie Universität Berlin, Takustraße 3, 14195 Berlin, Germany. E-mail: c.schalley@fu-berlin.de
[b] Fritz-Haber-Institut der Max-Planck-Gesellschaft, Faradayweg 4-6, 14195 Berlin, Germany
[c] Department of Chemistry, NanoScience Center, University of Jyvaskyla, P.O. Box 35, 40014 Jyväskylä, Finland
[d] School of Life Sciences, Northwestern Polytechnical University, 127 Youyi Xilu, Xi'an, Shaanxi 710072, P. R. China
† Currently at Hunter College, The City University of New York
Electronic Supplementary Information (ESI) available: [details of any supplementary information available should be included here]. See DOI: 10.1039/x0xx00000x

(IM-MS) accomplishes ion separation not only based on their *m/z*, but also differences in charge, size, and shape.[20] The drift time of an ion can be further converted to a collision cross section (CCS), which represents an intrinsic molecular property independent from instrumental parameters.[21,22] Comparison of CCS values to reference experimental or theoretical values can provide quite detailed insight into the molecular structure. Hence, the characterization of supramolecular complexes in solution can largely benefit from gas-phase techniques such as MS and IMS.[23]

Theoretical modelling of large supramolecular complexes presents challenges due to their size and delicate balance of various forces governing their stability. Grimme *et al.* presented quantum chemical calculations on a neutral halogen-bonded, heterodimeric capsule using semi-empirical methods tailored for the treatment of such systems.[24] Alternatively, composite methods, in which a more advanced quantum-mechanical treatment of the XB can be combined with a lower level of theory for the remaining framework of the capsules,[25] offer a feasible solution to study larger complexes.

Recently, we reported the synthesis and characterization of dimeric and hexameric halogen-bonded capsules self-assembling from the different pyridyl-substituted resorcin[4]arene cavitands **C_D** and **C_H** and positively charged iodonium ions through coordinative [N···I⁺···N] halogen bonds (Scheme 1).[6,7] Their syntheses follow a two-step protocol. First, the cavitands are reacted with silver(I) *p*-toluenesulfonate to yield the Ag(I)-containing capsules. Then, a reaction with molecular iodine leads to an [N···Ag⁺···N] → [N···I⁺···N] exchange reaction. The halogen-bonded capsules were characterized by NMR and diffusion ordered spectroscopy (DOSY), together with preliminary MS experiments.

Here, we focus on a detailed structural analysis of dimeric and hexameric halogen-bonded capsules **1** and **2** in the gas phase (Scheme 1). Collision cross sections derived from DT-IM-MS measurements in helium buffer gas ($^{DT}CCS_{He}$) were compared with theoretical values obtained from structures optimized with composite density-functional theory (DFT) and semi-empirical calculations. The calculations confirm formation of highly regular complexes and provide insights into their anion-guest binding behaviour. We furthermore observe a selective, solvent-dependent rearrangement of the hexamer into new pentameric halogen-bonded capsules **3** upon a rather subtle change of the solvent from chloroform to dichloromethane. The capsules are thus responsive to a chemical stimulus. The novel structure has been identified to exhibit an unusual pseudo-trigonal bipyramidal geometry with nine [N···I⁺···N] bonds along the edges and two pyridines uncomplexed.

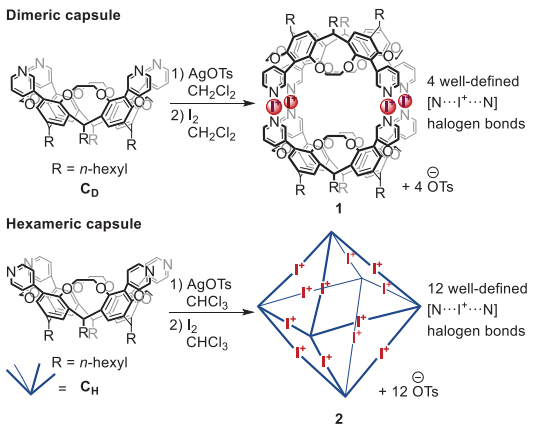

Scheme 1. Assembly of dimeric and hexameric halogen-bonded capsules **1** and **2**.

Material and methods

Sample Preparation

For the assembly of the [N···I⁺···N] halogen-bonded dimeric capsule **1**, the hexameric capsule **2**, and the pentameric capsule **3** (1 mM), a solution of the corresponding cavitand **C_D** (for **1**, 1 eq.) or **C_H** (for **2** and **3**, 1 eq.) was first mixed with AgOTs (2.0 eq.), stirred for 1 h and subsequently treated with I_2 (2.5 eq.), stirred for 20 min and centrifuged to remove precipitated AgI from the mixture. Dimeric and pentameric capsules (**1**, **3**) were assembled and investigated using dichloromethane as the reaction and electrospray solvent; for the hexameric capsule **2**, chloroform was used instead.[6,7]

Electrospray Ionization Mass Spectrometry

Positive-mode electrospray ionization quadrupole-time-of-flight high resolution mass spectrometric (ESI-Q-TOF-HRMS) experiments were performed with a Synapt G2-S HDMS (Waters Co., Milford, MA, USA) instrument. The following settings were used: flow rate 5-10 µL min^{-1}, capillary voltage 3.3 kV, sample cone voltage 40 V, source offset 80 V, source temperature 90 °C, desolvation temperature 250 °C, nebulizer gas 6 bar, desolvation gas flow 500 Lh^{-1}. For collision-induced dissociation (CID), N_2 was used as the collision gas. Fragmentation experiments were conducted in the trap cell of the Synapt G2-S HDMS instrument with collision energies of 2-25 V. Data acquisition and processing was carried out using MassLynxTM (version 4.1).

Drift Tube Ion Mobility-Mass Spectrometry

Measurements to obtain experimental collision cross sections ($^{DT}CCS_{He}$) have been conducted on an in-house-constructed DT-IM-MS instrument (iMob), which is described in detail elsewhere.[26] Briefly, ions are generated using a *nano*-electrospray ionization (*n*ESI) source and subsequently pulsed into an ion mobility cell in which they travel under the influence of a weak electric field (10-15 Vcm^{-1}) through helium buffer gas (~ 5 mbar). After ion separation in the ion mobility cell, the ions of interest are *m/z*-selected using a quadrupole mass filter and their arrival time distributions (ATDs) are recorded by measuring their time-dependent ion current. ATDs have been recorded at six different drift voltages (950 – 1,200 V) and were fitted by Gaussian functions. The center of each Gaussian corresponds to the drift time of a single species and is further converted into a $^{DT}CCS_{He}$ using the Mason-Schamp equation.[21,22]

DOI: 10.1039/C8SC03040E

Theoretical Calculations

The size of the capsules under consideration prohibits full treatment at the density-functional theory level. To decrease the computational effort while maintaining the quantum mechanical description of the halogen bond, the multilayered ONIOM method was used as implemented in the Gaussian09 rev.D01 code.[27] The DFT level of theory has been applied to the iodonium ions, the pyridine groups and the tosylate counterions (see Figure 2), while the cavitand scaffold was described with the semi-empirical AM1 method.[28]

To choose a suitable exchange-correlation density functional, we first evaluated the performance of commonly used methods on the [pyridine···I⁺···pyridine] model system. The structure has been optimized at the MP2 level of theory with a def2-TZVP basis set and the binding energy has been calculated. Next, the binding energy of various functionals in def2-type[29] basis sets were computed (see Supporting Information, Table S1) and compared with MP2/def2-QZVPP single-point energies. Among the tested methods, the PBE0[30] hybrid exchange-correlation functional in a small def2-SVP basis set yields a small absolute error of 8.8 kJ·mol^{-1} which promises a good balance between accuracy and tractability of calculations. Moreover, the comparison of geometric parameters of the [pyridine···I⁺···pyridine] model system optimized at the PBE0/def2-SVP level of theory with the corresponding MP2-optimized complex resulted only in very minor geometrical differences. Hereafter, we will refer to the ONIOM(PBE0/def2-SVP:AM1) method used in this work simply as DFT/AM1.

The theoretical collision cross sections $^{TM}CCS_{He}$ were calculated using a trajectory method, as implemented in the Mobcal program.[31] We used a uniform charge model for all atoms and adopted silicon parameters for the iodonium ions.

All calculated structures were optimized with the *n*-hexyl sidechains in a fully extended zigzag conformation. The CCS values derived from such arbitrary structures are likely to be overestimated by some constant increment per cavitand associated with the flexibility of the side chains. Therefore, we introduced a correction which was estimated as follows: A short molecular dynamics simulation was performed for a dimeric capsule for which the halogen-bonds were constrained to equilibrium bond lengths and angles, as derived from the [pyridine···I⁺···pyridine] model.[32] Next, we extracted 30 random snapshots which featured *n*-hexyl chains in diverse orientations. The *n*-hexyl dihedral angles were translated to a pre-optimized capsule and the structure was again reoptimized at the DFT/AM1 level of theory. The geometry-optimized structures, which span several kJ·mol^{-1} energy range, exhibit CCS values between 560 and 590 Å^2 (see Supporting Information, Figure S9) with a mean of approximately 575 Å^2, significantly below the 610 Å^2 calculated for a dimer with fully extended side chains. To account for this inherent flexibility of the *n*-hexyl chains, we corrected all reported $^{TM}CCS_{He}$ values by an increment of (610 Å^2 – 575 Å^2)/2 cavitands ≈ 20 Å^2/cavitand.

Results and discussion

Structural analysis of halogen-bonded dimeric and hexameric capsules in the gas phase

Dimeric capsule

A dichloromethane solution of dimeric [N···I⁺···N] halogen-bonded capsule **1** was electrosprayed and the ions were transferred into a DT-IM-MS instrument. The ATDs of the capsule-derived ions all feature a single narrow and Gaussian-shaped peak. The two most prominent peaks in the mass spectrum correspond to intact capsules in two different charge states with one and two tosylates ([2·**C$_D$**+4I+OTs]$^{3+}$ and [2·**C$_D$**+4I+2·OTs]$^{2+}$). Both ions exhibit virtually identical $^{DT}CCS_{He}$ values of 558 and 557 Å^2, respectively (Figure 1). This clearly indicates the tosylate anions to be located inside the capsule's cavity, as a clear size difference between the +2 and +3 charge states would be expected if one or both counterions would bind to the outer periphery.

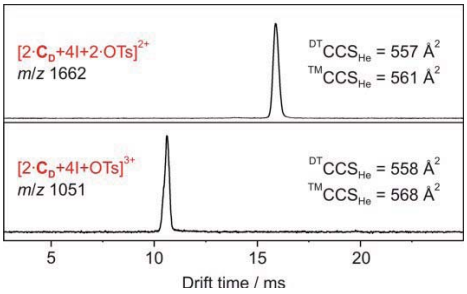

Fig. 1. DT-IM-MS ATDs of ions derived from dimeric halogen-bonded capsule **1**. Experimental $^{DT}CCS_{He}$ and theoretical $^{TM}CCS_{He}$ values are given.

The optimized structure of the empty dimeric halogen-bonded capsule (Figure 2a) reveals a slight helical twist of the two cavitands against each other to allow the formation of four linear [N···I⁺···N] bonds with an equilibrium N···I⁺ distance of 2.28 Å. The twist between two capsules is significantly smaller than that observed in the previously reported crystal structure for the silver-coordinated precursor capsule.[6] The smaller twist can be attributed to the linearity of the halogen bonds with N-I-N angles close to 180 degrees, whereas the [N···Ag⁺···N] motif adopts an angle of 150-160 degrees.[6,12]

For calculations of capsular complexes with one tosylate counterion, several different starting structures were considered, which included positions of the anion inside and outside of the cavity (see Supporting Information, Figure S10). A tosylate ion inside the cavity has been found to be more stable, however, the energy preference is small (<4 kJ·mol^{-1}). In the optimized geometry, the tosylate anion does not interact with any iodonium ion directly, but rather with the cavitand through [C_{aryl}-H···O$^-$] interactions (Figure 2b).[33] The insertion of the second tosylate ion into the cavity leads to a cooperative stabilization of 35 kJ mol^{-1} – more than any other position around the capsule. Their antiparallel arrangement does not only reduce charge repulsion, but forms stabilizing van der Waals interactions between the two aromatic rings of the tosylates (Figure 2c).

View Article Online
DOI: 10.1039/C8SC03040E

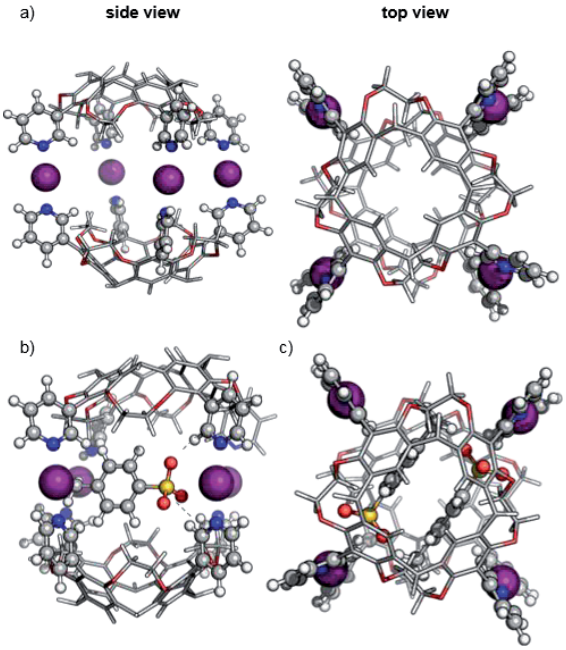

Fig. 2. Geometry-optimized structures of dimeric halogen-bonded capsule **1** a) in the absence of tosylate counterions ([2·$\mathbf{C_D}$+4I]$^{4+}$; side and top view); b) with one tosylate inside the cavity ([2·$\mathbf{C_D}$+4I+·OTs]$^{3+}$), [C_{aryl}-H···O$^-$] interactions are marked with dotted lines; c) with two tosylates inside the cavity ([2·$\mathbf{C_D}$+4I+2·OTs]$^{4+}$). PBE0/def2-SVP was used for I$^+$, pyridines and tosylates (ball-and-stick representation); AM1 for the cavitand scaffold (stick representation). For clarity, the *n*-hexyl chains are omitted in the images.

The predicted $^{TM}CCS_{He}$ values (corrected by 20 Å^2 per cavitand; see above and Supporting Information, Figure S8) are 568 and 561 Å for the ions carrying one and two tosylate ions, respectively and agree well with experimental data (Figure 1). We conclude that both anions bind cooperatively inside the cavity. The virtually identical collision cross sections suggest that already the first anion occupies the cavity.

Hexameric capsules

DT-IM-MS experiments were also performed on the hexameric halogen-bonded capsule **2** in its +6 and +7 charge states ([6·$\mathbf{C_H}$+12I+6·OTs]$^{6+}$ and [6·$\mathbf{C_H}$+12I+5·OTs]$^{7+}$). Both ATDs feature a prominent, narrow peak, which indicates the presence of a well-defined structure in the gas phase. Their corresponding $^{DT}CCS_{He}$ values of 1517 and 1499 Å^2 are again very similar to each other, suggesting that an additional counterion does not have a significant influence on the overall shape (Figure 3). The DFT/AM1-optimized structure of the hexameric capsule is an octahedron held together by twelve linear [N···I$^+$···N] bonds along the edges with N···I$^+$ distances of 2.29 Å (Figure 4a). Tosylate ions can attach to this capsule in several accessible locations: in the proximity of the halogen bond as observed inside the dimer or above the upper rim of the cavitand, located in between two pyridine units and stabilized by [C_{aryl}-H···O$^-$] interactions (Figure 4b, inset). The calculations predict that the latter binding mode, above the upper rim and inside a pocket of the cavitand, is more favourable by 31 kJ·mol^{-1}.

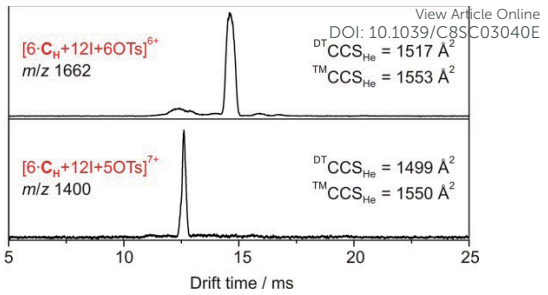

Fig. 3. DT-IM-MS ATDs of ions derived from hexameric halogen-bonded capsule **2**. Experimental $^{DT}CCS_{He}$ and theoretical $^{TM}CCS_{He}$ values are given.

Accordingly, six spatially distributed binding pockets at such positions provide binding sites for six tosylates (Figure 4b). The calculated $^{TM}CCS_{He}$ for the [6·$\mathbf{C_H}$+12I+6·OTs]$^{6+}$ and [6·$\mathbf{C_H}$+12I+5·OTs]$^{7+}$ ions of 1550 and 1553 Å^2 are in good agreement with the experiment thus indicating that the hexameric capsule retains an intact octahedral geometry upon transfer into the gas phase with linear [N···I$^+$···N] halogen bonds along all edges (Figure 3). An anion-binding mode with tosylates bridging two adjacent pyridine rings of the same cavitand by multiple [C_{aryl}-H···O$^-$] interactions is proposed. It also appears to be well-suited in terms of size and shape complementarity of this host-guest complex.

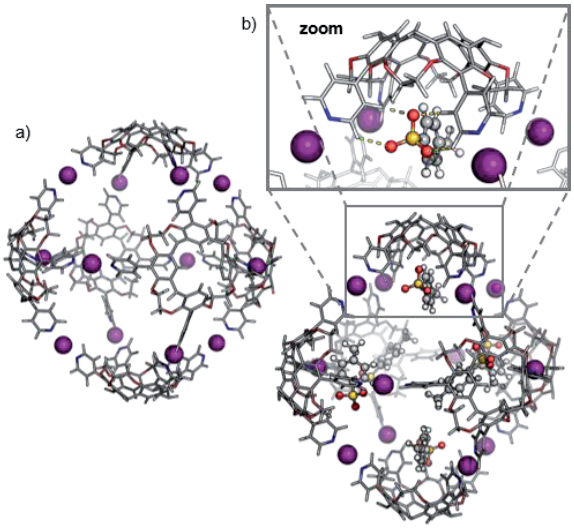

Fig. 4. Geometry-optimized structure of the hexameric halogen-bonded capsule **2** a) in the absence of tosylate ions ([6·$\mathbf{C_H}$+12I]$^{12+}$) and b) with six tosylate anions ([6·$\mathbf{C_H}$+12I+6·OTs]$^{6+}$). The *n*-hexyl chains are omitted for clarity. Inset: Binding situation of a tosylate counterion.

Solvent-dependent formation of pentameric capsules

Structure elucidation

Upon successively exchanging chloroform as the solvent by dichloromethane, a solvent-dependent transition of the hexameric capsule **2** into a novel pentameric complex (**3**, Scheme 2) was observed. To investigate the effect in more detail, we first conducted the assembly of cavitand $\mathbf{C_H}$ with

silver(I) *p*-toluenesulfonate in dichloromethane, which clearly gave the silver-coordinated hexameric capsule **4** (Supporting Information, Figure S4). The $[N\cdots Ag^{+}\cdots N] \rightarrow [N\cdots I^{+}\cdots N]$ exchange reaction in dichloromethane results in a ^{1}H NMR spectrum significantly different from that of the highly symmetrical, octahedral capsule **2** (Supporting Information, Figure S3). A rather complex NMR spectrum with several sets of rather broad signals at positions comparable to the NMR spectrum of the hexamer is obtained for **3**. This suggests the formation of an assembly of lower symmetry and/or the formation of a mixture of different assemblies. A straightforward signal assignment is, however, impossible.

The corresponding ESI mass spectrum (90 μM in CH_2Cl_2) clearly shows the selective formation of a halogen-bonded pentamer **3** (Figure 5). The almost exclusive appearance of pentameric species, instead of a non-specific distribution of oligomers, strongly suggests stable and well-defined structures to form. The signals can be assigned to charge states 6+ to 3+ and the most abundant signal of each charge state belongs to a complex with a formal $[5\cdot\mathbf{C_H}+9I]^{9+}$ core to which a varying number of anions is attached. The most dominant peak at *m/z* 1602 belongs to the complex $[5\cdot\mathbf{C_H}+9I+4\cdot OTs]^{5+}$. The observed exact mass and experimental isotope pattern agree with those simulated based on natural abundances. The mass spectrum furthermore exhibits ions which correspond to singly and doubly protonated species for each charge state accompanying the $[5\cdot\mathbf{C_H}+9I+x\cdot OTs]^{(9-x)+}$ peaks, *e.g.* $[5\cdot\mathbf{C_H}+9I+H+5\cdot OTs]^{5+}$ and $[5\cdot\mathbf{C_H}+9I+2H+6\cdot OTs]^{5+}$ ions at *m/z* 1637 and 1671. Considering possible pentameric assemblies which would maintain linear $[N\cdots I^{+}\cdots N]$ halogen bonds quickly makes clear that the formation of a complex which has all pyridine binding sites coordinated is impossible. Two possible candidates that maintain structural specificity, a bowl-shaped square pyramid and a pseudo-trigonal bipyramid, are possible (Scheme 2). In order to accommodate the geometrical constrains, both structures must feature uncomplexed pyridines, i.e. two for the pseudo-trigonal bipyramid and four for the square pyramid. Similarly, earlier studies by Aakeröy *et al.* demonstrated the formation of a heterodimeric halogen-bonded capsule in the solid state, in which one of four possible XBs is sacrificed in a fraction of the complexes due to steric congestion.[8]

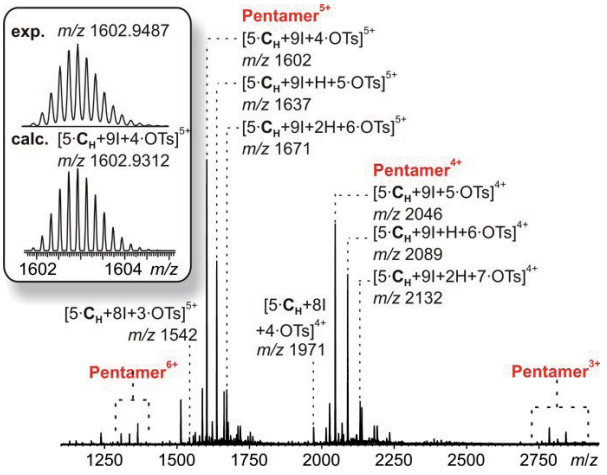

Fig. 5. ESI-Q-TOF-HRMS spectrum of pentameric halogen-bonded capsule **3** (90 μM in CH_2Cl_2) with experimental and calculated isotopic pattern (inset).

The two most prominent peaks for $[5\cdot\mathbf{C_H}+9I+x\cdot OTs]^{(9-x)+}$ ions contain five and four tosylate counterions (x = 4, 5). This agrees with the trends observed for dimeric and hexameric $[N\cdots I^{+}\cdots N]$ capsules: each cavitand monomer offers one tosylate binding site within the capsule cavity. Upon ionization, the additional outer counterions are easily stripped off. In addition, the elimination of one of the inner tosylates can occur, but is energetically somewhat more demanding. This observation thus supports the assumption that the pentamer is a closed capsule and consequently speaks in favour of the bipyramidal structure. The 5:9 cavitand-to-iodonium stoichiometry observed in the prominent peaks of the mass spectrum is also in good agreement with the bipyramidal structure of the pentamer, as the square pyramid only requires eight $[N\cdots I^{+}\cdots N]$ halogen bonds, while the bipyramid bears nine. Capsule-derived complexes with singly coordinated I^{+} have not been observed, neither in this nor in our previous study.[6] Consequently, the $[N\cdots I^{+}\cdots N]$ bond is likely much more stable than the hypothetical $[N\cdots I^{+}]$ group. Furthermore, the observed single and double – but not triple or quadruple – protonation indicates the presence of two free pyridines as in the bipyramid rather than the four of the square pyramid. All these findings thus agree that the structure of the pentamer is that of a bipyramid that bears two non-coordinated pyridines. Nevertheless, low-abundant signals corresponding to ions with a formal $[5\cdot\mathbf{C_H}+8I]^{8+}$ core, which appear at *m/z* 1542 and 1971, may indicate that the square pyramidal complex is present in solution at low concentrations. Therefore, the pseudo-trigonal bipyramidal pentameric $[5\cdot\mathbf{C_H}+9I]^{9+}$ and the square pyramidal

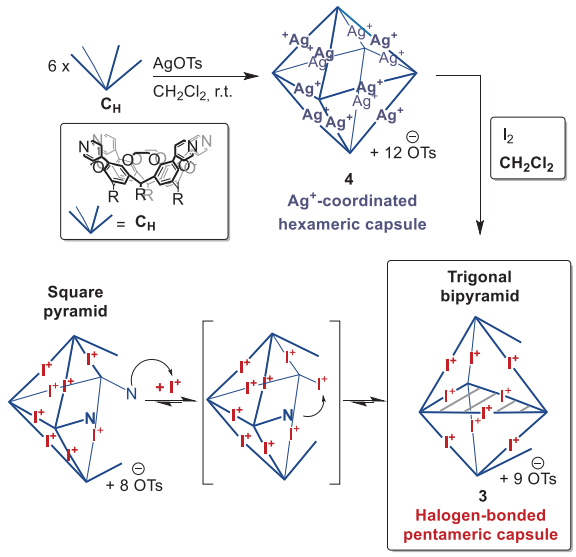

Scheme 2. Selective formation of halogen-bonded pentameric capsule **3** using CH_2Cl_2 as the solvent.

$[5{\cdot}\mathbf{C_H}{+}8\mathrm{I}]^{8+}$ complexes may exist in an equilibrium with each other. This equilibrium, however, is strongly shifted towards the pseudo-trigonal bipyramidal complex as this structure helps maximizing the number of halogen bonds within the pentamer (Scheme 2).

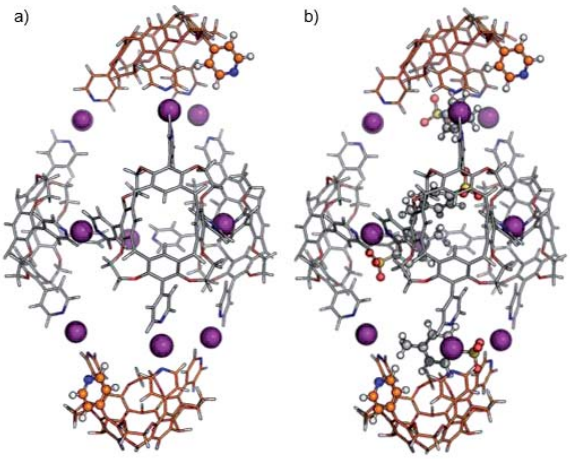

Fig. 6. Calculated structures of the pentameric halogen-bonded capsule **3** with pseudo-trigonal bipyramidal arrangement a) in the absence of tosylate ions ($[5{\cdot}\mathbf{C_H}{+}9\mathrm{I}]^{9+}$) and b) with four tosylate anions ($[5{\cdot}\mathbf{C_H}{+}9\mathrm{I}{+}4{\cdot}\mathrm{OTs}]^{5+}$). For clarity, the *n*-hexyl side chains are omitted. Cavitands in axial positions, unbound pyridines and tosylates are highlighted.

Theory confirms the individual cavitands to be sufficiently flexible to form a stable pseudo-trigonal bipyramidal pentameric capsule. Three cavitands in equatorial positions participate with all four pyridine groups in linear [N···I⁺···N] bonds (Figure 6a). These cavitands are capped axially by the other two which bind in a somewhat distorted conformation. The two apical cavitands form only three [N···I⁺···N] bonds each and the fourth pyridine moiety remains unbound. In principle, two different configurational isomers of this pentameric capsule are possible: the two unbound pyridines can adopt an eclipsed or a gauche position relative to each other. This accounts for the complex ^{1}H NMR of capsule **3**; multiple sets of signals likely originate from a mixture of two different complexes that both have lower symmetry than the hexamer. Alike the hexameric capsule, tosylate ions can bind inside the cavity of the pentameric capsule above the upper rim of the cavitands stabilized by [C_{aryl}-H···O$^-$] interactions (Figure 6b). In contrast to the hexameric capsules, the binding sites are not equivalent anymore; the tosylates prefer to populate the more remote apical cavitands first, and then bind to more crowded equatorial cavitands.

The ATD obtained for the $[5{\cdot}\mathbf{C_H}{+}9\mathrm{I}{+}4{\cdot}\mathrm{OTs}]^{5+}$ ion in a DT-IM-MS experiment shows a single narrow peak which is consistent with the presence of a well-defined species in the gas phase (Figure 7). The difference in size and shape of the two possible configurational isomers of capsule **3** is apparently not sufficient to differentiate the species in the ATD. The measured $^{DT}CCS_{He}$ for capsule **3** of 1286 Å^2 is approximately 20% smaller than that of the hexameric capsule **2**. The optimized structure of the pseudo-trigonal bipyramidal pentamer capsule, with four tosylates occupying the cavity, yielded a calculated $^{TM}CCS_{He}$ value of 1279 Å^2 which is in excellent agreement with the experimental value.

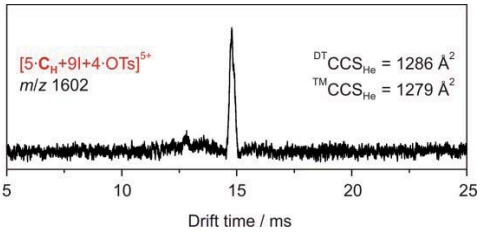

Fig. 7. DT-IM-MS ATDs of ions derived from pentameric halogen-bonded capsule **3**. Experimental $^{DT}CCS_{He}$ and theoretical $^{TM}CCS_{He}$ values are given.

These results confirm the discovery of a new type of large, well-behaved supramolecular complex based on [N···I⁺···N] halogen bonds. This is the first example of a resorcinarene-based pentameric supramolecular capsule. The selective formation of pentameric capsules illustrates the possible interplay of preorganized, but inherently flexible cavitands and directional halogen bonds being modulated by a third factor – solvent effects. Solvent-induced transformations in discrete supramolecular assemblies have been described for numerous other systems and are most likely to arise from changes between protic/aprotic and polar/apolar solvents.[16] However, examples which feature the change between two very similar solvents, as in our case chloroform and dichloromethane, are extremely rare which makes this finding especially intriguing.[24] Self-assembly most often leads to the smallest possible, not too highly strained assembly in which all binding sites are coordinatively saturated. This is the best compromise between entropic (particle number) and enthalpic effects (avoiding strain and unsaturated binding sites). It is thus surprising that a solvent effect can be large enough to energetically overcome the energetic penalty associated with two pyridine binding sites remaining unsaturated. However, when considering all effects that come into play here, the hexamer → pentamer rearrangement appears reasonable: (i) Dichloromethane has a significantly higher polarity than chloroform as expressed in their dielectric constants ε of 8.93 and 4.81, respectively, and thus provides better solvation to the free pyridines. (ii) More pentamers can form from the same number of building blocks, increasing particle number and thus entropy. (iii) The formation of mixtures of isomers also contributes to a favourable entropy of the pentamer. (iv) Space filling[34] of the voids between the encapsulated tosylates inside the capsules with solvent molecules likely contributes differently for the hexamer (larger voids) and the pentamer (smaller voids). Chloroform and dichloromethane differ in size and might therefore template the assembly of one complex or the other by providing a more optimal filling of this particular cavity.[35] All these (and maybe more) effects help balancing the energetic penalty arising from leaving two binding sites open. We therefore propose an equilibrium between the hexameric and the pentameric capsules which is susceptible to the small shift in energetics associated with the solvent change.

View Article Online
DOI: 10.1039/C8SC03040E

Solvent-dependent switching

To account for this hypthesis, a switching experiment was performed (see Supporting Information, Scheme S1, Figures S1, S2, S5). A 1 mM sample solution of hexameric halogen-bonded capsule **2** in chloroform was diluted using different ratios of chloroform to dichloromethane, resulting in a constant sample concentration of 0.1 mM, but different solvent ratios. These samples were analyzed by ESI-MS two minutes after dilution. The mass spectrum of the sample in pure chloroform reveals the presence of the intact octahedral hexameric capsule in form of a prominent peak at *m/z* 1662 ([6·$\mathbf{C_H}$+12I+6·OTs]$^{6+}$, Figure 8a, top). Upon increase of the dichloromethane fraction to 50%, signals corresponding to pentameric complexes appear in the spectrum at *m/z* 1602, 1637 and 1672 (Figure 8a, center). When the ratio of chloroform to dichloromethane is at 1:9, the hexameric capsule vanishes and the pentamer prevails (Figure 8a, bottom). Note that the remaining peak at *m/z* 1662 belongs to a dimeric ion which is likely an ionization artifact.

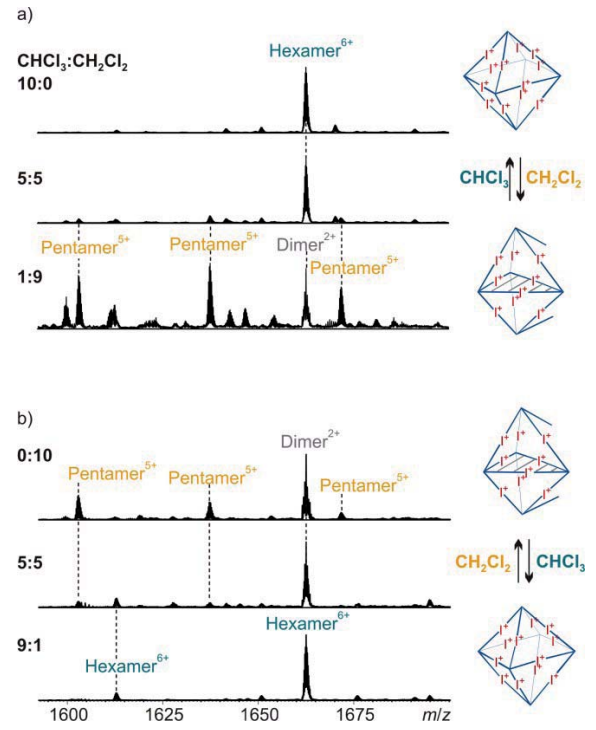

Fig. 8. ESI-Q-TOF-HRMS spectra of titration experiments to investigate the solvent-dependent transitions a) from the hexameric to the pentameric halogen-bonded capsule (from top to bottom: $CHCl_3/CH_2CL_2$ 1:0→1:1→1:9) and b) from the pentameric halogen-bonded capsule to the hexameric halogen-bonded capsule (from top to bottom: $CHCl_3/CH_2CL_2$ 0:1→1:1→9:1). Isobaric hexamers and dimers can be distinguished by isotope pattern analysis.

The experiment can be carried out in the opposite direction as well. Starting from a clear solution (1 mM) of pentameric halogen-bonded capsule **3** in dichloromethane, dilution of the sample to 0.1 mM in a 1:1 mixture of chloroform and dichloromethane leads to a mixture of pentameric and hexameric complexes in a very similar ratio as observed in the first experiment (Figure 8b, center). An increase of the amount of chloroform to 90% of the spray solvent gives exclusively hexameric complexes (Figure 8b, bottom). These switching experiments indeed demonstrate the solvent-dependent equilibrium between the two capsules **2** and **3**.

A CID tandem MS experiment provides evidence that the hexamer-pentamer transition is solely taking place in solution. No gas-phase rearrangement leading preferentially from hexameric to pentameric complexes was observed (see Supporting Information, Figure S6, S7).

These results emphasize the certainly unexpected solvent effects and clearly demonstrate the halogen-bonded hexameric capsule to be a stimuli-responsive assembly, which reacts to changes in its environment by substantial structural rearrangements.

Conclusions

The first study on the solution reactivity of large [N···I$^+$···N] halogen-bonded capsules revealed a solvent-dependent rearrangement of the known hexameric capsule into a novel pentameric [N···I$^+$···N] halogen-bonded capsule. While condensed phase methods could not provide detailed insight, the combination of ESI-MS, DT-IM-MS and theoretical calculations enabled us to elucidate the structure of this new [N···I$^+$···N] halogen-bonded capsule. The complex possesses an unusual pseudo-trigonal bipyramidal geometry with nine [N···I$^+$···N] bonds along the edges and two of the five incorporated cavitands partially uncomplexed. We demonstrate that this fascinating and rather unexpected equilibrium between the hexameric and the pentameric complex originates solely from a subtle change of solvent from chloroform to dichloromethane. This stimuli-responsive rearrangement is rationalized by a combination of microsolvation, space-filling, and different entropic contributions.

Moreover, we provide first evidence for the anion guest-binding in the different [N···I$^+$···N] halogen-bonded capsules by a combination of experimental and theoretical gas-phase methods. Each cavitand incorporated into the dimeric, pentameric and hexameric complexes is capable of binding one tosylate ion within the capsule`s cavity, resulting in the binding of up to two, five and six anions, in **1**, **3**, and **2** respectively. Two different binding modes depending on the size of the complex were predicted by DFT-level calculations. Especially the binding in the less sterically crowded pentamers and hexamers is interesting. It shows the tosylate ions without interaction with the [N···I$^+$···N] moieties, but rather between the two pyridine units and above the upper rim of the cavitand stabilized by [C_{aryl}-H···O$^-$] interactions. This agrees well with studies on similar, yet significantly less complex systems investigated by Erdélyi and coworkers.[12] Furthermore, this is also in marked contrast to the anion binding of the silver-coordinated, dimeric precursor capsule, for which X-ray crystal structure analysis showed the anions to be located outside the cavity and in direct interaction with the silver cations.[6]

View Article Online
DOI: 10.1039/C8SC03040E

In conclusion, the large [N···I⁺···N] halogen-bonded capsules feature [C_{aryl}-H···O^-] interactions and halogen bonds as orthogonal noncovalent interactions which determine the assembly of the host and the guest binding. This underlines the potential for their application for the hierarchical self-assembly of supramolecular architectures in solution.

Conflicts of interest

There are no conflicts to declare.

Acknowledgements

This project has been supported by the Deutsche Forschungsgemeinschaft (CRC 765).

References

1 R. Wyler, J. de Mendoza and J. Rebek, *Angew. Chem. Int. Ed. Engl.*, 1993, **32**, 1699–1701.
2 J. Rebek, T. Heinz and D. M. Rudkevich, *Nature*, 1998, **394**, 764–766.
3 M. Fujita, S. Nagao and K. Ogura, *J. Am. Chem. Soc.*, 1995, **117**, 1649–1650.
4 G. V. Oshovsky, D. N. Reinhoudt and W. Verboom, *J. Am. Chem. Soc.*, 2006, **128**, 5270–5278.
5 a) O. Dumele, B. Schreib, U. Warzok, N. Trapp, C. A. Schalley and F. Diederich, *Angew. Chem. Int. Ed.*, 2017, **56**, 1152–1157; b) O. Dumele, N. Trapp and F. Diederich, *Angew. Chem. Int. Ed.*, 2015, **54**, 12339–12344.
6 L. Turunen, U. Warzok, R. Puttreddy, N. K. Beyeh, C. A. Schalley and K. Rissanen, *Angew. Chem. Int. Ed.*, 2016, **55**, 14033–14036.
7 L. Turunen, U. Warzok, C. A. Schalley and K. Rissanen, *Chem*, 2017, **3**, 861–869.
8 C. B. Aakeröy, A. Rajbanshi, P. Metrangolo, G. Resnati, M. F. Parisi, J. Desper and T. Pilati, *CrystEngComm*, 2012, **14**, 6366–6368.
9 L. C. Gilday, S. W. Robinson, T. A. Barendt, M. J. Langton, B. R. Mullaney and P. D. Beer, *Chem. Rev.*, 2015, **115**, 7118–7195.
10 a) G. Cavallo, P. Metrangolo, R. Milani, T. Pilati, A. Priimagi, G. Resnati and G. Terraneo, *Chem. Rev.*, 2016, **116**, 2478–2601; b) M. Erdélyi, *Chem. Soc. Rev.*, 2012, **41**, 3547–3557.
11 a) A.-C. C. Carlsson, M. Uhrbom, A. Karim, U. Brath, J. Gräfenstein and M. Erdélyi, *CrystEngComm*, 2013, **15**, 3087–3092; b) A.-C. C. Carlsson, J. Gräfenstein, A. Budnjo, J. L. Laurila, J. Bergquist, A. Karim, R. Kleinmaier, U. Brath and M. Erdélyi, *J. Am. Chem. Soc.*, 2012, **134**, 5706–5715; c) S. B. Hakkert and M. Erdélyi, *J. Phys. Org. Chem.*, 2015, **28**, 226–233; d) A.-C. C. Carlsson, K. Mehmeti, M. Uhrbom, A. Karim, M. Bedin, R. Puttreddy, R. Kleinmaier, A. A. Neverov, B. Nekoueishahraki, J. Gräfenstein, K. Rissanen and M. Erdélyi, *J. Am. Chem. Soc.*, 2016, **138**, 9853–9863.
12 M. Bedin, A. Karim, M. Reitti, A.-C. C. Carlsson, F. Topić, M. Cetina, F. Pan, V. Havel, F. Al-Ameri, V. Sindelar, K. Rissanen, J. Gräfenstein and M. Erdélyi, *Chem. Sci.*, 2015, **6**, 3746–3756.
13 L. Turunen, A. Peuronen, S. Forsblom, E. Kalenius, M. Lahtinen and K. Rissanen, *Chem. Eur. J.*, 2017, **23**, 11714–11718.
14 a) D. Beaudoin, F. Rominger and M. Mastalerz, *Angew. Chem. Int. Ed.*, 2016, **55**, 15599–15603; b) L. R. MacGillivray and J. L. Atwood, *Nature*, 1997, **389**, 469–472; c) T. Gerkensmeier, W. Iwanek, C. Agena, R. Fröhlich, S. Kotila, C. Näther and J. Mattay, *Eur. J. Org. Chem.*, 1999, 2257–2262; d) R. M. McKinlay, G. W. V. Cave and J. L. Atwood, *Proc. Natl. Acad. Sci. USA*, 2005, **102**, 5944–5948; e) T. Schröder, R. Brodbeck, M. C. Letzel, A. Mix, B. Schnatwinkel, M. Tonigold, D. Volkmer and J. Mattay, *Tetrahedron Lett.*, 2008, **49**, 5939–5942; f) O. Ugono, J. P. Moran and K. T. Holman, *Chem. Commun.*, 2008, 1404–1406.
15 R. Custelcean, *Chem. Soc. Rev.*, 2014, **43**, 1813–1824.
16 W. Wang, Y.-X. Wang and H.-B. Yang, *Chem. Soc. Rev.*, 2016, **45**, 2656–2693.
17 a) S. Sato, Y. Ishido and M. Fujita, *J. Am. Chem. Soc.*, 2009, **131**, 6064–6065; b) S. P. Black, D. M. Wood, F. B. Schwarz, T. K. Ronson, J. J. Holstein, A. R. Stefankiewicz, C. A. Schalley, J. K. M. Sanders and J. R. Nitschke, *Chem. Sci.*, 2016, **7**, 2614–2620; c) N. K. Beyeh, M. Kogej, A. Ahman, K. Rissanen and C. A. Schalley, *Angew. Chem. Int. Ed.*, 2006, **45**, 5214–5218; d) W. Hoffmann, K. Folmert, J. Moschner, X. Huang, H. von Berlepsch, B. Koksch, M. T. Bowers, G. von Helden and K. Pagel, *J. Am. Chem. Soc.*, 2018, **140**, 244–249.
18 a) D. Fujita, Y. Ueda, S. Sato, H. Yokoyama, N. Mizuno, T. Kumasaka and M. Fujita, *Chem*, 2016, **1**, 91–101; b) B. Baytekin, H. T. Baytekin and C. A. Schalley, *Org. Biomol. Chem.*, 2006, **4**, 2825–2841; c) C. A. Schalley (Ed.), *Analytical methods in supramolecular chemistry*, Wiley-VCH, Weinheim, 2012.
19 a) L. Cera and C. A. Schalley, *Chem. Soc. Rev.*, 2014, **43**, 1800–1812; b) Z. Qi, T. Heinrich, S. Moorthy and C. A. Schalley, *Chem. Soc. Rev.*, 2015, **44**, 515–531.
20 F. Lanucara, S. W. Holman, C. J. Gray and C. E. Eyers, *Nat. Chem.*, 2014, **6**, 281–294.
21 C. Uetrecht, R. J. Rose, E. van Duijn, K. Lorenzen and A. J. R. Heck, *Chem. Soc. Rev.*, 2010, **39**, 1633–1655.
22 E. S. Baker, B. H. Clowers, F. Li, K. Tang, A. V. Tolmachev, D. C. Prior, M. E. Belov and R. D. Smith, *J. Am. Soc. Mass Spectrom.*, 2007, **18**, 1176–1187.
23 a) P. Bonakdarzadeh, F. Topić, E. Kalenius, S. Bhowmik, S. Sato, M. Groessl, R. Knochenmuss and K. Rissanen, *Inorg. Chem.*, 2015, **54**, 6055–6061; b) O. Jurček, P. Bonakdarzadeh, E. Kalenius, J. M. Linnanto, M. Groessl, R. Knochenmuss, J. A. Ihalainen and K. Rissanen, *Angew. Chem. Int. Ed.*, 2015, **54**, 15462–15467; c) A. Kiesilä, L. Kivijärvi, N. K. Beyeh, J. O. Moilanen, M. Groessl, T. Rothe, S. Götz, F. Topić, K. Rissanen, A. Lützen and E. Kalenius, *Angew. Chem. Int. Ed.*, 2017, **56**, 10942–10946; d) M. Petryk, A. Troć, B. Gierczyk, W. Danikiewicz and M. Kwit, *Chem. Eur. J.*, 2015, **21**, 10318–10321; e) J. Ujma, M. de

View Article Online
DOI: 10.1039/C8SC03040E

Cecco, O. Chepelin, H. Levene, C. Moffat, S. J. Pike, P. J. Lusby and P. E. Barran, *Chem. Commun.*, 2012, **48**, 4423–4425; f) C. Wang, X.-Q. Hao, M. Wang, C. Guo, B. Xu, E. N. Tan, Y.-Y. Zhang, Y. Yu, Z.-Y. Li, H.-B. Yang, M.-P. Song and X. Li, *Chem. Sci.*, 2014, **5**, 1221–1226; g) M. Wang, C. Wang, X.-Q. Hao, X. Li, T. J. Vaughn, Y.-Y. Zhang, Y. Yu, Z.-Y. Li, M.-P. Song, H.-B. Yang and X. Li, *J. Am. Chem. Soc.*, 2014, **136**, 10499–10507.

24 R. Sure and S. Grimme, *Chem. Commun.*, 2016, **52**, 9893–9896.

25 a) T. Vreven, K. S. Byun, I. Komáromi, S. Dapprich, J. A. Montgomery, K. Morokuma and M. J. Frisch, *J. Chem. Theory Comput.*, 2006, **2**, 815–826; b) L. W. Chung, W. M. C. Sameera, R. Ramozzi, A. J. Page, M. Hatanaka, G. P. Petrova, T. V. Harris, X. Li, Z. Ke, F. Liu, H.-B. Li, L. Ding and K. Morokuma, *Chem. Rev.*, 2015, **115**, 5678–5796; c) R. Wieczorek and J. J. Dannenberg, *J. Am. Chem. Soc.*, 2003, **125**, 8124–8129.

26 a) S. Warnke, C. Baldauf, M. T. Bowers, K. Pagel and G. von Helden, *J. Am. Chem. Soc.*, 2014, **136**, 10308–10314; b) P. R. Kemper, N. F. Dupuis and M. T. Bowers, *Int. J. Mass Spectrom.*, 2009, **287**, 46–57.

27 Gaussian 09, Revision rev.D01, M. J. Frisch, G. W. Trucks, H. B. Schlegel, G. E. Scuseria, M. A. Robb, J. R. Cheeseman, G. Scalmani, V. Barone, G. A. Petersson, H. Nakatsuji, X. Li, M. Caricato, A. Marenich, J. Bloino, B. G. Janesko, R. Gomperts, B. Mennucci, H. P. Hratchian, J. V. Ortiz, A. F. Izmaylov, J. L. Sonnenberg, D. Williams-Young, F. Ding, F. Lipparini, F. Egidi, J. Goings, B. Peng, A. Petrone, T. Henderson, D. Rana-singhe, V. G. Zakrzewski, J. Gao, N. Rega, G. Zheng, W. Liang, M. Hada, M. Ehara, K. Toyota, R. Fukuda, J. Hasegawa, M. Ishida, T. Nakajima, Y. Honda, O. Kitao, H. Nakai, T. Vreven, K. Throssell, J. A. Montgomery, Jr., J. E. Peralta, F. Ogliaro, M. Bearpark, J. J. Heyd, E. Brothers, K. N. Kudin, V. N. Staroverov, T. Keith, R. Kobayashi, J. Normand, K. Raghavachari, A. Rendell, J. C. Burant, S. S. Iyengar, J. To-masi, M. Cossi, J. M. Millam, M. Klene, C. Adamo, R. Cammi, J. W. Ochterski, R. L. Martin, K. Morokuma, O. Farkas, J. B. Foresman, and D. J. Fox, Gaussian, Inc., Wallingford CT, 2016.

28 M. J. S. Dewar, E. G. Zoebisch, E. F. Healy and J. J. P. Stewart, *J. Am. Chem. Soc.*, 1985, **107**, 3902–3909.

29 F. Weigend, *Phys. Chem. Chem. Phys.*, 2006, **8**, 1057–1065.

30 C. Adamo and V. Barone, *J. Chem. Phys.*, 1999, **110**, 6158–6170.

31 M. F. Mesleh, J. M. Hunter, A. A. Shvartsburg, G. C. Schatz and M. F. Jarrold, *J. Phys. Chem.*, 1996, **100**, 16082–16086.

32 Maestro Schrödinger Release 2017-4: Maestro, Schrödinger, LLC, New York, NY, 2017.

33 S. S. Zhu, H. Staats, K. Brandhorst, J. Grunenberg, F. Gruppi, E. Dalcanale, A. Lützen, K. Rissanen and C. A. Schalley, *Angew. Chem. Int. Ed.*, 2008, **47**, 788–792.

34 S. Mecozzi and J. J. Rebek, *Chem. Eur. J.*, 1998, **4**, 1016–1022.

35 B. Kilbas, S. Mirtschin, R. Scopelliti and K. Severin, *Chem. Sci.*, 2012, **3**, 701–704.

View Article Online
DOI: 10.1039/C8SC03040E

Table of Contents Text & Graphic

Ion-mobility mass spectrometry and DFT calculations reveal the surprisingly solvent-dependent formation of large pentameric [N···I^+···N] halogen-bonded capsules.

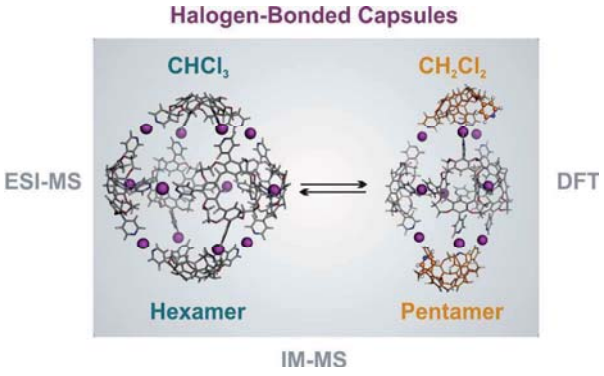

Surprising Solvent-Induced Structural Rearrangements in Large [N···I+···N] Halogen-Bonded Supramolecular Capsules: An Ion Mobility-Mass Spectrometry Study

Ulrike Warzok,[1] Mateusz Marianski,[2,‡] Waldemar Hoffmann,[1,2] Lotta Turunen,[3] Kari Rissanen,[3] Kevin Pagel,[1,2] and Christoph A. Schalley[1,*]

[1] Institut für Chemie und Biochemie, Freie Universität Berlin, Takustraße 3, 14195 Berlin, Germany
[2] Fritz-Haber-Institut der Max-Planck-Gesellschaft, Faradayweg 4-6, 14195 Berlin, Germany
[3] Department of Chemistry, NanoScience Center, University of Jyvaskyla, Department of Chemistry, P.O. Box 35, 40014 Jyväskylä, Finland

Supporting Information

Table of Content

1. General Information

Reagents were purchased from commercial suppliers and used without further purification. The hexyl-substituted ethylene-bridged tetrakis(4-pyridyl)cavitand $\mathbf{C_H}$, the hexyl-substituted ethylene-bridged tetrakis(3-pyridyl)cavitand $\mathbf{C_D}$ and the *iso*-butyl-substituted ethylene-bridged tetrabromocavitand were prepared according to reported procedures.[1,2] ^{1}H and ^{13}C NMR spectra were recorded on a Bruker Avance III 500 or Avance 400 spectrometers. All signals are given as δ values in ppm using residual solvent signals as the internal standard. Coupling constants are given in Hz. Melting points were determined with melting point apparatus SMP3. Positive-mode electrospray ionization quadrupole-time-of-flight high resolution mass spectrometry (ESI-Q-TOF-HRMS) measurements were performed with a micromass LCT ESI-TOF instrument for analysis of *iso*-butyl-substituted ethylene-bridged tetrakis(4-pyridyl)cavitand.

2. Synthesis and Characterization

C_4-ethylene-bridged tetrakis(4-pyridyl)cavitand C_{H4}

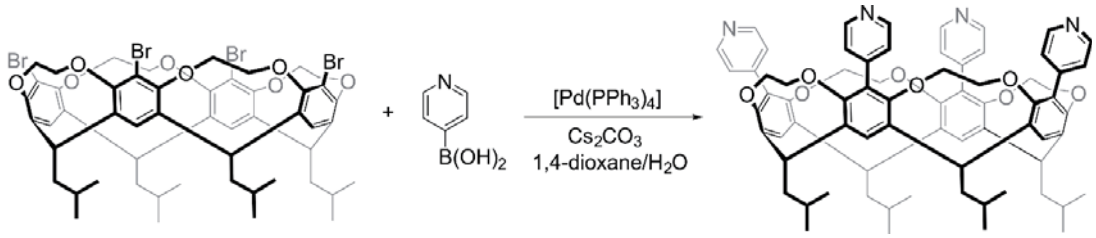

Scheme S1: Synthesis of ethylene-bridged tetrakis(4-pyridyl) cavitand.

The *iso*-butyl-substituted tetrakis(4-pyridyl)ethylenecavitand was synthesized according to a reported procedure.[1] To the flask containing *iso*-butyl-substituted ethylene-bridged tetrabromocavitand (500 mg, 420 μmol), pyridyl-4-boronic acid (270 mg, 2.2 mmol), $[Pd(PPh_3)_4]$ (130 mg, 110 μmol) and Cs_2CO_3 (2.2 g, 6.6 mmol), degassed 1,4-dioxane (100 mL) and water (2.0 mL) were added under argon. The reaction mixture was degassed three times, then refluxed at 110 °C for 2 d. The mixture was cooled to room temperature and the solvent was evaporated under reduced pressure. The residue was dissolved in CH_2Cl_2 (70 mL) and water (70 mL) was added. After the phases were separated, the aqueous phase was extracted with CH_2Cl_2

(2 x 70 ml). The combined organic phases were dried over $MgSO_4$. The solvent was removed under reduced pressure to give the crude product, which was purified by column chromatography (SiO_2, CH_2Cl_2/MeOH 9:1). The product was obtained as a white solid (220 mg, 44 %). m.p. >270 ^oC (decomposition); ^1H NMR (500 MHz, $CDCl_3$, 303 K) δ (ppm): 1.00 (d, J = 6.8 Hz, 24H, CH_3), 1.40-1.48 (m, 4H, CH), 2.10-2.13 (m, 8H, CH_2), 3.40-3.43 (m, 8H, CH_{2in}), 3.86-3.90 (m, 8H, CH_{2out}), 5.41 (t, J = 8.0 Hz, 4H, CH), 7.10 (d, J = 5.4 Hz, 8H, pyr-H), 7.62 (s, 4H, Ar-H), 8.60 (d, J = 4.9 Hz, 8H, pyr-H)). ^{13}C NMR (126 MHz, $CDCl_3$, 303 K) δ (ppm): 22.8, 26.3, 31.6, 43.8, 72.4, 125.0, 125.2, 128.7, 136.4, 143.8, 149.4, 151.2; LCT ESI-TOF: found 1125.5751 $[M+H]^+$, calc. 1125.5736 $[M+H]^+$.

^1H and ^{13}C NMR spectra

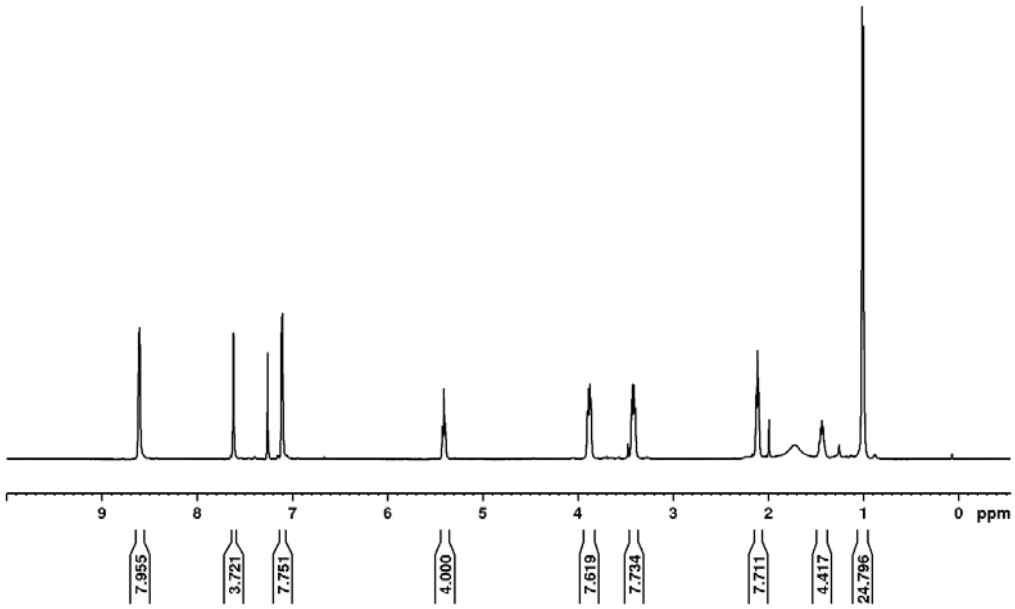

Figure S1: ^1H NMR spectrum of *iso*-butyl-substituted ethylene-bridged tetrakis(4-pyridyl)cavitand ($CDCl_3$, 303K, 400 MHz).

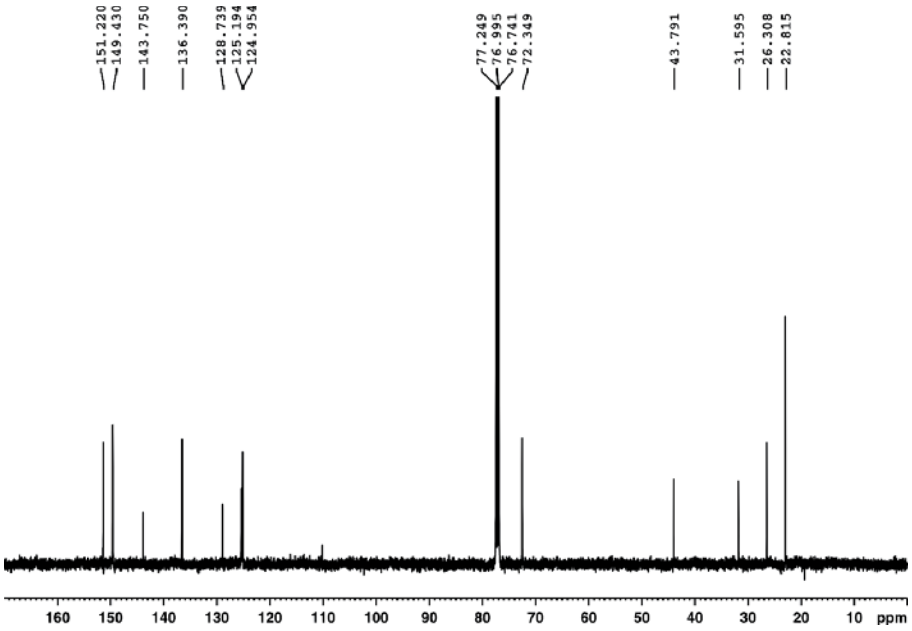

Figure S2: ^{13}C NMR spectrum of *iso*-butyl-substituted ethylene-bridged tetrakis(4-pyridyl)cavitand ($CDCl_3$, 303 K, 126 MHz).

3. Solvent-dependent Formation of Pentameric Capsules

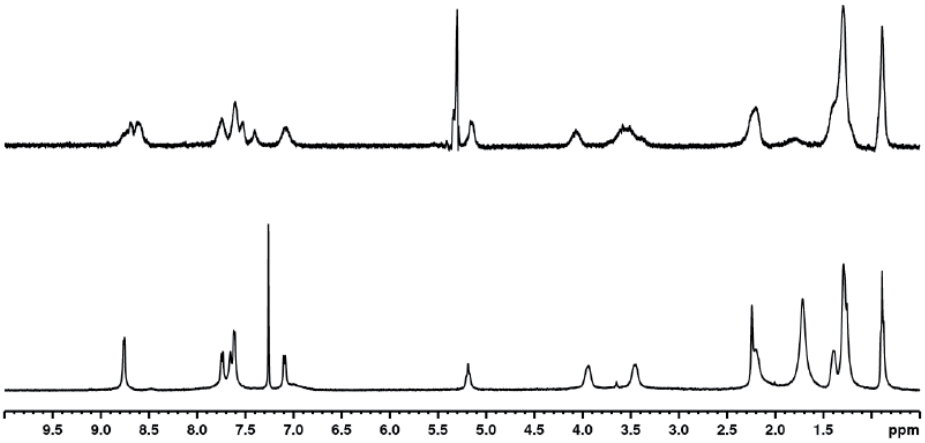

Figure S3: ^{1}H NMR spectra of halogen-bonded pentameric capsule **3** in CD_2Cl_2 (top) and hexameric capsule **2** in $CDCl_3$ (bottom, as previously published[2]). Clearly, both samples exhibit signals with similar chemical shifts. In contrast to the hexamer, which exhibits only one set of signals due to its high symmetry, the pentamer spectrum consists of several sets of signals in agreement with the presence of two different isomers each of which have a lower symmetry than the hexamer.

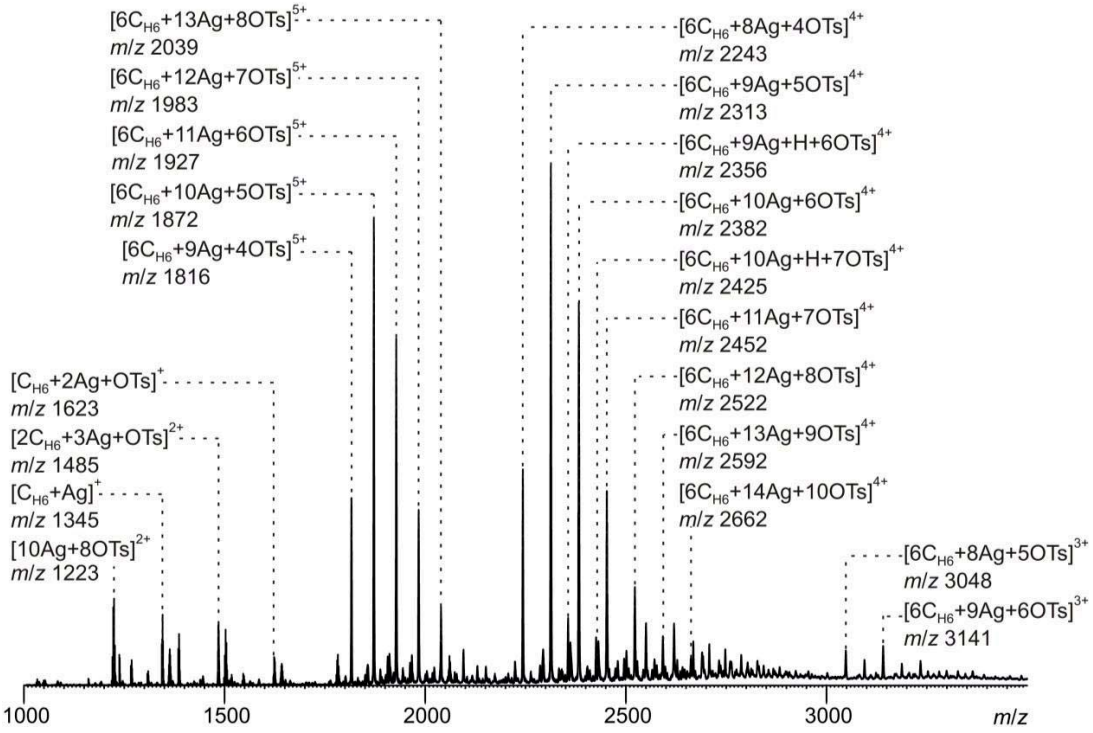

Figure S4: ESI-Q-TOF-HRMS spectrum of hexameric silver-coordinated capsule **4** (100 μM in CH_2Cl_2).

The solution exchange between preformed hexameric I^+-capsule **2** and free cavitand was examined by mixing a 1 mM solution of hexameric capsule **3** in $CHCl_3$ with 6 equivalents of a 1 mM solution of *iso*-butyl cavitand $\mathbf{C_{H4}}$. The mixed solution was diluted to 100 μM with $CHCl_3$ prior to the measurements and 10% of acetonitrile were added. Mass spectra were recorded after 2 minutes and after 20 hours equilibration time. No significant difference between these two spectra was observed. This experiment thus indicates that the exchange of the cavitands in the capsule occurs on a below-minutes time scales. No significant capsule dissociation occurs.

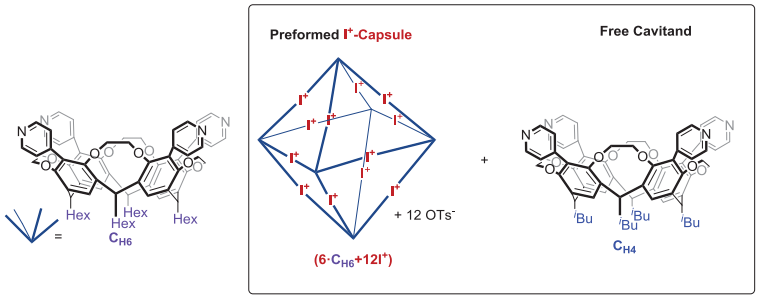

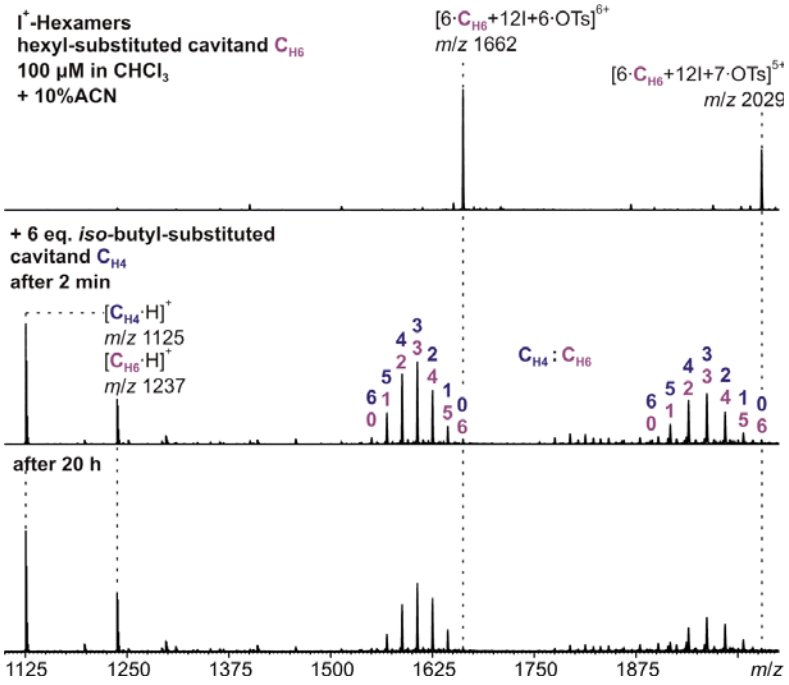

Figure S5: Mixing experiment hexameric capsule **2** and free *iso*-butyl cavitand $\mathbf{C_{H4}}$.

4. Tandem Mass Spectrometry

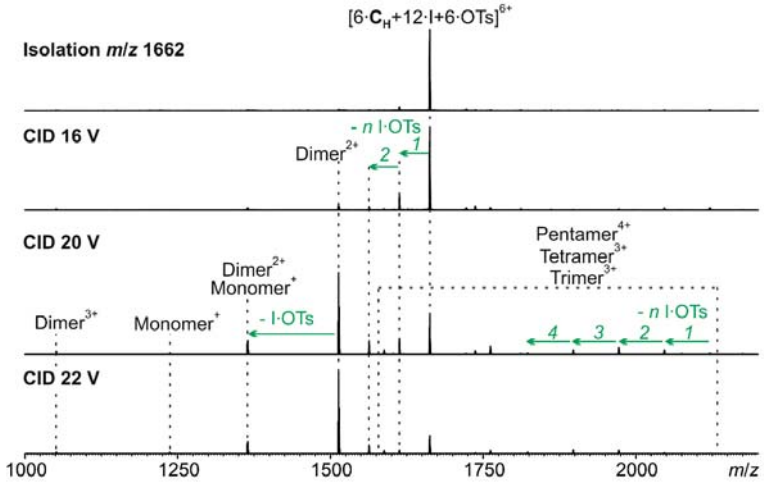

Figure S6: Tandem MS experiment performed with mass-selected ions $[6\cdot\mathbf{C_H}+12I+6\cdot OTs]^{6+}$ derived from the hexameric capsule **2**.

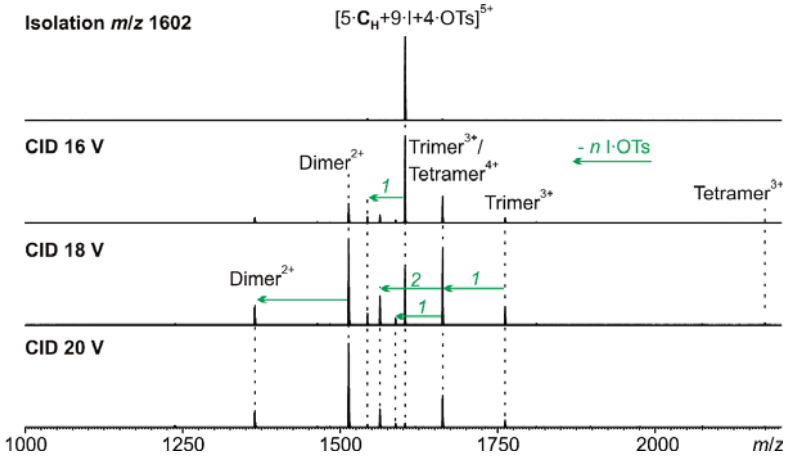

Figure S7: Tandem MS experiment performed with mass-selected ions $[5{\cdot}\mathbf{C_H}{+}9I{+}4{\cdot}OTs]^{5+}$ derived from the pentameric capsule **3**.

5. Theoretical calculations

Table S1. The difference between single point energies of MP2/def2-QZVPP and different density functional in $kJ{\cdot}mol^{-1}$. The MP2/def2-TZVP optimized geometry of the [pyridine···I^+···pyridine] model system has been used for energy evaluation.

Functional	type	def2-SVP	def2-TZVP	def2-TZVPP	def2-QZVPP
TPSS	GGA	5.4	-2.1	-2.1	15.1
BLYP	GGA	-24.3	-47.3	-47.3	-48.1
PBE	GGA	14.2	1.7	1.7	33.9
PBE+D3	GGA	25.5	12.6	12.6	45.2
B3LYP	Hybrid	-38.9	-61.9	-61.9	-62.3
B3LYP+D3	Hybrid	-18.4	-41.4	-41.4	-41.8
PBE0	Hybrid	-8.8	-26.4	-26.4	-25.9
PBE0+D3	Hybrid	3.3	-14.2	-13.8	-13.4
M06	Hybrid	-38.9	-57.7	-56.5	-53.6
M06-2X	Hybrid	-49.8	-67.8	-68.2	-68.6
WB97-XD	Hybrid	-32.6	-52.3	-52.3	-51.5
X3LYP	Hybrid	-33.5	-56.5	-56.5	-56.9

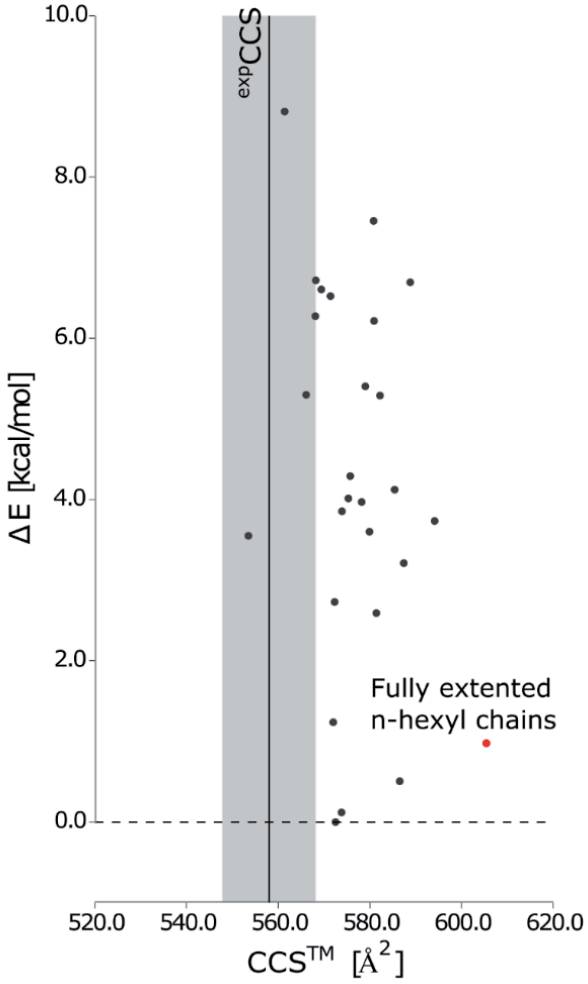

Figure S8: The distribution of CCS for the dimeric capsule **1** ($[2\mathbf{C_D}+4I]^{4+}$) computed for various conformations of *n*-hexyl chains using the trajectory method. The y-axis shows relative energies of optimized capsules. The fully extended chains give CCS larger that 600Å, whereas the chains can easily adopt more compact conformations.

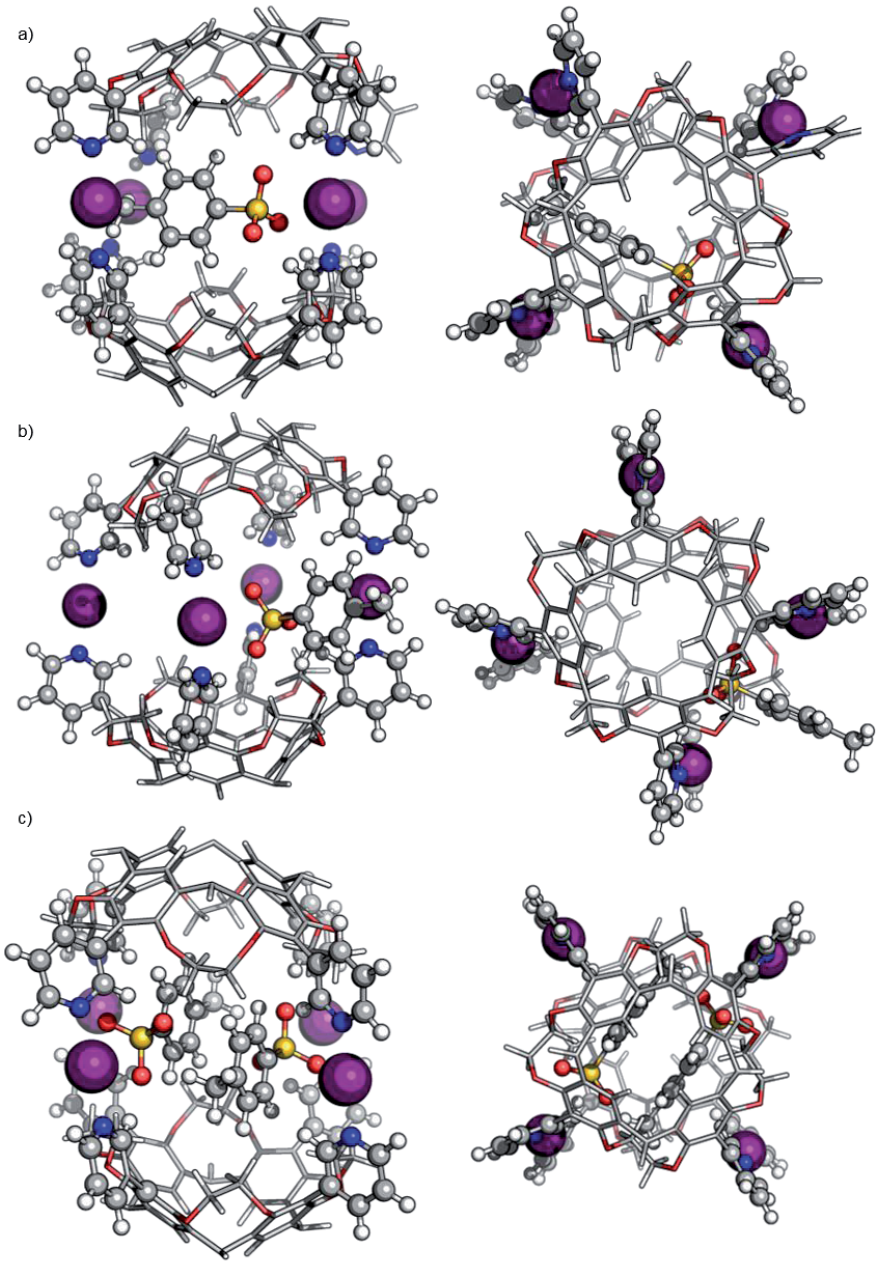

Figure S9: Calculated structures of dimeric halogen-bonded capsule **1** a) with one tosylate inside the cavity ($[2{\cdot}\mathbf{C_D}{+}4\ I{+}{\cdot}OTs]^{3+}$), b) with one tosylate outside the cavity ($[2{\cdot}\mathbf{C_D}{+}4\ I{+}{\cdot}OTs]^{3+}$) and c) with two tosylates inside the cavity ($[2{\cdot}\mathbf{C_D}{+}4I{+}2{\cdot}OTs]^{4+}$). PBE0/def2-SVP was used for I^+, pyridines and tosylates (ball-and-stick representation); AM1 for cavitand (stick representation). For clarity, the *n*-hexyl side chains have been reduced to hydrogens in the image, but were included in the calculations.

6. References

[1] Turunen, L.; Warzok, U.; Puttreddy, R.; Beyeh, N. K.; Schalley, C. A.; Rissanen, K. *Angew. Chem. Int. Ed.* **2016**, *55*, 14033–14036.

[2] Turunen, L.; Warzok, U.; Schalley, C. A.; Rissanen, K. *Chem* **2017**, *3*, 861–869.

6.3.5. Catalysis of “outer-phase” oxygen atom exchange reactions by encapsulated “inner-phase” water in {$V_{15}Sb_6$}-type polyoxovanadates

Michael Wendt*, Ulrike Warzok*, Christian Näther, Jan van Leusen, Paul Kögerler, Christoph A. Schalley, and Wolfgang Bensch

* Authors contributed equally to this work.

Chem. Sci. **2016**, *7*, 2684–2694.

Submitted on November 27, 2015, first published on January 8, 2016 in Chemical Science. Reprinted from Wendt *et al.*[224] (Published by The Royal Society of Chemistry).

An electronic version of the article is available (http://doi.org/10.1039/C5SC04571A).

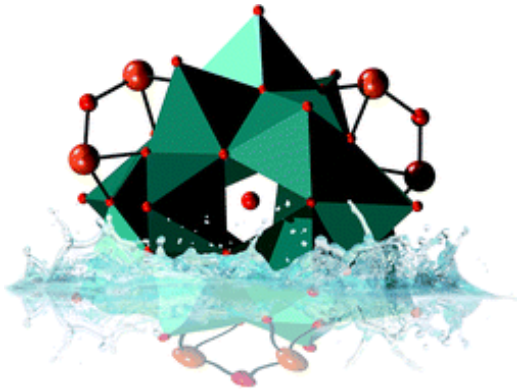

Figure A.5: The graphical abstract. Reproduced from Wendt *et al.*[224] (Published by The Royal Society of Chemistry).

Chemical Science

EDGE ARTICLE

Cite this: *Chem. Sci.*, 2016, **7**, 2684

Catalysis of "outer-phase" oxygen atom exchange reactions by encapsulated "inner-phase" water in $\{V_{15}Sb_6\}$-type polyoxovanadates†

Michael Wendt,‡[a] Ulrike Warzok,‡[b] Christian Näther,[a] Jan van Leusen,[c] Paul Kögerler,[c] Christoph A. Schalley*[b] and Wolfgang Bensch*[a]

Received 27th November 2015
Accepted 8th January 2016

DOI: 10.1039/c5sc04571a

www.rsc.org/chemicalscience

Antimonato polyoxovanadate (POV) cluster compounds $\{M(en)_3\}_3[V_{15}Sb_6O_{42}(H_2O)_x]\cdot nH_2O$ (M = Fe^{II}, Co^{II}, Ni^{II} and $x = 0$ or 1) obtained under solvothermal conditions exhibit unusual high water solubility making these compounds promising synthons for generation of new POV structure types. Electrospray ionization mass spectrometry provides evidence (i) for a water molecule encapsulated inside the cavity of a fraction of the spherical cluster shells, (ii) for a post-functionalization in water, namely a slow exchange of VO against Sb_2O, (iii) for the inner-phase reactivity of the encapsulated water that is capable of opening an oxo-bridge, and (iv) for a significant acceleration of the $^{16}O/^{18}O$ exchange reactions of oxygen atoms in the cluster periphery with surrounding $H_2{}^{18}O$, when encapsulated water is present. To the best of our knowledge, this is the first example in polyoxovanadate chemistry for the transduction of inner-phase reactivity of an encapsulated guest molecule into changes in the outer-phase reactivity of the cluster. Magnetic susceptibility measurements reflect the individual contributions of the frustrated $\{V_{15}\}$ spin polytope and the $\{M(en)_3\}^{2+}$ complexes, with very weak coupling between these groups.

Introduction

The chemistry of high-nuclearity polyoxomolybdate and polyoxotungstate (POMs) cluster shells significantly differs from that of polyoxovanadate clusters (POVs): (i) POMs are generally synthesised in acidic media, while POVs are usually prepared under basic conditions; (ii) POMs are mostly obtained applying soluble precursors consisting of pre-formed POM cluster shells, while POVs are synthesised from NH_4VO_3, V_2O_5, or $VOSO_4$ because no soluble pre-formed hetero-POV clusters are at hand; (iii) POMs normally crystallise under ambient conditions, whereas POVs often require solvothermal reactions; (iv) in the overwhelming number of structures of POM clusters MO_6 octahedra (M = Mo, W) are observed, while most POV cluster shells contain interconnected VO_5 square pyramids; (v) in POMs the metal centres are generally in the highest oxidation state, whereas POVs are characterised by V^{IV} or mixed-valent V^{IV}/V^{V} centres. Both groups of cluster compounds can be chemically and structurally modified by either attaching further building blocks such as transition metal complexes to the cluster shell or by replacement of Mo, W or V by heteroatoms.[1]

A unique class of heteroatom-modified POV clusters was discovered more than 25 years ago by Müller *et al.* who reported the first As-POV with the chemical formula $[V^{IV}{}_{15}As_6O_{42}(H_2O)]^{6-}$, which can be structurally derived from the $\{V_{18}O_{42}\}$ archetype structure.[2] Since then, several heteroatom-modified POV compounds containing As, Si, Ge and even Sb were discovered and characterised.[3–5]

Only little is known about the reactivity of polyoxovanadate clusters in solution despite of the increasing number of reports on novel POVs. This might be traced back to the fact that, in contrast to POMs, most POVs with high-nuclearity cluster shells are practically insoluble. This is a significant drawback compared to POM chemistry, because only a few V containing compounds are available that can be used as the starting material for the preparation of new POVs (*e.g.* $\{V_{10}O_{28}\}$)[6–8] but they do not include heteroatoms. In addition, nuclearity of the vanadate species in solution strongly depends on the pH value and polymerization at low pH resulting in formation of iso-POVs.[9] If a well soluble hetero-POV were at hand, it could be applied as a precursor in post-functionalisation studies to prepare new polyoxovanadate clusters. This strategy is well established for POMs, but virtually unknown for POVs. In this

[a]*Institut für Anorganische Chemie, Christian-Albrechts-Universität zu Kiel, Max-Eyth-Str. 2, 24118 Kiel, Germany. E-mail: wbensch@ac.uni-kiel.de*

[b]*Institut für Chemie und Biochemie der Freien Universität, Takustr. 3, 14195 Berlin, Germany. E-mail: c.schalley@fu-berlin.de*

[c]*Institut für Anorganische Chemie, RWTH Aachen, Landoltweg 1, 52074 Aachen, Germany*

† Electronic supplementary information (ESI) available: IR spectra, thermogravimetric analysis data, powder diffraction patterns, crystal morphology data, details of solubility studies, additional crystallographic and magnetochemical data and comment on the unassigned signals in the ESI mass spectra. CCDC 1432847–1432850. For ESI and crystallographic data in CIF or other electronic format see DOI: 10.1039/c5sc04571a

‡ MW and UW contributed equally to this work.

context, some fundamental questions arise concerning the stability of such POV clusters in solution, for example whether they will be intact or transform into other clusters or fragments and how this will depend on encapsulated guest molecules. A few studies on reactions of encapsulated or templating guest ions in POM clusters have unravelled some intriguing reactivity.[10] Analogous cases are unknown so far for POV clusters.

In this context, electrospray ionisation mass spectrometry (ESI-MS) has become a valuable tool in oxo-cluster chemistry and a significant body of knowledge has been acquired on the MS investigation of polyoxometallates.[11] ESI-MS experiments range from the clusters' analytical characterisation[12] to studies of their solution reactivity[13] and to gas-phase experiments aiming at unravelling reaction patterns in the gas phase[14] including the activation of small molecules such as methane.[15] Mass spectrometry together with isotope exchange reactions can provide profound insight into cluster reactivity as evidenced by elegant studies of Schüth *et al.* on silicate clusters.[16] ESI-MS experiments depend on the availablility of soluble samples. Consequently, detailed studies into the reactivity of POVs in solution by mass spectrometry are virtually unknown.

Here, we report the synthesis of three new compounds **I–III** with the composition $\{M(en)_3\}_3[V_{15}Sb_6O_{42}(H_2O)_x]\cdot nH_2O$ ($x = 0$, 1; $n \approx 15$; M = Ni^{II} (**I**), Co^{II} (**II**), Fe^{II} (**III**); en = ethylenediamine), that all crystallise in the non-centrosymmetric monoclinic space group *C*2. A second pseudopolymorph (**IV**), $\{Ni(en)_3\}_3[V_{15}Sb_6O_{42}(H_2O)_x]\cdot nH_2O$ ($n \approx 28$) crystallising in the trigonal space group *P*321 has been obtained by altering the synthesis conditions. In the present contribution, we report solvothermal syntheses, crystal structures, magnetic properties and electrospray ionisation mass spectrometric studies of cluster reactivity in water. Interestingly, these POVs exhibit a strikingly good solubility in water. Thorough ESI-TOF MS studies on **I** provide evidence for the occurrence of intact clusters in solution and the time-dependent transition of the $\{V_{15}Sb_6\}$ cluster shell into the Sb-richer $\{V_{14}Sb_8\}$ cluster at room temperature. Furthermore, $^{16}O/^{18}O$ exchange studies demonstrate that the rate of oxygen exchange is significantly higher, when a single water molecule is encapsulated within the cluster's cavity. This "inner-phase" water molecule thus affects strongly the "outer-phase" reactivity of the cluster with water and catalyses the oxygen exchange in the clusters' peripheries.

Experimental

General

CHN elemental analysis was done with a EUROEA Elemental Analyzer (EURO VECTOR Instruments and Software). IR spectroscopy (400–4000 cm^{-1}) was performed at room temperature using a Genesis FTIRTM spectrometer (ATI Mattson). Differential thermal analysis and thermogravimetry (DTA–TG) were carried out in nitrogen atmosphere (purity: 5.0; heating rate 1 K min^{-1}; flow rate: 75 mL min^{-1}; Al_2O_3 crucibles) using a Netzsch STA-409CD instrument. Energy dispersive X-ray analyses (EDX) and scanning electron microscopy (SEM) investigations were performed with a Philips Environmental Scanning Electron Microscope ESEM XL30 equipped with an EDX detector. X-Ray powder patterns were recorded on a STOE STADI-P diffractometer in transmission geometry (Cu-Kα_1 radiation, λ = 1.540598 Å; Ge monochromator; flat sample holders). The phase purity of the reaction products becomes obvious when the experimental patterns are compared with those calculated from single-crystal X-ray data. UV/Vis spectra were recorded on an Agilent 8453 spectrophotometer from Agilent Technologies, Waldbronn, in a wavelength range from 190 nm–1100 nm (deviation: ±0.5 nm, wavelength reproducibility: ±0.02 nm).

Syntheses

All chemicals (NH_4VO_3, Sb_2O_3, $NiCl_2\cdot 6H_2O$ (Merck); $CoCl_2\cdot 6H_2O$, $FeCl_2\cdot 4H_2O$ (Fluka); ethylenediamine (Grüssing); 1-(2-aminoethyl)piperazine (Alfa Aesar)) were purchased and used without further purification. All compounds were prepared under solvothermal conditions in DURAN® glass tubes (inner volume 11 mL) at 150 °C for 7 d using similar ratios for the reactants (see below for exact amounts used). After cooling to room temperature, the products were filtered off, washed with water and ethanol and dried *in vacuo*. The compounds were obtained as brown crystals. Compounds **I–III** could be prepared within a wide temperature range from 120–160 °C and the first crystals were observed after 3 d reaction time. Remarkably, crystals of **IV** were observed, when 1-(2-aminoethyl)piperazine was added to the reaction slurry and the reactant ratios were slightly altered compared to those for **I–III**. The role of 1-(2-aminoethyl)piperazine for product formation is not clear. In the following, the reaction conditions giving the best yields are summarised. The Ni and Co containing compounds (**I** and **II**) crystallised also applying an en : H_2O ratio of 1 : 3, while **III** could only be obtained for a fixed en:H_2O ratio of 1 : 5.

$\{Ni(en)_3\}_3[V_{15}Sb_6O_{42}(H_2O)_x]\cdot nH_2O$ ($n \approx 15$) in *C*2 (I). A solution of 1.7 mL ethylenediamine (25.4 mmol) and 2.3 mL H_2O was added to a mixture of 0.1573 g (1.34 mmol) NH_4VO_3, 0.3081 g (1.06 mmol) Sb_2O_3 and 0.1565 g (0.658 mmol) $NiCl_2\cdot 6H_2O$. The yield based on V was 86%. Elemental analysis: C 7.43, H 3.19, N 8.64%; calc. ($C_{18}H_{90}N_{18}Ni_3V_{15}Sb_6O_{51}$): C 7.10, H 2.98, N 8.28%. EDX analysis: V 46.0%, Sb 44.3%, Ni 9.7%; calc. ($V_{15}Sb_6Ni_3$): V 45.7%, Sb 43.7%, Ni 10.6%.

$\{Co(en)_3\}_3[V_{15}Sb_6O_{42}(H_2O)_x]\cdot nH_2O$ ($n \approx 15$) (II). A solution of 1.7 mL (25.4 mmol) ethylenediamine and 2.3 mL H_2O was mixed with 0.1573 g (1.34 mmol) NH_4VO_3, 0.3095 g (1.06 mmol) Sb_2O_3 and 0.2443 g (1.03 mmol) $CoCl_2\cdot 6H_2O$. The yield based on V was 48%. Elemental analysis: C 7.14, H 3.03, N 8.43%; calc. ($C_{18}H_{90}N_{18}Co_3V_{15}Sb_6O_{51}$): C 7.10, H 2.98, N 8.28%. EDX analysis: V 45.7%, Sb 43.9%, Co 10.4%; calc. ($V_{15}Sb_6Co_3$): V 45.7%, Sb 43.7%, Co 10.6%.

$\{Fe(en)_3\}_3[V_{15}Sb_6O_{42}(H_2O)_x]\cdot nH_2O$ ($n \approx 15$) (III). 2.3 mL (34.4 mmol) ethylenediamine and 1.7 mL H_2O were added to a mixture of 0.1571 g (1.34 mmol) NH_4VO_3, 0.3095 g (1.06 mmol) Sb_2O_3 and 0.1313 g (0.660 mmol) $FeCl_2\cdot 4H_2O$. The yield based on V was 68%. Elemental analysis: C 7.65, H 2.92, N 8.53%; calc. ($C_{18}H_{90}N_{18}Fe_3V_{15}Sb_6O_{51}$): C 7.12, H 2.99, N 8.30%. EDX analysis: V 46.5%, Sb 43.2%, Fe 10.3%; calc. ($V_{15}Sb_6Fe_3$): V 46.0%, Sb 44.0%, Fe 10.0%.

$\{Ni(en)_3\}_3[V_{15}Sb_6O_{42}(H_2O)_x]\cdot nH_2O$ ($n \approx 28$) in $P321$ (IV). A solution of 3 mL (22.9 mmol) 1-(2-aminoethyl)piperazine, 1 mL H_2O and 0.15 mL ethylenediamine (2.24 mmol) was added to a mixture of 0.1177 g (1.00 mmol) NH_4VO_3, 0.2326 g (0.800 mmol) Sb_2O_3 and 0.1260 g (0.531 mmol) $NiCl_2\cdot 6H_2O$. The yield based on V was 54%. Elemental analyses: C 7.58, H 2.61, N 8.73%; calc. ($C_{18}H_{72}N_{18}Ni_3V_{15}Sb_6O_{42}$): C 7.50, H 2.52, N 8.74%. EDX analysis: V 45.6%, Sb 44.1%, Ni 10.3%; calc. ($V_{15}Sb_6Ni_3$): V 45.7%, Sb 43.7%, Ni 10.6%.

Single-crystal structure analysis

Data collection was performed with a STOE Imaging Plate Diffraction System (IPDS-1) with Mo-Kα radiation ($\lambda = 0.71073$ Å). The crystal structures were solved with the program SHELXS-97 (ref. 17) and refined against F^2 using SHELXL-97 (ref. 18) for **II–III**, for **IV** with the version of 2013 and for **I** with the version of 2014. All non-hydrogen atoms were refined anisotropically. The C–H and N–H hydrogen atoms were positioned with idealised geometry and refined using a riding model. Water hydrogen atoms could not be located. A numerical absorption correction was performed (min./max. transmission: 0.4902/0.6693 for **I**, 0.5249/0.6407 for **II**, 0.3124/0.7136 for **III** and 0.5900/0.6543 for **IV**). The absolute structures were determined and agree with the selected setting (Flack *x*-parameter: −0.02(2) for **I**, −0.07(3) for **II**, −0.006(19) for **III** and −0.028(19) for **IV**). In total, nine water molecules could be located during structure refinements. After structure refinement of compounds **I–III**, several low electron density maxima were found which indicate the presence of additional disordered water molecules. These positions are not fully occupied and no reasonable structure model was found. Therefore, the data were corrected for disordered solvent using the SQUEEZE option in Platon.[19] For compound **IV**, all of the water atoms are fully disordered and thus, these data were also corrected for disordered solvent using SQUEEZE. The crystal of **IV** was merohedrally twinned around a 2-fold axis and therefore, a twin refinement (twin matrix $(0\bar{1}0)$ $(\bar{1}00)$ $(00\bar{1})$) was performed leading to a BASF parameter of 0.0297(9). One of the three independent $Ni(en)_3^{2+}$ counterions in **IV** exhibits slightly enlarged displacement parameters indicating some disorder. This complex is located on a special position, but if the refinement is performed in space groups of lower symmetry, the displacement parameters remain unchanged.

CCDC-1432847 (**I**), CCDC-1432848 (**II**), CCDC-1432849 (**III**), and CCDC-1432850 (**IV**) contain the supplementary crystallographic data for this paper.

Magnetochemical characterisation

Magnetic data of **I–III** were recorded using a Quantum Design MPMS-5XL SQUID magnetometer. The polycrystalline samples were compacted and immobilised into cylindrical PTFE capsules. Data were acquired as a function of the field (0.1–5.0 T at 2 K) and temperature (2.0–290 K at 0.1 T). They were corrected for the diamagnetic contributions of the sample holder and the corresponding compound (**I–III**: $\chi_{dia} = -6.27 \times 10^{-4}$ cm^3 mol^{-1}).

Mass spectrometry

Electrospray ionisation quadrupole-time-of-flight high resolution mass spectrometric (ESI-Q-TOF-HRMS) experiments were performed with a Synapt G2-S HDMS (Waters Co., Milford, MA, USA) instrument. The flow rate was set to 10 μL min^{-1}, the spray voltage to 1.6 kV, the sample cone voltage to 10 V, the source offset to 80 V, the nebuliser gas to 6 bar and the desolvation gas flow to 500 L h^{-1}. Around these initial settings, the parameters were optimised for maximum abundance of the desired intact $[M]^{n-}$ and $[M\cdot H_2O]^{n-}$ cluster ions (n = 2, 3) and minimum abundance of fragments. For collision-induced dissociation (CID), N_2 was used as the collision gas. Fragmentation experiments were conducted in the transfer cell of the Synapt G2-S HDMS instrument with collision energies of 15–25 V.

60 μM solutions from crystalline samples of **I** were prepared in H_2O, D_2O (Euriso-top, 99.90% D) and $H_2{}^{18}O$ (Campro Scientific, 97% ^{18}O), respectively. If not specified otherwise, the aqueous sample solutions were measured at this concentration after 30 min. Isotopic labelling experiments were accompanied by the corresponding control experiments in non-labelled H_2O. Time-dependent measurements were conducted on samples kept at 4 °C from which aliquots were taken and directly subjected to the mass spectrometric experiments. All reaction times given therefore refer to the reaction at 4 °C.

Results and discussion

Syntheses

Compounds **I–III** crystallised from slurries of NH_4VO_3, Sb_2O_3, the corresponding transition metal chlorides and ethylenediamine at pH ≈ 14. According to the structural results, the V^V centres are reduced to V^{IV} which is a common observation, when such syntheses are performed in the presence of reducing amines. The formation of **I–III** is relatively insensitive against changes of the synthetic parameters. Compound **IV** could only be crystallised in the presence of 1-(2-aminoethyl)piperazine (aep). Originally, the synthesis with aep was performed to prepare antimonato POVs functionalised with an organic molecule as recently observed in the two compounds $(C_6H_{17}N_3)_2[V_{15}Sb_6(C_6H_{15}N_3)_2O_{42}(H_2O)]\cdot 2.5H_2O$ and $[V_{14}Sb_8(C_6H_{15}N_3)_4O_{42}(H_2O)]\cdot 4H_2O$.[4] The Ni source and en were added to enhance the structural diversity by an *in situ* formed complex. Surprisingly, the presence of aep in the reaction afforded crystallisation of **IV** as a (pseudo)polymorph of **I**.

Characterisation and solubility studies

The IR spectra of **I–IV** (Fig. S1 and Table S1; ESI†) show the typical strong stretching vibration of the V^{IV}=O group at around 960 cm^{-1}. The DTA-TG curves of the samples are complex and exhibit no pronounced weight loss steps (Fig. S2, ESI†). For **I–III**, the total weight change observed up to *ca.* 250 °C corresponds to a loss of *ca.* 15 water molecules. Phase purity of the crystalline products was verified by X-ray powder diffraction (Fig. S3 and S4, ESI†). The crystal sizes and morphology were analyzed by SEM (Fig. S5, ESI†).

While solubility tests with less polar solvents such as alcohols, acetone, dichloromethane, chloroform and alkanes failed, compounds **I–IV** are surprisingly well soluble in distilled water. The maximum solubility in water has been determined for **I** to be 1.19 g L^{-1}. The pH-value of a saturated solution increases from 6.5 (distilled water) to 8.2 (for details, see ESI†).

The product recovered after crystallisation from a saturated water solution was again characterised by X-ray powder diffraction, CHN analysis and IR spectroscopy. No significant changes were observed compared to the sample before dissolution. The starting material could thus be recovered unchanged, although with somewhat poorer crystallinity.

Crystal structures

Compounds **I–III** crystallise in the chiral Sohncke space group *C*2 and **IV** in *P*321. Selected crystallographic data and refinement results are summarised in Table S2 (ESI†). In **I–III**, the three unique Sb atoms are on general positions, one of the eight crystallographically independent V atoms is located on a general position, and one of the three Ni centres is on a special position. In the structure of **IV**, the atoms V2, O1, O5, Ni1 and Ni3 are on special positions, whereas all other atoms are on general positions. All structures consist of isolated $[V_{15}Sb_6O_{42}(H_2O)_x]^{6-}$ ($x = 0$, 1) clusters with charge-compensating $\{M(en)_3\}^{2+}$ complexes. Residual electron density in the cluster cavities is consistent with single water molecules encapsulated in a fraction of the clusters. The cluster shell is constructed from 15 VO_5 square pyramids sharing common edges and vertices and three Sb_2O_5 handles formed by corner-sharing of two SbO_3 moieties (Fig. 1). The anion is structurally related to the $\{V_{18}O_{42}\}$ archetype. Replacing three VO_5 square pyramids by three Sb_2O_5 moieties yields the anions of the compounds under study here. The V–O bond lengths in the VO_5 square pyramids are characterised by a short terminal V=O bond (*ca.* 1.6 Å) and four bonds to μ_3-bridging O atoms (*ca.* 1.9–2.0 Å; Tables S3–S6, ESI†); as also observed in many POVs and chemically modified polyoxovanadates.[3] The Sb–O bond lengths (1.9–2.0 Å) are typical for Sb^{III}–O and match well those reported for other Sb-POVs.[5,20] The cluster shells and $\{M(en)_3\}^{2+}$ counterions in **I–III** are arranged in a layer-like fashion with alternating anions and cations along all three axes (Fig. 2). The constituents in the structure of **IV** exhibit a similar arrangement (Fig. S7, ESI†). The oxidation states of Sb and V were determined as +III and +IV applying the bond valence sum method[21] (BVS; see ESI† for details).

All four compounds contain three $\{M(en)_3\}^{2+}$ cations in distorted octahedral coordination geometries adopting the Δ and Λ isomer as configurations (Fig. 3). The M–N bond lengths (Tables S7–S10, ESI†) are in accordance with literature data.[22] The distortion of the octahedra is evidenced by the N–M–N angles.

A dense hydrogen bonding network exists in the crystals between the NH hydrogen atoms of the ethylenediamine ligands and the oxygen atoms of the cluster anions (Tables S11–S14, ESI†). Not only terminal oxygen atoms are involved in H-bonding interactions, but also μ_3-bridging O atoms. The ethylenediamine molecules also form hydrogen bonds to crystal water.

Magnetic properties

The experimental magnetic susceptibility data for compounds **I–III** are shown in Fig. 4 as the temperature dependence of $\chi_m T$ at 0.1 Tesla, and in Fig. S8 (ESI†) as molar magnetisation M_m *vs.* magnetic field B at 2 K. The $\chi_m T$ *vs.* T curves of all compounds are approximately linear from 290 K to 150 K. Aside from the differences in the absolute values of $\chi_m T$, the compounds show distinctly different $\chi_m T$ evolution on further decrease in temperature, which primarily reflects the single-ion contributions of the different $\{M(en)_3\}^{2+}$ spin centres: for **I**, $\chi_m T$ remains almost constant from 100 K to 20 K and subsequently decreases down to 3.76 cm^3 K mol^{-1} at 2 K. For **II**, $\chi_m T$ displays a steady decrease, reaching $\chi_m T = 5.35$ cm^3 K mol^{-1} at 2 K. For **III**, the slope slightly decreases for 150 K $\geq T \geq$ 100 K, and rapidly increases for lower temperatures, resulting in 3.48 cm^3 K mol^{-1}

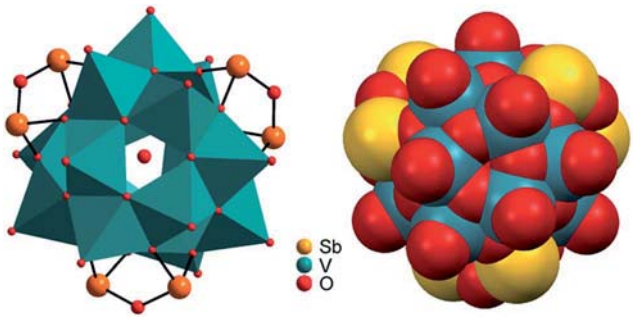

Fig. 1 Left: Polyhedral representation of the $[V_{15}Sb_6O_{42}(H_2O)_x]^{6-}$ cluster anion. A part of the cluster anions contains encapsulated water molecules. Red: oxygen; orange: antimony. Right: Space-filling representation showing the cluster to be tightly closed so that the encapsulated water is trapped inside the cluster cavity.

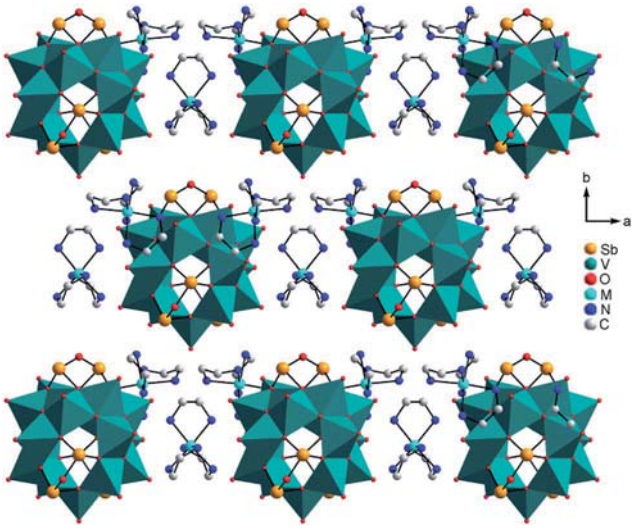

Fig. 2 Arrangement of the cluster anions and cations in the structures of **I–III**. Hydrogen atoms and water molecules are not shown.

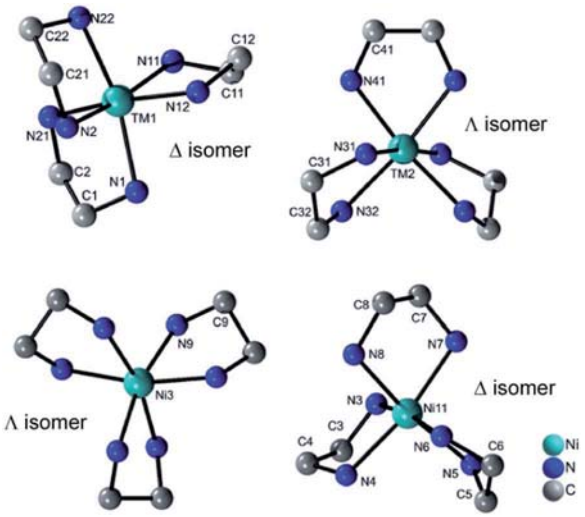

Fig. 3 Molecular structures of the two different isomers of the $\{M(en)_3\}^{2+}$ cations in the structures of I–III (top) and of IV (bottom). H atoms are not displayed.

at 2 K. At 290 K, the $\chi_m T$ values of compounds **I–III** are above those expected for three non-interacting high-spin transition metal centres M (**I**: 5.72 cm^3 K mol^{-1}, expected:[23] 2.94–4.60 cm^3 K mol^{-1}, **II**: 10.41 cm^3 K mol^{-1}, expected:[23] 6.94–10.14 cm^3 K mol^{-1}, **III**: 13.58 cm^3 K mol^{-1}, expected:[23] 9.76–12.19 cm^3 K mol^{-1}). On the other hand, these values are significantly below the expected values that are obtained by adding the contributions of 15 non-interacting V^{4+} centres, a consequence of the very strong antiferromagnetic coupling between the spin-1/2 vanadyl groups in the two outer V_6 rings in $\{V_{15}Sb_6\}$.

Due to the rather large metal–metal distances and the absence of bridging ligands, the exchange interactions between the $\{M(en)_3\}^{2+}$ complexes and the POV cluster are expected to be negligible. Since the susceptibility data for the isolated $\{V_{15}Sb_6\}$ cluster are known,[5a] a first estimation of the magnetic properties of the $\{M(en)_3\}^{2+}$ complexes within the compounds can be obtained by the following subtraction method. We use **I** as the reference system, since an octahedrally coordinated Ni^{2+} (d^8) centre can be treated as a spin-only system due to the orbital singlet ground term $^3A_2$, resulting in nearly temperature-independent $\chi_m T$ values. $\chi_m T$ data of **I** are subtracted by scaled $\chi_m T$ data of $[V_{15}Sb_6O_{42}(H_2O)_x]^{6-}$, yielding a curve (Fig. 4a, blue circles) corresponding to the expected single-ion contributions of three spin-1 Ni^{2+} centres. The thus-determined scaling factor of *ca.* 0.9 reflects differences in the amount of crystal solvents and the cationic lattice. The corresponding scaled contribution for the individual $\{V_{15}Sb_6\}$ polyoxoanion is shown in Fig. 4a–c as green circles for reference. The same subtractive method, employing the same scaling factor, is then applied to compounds **II** (Co^{2+}, d^7) and **III** (Fe^{2+}, d^6) in which ligand field effects dominate the lower temperature behaviour of $\chi_m T$.

Our computational framework CONDON 2.0,[24] employing a "full model" Hamiltonian has been used to model the post-subtraction susceptibility data of **I–III** (Fig. 4 and S8,† open blue circles). Since the octahedral site symmetry is slightly distorted,

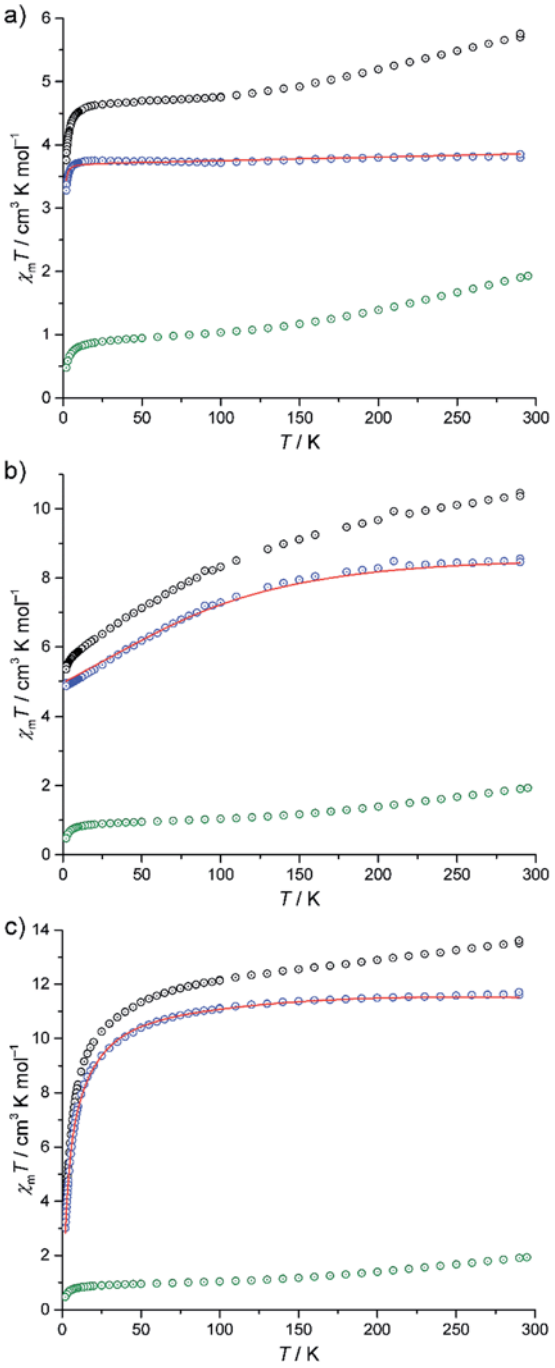

Fig. 4 Temperature dependence of $\chi_m T$ for (a) **I**, (b) **II** and (c) **III**. Black circles: experimental data; green circles: $\chi_m T([V_{15}Sb_6O_{42}(H_2O)_x]^{6-})$ (scaled); blue circles: difference of the experimental and $[V_{15}Sb_6O_{42}(H_2O)_x]^{6-}$ data. Red lines: least-squares fits.

a single additional ligand field parameter B_0^2 (with respect to perfect octahedral symmetry O_h) is introduced which reflects C_{4v} site symmetry. The mean field parameter zJ' representing potential exchange interactions is allowed to vary to test the hypothesis of negligible exchange interactions. The least-squares fits (of moderate goodness-of-fit, SQ ≈ 2% for **I–III**) are shown as red lines in Fig. 4 and S8 (ESI†), and the

corresponding model parameters are given in Table S15 (ESI†). We emphasise that the subtraction method employed here can only be understood as a first approximation and the fit parameters should be interpreted accordingly. The ligand field parameters represent a ligand field of distorted octahedral symmetry, and a ligand field splitting of 10 Dq approximately 10 000 cm^{-1} (**I**), 16 000 cm^{-1} (**II**), and 7000 cm^{-1} (**III**). Within the limits of method, the small mean field parameters zJ' (**I**: -0.01 cm^{-1}, **II**: +0.01 cm^{-1}, **III**: -0.53 cm^{-1}) are in agreement with virtual absence of exchange interactions between the transition metals of the $\{M(en)_3\}^{2+}$ complexes and neighbouring POV groups in the solid state. The different signs should also be understood as remnants of the subtraction method, as the absolute zJ' values are very small. Therefore, the apparent temperature dependences of $\chi_m T$ of **II** and **III** are not a consequence of potential exchange but due to ligand field effects within the $\{M(en)_3\}^{2+}$ complexes.

Electrospray ionisation mass spectrometry

Negative-mode electrospray ionisation of a 60 μM water solution of compound **I** 30 min after dissolving the crystalline sample results in the ESI mass spectrum shown in Fig. 5a. Two very similar series of signals are observed, one with doubly (*m*/*z* 1050–1300) and one with triply charged anions (*m*/*z* 650–800). Signals of the intact cluster appear as the triply charged $[V_{15}Sb_6O_{42}]^{3-}$ ($\mathbf{M}^{3-}$) ion at *m*/*z* 722 and its complex $[\mathbf{M}\cdot Ni(en)]^{2-}$ at *m*/*z* 1141. Overall, the cluster core in the crystalline sample is a hexaanion. As it appears in the mass spectrum at *m*/*z* 722 as a triply charged ion, three one-electron oxidation steps of V^{IV} to V^{V} have taken place, likely induced by the high voltage of the electrospray needle and supported by significant charge repulsion among the six charges in the absence of stabilizing counterions and solvent molecules after ionisation. As the $Ni(en)^{2+}$ fragment is doubly charged, the cluster core must be tetraanionic in the ion at *m*/*z* 1141 ($\mathbf{M}^{4-}$). This indicates that higher charge states can form even in the gas phase, when stabilizing counterions are present. A detailed look at the isotopic pattern of the *m*/*z* 722 trianion (Fig. 6a) reveals that actually two patterns overlap that are shifted against each other by $\Delta m/z = 0.33$. They can be assigned to $[V_{15}Sb_6O_{42}]^{3-}$ ($\mathbf{M}^{3-}$) and $[HV_{15}Sb_6O_{42}]^{3-}$ ($[\mathbf{M}\cdot H]^{3-}$), the latter of which also contains a quadruply charged cluster core with one charge compensated by a proton. From the calculated isotope patterns of these two ions, the experimental one can be simulated and one obtains a 4 : 1 ratio of the two ions when sprayed from pure water solution. As controls, the

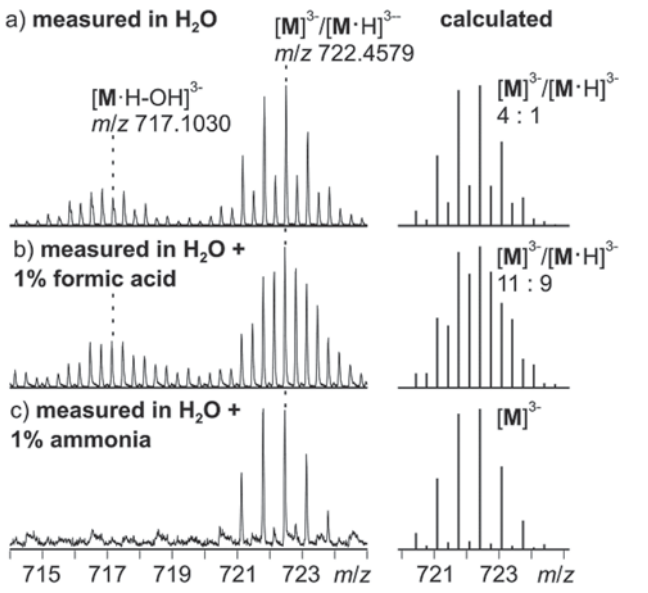

Fig. 6 Left: Experimental isotopic patterns of the trianion at *m*/*z* 722 as obtained from 60 μM solutions of **I** in (a) H_2O, (b) H_2O + 1% formic acid and (c) H_2O + 1% ammonia. Right: Calculated isotopic patterns of $\mathbf{M}^{3-}/[\mathbf{M}\cdot H]^{3-}$ mixtures with compositions fitted to approximate the experimental isotopic patterns.

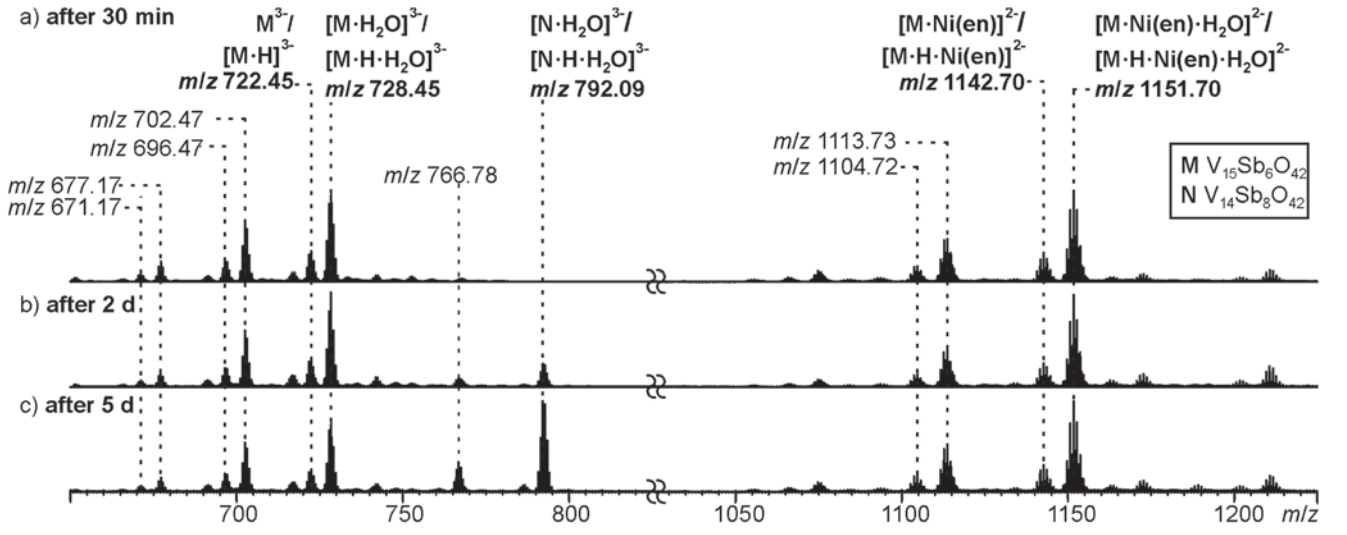

Fig. 5 ESI-Q-TOF-HRMS spectra of compound **I** (60 μM in H_2O) recorded from the same sample after (a) 30 minutes, (b) 2 days, (c) 5 days. For a more detailed discussion of the non-labeled signals, see ESI.†

same experiments were repeated with 1% of formic acid (Fig. 6b) and 1% of ammonia (Fig. 6c) added to the sample solution. Clearly, the ratio of the two ions is shifted towards protonated cluster under acidic and to the non-protonated one under basic conditions. This confirms the peak assignment. The signal at *m*/*z* 722 is accompanied by a somewhat smaller signal at *m*/*z* 717, which can be assigned to $[\mathbf{M}\cdot\mathrm{H}\text{–}\mathrm{OH}]^{3-}$. As this signal completely vanishes together with the protonated tri-anion cluster under basic conditions (Fig. 6c), it is very likely due to a fragmentation of $[\mathbf{M}\cdot\mathrm{H}]^{3-}$ during ionisation. The other signal at *m*/*z* 728 (Fig. 5a) corresponds to a superposition of the two water adducts $[\mathbf{M}\cdot\mathrm{H_2O}]^{3-}$ and $[\mathbf{M}\cdot\mathrm{H}\cdot\mathrm{H_2O}]^{3-}$. Similar considerations also apply to the doubly charged ions.

Cluster reactivity with water

In order to investigate the stability of **I** in water, the mass spectrometric experiments were repeated after longer reaction intervals up to five days (Fig. 5b and c). Over time, a new signal appears at *m*/*z* 792 which can be assigned to $[\mathrm{V_{14}Sb_8O_{42}}\cdot\mathrm{H_2O}]^{3-}$ ($[\mathbf{N}\cdot\mathrm{H_2O}]^{3-}$) and $[\mathbf{N}\cdot\mathrm{H}\cdot\mathrm{H_2O}]^{3-}$, an Sb-richer cluster formed by a net exchange of a V=O against an Sb–O–Sb unit. This rearrangement reveals an astonishing reactivity; especially when taking into account that all $\{\mathrm{V_{14}Sb_8O_{42}}\}$ clusters known so far were prepared under solvothermal conditions. From these findings, we conclude that the comparably high solubility of compound **I** enables its use for post-functionalisation into other cluster compounds. At longer reaction times, also a visible precipitate forms, which we attribute to the corresponding $[\mathrm{V_{16}Sb_4O_{42}(H_2O)}_x]$ product cluster that is expected to be cogenerated in a V=O against Sb–O–Sb exchange reaction.

H/D-exchange experiments

The solution-phase exchange of labile hydrogen atoms against deuterium can be followed by ESI mass spectrometry, when cluster **I** is dissolved in D_2O and then sprayed after different reaction times. The exchange of the ethylenediamine NH atoms is expected to be fast and should be easily monitored for the doubly charged ions $[\mathbf{M}\cdot\mathrm{Ni(en)}]^{2-}$ and $[\mathbf{M}\cdot\mathrm{Ni(en)}\cdot\mathrm{H_2O}]^{2-}$as they still contain one ethylenediamine ligand with four N-centred hydrogen atoms. Indeed, a complete exchange of these four hydrogen atoms occurs instantly for all en-containing ions (Fig. 7). Already after two minutes, a shift of the isotope patterns of $[\mathbf{M}\cdot\mathrm{Ni(en)}]^{2-}$ and $[\mathbf{M}\cdot\mathrm{Ni(en)}\cdot\mathrm{H_2O}]^{2-}$ by $\Delta m/z = 2$ is observed indicating that all four NH hydrogen atoms have been fully exchanged. Remarkably, the exchange of the two water hydrogen atoms in the water adduct $[\mathbf{M}\cdot\mathrm{Ni(en)}\cdot\mathrm{H_2O}]^{2-}$ is very slow and proceeds only over days (Fig. 7). This result is not in agreement with an intact cluster structure that is incompletely desolvated during ionisation. Any weakly bound solvent water molecule in the cluster periphery should be replaced by a D_2O immediately, when the cluster is sprayed from deuterated water. Therefore, the H_2O molecule must be an integral part of the cluster structure in solution. Two possibilities exist: either the water molecule has added to and opened one of the oxo-bridges resulting in a structure bearing two OH groups in the cluster shell or one water molecule is encapsulated inside the

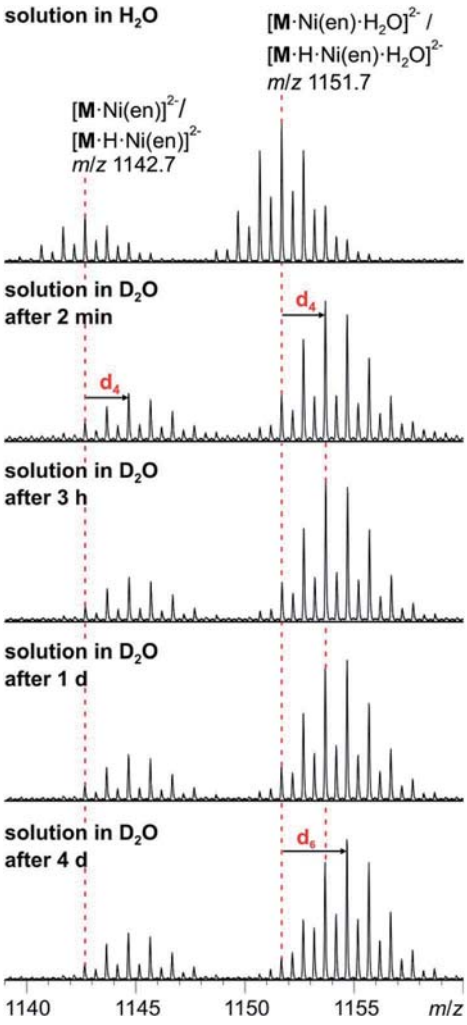

Fig. 7 H/D-exchange experiment. ESI-MS measurements with compound **I** (60 μM solution in D_2O) after different reaction intervals.

cavity of the closed cluster. As one would certainly expect, the metal ion-centred OH groups to be acidified by the metal ion, the dihydroxy structure is also expected to undergo a fast H/D-exchange reaction. Consequently, the only structure of the water adduct, which is in agreement with the slow H/D-exchange, is a closed capsule with a single water ion inside. This structure is not only in agreement with the fact that a potential adduct containing two water molecules has never been observed, but is also in agreement with the residual electron density observed in the crystal structure (see above). Given the tightly closed cluster shell (Fig. 1, right), a slow exchange of the intact encapsulated water molecule through portals in the cluster walls can be ruled out. We thus rationalise the finding of the slow H/D-exchange as follows: the inner-phase water attacks one of the vanadium ions as a weak nucleophile. This step is followed by opening one of the oxo-bridges so that two OH groups exist, which can undergo the H/D-exchange reaction. One of the initial steps (attack of the vanadium ion or oxo-bridge opening) is rate-determining so that the exchange is slow, even when the exchange of the hydrogen atoms in the open, dihydroxy intermediate is fast.

Back reaction after the exchange leads back to the closed capsule with a water molecule residing in the cavity. These experiments thus demonstrate that the water-filled cluster under study exhibits quite remarkable inner-phase reactivity that can be monitored by ESI-MS.

Tandem MS experiments

MS/MS experiments were performed by first mass-selecting either one of the complexes $\mathbf{M}^{3-}/[\mathbf{M}\cdot\mathrm{H}]^{3-}$, $[\mathbf{M}\cdot\mathrm{H_2O}]^{3-}/[\mathbf{M}\cdot\mathrm{H}\cdot\mathrm{H_2O}]^{3-}$, $\mathbf{N}^{3-}/[\mathbf{N}\cdot\mathrm{H}]^{3-}$ and $[\mathbf{N}\cdot\mathrm{H_2O}]^{3-}/[\mathbf{N}\cdot\mathrm{H}\cdot\mathrm{H_2O}]^{3-}$ (m/z 722, 728, 786, 792) and subsequently subjecting them to collision-induced dissociation (CID). Note that the intensity of the pure $\mathbf{M}^{3-}$ trianion obtained, when ammonia is added to the sample solution, is too low for this experiment. Therefore, the experiments have been conducted with the overlapping clusters.

The fragmentation of the clusters encapsulating water begins with a loss of a water molecule yielding $\mathbf{M}^{3-}/[\mathbf{M}\cdot\mathrm{H}]^{3-}$ and $\mathbf{N}^{3-}/[\mathbf{N}\cdot\mathrm{H}]^{3-}$, respectively (Fig. 8a and c). All subsequent fragmentation reactions are qualitatively the same as those observed for mass-selected $\mathbf{M}^{3-}/[\mathbf{M}\cdot\mathrm{H}]^{3-}$ and $\mathbf{N}^{3-}/[\mathbf{N}\cdot\mathrm{H}]^{3-}$ generated in the ion source (Fig. 8b and d): loss of a hydroxyl radical from the protonated clusters and electron losses to yield the corresponding doubly charged clusters $\mathbf{M}^{2-}/[\mathbf{M}\cdot\mathrm{H}]^{2-}$ and $\mathbf{N}^{2-}/[\mathbf{N}\cdot\mathrm{H}]^{2-}$. Subsequent losses of SbO units and further fragmentation of the cluster core produce the other fragments observed.

Most interestingly, the water loss from $[\mathbf{M}\cdot\mathrm{H_2O}]^{3-}/[\mathbf{M}\cdot\mathrm{H}\cdot\mathrm{H_2O}]^{3-}$ is clearly less energy demanding than the electron loss as no $[\mathbf{M}\cdot\mathrm{H_2O}]^{2-}/[\mathbf{M}\cdot\mathrm{H}\cdot\mathrm{H_2O}]^{2-}$ ions are visible in the spectrum in Fig. 8a. Its activation barrier must consequently be smaller than the (unfortunately unknown) electron affinity of the cluster dianion in the gas phase. However, the ions $[\mathbf{M}\cdot\mathrm{H}-\mathrm{OH}]^{3-}$ (very small signal) and $[\mathbf{M}\cdot\mathrm{H}]^{2-}$ appear simultaneously as fragments from $[\mathbf{M}\cdot\mathrm{H}]^{3-}$. This implies that the electron and OH losses compete and thus are similar in energy. Consequently, the water loss from $[\mathbf{M}\cdot\mathrm{H}\cdot\mathrm{H_2O}]^{3-}$ has a lower barrier than the OH loss from $[\mathbf{M}\cdot\mathrm{H}]^{3-}$.

These considerations render mechanisms for the water loss from $[\mathbf{M}\cdot\mathrm{H}\cdot\mathrm{H_2O}]^{3-}$ unlikely which involve the simultaneous cleavage of more than one metal–oxygen bond. Therefore, we suggest the "swinging-door" mechanism shown in Scheme 1 (left) for the $\mathrm{H_2O}$ loss. The encapsulated water molecule initially attacks one of the vanadium ions and – as postulated above to rationalise the H/D-exchange – opens one of the oxo-bridges. After two proton transfer steps, the bridge closes again, this time however with a water molecule as the leaving group that is lost on the outside of the cluster. The water loss in the gas phase is entropically favourable due to particle number increase. Both the H/D-exchange reaction in water solution and the water loss mechanism in the gas phase thus share common elementary steps.

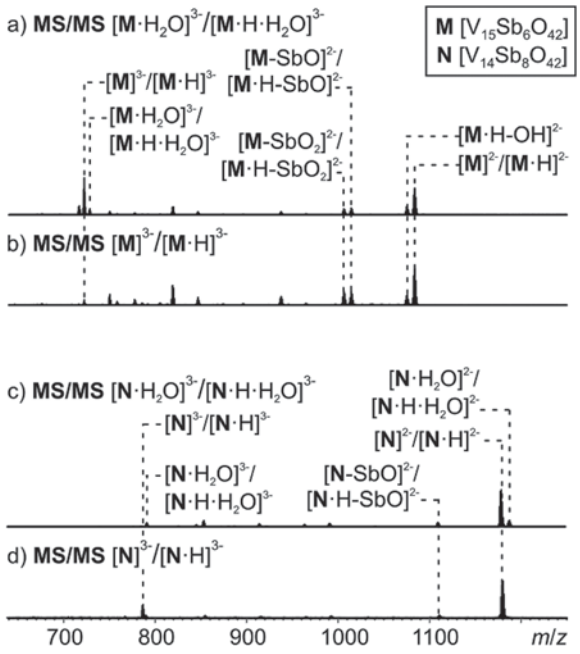

Fig. 8 Tandem MS experiment of (a) complex $[\mathbf{M}\cdot\mathrm{H_2O}]^{3-}$, (b) complex $\mathbf{M}^{3-}$, (c) complex $[\mathbf{N}\cdot\mathrm{H_2O}]^{3-}$, (d) complex $\mathbf{N}^{3-}$.

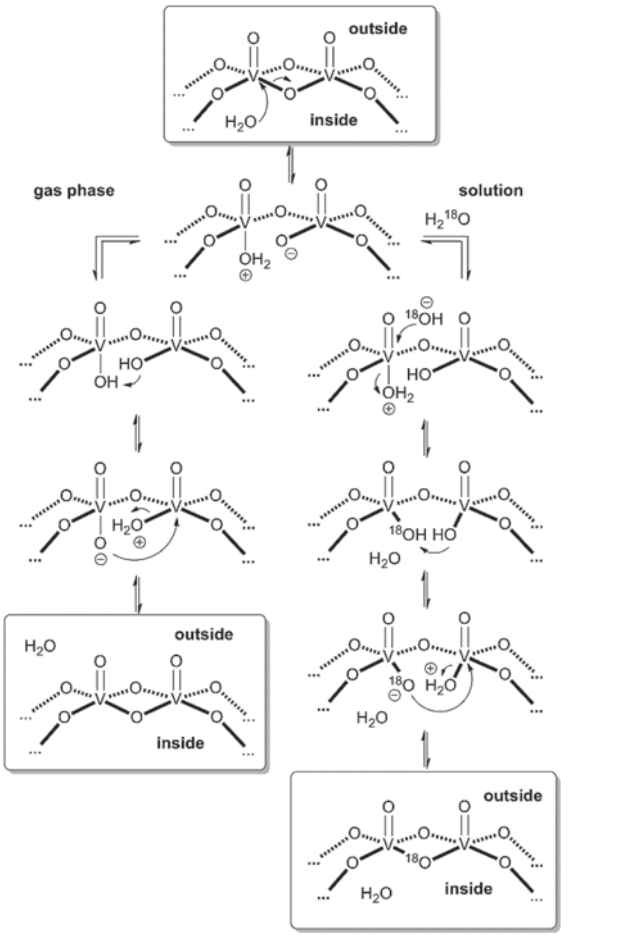

Scheme 1 "Swinging door" mechanism for the water loss from $[\mathbf{M}\cdot\mathrm{H_2O}]^{3-}$ in the gas phase (left) and mechanism for the solution-phase $^{16}O/^{18}O$ exchange in cluster **I** (right).

$^{16}O/^{18}O$ exchange experiments

When a sample of cluster **I** was prepared in $H_2{}^{18}O$, an exchange of ^{16}O against the water ^{18}O atoms is observed (Fig. 9). Again, the exchange is slow and proceeds over days being in agreement with further investigations of Murman *et al.*[25] However, most strikingly, all cluster ions with encapsulated water undergo a much faster $^{16}O/^{18}O$ exchange reaction than the water-free cluster ions. Even though a detailed kinetic fitting of the data is not straightforward because of overlapping isotope patterns and the need to apply different rate constants for different types of oxygen atoms in the cluster structure, the acceleration is easily seen qualitatively in the spectra after a reaction time of five days: the shift of the maximum of the isotopic patterns of water-free $\mathbf{M}^{3-}/[\mathbf{M}\cdot H]^{3-}$ corresponds to the exchange of only five oxygen atoms, while the isotopic patterns of the corresponding water-containing cluster ions $[\mathbf{M}\cdot H_2O]^{3-}$ and $[\mathbf{M}\cdot H\cdot H_2O]^{3-}$ have shifted by the equivalent of 19 oxygen atom exchanges.

This finding leads to several conclusions: (i) the interpretation of the H/D-exchange experiments is confirmed in that two distinctly different structures exist in solution – the cluster with and that without encapsulated water. The water molecule is thus not a solvate water. (ii) The two structures with and without encapsulated water do not interconvert quickly on the time scale of the $^{16}O/^{18}O$ exchange experiment. Otherwise, the remarkable rate differences between the two cluster ions would not be observed. (iii) As the only difference between the two ions is the absence/presence of encapsulated water, the inner-phase water molecule clearly has a significant effect on the outer-phase reactivity. The information that the water molecule is present inside is thus transduced through the cluster shell and influences the cluster's reactions with the surrounding environment.

The post-functionalised V=O-to-Sb_2O exchange product appears as the $[\mathbf{N}\cdot H_2O]^{3-}/[\mathbf{N}\cdot H\cdot H_2O]^{3-}$ trianion pair and has undergone even more $^{16}O/^{18}O$ exchange steps (31 after 5 days). Very likely, some intermediates encompassed during the metal ion exchange reactions are not fully saturated and thus can exchange ^{16}O against ^{18}O even faster.

Based on the mechanistic considerations above, we suggest the $^{16}O/^{18}O$ exchange to proceed through similar initial steps. The acceleration of this reaction can easily be rationalised by invoking again an attack of the encapsulated water at one of the vanadium ions followed by oxo-bridge cleavage, the exchange reaction and reformation of the cluster which then incorporates an ^{18}O atom (Scheme 1, right). In contrast to the gas phase, the cluster is now surrounded by water so that an escape of the encapsulated water from the cavity is neither favoured by entropy (exclusion volume inside the cavity) nor enthalpy (non-solvated inner surface of the cluster). As the inner-phase water molecule is reformed after the $^{16}O/^{18}O$ exchange reaction and thus able to accelerate many exchange reactions, one can consider it a catalyst.

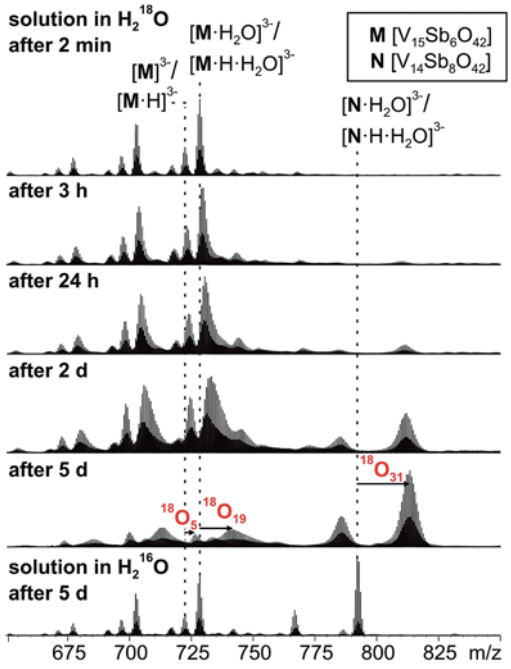

Fig. 9 $^{16}O/^{18}O$ exchange experiments performed with a 60 μM solution of **I** in $H_2{}^{18}O$ after different reaction intervals.

Conclusions

Four new heteroatom-modified polyoxovanadate compounds of the general composition $\{M(en)_3\}_3[V_{15}Sb_6O_{42}(H_2O)_x]\cdot nH_2O$ ($M = Fe^{II}$, Co^{II}, Ni^{II}) were synthesised under solvothermal conditions and characterised by a combination of complementary methods including crystallography and magnetic property measurements. The Ni compound crystallises in two pseudopolymorphs depending on the reaction conditions. Its unexpectedly high solubility in water makes it a perfect candidate for post-functionalisation studies which provide access to new polyoxovanadate clusters. While this strategy is well known for polyoxomolybdates and polyoxotungstates, the often limited solubility of larger polyoxovanadates so far hampered such an approach. The magnetic properties of the compounds can be rationalised by a qualitative model of additive contributions by strongly antiferromagnetically coupled $\{V_{15}Sb_6\}$ cluster units and the three high-spin $\{M(en)_3\}^{2+}$ complexes, with virtually no exchange coupling between those groups. In line with crystallography, the electrospray ionisation mass spectrometric experiments reveal that a large fraction of the clusters contains encapsulated water which is protected in solution against a fast H/D-exchange by the cluster shell. This inner-phase water molecule participates in the cluster's reactivity as it can accelerate oxo-bridge opening reactions by attacking a vanadium ion from the inside of the cluster cavity. Consequently, the water molecule inside the cavity displays inner-phase reactivity. Most fascinatingly, its presence also catalyses $^{16}O/^{18}O$ exchange reactions between the cluster shell and the surrounding water. Thus, the inner-phase reactivity of the encapsulated water has a significant effect on the outer-phase reactivity of the cluster as well. A transduction of the information that a water molecule is present inside thus affects the reactivity of the cluster periphery.

Acknowledgements

This work was supported by the Deutsche Forschungsgemeinschaft (priority program 1415 and CRC 1109) and the State of Schleswig-Holstein. We thank Dr Andreas Springer for introducing U. W. to the Synapt mass spectrometer and for inspiring discussions as well as Julian Hansen for his help in designing the TOC graphic.

Notes and references

1 (*a*) D.-L. Long, R. Tsunashima and L. Cronin, *Angew. Chem., Int. Ed.*, 2010, **49**, 1736; (*b*) K. Y. Monakhov, W. Bensch and P. Kögerler, *Chem. Soc. Rev.*, 2015, **44**, 8443; (*c*) A. Müller, H. Reuter and S. Dillinger, *Angew. Chem., Int. Ed. Engl.*, 1995, **34**, 2328; (*d*) Y. Haysashi, *Coord. Chem. Rev.*, 2011, **255**, 2270; (*e*) A. Dolbecq, E. Dumas, C. R. Mayer and P. Mialane, *Chem. Rev.*, 2010, **110**, 6009.

2 A. Müller and J. Döring, *Angew. Chem., Int. Ed. Engl.*, 1988, **27**, 1721.

3 (*a*) X. Wang, L. Liu, G. Zhang and A. J. Jacobson, *Chem. Commun.*, 2001, 2472; (*b*) Y. Gao, Y. Xu, Y. Cao and C. Hu, *Dalton Trans.*, 2012, **41**, 567; (*c*) A. Tripathi, T. Hughbanks and A. Clearfield, *J. Am. Chem. Soc.*, 2003, **125**, 10528; (*d*) Y. Gao, Y. Xu, S. Li, Z. Han, Y. Cao, F. Cui and C. Hu, *J. Coord. Chem.*, 2010, **63**, 3373; (*e*) T. Whitfield, X. Wang and A. J. Jacobson, *Inorg. Chem.*, 2003, **42**, 3728; (*f*) J. Wang, C. Näther, P. Kögerler and W. Bensch, *Inorg. Chim. Acta*, 2010, **363**, 4399; (*g*) J. Wang, C. Näther, P. Kögerler and W. Bensch, *Eur. J. Inorg. Chem.*, 2012, 1237; (*h*) J. Zhou, J. Zhang, W.-H. Fang and G.-Y. Yang, *Chem.–Eur. J.*, 2010, **16**, 13253; (*i*) Y. Gao, Y. Xu, K. Huang, Z. Han and C. Hu, *Dalton Trans.*, 2012, **41**, 6122; (*j*) J. Zhou, J.-W. Zhao, Q. Wei, J. Zhang and G.-Y. Yang, *J. Am. Chem. Soc.*, 2014, **136**, 5065; (*k*) J. Wang, C. Näther, M. Speldrich, P. Kögerler and W. Bensch, *CrystEngComm*, 2013, **15**, 10238; (*l*) S.-T. Zheng, M.-H. Wang and G.-Y. Yang, *Inorg. Chem.*, 2007, **46**, 9503; (*m*) S.-T. Zheng, J. Zhang and G.-Y. Yang, *J. Mol. Struct.*, 2004, **705**, 127; (*n*) X.-B. Cui, J.-Q. Xu, Y. Li, Y.-H. Sun and G.-Y. Yang, *Eur. J. Inorg. Chem.*, 2004, 1051; (*o*) A. Wutkowski, N. Evers and W. Bensch, *Z. Anorg. Allg. Chem.*, 2011, **637**, 2205; (*p*) A. Wutkowski, C. Näther, J. van Leusen, P. Kögerler and W. Bensch, *Z. Naturforsch., B: J. Chem. Sci.*, 2014, **69**, 1306; (*q*) C. Wang, G. Zhou, Z. Zhang, D. Zhu and Y. Xu, *J. Coord. Chem.*, 2011, **64**, 1198; (*r*) X.-X. Hu, J.-Q. Xu, X.-B. Cui, J.-F. Song and T. Wang, *Inorg. Chem. Commun.*, 2004, **7**, 264; (*s*) R. Kiebach, C. Näther and W. Bensch, *Solid State Sci.*, 2006, **8**, 964; (*t*) E. Antonova, A. Wutkowski, C. Näther and W. Bensch, *Solid State Sci.*, 2011, **13**, 2154; (*u*) Y. Gao, Z. Han, Y. Xu and C. Hu, *J. Cluster Sci.*, 2010, **21**, 163; (*v*) L. Zhang, X. Zhao, J. Xu and T. Wang, *J. Chem. Soc., Dalton Trans.*, 2002, 3275; (*w*) E. Antonova, C. Näther, P. Kögerler and W. Bensch, *Dalton Trans.*, 2012, **41**, 6957; (*x*) A. Wutkowski, C. Näther, P. Kögerler and W. Bensch, *Inorg. Chem.*, 2008, **47**, 1916.

4 E. Antonova, C. Näther, P. Kögerler and W. Bensch, *Angew. Chem., Int. Ed.*, 2011, **50**, 764.

5 (*a*) R. Kiebach, C. Näther, P. Kögerler and W. Bensch, *Dalton Trans.*, 2007, 3221; (*b*) E. Antonova, C. Näther and W. Bensch, *Dalton Trans.*, 2012, **41**, 1338; (*c*) E. Antonova, C. Näther and W. Bensch, *CrystEngComm*, 2012, **14**, 6853; (*d*) A. Wutkowski, C. Näther, P. Kögerler and W. Bensch, *Inorg. Chem.*, 2013, **52**, 3280; (*e*) E. Antonova, C. Näther, P. Kögerler and W. Bensch, *Inorg. Chem.*, 2012, **51**, 2311.

6 O. W. Howarth and M. Jarrold, *J. Chem. Soc., Dalton Trans.*, 1978, 503.

7 V. W. Day, W. G. Klemperer and O. M. Yaghi, *J. Am. Chem. Soc.*, 1989, **111**, 5959.

8 G. E. Johnson, N. M. Hasan and J. Laskin, *Int. J. Mass Spectrom.*, 2013, **354–355**, 333.

9 (*a*) M. T. Pope and B. W. Dale, *Q. Rev. Chem. Soc.*, 1968, **22**, 527; (*b*) N. McCann, M. Wagner and H. Hasse, *Dalton Trans.*, 2013, **42**, 2622.

10 (*a*) H. N. Miras, M. Sorus, J. Hawkett, D. O. Sells, E. J. L. McInnest and L. Cronin, *J. Am. Chem. Soc.*, 2012, **134**, 6980; (*b*) Q. Zheng, L. Vilà-Nadal, C. Busche, J. S. Mathieson, D.-L. Long and L. Cronin, *Angew. Chem., Int. Ed.*, 2015, **54**, 7895.

11 H. N. Miras, E. F. Wilson and L. Cronin, *Chem. Commun.*, 2009, 1297.

12 (*a*) M. N. Sokolov, V. P. Fedin, A. Müller, K. Hegetschweiler, W. Amrein and V. E. Fedorov, *Russ. J. Inorg. Chem.*, 1993, **38**, 828; (*b*) D. K. Walanda, R. C. Burns, G. A. Lawrance and E. I. von Nagy-Felsobuki, *J. Chem. Soc., Dalton Trans.*, 1999, 311; (*c*) D.-L. Long, Y.-F. Song, E. F. Wilson, P. Kögerler, S.-X. Guo, A. M. Bond, J. S. J. Hargreaves and L. Cronin, *Angew. Chem., Int. Ed.*, 2008, **47**, 4384; (*d*) H. N. Miras, M. N. C. Ochoa, D.-L. Long and L. Cronin, *Chem. Commun.*, 2010, **46**, 8148; (*e*) J. Gao, J. Yan, S. G. Mitchell, H. N. Miras, S. G. Boulay, D.-L. Long and L. Cronin, *Chem. Sci.*, 2011, **2**, 1502; (*f*) F. Li, D.-L. Long, J. M. Cameron, H. N. Miras, C. P. Pradeep, L. Xu and L. Cronin, *Dalton Trans.*, 2012, **41**, 9859; (*g*) Z.-G. Lin, B. Wang, J. Cao, B.-K. Chen, Y.-Z. Gao, Y.-N. Chi, C. Xu, X.-Q. Huang, R.-D. Han, S.-Y. Su and C.-W. Hu, *Inorg. Chem.*, 2012, **51**, 4435; (*h*) M. H. Rosnes, C. Yvon, D.-L. Long and L. Cronin, *Dalton Trans.*, 2012, **41**, 10071; (*i*) M. N. Corella-Ochoa, H. N. Miras, D.-L. Long and L. Cronin, *Chem.–Eur. J.*, 2012, **18**, 13743; (*j*) L. Miersch, T. Rüffer, D. Schaarschmidt, H. Lang, R. W. Troff, C. A. Schalley and M. Mehring, *Eur. J. Inorg. Chem.*, 2013, 1427; (*k*) S. S. Mal, O. Tröppner, I. Ivanović-Burmazović and P. Burger, *Eur. J. Inorg. Chem.*, 2013, 1960; (*l*) P. J. Robbins, A. J. Surman, J. Thiel, D.-L. Long and L. Cronin, *Chem. Commun.*, 2013, **49**, 1909; (*m*) K. Kastner, J. Forster, H. Ida, G. N. Newton, H. Oshio and C. Streb, *Chem.–Eur. J.*, 2015, **21**, 7686; (*n*) I. Nakamura, H. N. Miras, A. Fujiwara, M. Fujibayashi, Y.-F. Song, L. Cronin and R. Tsunashima, *J. Am. Chem. Soc.*, 2015, **137**, 6524.

13 See, for example: (*a*) J. Yan, D.-L. Long, E. F. Wilson and L. Cronin, *Angew. Chem., Int. Ed.*, 2009, **48**, 4376; (*b*) S. G. Mitchell, P. I. Molina, S. Khanra, H. N. Miras, A. Prescimone, G. J. T. Cooper, R. S. Winter, E. K. Brechin, D.-L. Long, R. J. Cogdell and L. Cronin, *Angew. Chem., Int.*

Ed., 2011, **50**, 9154; (*c*) E. F. Wilson, H. N. Miras, M. H. Rosnes and L. Cronin, *Angew. Chem., Int. Ed.*, 2011, **50**, 3720; (*d*) L. Miersch, M. Schlesinger, R. W. Troff, C. A. Schalley, T. Rüffer, H. Lang, D. Zahn and M. Mehring, *Chem.–Eur. J.*, 2011, **17**, 6985; (*e*) D. Mansfeld, L. Miersch, T. Rüffer, D. Schaarschmidt, H. Lang, T. Böhle, R. W. Troff, C. A. Schalley, J. Müller and M. Mehring, *Chem.–Eur. J.*, 2011, **17**, 14805; (*f*) C. Lydon, C. Busche, H. N. Miras, A. Delf, D.-L. Long, L. Yellowlees and L. Cronin, *Angew. Chem., Int. Ed.*, 2012, **51**, 2115; (*g*) M. Schlesinger, A. Pathak, S. Richter, D. Sattler, A. Seifert, T. Rüffer, P. C. Andrews, C. A. Schalley, H. Lang and M. Mehring, *Eur. J. Inorg. Chem.*, 2014, 4218; (*h*) M. N. Sokolov, S. A. Adonin, P. L. Sinkevich, C. Vicent, D. A. Mainichev and V. P. Fedin, *Dalton Trans.*, 2012, **41**, 9889; (*i*) A. M. Khenkin, I. Efremenko, J. M. L. Martin and R. Neumann, *J. Am. Chem. Soc.*, 2013, **135**, 19304; (*j*) M. Schlesinger, A. Pathak, S. Richter, D. Sattler, A. Seifert, T. Rüffer, P. C. Andrews, C. A. Schalley, H. Lang and M. Mehring, *Eur. J. Inorg. Chem.*, 2014, 4218; (*k*) Q. Jia, J. Cao, Y. Duan and C. Hu, *Dalton Trans.*, 2015, **44**, 553; (*l*) R. S. Winter, D.-L. Long and L. Cronin, *Inorg. Chem.*, 2015, **54**, 4151; (*m*) Q. Zheng, L. Vilà-Nadal, C. Busche, J. S. Mathieson, D.-L. Long and L. Cronin, *Angew. Chem., Int. Ed.*, 2015, **54**, 7895.

14 (*a*) L. Vilà-Nadal, A. Rodríguez-Fortea, L.-K. Yan, E. F. Wilson, L. Cronin and J. M. Poblet, *Angew. Chem., Int. Ed.*, 2009, **48**, 5452; (*b*) L. Vilà-Nadal, E. F. Wilson, H. N. Miras, A. Rodríguez-Fortea, L. Cronin and J. M. Poblet, *Inorg. Chem.*, 2011, **50**, 7811; (*c*) L. Vilà-Nadal, S. G. Mitchell, A. Rodríguez-Fortea, H. N. Miras, L. Cronin and J. M. Poblet, *Phys. Chem. Chem. Phys.*, 2011, **13**, 20136; (*d*) H. N. Miras, D. Stone, D.-L. Long, E. J. L. McInnes, P. Kögerler and L. Cronin, *Inorg. Chem.*, 2011, **50**, 8384; (*e*) L. Vilà-Nadal, S. G. Mitchell, D.-L. Long, A. Rodríguez-Fortea, X. Lopez, J. M. Poblet and L. Cronin, *Dalton Trans.*, 2012, **41**, 2264; (*f*) D. Sattler, M. Schlesinger, M. Mehring and C. A. Schalley, *ChemPlusChem*, 2013, **78**, 1005; (*g*) L. Vilà-Nadal, S. G. Mitchell, D.-L. Long, A. Rodríguez-Fortea, X. Lopez, J. M. Poblet and L. Cronin, *Dalton Trans.*, 2012, **41**, 2264; (*h*) L. Vilà-Nadal, S. G. Mitchell, D.-L. Long, A. Rodriguez-Fortea, X. Lopez, J. M. Poblet and L. Cronin, *Dalton Trans.*, 2012, **41**, 2264; (*i*) N. Al Hasan, G. Johnson and J. Laskin, *J. Am. Soc. Mass Spectrom.*, 2013, **24**, 1385; (*j*) Z. Lin, B. Wang, J. Cao, B. Chen, C. Xu, X. Huang, Y. Fan and C. Hu, *Eur. J. Inorg. Chem.*, 2013, 3458; (*k*) C. Vicent, S. A. Adonin, A. V. Anyushin, D. A. Mainichev and M. N. Sokolov, *Eur. J. Inorg. Chem.*, 2014, 5618.

15 (*a*) S. Feyel, D. Schröder, X. Rozanska, J. Sauer and H. Schwarz, *Angew. Chem., Int. Ed.*, 2006, **45**, 4677; (*b*) S. Feyel, D. Schöder and D. H. Schwarz, *J. Phys. Chem. A*, 2006, **110**, 2647; (*c*) S. Feyel, L. Scharfenberg, C. Daniel, H. Hartl, D. Schröder and H. Schwarz, *J. Phys. Chem. A*, 2007, **111**, 3278; (*d*) N. Dietl, M. Engeser and H. Schwarz, *Angew. Chem., Int. Ed.*, 2009, **48**, 4861; (*e*) N. Dietl, M. Engeser and H. Schwarz, *Chem.–Eur. J.*, 2009, **15**, 11100; (*f*) N. Dietl, M. Engeser and H. Schwarz, *Chem.–Eur. J.*, 2010, **16**, 4452; (*g*) N. Dietl, R. F. Höckendorf, M. Schlangen, M. Lerch, M. K. Beyer and H. Schwarz, *Angew. Chem., Int. Ed.*, 2011, **50**, 1430; (*h*) Z.-C. Wang, T. Weiske, R. Kretschmer, M. Schlangen, M. Kaupp and H. Schwarz, *J. Am. Chem. Soc.*, 2011, **133**, 16930.

16 (*a*) P. Bussian, F. Sobott, B. Brutschy, D. Schrader and F. Schüth, *Angew. Chem., Int. Ed.*, 2000, **39**, 3901; (*b*) S. A. Pelster, B. Weimann, B. B. Schaack, W. Schrader and F. Schüth, *Angew. Chem., Int. Ed.*, 2007, **46**, 6674; (*c*) B. B. Schaack, W. Schrader and F. Schüth, *Angew. Chem., Int. Ed.*, 2008, **47**, 9092; (*d*) B. B. Schaack, W. Schrader and F. Schüth, *Chem.–Eur. J.*, 2009, **15**, 5920; (*e*) B. B. Schaack, W. Schrader and F. Schüth, *J. Phys. Chem. B*, 2009, **113**, 11240.

17 G. M. Sheldrick, *Acta Crystallogr., Sect. A: Found. Crystallogr.*, 2008, **64**, 112.

18 G. M. Sheldrick, *SHELXS-97/2013/2014, Program for the Solution of Crystal Structures*, University of Göttingen, Göttingen, Germany, 1997/2013/2014.

19 A. L. Spek, *Acta Crystallogr., Sect. D: Biol. Crystallogr.*, 2009, **65**, 148.

20 E. Antonova, B. Seidlhofer, J. Wang, M. Hinz and W. Bensch, *Chem.–Eur. J.*, 2012, **18**, 15316.

21 M. O'Keeffe and N. E. Brese, *J. Am. Chem. Soc.*, 1991, **113**, 3226.

22 (*a*) C. L. Raston, A. H. White and A. C. Willis, *Aust. J. Chem.*, 1978, **31**, 415; (*b*) K. Cooke, A. V. Olenev and K. Kovnir, *Acta Crystallogr., Sect. E: Struct. Rep. Online*, 2013, **69**, m332; (*c*) H. Feng, B. Tu, Y. Q. Li, P. Lu and Z. M. Jin, *Acta Crystallogr., Sect. E: Struct. Rep. Online*, 2006, **62**, m14405.

23 H. Lueken, *Magnetochemie*, Teubner Verlag, Stuttgart, 1999.

24 (*a*) M. Speldrich, H. Schilder, H. Lueken and P. Kögerler, *Isr. J. Chem.*, 2011, **51**, 215; (*b*) J. van Leusen, M. Speldrich, H. Schilder and P. Kögerler, *Coord. Chem. Rev.*, 2015, **289–290**, 137.

25 G. K. Johnson, R. K. Murman and B. Bowman, *Transition Met. Chem.*, 1985, **10**, 181; R. K. Murman and K. C. Giese, *Inorg. Chem.*, 1978, **17**, 1160; R. K. Murman, *J. Am. Chem. Soc.*, 1974, **96**, 7836.

Electronic Supplementary Information

Catalysis of "Outer-Phase" Oxygen Atom Exchange Reactions by Encapsulated "Inner-Phase" Water in $\{V_{15}Sb_6\}$-type Polyoxovanadates

Michael Wendt[a,*], UlrikeWarzok[b,*], Christian Näther[a], Jan van Leusen[c], Paul Kögerler[c], Christoph A. Schalley[c,#], Wolfgang Bensch[a,#]

[a] *Institut für Anorganische Chemie, Christian-Albrechts-Universität zu Kiel, Max-Eyth-Str. 2, 24118 Kiel, Germany*
[b] *Institut für Chemie und Biochemie der Freien Universität, Takustr. 3, 14195 Berlin, Germany*
[c] *Institut für Anorganische Chemie, RWTH Aachen, Landoltweg 1, 52074 Aachen, Germany*

Contents

1. IR Spectra

In Figure S1, the IR spectra of compounds **I** – **III** are displayed. As compound **IV** is a (pseudo)polymorph of **I**, both have equal IR spectra. All bands were assigned to the organic molecules or to the cluster vibrations. The values and assignments are listed in Table S1.

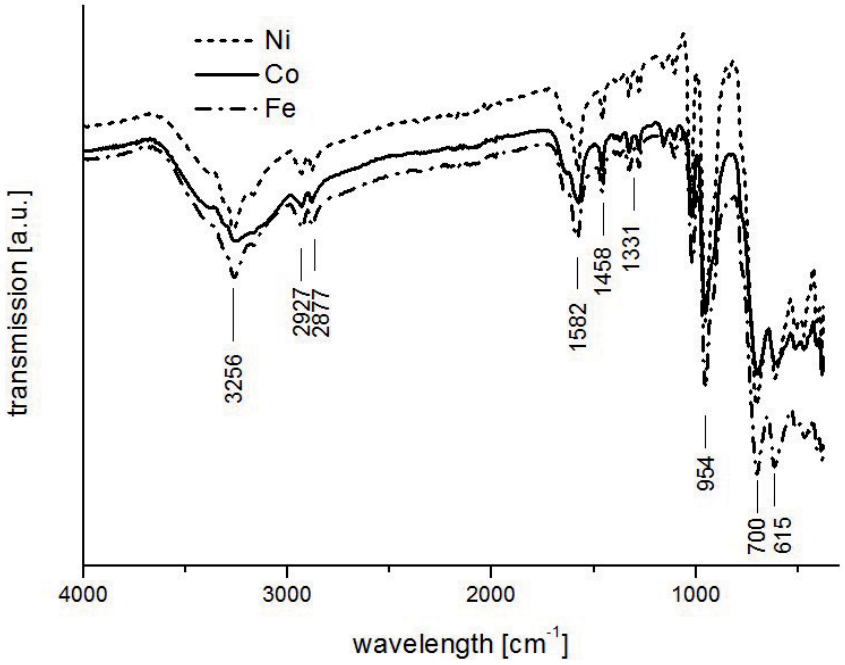

Figure S1. IR spectra of compounds **I** – **III**.

Table S1 Assignment of the IR peaks of compounds **I** – **III**.

	wavenumber [cm^{-1}]		**assignment**
Compound **I**	Compound **II**	Compound **III**	
3256	3257	3265	crystal water, NH_2-stretch
2927	2933	2934	CH_2 stretch
2877	2877	2884	
1582	1575	1575	NH_2 deformation
1458	1459	1460	CH_2 deformation
1331	1331	1331	OH deformation
954	953	954	V^{IV}=O stretch
700	696	701	M-O-M stretch
615	611	613	M-O-M stretch

2. Thermogravimetric Analysis

Figure S2 shows a DTA-TG curve of compound **I** as a representative example. For all compounds, first a weight loss due to water emission is observed being in accordance with the presence of ca. 15 water molecules in compounds **I** – **III**. The different not well resolved mass steps cannot be assigned to individual decomposition reactions. For compound **IV**, the first mass loss was ≈ 13 % and corresponds to the emission of ca. 28 water molecules.

Previous DTA-TG experiments on Sb-POVs[1] displayed analogous behavior resulting in no distinct steps for the decomposition and the weight loss above 700 °C is assigned to the sublimation of antimony, which is in agreement with our measurements.

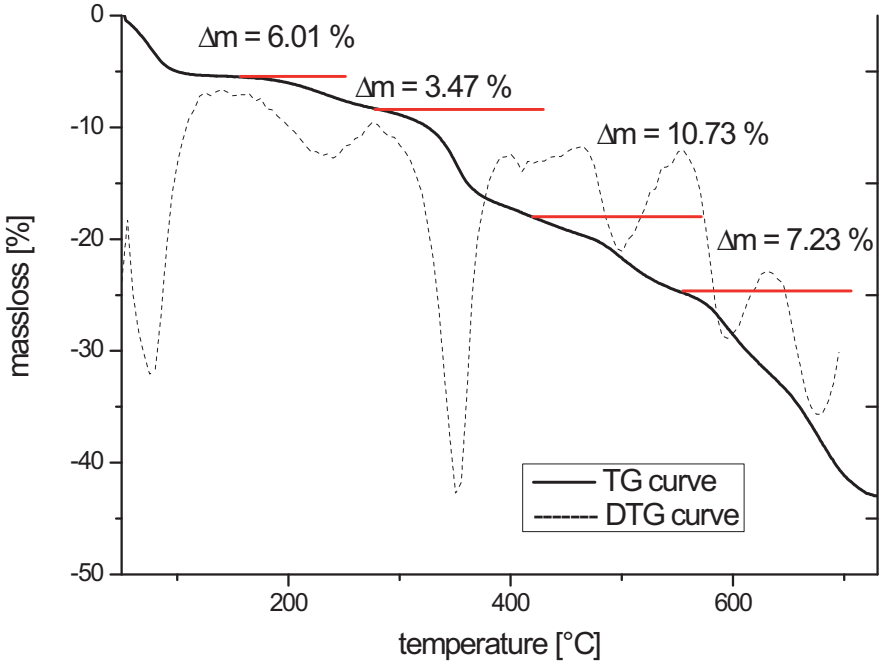

Figure S2. TG-curve (black) and DTG-curve (dotted) of compound **I** ($\{Ni(en)_3\}_3[V_{15}Sb_6O_{42}(H_2O)]\bullet xH_2O$ (heating rate: 1 K min^{-1}).

3. Powder Diffraction Patterns

Figures S3 and S4 indicate phase purity of all four compounds **I** – **IV** as evidenced by a comparison of experimental powder patterns with calculated patterns using single crystal data. Both reflection intensities and 2θ angles are in excellent agreement with the calculated diffractions.

a)

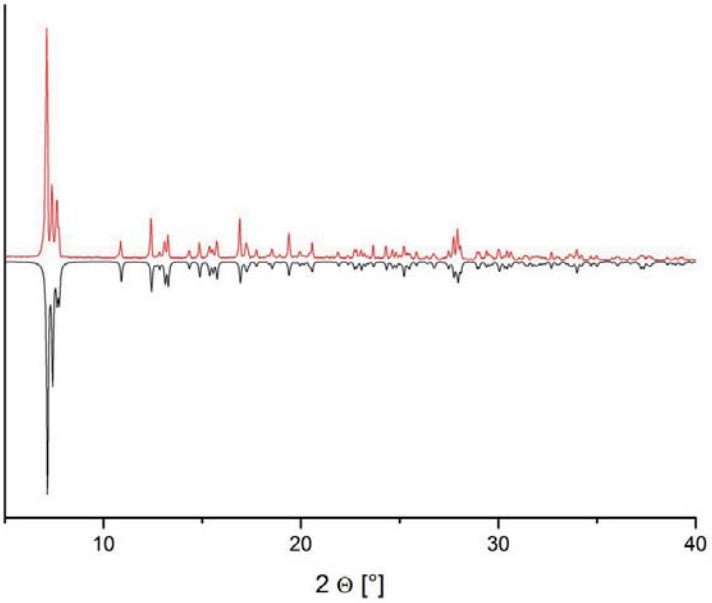

b)

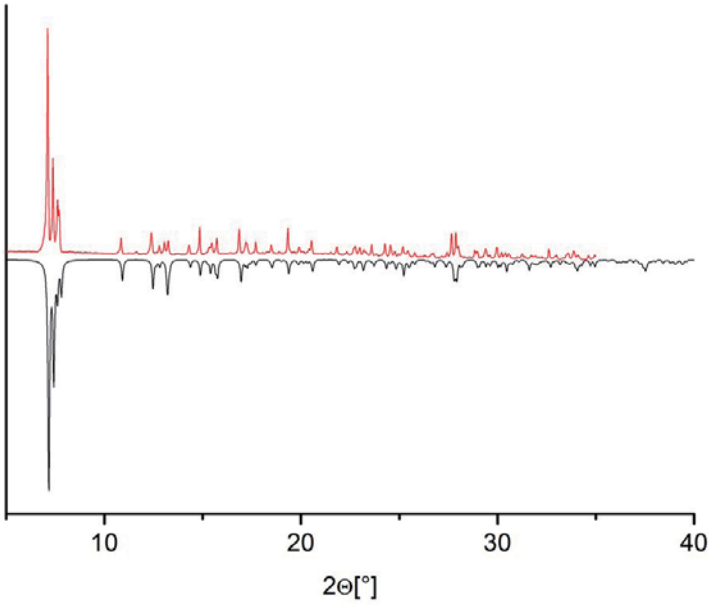

c)

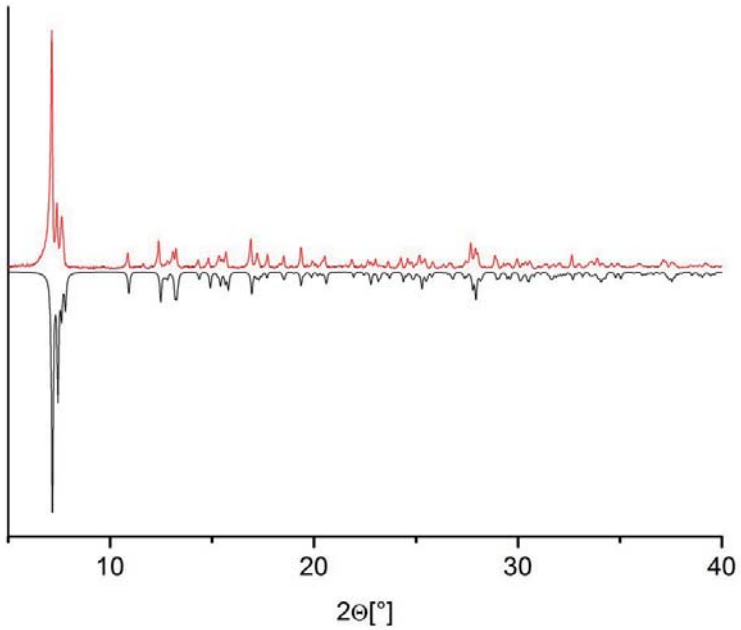

Figure S3. Measured (red) and calculated (black) powder diffraction patterns of compound **I**.

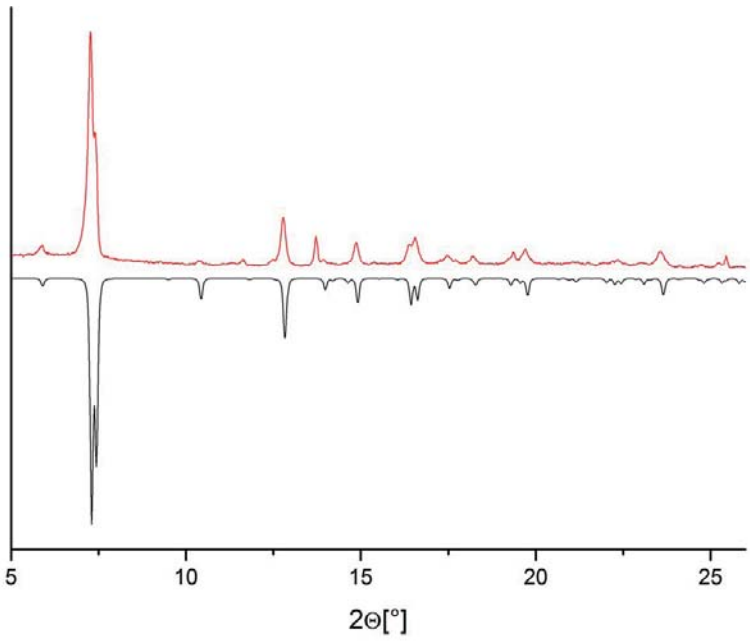

Figure S4. Measured (black) and calculated (red) powder diffraction patterns of compound **IV**.

4. Crystal Morphology

Figure S5 shows the morphology of the crystals of compounds **I** - **IV**. The crystal sizes could be determined to be around 1200 x 200 µm for **I**-**III** and 1000 x 125 µm for **IV**.

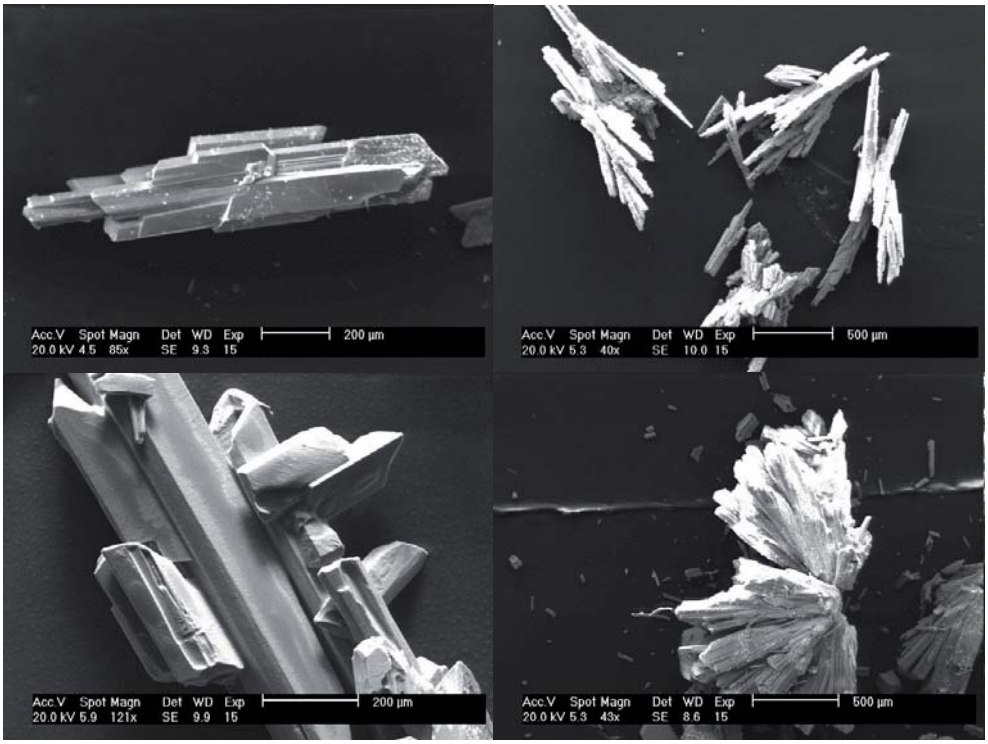

Figure S5. SEM pictures of compound **I** (top left), pseudopolymorphic compound **IV** (top right), bottom left: **II** and d) bottom right: **III**.

5. Calibration of the UV/Vis Absorption at 320 nm for Solubility Studies

The absorption vs. concentration calibration curve was obtained by dissolving **I** in different, defined concentrations in water ($1.31 \cdot 10^{-5}$ M, $2.30 \cdot 10^{-5}$ M, $3.28 \cdot 10^{-5}$ M, $4.27 \cdot 10^{-5}$ M, $5.58 \cdot 10^{-5}$ M) and measuring the UV/Vis spectra of these solutions. The peak maximum at 320 nm was evaluated and its absorption plotted against the sample concentration. A saturated solution of **I** in water was diluted by a factor of 1:25 to be in the concentration range of the calibration curve. The concentration was determined from its absorption at 320 nm and calculated back to that of the to determine the maximal solubility of **I** in water (1.19 g L^{-1}).

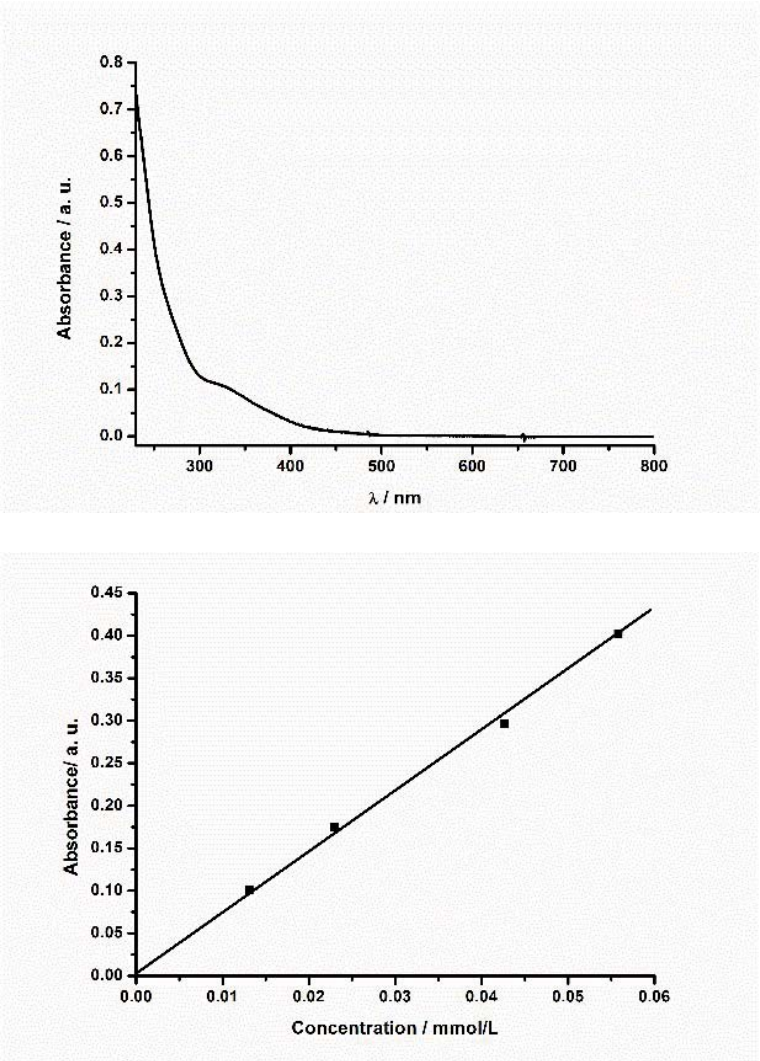

Figure S6. UV/Vis spectrum of **I** dissolved in water (top) and the calibration curve obtained from the peak maxima at 320 nm used to determine the maximal solubility (bottom).

6. Crystallographic Data

Table S2 summarizes information on single crystal structure refinement and shows clearly the similarity of the isostructural compounds **I** – **III** and the differences to the (pseudo)polymorphic compound **IV**.

Table S2 Selected crystal data and details of the structure refinement.

	III	**II**	**I**	**IV**
Formula	$C_{18}H_{92}N_{18}Fe_3$ $V_{15}Sb_6O_{52}$	$C_{18}H_{92}N_{18}Co_3$ $V_{15}Sb_6O_{52}$	$C_{18}H_{92}N_{18}Ni_3$ $V_{15}Sb_6O_{52}$	$C_{18}H_{74}N_{18}Ni_3$ $V_{15}Sb_6O_{43}$
MW / g·mol^{-1}	3055.24	3064.48	3063.82	2901.67
crystal system	monoclinic	monoclinic	monoclinic	trigonal
space group	*C*2	*C*2	*C*2	*P*321
a /Å	18.1991(4)	18.2302(14)	18.2404(7)	23.7437(5)
b / Å	22.6260(6)	22.6142(16)	22.7636(7)	23.7437(5)
c / Å	14.3614(3)	14.4067(11)	14.3542(5)	14.9586(3)
α / °	90	90	90	90
β / °	126.1930(10)	126.360(7)	126.449(3)	90
γ / °	90	90	90	120
V / Å^3	4772.49(19)	4783.0(6)	4794.2(3)	7303.3(3)
T / K	200	200	293	200
Z	2	2	2	3
D_{calc} / Mg·m^3	2.114	2.115	2.110	1.9767
μ / mm^{-1}	3.582	3.639	3.700	3.631
θ_{max} / °	27.94	28.00	27.00	25.00
measured refl.	37515	19592	14462	38040
unique refl.	11411	10404	8392	8614
R_{int}	0.0448	0.0647	0.0274	0.0717
refl. with $F_0>4\sigma(F_0)$	11411	10404	8392	8614
Parameters	503	503	503	463
$R_1[F_0>4\sigma(F_0)]$	0.0324	0.0453	0.0382	0.0580
wR_2 (all refl.)	0.0768	0.1187	0.0941	0.1438
GOF	1.058	1.045	1.027	0.987
$\Delta\rho_{max/min}$ /e·Å^{-3}	1.169/-0.922	1.867/-1.609	1.249/-1.070	1.338/-0.862

Flack-x-paramter	-0.02(2)	-0.07(3)	-0.006(19)	-0.028(19)

Bond valence sum (BVS) [2] yield following values:

Compound **I**: V 3.95 – 4.06, average: 4.00 and Sb 3.21 – 3.46, average: 3.37;

Compound **II**: V 3.90 – 4.06, average: 3.99 and Sb 3.21 – 3.48, average: 3.37;

Compound **III**: V 3.92 – 4.04, average 4.00 and Sb 3.38 – 3.61, average 3.51;

Compound **IV** V 3.82 – 4.12, average: 4.01 and Sb 3.29 – 3.53, average: 3.45.

All values are in the typical range of antimonato-polyoxovanadates.[1b,c,d,e,h]

The V-O bond lengths can be divided into four groups (Tables S3 – S6): Oa terminal V=O, O_b Sb-μ-O between two Sb atoms; O_c Sb/V-μ-O between two V and one Sb atom; O_d V-μ-O with only V atoms are involved.

Table S3 Bond lengths of the four different oxygen atom types of **I** in Å.

Type	Atom	V	V	V	Sb	Sb
Oa	O7	1.606(6)				
Oa	O9	1.596(8)				
Oa	O11	1.619(5)				
Oa	O13	1.620(6)				
Oa	O16	1.611(6)				
Oa	O19	1.609(5)				
Oa	O20	1.615(6)				
Oa	O21	1.600(5)				
Ob	O1				1.933(6)	1.909(6)
Ob	O22				1.926(4)	1.926(4)
Oc	O2	1.967(6)	2.009(5)		1.945(5)	
Oc	O3	1.966(5)	1.982(6)		1.977(5)	
Oc	O4	1.980(5)	1.983(5)		1.948(5)	
Oc	O5	1.975(6)	2.006(6)		1.927(5)	
Oc	O14	1.987(5)	1.984(6)		1.932(5)	
Oc	O17	2.011(6)	1.967(6)		1.953(6)	
Od	O6	1.913(5)	1.950(5)	1.930(5)		
Od	O8	1.955(5)	1.932(4)	1.955(5)		
Od	O10	1.931(6)	1.916(5)	1.927(6)		
Od	O12	1.941(6)	1.929(5)	1.957(5)		
Od	O15	1.922(5)	1.937(5)	1.946(5)		
Od	O18	1.912(6)	1.913(5)	1.940(6)		

Table S4 Bond lengths of the four different oxygen atom types of **II** in Å.

Type	Atom	V	V	V	Sb	Sb
Oa	O7	1.615(3)				
Oa	O9	1.597(7)				
Oa	O11	1.624(5)				
Oa	O13	1.628(5)				
Oa	O16	1.616(5)				
Oa	O19	1.621(5)				
Oa	O20	1.614(6)				
Oa	O21	1.600(6)				
Ob	O1				1.958(5)	1.921(6)
Ob	O22				1.939(3)	1.939(3)
Oc	O2	1.969(5)	2.007(5)		1.953(5)	
Oc	O3	1.960(5)	1.975(5)		2.007(5)	
Oc	O4	1.979(5)	1.981(5)		1.963(5)	
Oc	O5	1.969(5)	2.003(6)		1.942(6)	
Oc	O14	1.971(6)	1.986(6)		1.956(6)	
Oc	O17	2.012(6)	1.981(6)		1.953(6)	
Od	O6	1.927(5)	1.954(5)	1.920(5)		
Od	O8	1.955(5)	1.931(5)	1.963(5)		
Od	O10	1.928(5)	1.916(5)	1.940(5)		
Od	O12	1.945(6)	1.932(6)	1.956(6)		
Od	O15	1.943(5)	1.944(5)	1.926(5)		
Od	O18	1.914(5)	1.922(5)	1.939(5)		

Table S5 Bond lengths (Å) of the four different oxygen atom types of **III** in Å.

Type	Atom	V	V	V	Sb	Sb
Oa	O7	1.607(3)				
Oa	O9	1.612(5)				
Oa	O11	1.616(3)				
Oa	O13	1.628(4)				
Oa	O16	1.618(4)				
Oa	O19	1.619(4)				
Oa	O20	1.622(4)				
Oa	O21	1.598(4)				
Ob	O1				1.950(4)	1.928(4)
Ob	O22				1.942(3)	1.942(3)
Oc	O2	1.966(3)	2.007(3)		1.952(3)	
Oc	O3	1.960(3)	1.966(3)		2.005(3)	
Oc	O4	1.975(3)	1.978(3)		1.964(3)	
Oc	O5	1.967(4)	2.001(4)		1.941(3)	
Oc	O14	1.974(4)	1.972(4)		1.958(4)	
Oc	O17	2.007(4)	1.982(4)		1.950(4)	
Od	O6	1.913(3)	1.946(3)	1.929(3)		
Od	O8	1.951(3)	1.937(3)	1.960(3)		
Od	O10	1.933(4)	1.907(4)	1.929(4)		
Od	O12	1.942(4)	1.930(4)	1.959(4)		
Od	O15	1.950(4)	1.942(4)	1.916(4)		
Od	O18	1.914(4)	1.918(4)	1.938(4)		

Table S6 Bond lengths of the four different oxygen atom types in Å of **IV**.

Type	Atom	V	V	V	Sb	Sb
Oa	O16	1.608(12)				
Oa	O17	1.602(12)				
Oa	O20	1.605(12)				
Oa	O21	1.628(12)				
Oa	O22	1.653(11)				
Ob	O11				1.909(14)	1.966(15)
Oc	O12	1.981(13)	2.013(14)		1.942(13)	
Oc	O13	1.943(13)	1.993(12)		1.967(13)	
Oc	O14	1.966(12)	1.956(13)		1.984(12)	
Oc	O15	1.994(13)	2.003(14)		1.938(14)	
Od	O18	1.896(12)	1.920(12)	1.933(13)		
Od	O19	1.917(11)	1.927(11)	1.952(10)		
Od	O23	1.872(12)	1.915(12)	1.956(12)		
Od	O24	1.888(12)	1.958(12)	1.965(12)		

Figure S7 shows the arrangement of the (pseudo)polymorph compound **IV** with its discrete cluster anions and the Ni amine complexes as counter cations.

Table S7 shows the TM-N bond length and angles. All values are in typical ranges for known TM amine complex acting as counter cations in heteroatom incorporated POVs.

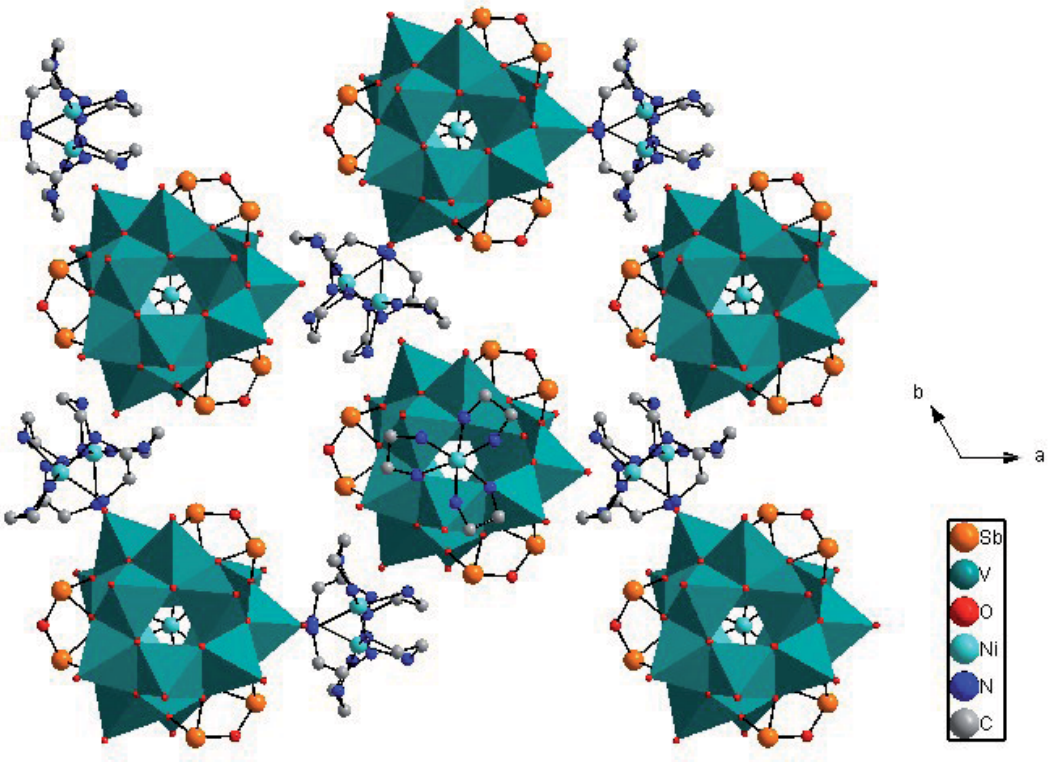

Figure S7. Arrangement of the cluster anions and transition metal complex cations of **IV**. Hydrogen atoms are not displayed for clarity.

Table S7 Selected bond lengths and bond angles of the $Ni(en)_3^{2+}$ cations in the crystal structure of compound **I**.

Bond Lengths		**Bond Angles**	
Ni(1)-N(2)	2.122(6)	N(2)-Ni(1)-N(11)	92.0(3)
Ni(1)-N(11)	2.124(9)	N(2)-Ni(1)-N(22)	92.1(3)
Ni(1)-N(22)	2.134(9)	N(11)-Ni(1)-N(22)	92.1(3)
Ni(1)-N(1)	2.139(8)	N(2)-Ni(1)-N(1)	80.1(3)
Ni(1)-N(12)	2.140(7)	N(11)-Ni(1)-N(1)	96.7(3)
Ni(1)-N(21)	2.146(8)	N(22)-Ni(1)-N(1)	168.4(3)
Ni(2)-N(41)	2.119(8)	N(2)-Ni(1)-N(12)	170.1(3)
Ni(2)-N(32)	2.123(9)	N(11)-Ni(1)-N(12)	81.3(3)
Ni(2)-N(31)	2.131(8)	N(41)-Ni(2)-N(32)	171.5(4)
		N(41)-Ni(2)-N(31)	93.4(4)
		N(32)-Ni(2)-N(31)	81.1(4)
		N(22)-Ni(1)-N(12)	95.3(3)
		N(1)-Ni(1)-N(12)	93.5(3)
		N(2)-Ni(1)-N(21)	94.4(3)
		N(11)-Ni(1)-N(21)	170.5(3)
		N(22)-Ni(1)-N(21)	80.6(3)
		N(1)-Ni(1)-N(21)	91.3(3)
		N(12)-Ni(1)-N(21)	93.2(3)

Table S8 Selected bond lengths and angles of the $Co(en)_3^{2+}$ cations in the crystal structure of compound **II**.

Bond Lengths		**Bond Angles**	
Co(1)-N(1)	2.201(7)	N(11)-Co(1)-N(1)	97.7(3)
Co(1)-N(2)	2.162(7)	N(12)-Co(1)-N(1)	92.4(3)
Co(1)-N(11)	2.169(7)	N(22)-Co(1)-N(1)	166.9(3)
Co(1)-N(12)	2.172(7)	N(21)-Co(1)-N(1)	90.9(3)
Co(1)-N(22)	2.184(7)	N(32)-Co(2)-N(41)	171.4(3)
Co(1)-N(21)	2.186(8)	N(32)-Co(2)-N(31)	80.1(3)
Co(2)-N(32)	2.168(8)	N(41)-Co(2)-N(31)	93.6(3)
Co(2)-N(31)	2.180(8)	N(2)-Co(1)-N(11)	91.5(3)
		N(2)-Co(1)-N(12)	168.4(3)
		N(11)-Co(1)-N(12)	80.7(3)
		N(2)-Co(1)-N(22)	91.6(3)
		N(11)-Co(1)-N(22)	92.6(3)
		N(12)-Co(1)-N(22)	97.3(3)
		N(2)-Co(1)-N(21)	95.3(3)
		N(11)-Co(1)-N(21)	169.8(3)
		N(12)-Co(1)-N(21)	93.6(3)
		N(22)-Co(1)-N(21)	79.7(3)
		N(2)-Co(1)-N(1)	80.1(3)

Table S9 Selected bond lengths and angles of the $Fe(en)_3^{2+}$ cations in the crystal structure of compound **III**.

Bond Lengths		**Bond Angles**	
Fe(1)-N(2)	2.193(5)	N(2)-Fe(1)-N(21)	96.74(18)
Fe(1)-N(12)	2.210(5)	N(12)-Fe(1)-N(21)	93.5(2)
Fe(1)-N(11)	2.211(5)	N(11)-Fe(1)-N(21)	167.40(19)
Fe(1)-N(22)	2.223(5)	N(22)-Fe(1)-N(21)	78.23(18)
Fe(1)-N(21)	2.234(5)	N(31)-Fe(2)-N(32)	78.4(2)
Fe(1)-N(1)	2.237(5)	N(31)-Fe(2)-N(41)	94.1(2)
Fe(2)-N(31)	2.208(5)	N(32)-Fe(2)-N(41)	169.6(2)
Fe(2)-N(32)	2.210(5)	N(2)-Fe(1)-N(12)	166.43(19)
Fe(2)-N(41)	2.215(5)	N(2)-Fe(1)-N(11)	91.9(2)
		N(12)-Fe(1)-N(11)	79.6(2)
		N(2)-Fe(1)-N(22)	91.29(19)
		N(12)-Fe(1)-N(22)	99.5(2)
		N(11)-Fe(1)-N(22)	92.5(2)
		N(2)-Fe(1)-N(1)	78.44(18)
		N(12)-Fe(1)-N(1)	92.4(2)
		N(11)-Fe(1)-N(1)	98.9(2)
		N(22)-Fe(1)-N(1)	164.87(19)
		N(21)-Fe(1)-N(1)	91.8(2)

Table S10 Selected bond lengths and angles of the $Ni(en)_3^{2+}$ cations in the crystal structure of compound **IV**.

Bond Lengths		**Bond Angles**	
Ni(1)-N(1)#7	2.110(17)	N(9)-Ni(3)-N(9)#4	92.6(12)
Ni(1)-N(1)#8	2.110(17)	N(9)-Ni(3)-N(9)#9	79(2)
Ni(1)-N(1)	2.110(17)	N(9)#4-Ni(3)-N(9)#9	167(3)
Ni(1)-N(2)#7	2.119(17)	N(9)-Ni(3)-N(9)#10	167(3)
Ni(1)-N(2)	2.119(17)	N(9)#4-Ni(3)-N(9)#10	98(2)
Ni(1)-N(2)#8	2.119(17)	N(9)#9-Ni(3)-N(9)#10	92.6(12)
Ni(11)-N(3)	2.110(13)	N(9)-Ni(3)-N(9)#11	98(2)
Ni(11)-N(6)	2.112(19)	N(9)#4-Ni(3)-N(9)#11	79(2)
Ni(11)-N(8)	2.12(2)	N(9)#9-Ni(3)-N(9)#11	92.6(12)
Ni(11)-N(5)	2.121(16)	N(9)#10-Ni(3)-N(9)#11	92.6(12)
Ni(11)-N(4)	2.12(2)	N(9)-Ni(3)-N(9)#3	92.6(12)
Ni(11)-N(7)	2.14(2)	N(9)#4-Ni(3)-N(9)#3	92.6(12)
Ni(3)-N(9)#4	2.10(3)	N(9)#9-Ni(3)-N(9)#3	98(2)
Ni(3)-N(9)#9	2.10(3)	N(9)#10-Ni(3)-N(9)#3	79(2)
Ni(3)-N(9)#10	2.10(3)	N(1)#7-Ni(1)-N(1)#8	92.0(6)
Ni(3)-N(9)#11	2.10(3)	N(1)#7-Ni(1)-N(1)	92.0(6)
Ni(3)-N(9)#3	2.10(3)	N(1)#8-Ni(1)-N(1)	92.0(6)
		N(1)#7-Ni(1)-N(2)#7	173.6(7)
		N(1)#8-Ni(1)-N(2)#7	91.7(7)
		N(1)-Ni(1)-N(2)#7	82.7(6)
		N(1)#7-Ni(1)-N(2)	91.7(7)
		N(1)#8-Ni(1)-N(2)	82.7(6)
		N(1)-Ni(1)-N(2)	173.6(7)
		N(2)#7-Ni(1)-N(2)	94.0(6)
		N(1)#7-Ni(1)-N(2)#8	82.7(6)
		N(1)#8-Ni(1)-N(2)#8	173.6(7)
		N(1)-Ni(1)-N(2)#8	91.7(7)
		N(2)#7-Ni(1)-N(2)#8	94.0(6)
		N(2)-Ni(1)-N(2)#8	94.0(6)
		N(3)-Ni(11)-N(6)	170.5(7)
		N(3)-Ni(11)-N(8)	93.6(7)

	N(6)-Ni(11)-N(8)	94.8(8)
	N(3)-Ni(11)-N(5)	91.4(6)
Table S10 continued	N(6)-Ni(11)-N(5)	81.0(8)
	N(8)-Ni(11)-N(5)	170.6(7)
	N(3)-Ni(11)-N(4)	82.7(7)
	N(6)-Ni(11)-N(4)	92.6(8)
	N(8)-Ni(11)-N(4)	91.4(7)
	N(5)-Ni(11)-N(4)	97.2(8)
	N(3)-Ni(11)-N(7)	90.2(8)
	N(6)-Ni(11)-N(7)	95.6(8)
	N(8)-Ni(11)-N(7)	80.0(8)
	N(5)-Ni(11)-N(7)	92.0(8)
	N(4)-Ni(11)-N(7)	168.6(7)
	N(9)#11-Ni(3)-N(9)#3	167(3)

The discrete cluster anions and the discrete $M(en)_3^{2+}$ cations form a complex hydrogen network. The hydrogen bond lengths and the corresponding interacting atoms for all four compounds are listed in Tables S8 – S11.

Table S11 Hydrogen bonds with H-A < r(A) + 2.000 Å and °DHA > 110 ° of compound **I**.

D-H	d(D-H)	d(H-A)	°DHA	d(D-A)	A
N1-H1N	0.920	2.357	141.34	3.128	O21 [x, y, z+1]
N2-H3N	0.920	2.022	164.17	2.918	O16
N2-H4N	0.920	2.283	167.58	3.188	O32 [-x+2, y, -z+2]
N11-H5N	0.920	2.206	154.72	3.063	O20 [x, y, z+1]
N11-H6N	0.920	2.212	153.73	3.064	O7 [-x+3/2, y+1/2, -z+1]
N12-H7N	0.920	2.093	155.43	2.954	O9 [x-1/2, y+1/2, z]
N12-H8N	0.920	2.172	152.56	3.019	O31 [-x+1, y, -z+1]
N21-H9N	0.920	2.535	140.58	3.298	O16
N22-H11N	0.920	2.361	150.53	3.194	O8 [-x+3/2, y+1/2, -z+1]
N31-H13N	0.920	2.188	163.43	3.081	O11 [-x+1, y, -z]
N31-H14N	0.920	2.360	148.09	3.179	O31 [-x+1, y, -z]
N32-H15N	0.920	2.245	158.72	3.121	O6
N32-H16N	0.920	2.566	118.50	3.112	O11
N41-H17N	0.920	2.425	130.19	3.099	O18 [-x+1, y, -z]
N41-H17N	0.920	2.492	148.45	3.311	O19 [-x+1, y, -z]
N41-H18N	0.920	2.220	149.86	3.050	O21 [-x+1, y, -z]

TableS12. Hydrogen bonds with H-A < r(A) + 2.000 Å and °DHA > 110 ° of compound **II**.

D-H	d(D-H)	d(H-A)	°DHA	d(D-A)	A
N1-H1N	0.920	2.353	139.09	3.107	O21 [x, y, z+1]
N2-H3N	0.920	2.021	165.98	2.922	O16
N2-H4N	0.920	2.302	164.36	3.197	O32 [-x+2, y, -z+2]
N11-H5N	0.920	2.202	152.22	3.046	O20 [x, y, z+1]
N11-H6N	0.920	2.245	152.02	3.088	O7 [-x+3/2, y+1/2, -z+1]
N12-H7N	0.920	2.098	156.55	2.964	O9 [x-1/2, y+1/2, z]
N12-H8N	0.920	2.248	150.48	3.082	O31 [-x+1, y, -z+1]
N21-H9N	0.920	2.482	142.36	3.259	O16
N22-H11N	0.920	2.389	147.98	3.206	O8 [-x+3/2, y+1/2, -z+1]
N31-H13N	0.920	2.196	161.51	3.083	O11 [-x+1, y, -z]
N31-H14N	0.920	2.362	147.25	3.175	O31 [-x+1, y, -z]
N32-H15N	0.920	2.242	160.50	3.124	O6
N32-H16N	0.920	2.538	118.68	3.087	O11
N41-H17N	0.920	2.429	130.14	3.103	O18 [-x+1, y, -z]
N41-H17N	0.920	2.492	148.81	3.314	O19 [-x+1, y, -z]
N41-H18N	0.920	2.214	150.98	3.051	O21 [-x+1, y, -z]

Table S13. Hydrogen bonds with H-A < r(A) + 2.000 Å and °DHA > 110 ° of compound **III**.

D-H	d(D-H)	d(H..A)	°DHA	d(D..A)	A
N1-H2N	0.900	2.383	138.19	3.112	O21 [x, y, z-1]
N2-H3N	0.900	2.386	164.69	3.262	O32 [-x, y, -z]
N2-H4N	0.900	2.040	165.97	2.921	O16
N11-H5N	0.900	2.313	150.79	3.130	O7 [-x+1/2, y-1/2, -z+1]
N11-H6N	0.900	2.219	152.64	3.046	O20 [x, y, z-1]
N12-H7N	0.900	2.274	151.69	3.096	O31 [-x+1, y, -z+1]
N12-H8N	0.900	2.109	154.88	2.949	O9 [x+1/2, y-1/2, z]
N21-H10N	0.900	2.489	143.94	3.260	O16
N22-H12N	0.900	2.458	144.75	3.235	O8 [-x+1/2, y-1/2, -z+1]
N31-H13N	0.900	2.442	143.57	3.211	O31 [-x+1, y, -z+2]
N31-H14N	0.900	2.246	161.54	3.113	O11 [-x+1, y, -z+2]
N32-H15N	0.900	2.539	122.39	3.115	O11
N32-H16N	0.900	2.276	156.25	3.121	O6
N41-H17N	0.900	2.248	149.94	3.060	O21 [-x+1, y, -z+2]
N41-H18N	0.900	2.477	132.08	3.151	O18 [-x+1, y, -z+2]
N41-H18N	0.900	2.546	148.99	3.349	O19 [-x+1, y, -z+2]

Table S14. Hydrogen bonds with H..A < r(A) + 2.000 Å and <DHA > 110 ° of compound **IV**.

D-H	d(D-H)	d(H..A)	°DHA	d(D..A)	A
N1-H1N1	0.990	2.359	146.28	3.230	O22 [y, x, -z+2]
N1-H1N1	0.990	2.316	135.82	3.104	O23 [x-y+1, -y+1, -z+2]
N1-H2N1	0.990	2.307	142.40	3.150	O22 [x-y+1, -y+1, -z+2]
N2-H1N2	0.990	2.334	144.61	3.192	O17 [-x+1, -x+y, -z+1]
N2-H1N2	0.990	2.321	138.51	3.132	O18 [x-y+1, -y+1, -z+1]
N2-H2N2	0.990	2.397	133.80	3.164	O17 [x-y+1, -y+1, -z+1]
N3-H1N3	0.990	1.996	164.95	2.963	O20 [-x+y, -x+1, z]
N4-H1N4	0.990	2.401	133.90	3.169	O17 [-x+1, -x+y, -z+1]
N5-H1N5	0.990	2.183	149.08	3.075	O16 [y, x, -z+1]
N5-H2N5	0.990	2.297	148.78	3.185	O4 [y, x, -z+2]
N6-H1N6	0.990	1.972	154.28	2.895	O5
N7-H1N7	0.990	2.414	147.12	3.290	O6
N8-H1N8	0.990	2.378	145.14	3.240	O20 [-x+y, -x+1, z]
N9-H1N9	0.990	2.195	159.46	3.141	O7
N9-H1N9	0.990	2.477	123.67	3.136	O8
N9-H2N9	0.990	2.414	149.25	3.304	O7 [-x+y+1, -x+2, z]

7. Magnetic Properties

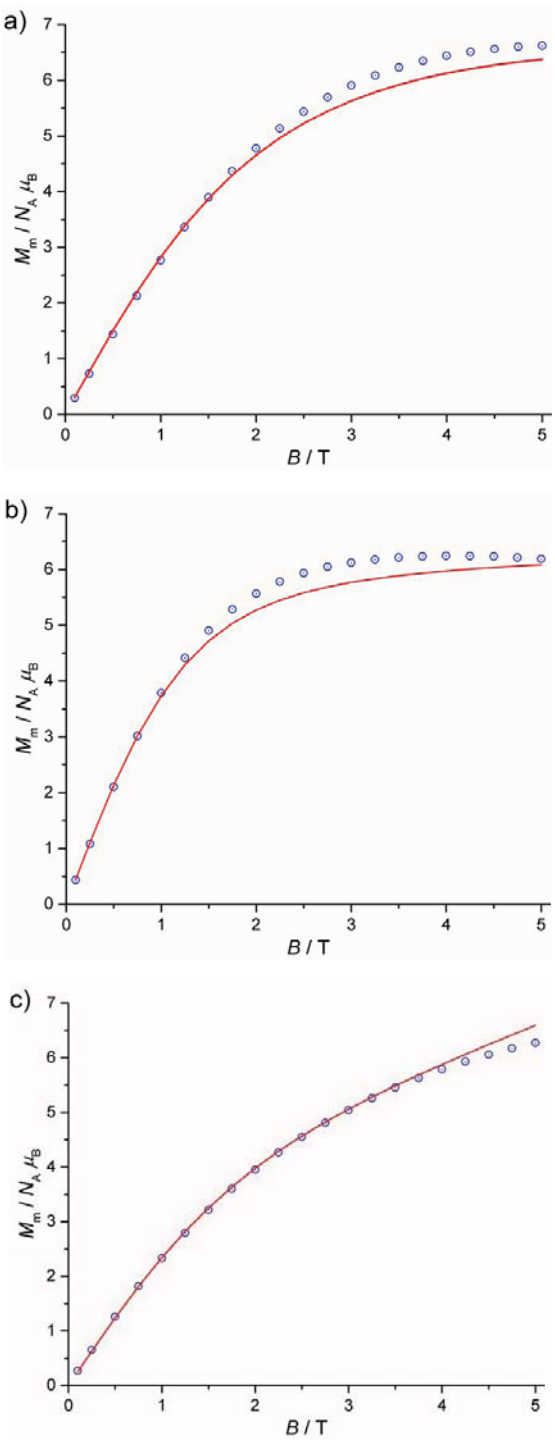

Figure S8. Molar magnetization M_m as a function of the applied field B: M_m(exp) – M_m($[V_{15}Sb_6O_{42}]^{6-}$) for compound **I** (a), **II** (b), **III**), shown as blue open circles;
best fits: red lines.

Table S15. Parameters of the "full model" simulations of **I** – **III**.

Parameter	**I** (M = Ni)	**II** (M = Co)	**III** (M = Fe)
Racah *B* [a] / cm^{-1}	1084	1115	1058
Racah *C* [a] / cm^{-1}	4831	4366	3901
ζ_{3d} [a] / cm^{-1}	649	533	410
*B***Error!** [b] / cm^{-1}	–24307 ± 484	–842 ± 80	13426 ± 43
*B***Error!** [b] / cm^{-1}	26213 ± 98	43382 ± 50	39262 ± 15
*B***Error!** [b] / cm^{-1}	13898 ± 167	25154 ± 16	10064 ± 35
zJ' [c] / cm^{-1}	–0.01 ± 0.01	+0.01 ± 0.01	–0.53 ± 0.01
SQ [d]	2.1%	2.6%	1.6%

[a] Griffith, J.S. *The Theory of Transition-Metal Ions*, Cambridge University Press, Cambridge, 1971; [b] ligand field parameter in Wybourne notation; [c] mean field parameter ("–2*J*" notation) [d] goodness of fit.

8. Electrospray ionization mass spectrometry

Besides the known signals of $[\mathbf{M}]^{3-}$/$[\mathbf{M}\cdot H]^{3-}$, $[\mathbf{M}\cdot H_2O]^{3-}$/$[\mathbf{M}\cdot H\cdot H_2O]^{3-}$, $[\mathbf{M}\cdot Ni(en))]^{2-}$/ $[\mathbf{M}\cdot H\cdot Ni(en)]^{2-}$, $[\mathbf{M}\cdot Ni(en)\cdot H_2O]^{2-}$/$[\mathbf{M}\cdot H\cdot Ni(en)\cdot H_2O]^{2-}$ and $[\mathbf{N}\cdot H_2O]^{3-}$/$[\mathbf{N}\cdot H\cdot H_2O]^{3-}$ at *m*/*z* 722, 728, 1142, 1151 and 792, respectively, in the ESI-Q-TOF-HRMS spectra of $\{Ni(en)_3\}_3[V_{15}Sb_6O_{42}]$, a series of peaks exists for which no conclusive assignment could be made (*m*/*z* 671, 677, 696, 702, 766, 1104, 1113).

In all experiments performed (ESI mass spectra at different ionization conditions, H/D- and $^{16}O/^{18}O$-exchange experiments, collision-induced fragmentation experiments), these ions behave in close analogy to the parent cluster. It can thus be assumed that they belong to structurally closely related cluster species, for which we were nevertheless unable to find a fully convincing elemental composition, which is in line with all experimental data.

As the powder diffraction patterns of a sample that was used for the mass spectrometric experiments clearly showed the sample not to contain significant amounts of impurities, we assume that these signals correspond to a marginal level of impurities, which are more easily ionized and thus appear with higher intensities in the mass spectra than expected from their abundance in the sample.

9. References

(1) (a) Y. Gao, Z. Han, Y. Xu, C. Hu, *J. Clust. Sci*., 2010, **21**, 163; (b) E. Antonova C. Näther, P. Kögerler, W. Bensch, *Angew. Chem*., 2011, **123**, 790 ; (c) R. Kiebach, C. Näther, P. Kögerler, W. Bensch, *Dalton Trans.,* 2007, 3221; (d) E. Antonova, C. Näther, W. Bensch, *Dalton Trans.,* 2012, **41**, 1338; (e) E. Antonova, C. Näther, W. Bensch, *CrystEngComm.,* 2012, **14**, 6853; (f) E. Antonova, C. Näther, P. Kögerler, W. Bensch, *Dalton Trans*., 2012, **41**, 6957; (g) L. Yu, J.-P. Liu, J.-P. Wang, J.-Y. Niu, *Chem. Res. Chinese Universities,* 2009, **25**, 426; (h) E. Antonova, C. Näther, P. Kögerler, W. Bensch, *Inorg. Chem.,* 2012, **51**, 2311.

(2) M. O'Keeffe, N. E. Brese, *J. Am. Chem. Soc*., 1991, **113**, 3226.

6.3.6. Configurational Isomerism in Polyoxovanadates

Lisa K. Mahnke, Aleksandar Kondinski, Ulrike Warzok, Christian Näther, Jan van Leusen, Christoph A. Schalley, Kirill Y. Monakhov, Paul Kögerler, Wolfgang Bensch

Angew. Chem. Int. Ed. **2018**, *57*, 2972–2975; *Angew. Chem.* **2018**, *130*, 3024–3028.

Submitted on June 19, 2017, resubmitted on December 4, 2017, first published online as an accepted manuscript on January 12, 2018 in Angewandte Chemie International Edition and Angewandte Chemie. Electronic versions of the article are available (https://doi.org/10.1002/anie.201712417, https://doi.org/10.1002/ange.201712417).

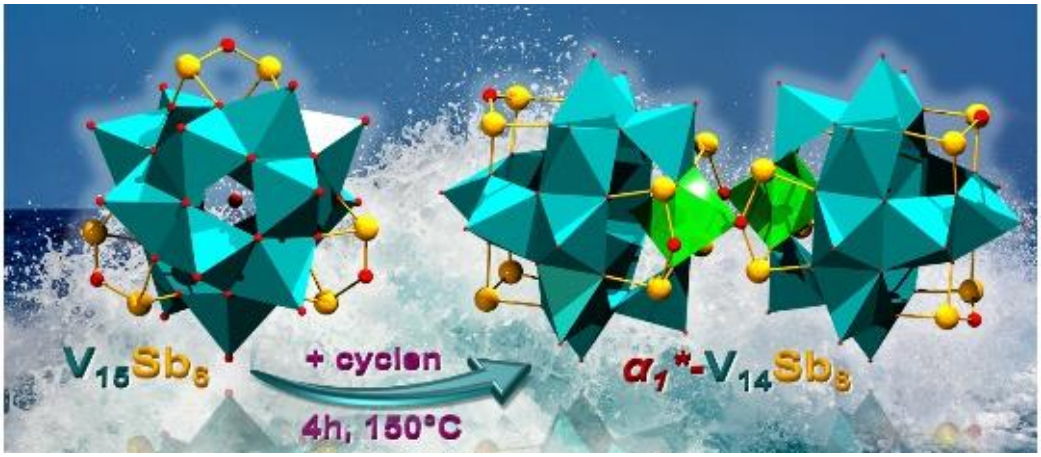

Figure A.6: Graphical abstract. Reprinted from Mahnke *et al.*[225] (© 2018 WILEY-VCH Verlag GmbH & Co. KGaA, Weinheim).

A copy of the original work is not included in the online version due to restrictions by the publisher.

6.3.7. The New Water-Soluble Cluster Compound $\{Zn(en)_3\}_3[V_{15}Sb_6O_{42}(H_2O)]\cdot(ethylenediamine)_3\cdot 10H_2O$ as a Synthon for the Generation of two New Antimonato Polyoxovanadates

Lisa K. Mahnke, Ulrike Warzok, Mengxi Lin, Christian Näther, Christoph A. Schalley, Wolfgang Bensch

Chem. Eur. J. **2018**, *24*, 5522–5528.

Submitted on December 4, 2017, first published online on February 21, 2018 in Chemistry- A European Journal.

An electronic version of the article is available (https://doi.org/10.1002/chem.201705732).

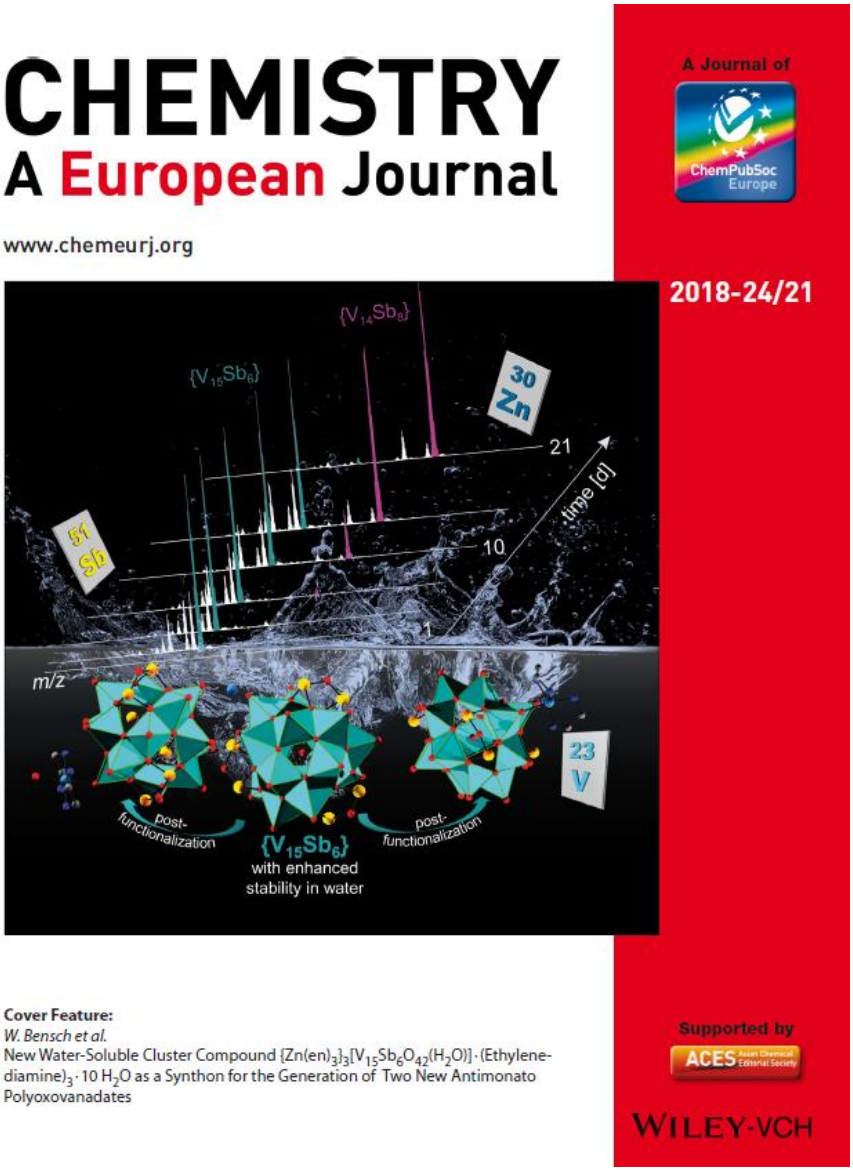

Figure A.7: Cover picture. Reprinted from Mahnke *et al.*[226] (© 2018 WILEY-VCH Verlag GmbH & Co. KGaA, Weinheim).

A copy of the original work is not included in the online version due to restrictions by the publisher.

6.3.8. Polyamide–Polyamine Cryptand as Dicarboxylate Receptor: Dianion Binding Studies in the Solid State, in Solution, and in the Gas Phase

Sourav Chakraborty, Subrata Saha, Luís M. P. Lima, Ulrike Warzok, Sayan Sarkar, Bidyut Akhuli, Mandira Nandi, Somnath Bej, Nayarassery N. Adarsh, Christoph A. Schalley, Rita Delgado, and Pradyut Ghosh

J. Org. Chem. **2017**, *82*, 10007–10014.

Submitted on June 9, 2017, first published on August 28, 2017 in Journal of Organic Chemistry.

An electronic version of the article is available (https://doi.org/10.1021/acs.joc.7b01431).

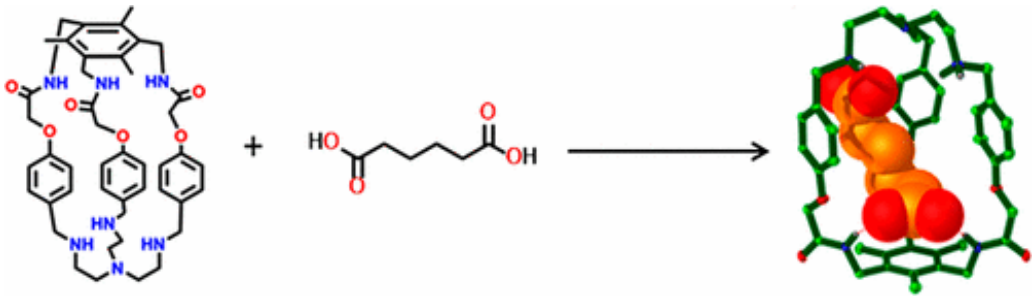

Figure A.8: Graphical abstract. Reprinted with permission from Chakraborty *et al*.[230] (© 2017, American Chemical Society).

A copy of the original work is not included in the online version due to restrictions by the publisher.